Processing and integrity of DC/DF GBAS for CAT II/III operations

Giuseppe Rotondo

Giuseppe Rotondo. Processing and integrity of DC/DF GBAS for CAT II/III operations. Signal and Image processing. Institut National Polytechnique de Toulouse - INPT, 2016. English. NNT : 2016INPT0115 . tel-04260928v2

HAL Id: tel-04260928
https://theses.hal.science/tel-04260928v2

Submitted on 26 Oct 2023

THÈSE

En vue de l'obtention du

DOCTORAT DE L'UNIVERSITÉ DE TOULOUSE

Délivré par :
Institut National Polytechnique de Toulouse (INP Toulouse)

Discipline ou spécialité :
Signal, Image, Acoustique et Optimisation

Présentée et soutenue par :
M. GIUSEPPE ROTONDO
le lundi 12 décembre 2016

Titre :

Processing and Integrity of DC/DF GBAS for CAT II/III Operations

---

Ecole doctorale :
Mathématiques, Informatique, Télécommunications de Toulouse (MITT)

Unité de recherche :
Laboratoire de Télécommunications (TELECOM-ENAC)

Directeur(s) de Thèse :
M. OLIVIER JULIEN
M. PAUL THEVENON

Rapporteurs :
M. BERND EISSFELLER, UNIVERSITAT DER BUNDESWEHR MUNICH
M. JAUME SANZ SUBIRANA, UNIV POLITECNICA DE CATALUNYA BARCELONA

Membre(s) du jury :
M. BERND EISSFELLER, UNIVERSITAT DER BUNDESWEHR MUNICH, Président
M. OLIVIER JULIEN, ECOLE NATIONALE DE L'AVIATION CIVILE, Membre
M. PAUL THEVENON, ECOLE NATIONALE DE L'AVIATION CIVILE, Membre

Abstract

In Civil Aviation domain, to cope with the increasing traffic demand, research activities are pointed toward the optimization of the airspace capacity. Researches are thus ongoing on all Civil Aviation areas: Communication, Navigation, Surveillance (CNS) and Air Traffic Management (ATM). Focusing on the navigation aspect, the goals are expected to be met by improving performances of the existing services through the developments of new NAVigation AIDS (NAVAIDS) and the definition of new procedures based on these new systems.

The Global Navigation Satellite System (GNSS) is recognized as a key technology in providing accurate navigation services with a worldwide coverage. A symbol of its importance, in civil aviation, can be observed in the avionics of new civil aviation aircraft since a majority of them are now equipped with GNSS receivers. The GNSS concept was defined by the International Civil Aviation Organization (ICAO).It, includes the provision of an integrity monitoring function by an augmentation system in addition to the core constellations. This is needed to meet all the required performance metrics of accuracy, integrity, continuity and availability which cannot be met by the stand-alone constellations such as GPS. Three augmentation systems have been developed within civil aviation: the GBAS (Ground Based Augmentation System), the SBAS (Satellite Based Augmentation System) and the ABAS (Aircraft Based Augmentation System).

GBAS, in particular, is currently standardized to provide precision approach navigation services down to Category I (CAT I) using GPS or Glonass constellations and L1 band signals. This service is known as GBAS Approach Service Type-C (GAST-C). In order to extend this concept down to CAT II/III service, research activities is ongoing to define the new service called a GAST-D. Among other challenges, the monitoring of the ionospheric threat is the area where the integrity requirement is not met.

Thanks to the deployment of new constellations, Galileo and Beidou, and the modernization process of the existing ones, GPS and Glonass, the future of GNSS is envisaged to be Multi-Constellation (MC) and Multi-frequency (MF). In Europe, research activities have been focused on a Dual-Constellation (DC) GNSS and DC GBAS services based on GPS and Galileo constellations. Benefits, brought by DC and DF, are related to

- the robustness of the entire system against unintentional interference thanks to the use of measurements in two protected frequency bands,
- the robustness against a constellation failure,
- the accuracy improvement by using new signals with improved performance, and more satellites.

- improved detection of ionosphere anomalous condition thanks to the use of DF measurements.
- mitigation of the residual ionospheric induced range error

These last points in particular are considered as one of the biggest benefits brought by the DF GBAS. To overcome the problems experienced by Single-Frequency (SF) GBAS due to ionosphere anomalies, the use of two frequencies (Dual Frequency, DF) has been selected as a mean to improve ionosphere anomalies detection and to mitigate ionosphere residual errors. Advantages in using a DC/DF GBAS (GAST-F) system are, however, not only related to the integrity monitoring performance improvement.

However, the use of new signals and a new constellation, does not bring only benefits. It also raises a series of challenges that have to be solved to fully benefit from the new concept.

In this thesis, some challenges, related to DC/DF GBAS, have been investigated. One of them, rising from the use of new GNSS signals, is to determine the impact of error sources that are uncorrelated between the ground station and the aircraft and that induce an error on the estimated position. Using two frequencies, there is the possibility to form measurement combinations like Divergence-free (D-free) and Ionosphere-free (I-free) for which the errors impact has to be analyzed. In this thesis, the impact of the uncorrelated errors (noise and multipath as main sources) on ground measurements is analyzed. The aim is to compare the derived performances with the curve proposed in (RTCA Inc.; DO253-C, 2008) for the ground correction accuracy and derived for GPS L1 C/A.

Another issue raised by the use of DC/DF GBAS is the increased number of satellites and the presence of a second frequency. This leads to the constraint of having a big number of channels in GNSS receivers to track all available signals. Moreover, to broadcast a bigger number of corrections from the ground to the aircraft, the messages capacity has to be increased with respect to the current SF/SC GBAS. To solve this problem, some solutions have been proposed, one of these is the implementation of a satellite selection algorithm. In this PhD, the impact of some algorithms proposed in literature has been analyzed on a simulated DC GBAS system.

The last analysis performed in this thesis regards some of the challenges in the integrity monitoring domain. GBAS has been validated, nowadays, only for GAST-C to provide CAT I service. Although almost the same architecture has been used to provide CAT II/III service within GAST-D (but with new monitors on the ground architecture), the concept to derive the airworthiness between the two services is totally different. This major difference is justified by the fact that for CAT III operations, requirements are more stringent than for CAT I. Despite all the efforts done, GAST-D for CATII/III has not been validated. The cause of the non-validation of GAST-D is the lack of integrity performances in monitoring the ionosphere anomalous activity with the proposed monitoring scheme. Even if for GAST-F, relying on DF combinations, the monitoring of the ionosphere could not represent the main issue and the integrity performances of current monitors may be sufficient to meet the requirements, two considerations have to be done

- In case of loss of frequency, for GAST-F, the ionosphere monitoring presents the same condition as for GAST-D. If the latter is not validated, the fallback mode is GAST-C, limiting the availability of CAT II/III operations.
- Improving the integrity performances of GAST-D will permit to create a system with an enhanced CAT II/III operations availability thanks to the use of GAST-D as fallback mode in case of frequency loss whenever GAST-F is used as primary mode. In case of GAST-D as primary mode, GAST-F can be considered the fallback mode for cases of ionosphere anomalous conditions.

Considering previous conditions, the work done in this thesis has focused on the monitoring of the ionospheric conditions that are impeding GAST-D to be validated. A solution combining RAIM SC/SF GBAS differential corrections and foreseen GAST-D monitors is proposed. The combination of these integrity monitoring functions permit to get closer to GAST-D requirements for particular ionospheric scenarios where the maximum ionospheric induced range error can be assumed. The consideration of dual constellation in the same mix of integrity monitoring functions has also been studied, as a possible fallback mode of GAST-F when one of the two frequencies is lost.

The ionosphere is not the only integrity issue for GAST-F. Other analysis have been done considering the impact of new signals or new processing modes on the existing monitors. Concerning this, the impact of a lower update rate, for the PRC and RRC, on the Excessive Acceleration (EA) monitor has been analyzed. The aim is to verify the feasibility of the monitor in extending the current update interval from 0.5 seconds up to a proposed value of 2.5 seconds.

Résumé

Dans le domaine de l'aviation civile, afin de répondre à la demande croissante du trafic, les activités de recherche sont guidées par la volonté d'améliorer la capacité de l'espace aérien. Des recherches sont en cours dans tous les domaines de l'aviation civile: Communication, Navigation, Surveillance (CNS) et de gestion du trafic aérien (Air Traffic Management, ATM). En ce que concerne la navigation, les objectifs devraient être atteints par l'amélioration des performances des services existants grâce au développement des nouvelles aides à la navigation et la définition de nouvelles procédures basées sur ces nouveaux systèmes.

La navigation par satellite, grâce au concept de Global Navigation Satellite System (GNSS), est reconnue comme une technologie clé pour fournir des services de navigation précis avec une couverture mondiale. Le concept GNSS a été défini par l'Organisation de l'Aviation Civile Internationale (OACI). Son importance dans l'aviation civile peut être observée dans l'avionique de nouveaux avions puisque la majorité d'entre eux sont maintenant équipés de récepteurs GNSS. Le GNSS comprend une fonction de surveillance de l'intégrité fournie par un système d'augmentation en plus de la constellation de base. Ceci est nécessaire pour répondre à toutes les exigences concernant la précision, l'intégrité, la continuité et la disponibilité qui ne peuvent pas être fournis par les constellations autonomes comme le GPS ou Glonass. Trois systèmes d'augmentation ont été développés au sein de l'aviation civile: le GBAS (Ground Based Augmentation System), le SBAS (Satellite Based Augmentation System) et l'ABAS (Aircraft Based Augmentation System).

Le système GBAS, en particulier, est actuellement standardisé pour fournir des services de navigation, comme l'approche de précision, jusqu'à la Catégorie I (CAT I) en utilisant les constellations GPS ou Glonass et des signaux dans la bande L1. Ce service est connu sous le nom de GBAS Approach Service Type-C (GAST-C). Afin d'étendre ce concept jusqu'à des approche de précision CAT II/II, les activités de recherche sont en cours pour définir le nouveau service appelé GAST-D. Parmi tous les défis, la surveillance de la menace ionosphérique est le secteur où le niveau d'intégrité est insuffisant.

Grâce au développement des nouvelles constellations, Galileo et Beidou, et grâce au processus de modernisation des autres constellations existantes, GPS et Glonass, l'avenir du GNSS sera Multi-Constellation (MC) et Multi-Fréquence (MF). En Europe, les activités de recherche se sont concentrées sur un système GNSS Bi-Constellation (Dual-Constellation, DC) basé sur GPS et Galileo. Les avantages d'un système DC/DF GBAS (GAST-F) sont :

- la robustesse de l'ensemble du système contre toute interférence involontaire grâce à l'utilisation de mesures effectuées dans deux bandes de fréquences protégées,
- la robustesse contre une panne d'une des deux constellations,

- l'amélioration de la précision à l'aide de nouveaux signaux avec des performances améliorées, et plusieurs satellites.
- l'amélioration de la détection d'anomalies ionosphérique
- atténuation des erreurs résiduelles dues à l'ionosphère

Ces derniers points sont considérés comme les plus grande avantage apportée par le GBAS double fréquence. Afin de surmonter les problèmes rencontrés par en fonctionnement Mono-Fréquence (Single-Frequency, SF) en présence d'anomalies ionosphériques, l'utilisation de deux fréquences (Dual-Frequency, DF) a été sélectionnée comme un moyen d'améliorer la détection des anomalies ionosphériques et d'atténuer les erreurs résiduelles ionosphériques.

Cependant, l'utilisation de nouveaux signaux et d'une nouvelle constellation, n'apporte pas que des avantages. Elle soulève également une série de défis qui doivent être résolus de profiter pleinement de ce nouveau concept.

Dans cette thèse, certains défis, liés à un système DC/DF GBAS ont été étudiés. Un d'entre eux, causé par l'utilisation de nouveaux signaux GNSS, est de déterminer l'impact des sources d'erreur qui sont décorrélées entre la station au sol et l'avion et qui induisent une erreur sur la position estimée. De plus, avec l'utilisation de deux fréquences, il y a la possibilité de former des combinaisons de mesure comme les mesures Divergence-free (D-free) et Ionosphère-free (I-free) pour lesquelles l'impact des erreurs doit être analysé. Dans cette thèse, l'impact des erreurs décorrélées (bruit et multitrajet principalement) sur les mesures au sol est analysé. L'objectif est de comparer les performances des nouveaux signaux et des différentes combinaisons possibles, avec la courbe proposée dans (RTCA Inc.; DO253-C, 2008) pour la précision des corrections calculées dans la station au sol pour GPS L1 C/A.

Un autre problème soulevé par l'utilisation de DC/DF GBAS est l'augmentation du nombre de satellites et la présence d'une deuxième fréquence. Cela nécessite un grand nombre de canaux dans les récepteurs pour poursuivre tous les signaux disponibles. En outre, pour envoyer un grand nombre de corrections, la capacité des messages de correction doit être augmentée. Pour résoudre ce problème, certaines solutions ont été proposées, l'une d'entre elles est la mise en œuvre d'un algorithme de sélection de satellite. Dans cette thèse, l'impact de certains algorithmes proposés dans la littérature a été analysé sur un système GBAS DC simulé.

La dernière analyse effectuée dans cette thèse concerne le domaine de la surveillance de l'intégrité. De nos jours, le GBAS a été validé uniquement dans le cadre du GAST-C pour fournir un service d'approche CAT I. Même si une architecture identique est utilisée pour fournir un service CAT II/III dans un cadre GAST-D (mais avec de nouveaux moniteurs sur la station de référence), le concept pour valider la navigabilité entre les deux services est totalement différent. Cette différence est justifiée par le fait que pour les opérations de CAT III, les exigences sont plus strictes que pour celles de CAT I.

Malgré tous les efforts faits, le GAST-D pour CAT II/III n'a pas été validé. La cause de la non-validation du GAST-D est le manque de performances d'intégrité dans la détection des activités ionosphériques anormales avec le système de surveillance proposé. Même si pour le GAST-F, en se fondant sur des combinaisons DF, la surveillance de l'ionosphère ne représentera pas le principal problème et même si les performances de l'intégrité des moniteurs actuels peuvent être suffisantes pour répondre aux exigences, deux considérations doivent être faites :

- En cas de perte d’une fréquence, pour GAST-F, la surveillance de l’ionosphère présente les mêmes conditions que pour GAST-D. Si celui-ci n'a pas été validé, le mode de repli est GAST-C, ce qui limite la disponibilité des CAT II / III.
- L’amélioration des performances de l'intégrité de GAST-D permettra de créer un système avec une disponibilité améliorée pour les opérations en CAT II/III grâce à l'utilisation de GAST-D en tant que mode de repli en cas de perte d’une fréquence à chaque fois que GAST-F est utilisé comme mode primaire. En cas d’utilisation de GAST-D en mode primaire, GAST-F peut être considéré comme le mode de repli en cas de conditions ionosphériques anormales.

Compte tenu des conditions précédentes, le travail effectué dans cette thèse a mis l'accent sur le suivi des conditions ionosphériques qui entravent la validation du GAST-D. Une solution combinant un algorithme de type RAIM, des corrections différentielles SF/SC GBAS et les moniteurs prévus en GAST-D est proposée. La combinaison de ces moniteurs permet de se rapprocher des exigences GAST-D pour certains scénarios où l’erreur ionosphériques maximale peut être modélisée. La prise en compte d’une deuxième constellation avec la même combinaison de fonctions de contrôle d'intégrité a également été étudiée, en tant que mode de repli possible de GAST-F lorsque l'une des deux fréquences est perdue.

L'ionosphère n’est pas le seul problème d'intégrité pour GAST-F. D'autres analyses doivent être faites compte tenu de l'impact des nouveaux signaux ou de nouveaux modes de traitement sur les moniteurs existants. Sur ce sujet, l'impact d'un taux de mise à jour plus bas des corrections différentielles sur le moniteur « Excessive Acceleration » a été analysé. Le but est de vérifier les bonnes performances du moniteur lorsque l'intervalle de mise à jour passe de la valeur actuelle de 0,5 seconde jusqu'à une valeur proposée de 2,5 secondes.

Acknowledgements

I would like to thank Professor Bernd Eissfeller and Professor Jaume Sanz Subirana for accepting to review my thesis manuscript, for their corrections and to attend to my thesis defence.

I would like to thank as well my thesis director Olivier Julien and, Christophe Macabiau and Carl Milner, for their help in these last three years. As well I have to thank Pierre Ladoux for its support and suggestions for the thesis work. I would like also to thank Frieder Beck for the provisions of ground measurements used in the thesis. Thanks to all SESAR 15.3.7 members for their help and for good moments had together.

A huge thank to my thesis co-director Paul Thevenon for its help and advice for the thesis work and for its help when the French language was the “unknown term” at the beginning of these three years.

As well as I would like to thank all people from the SIGNAV and EMA groups for all good moments spend together, in particular, my GBAS colleague Alizé who shared the office with me. Jeremy who tried to explain me rugby rules. Jean Baptiste for sharing the passion for food. Amany, Quentin and Capucine for sharing the office with me in the last months avoiding to let me alone. Johan for its bad results in learning the Italian language…but essentially THANKS TO ALL.

A “good luck” to all future Ph. D. student for their works.

Thanks to my friends, Alessio, Marco, Enik and Simon for keeping the motivation high with some beers, and all kind of liquors, in bad moments.

Last but not least, I would like to thank my family for the support given during these years.

Author(s) consulted Deliverable D03 of the SESAR 15.03.07 project .

Deliverable D03 of the SESAR 15.03.07 project has been developed by AENA, Airbus, DFS, DSNA, ENAC, ENAV, EUROCONTROL, Honeywell, INDRA, NATMIG, Selex, Thales and AT-One for the SESAR Joint Undertaking within the frame of the SESAR Programme co-financed by the EU and EUROCONTROL. It was provided "as is", without warranty of any kind, either express or implied, including, without limitation, warranties of merchantability, fitness for a particular purpose and non-infringement. Therefore, the provided document after review of the SJU may change, improve, be updated or replaced by another version without notice.

Deliverable D03 of the SESAR 15.03.07 project has been provided for informative purposes only. Under no circumstances shall the SJU be liable for any loss, damage, liability or expense incurred or suffered that is claimed to have resulted from the use of this document, including, without limitation, any fault, error, omission, interruption or delay with respect thereto.
This document may contain advice, opinions and statements of its author[s]. The SJU does not represent or endorse the accuracy or reliability of any advice, opinion, statement or other information provided by any information provider or any other person or entity involved in the drafting of this document.

Table of Contents

1 Introduction 29

1.1 Background and Motivations 29

1.1.1 SESAR Project 30

1.2 Objectives and Contributions 32

1.2.1 Objectives 32

1.2.2 Original Contributions 33

1.3 Dissertation Organization 34

2 GNSS in Civil Aviation 37

2.1 GNSS Background 37

2.1.1 GNSS Signals 37

2.1.2 PVT Computation and Pseudorange Measurement 38

2.1.3 The Geometry Aspect 39

2.1.4 Measurement Model and Error Budget 40

2.2 Civil Aviation Applications 50

2.2.1 GNSS Signals for Civil Aviation 52

2.2.2 Accuracy Improvement 53

2.2.3 Integrity Improvement 61

2.2.4 Augmentation Systems 62

2.3 GBAS 65

2.3.1 GBAS Architecture 67

2.3.2 GBAS Measurements Processing 69

2.3.3 GBAS Integrity Monitoring 73

2.3.4 GBAS Approach Service Type 80

3 MC/MF GBAS Ground Multipath and Noise Model 89

3.1 Objectives and Motivations 89

3.2 Methodology to Characterize Noise and Multipath at the Ground Station 89

3.2.1 The CMC: a Useful Combination to Evaluate Noise and Multipath 90

3.2.2 Impact of Modulation on Noise and Multipath 95

3.2.3 Residual Biases Detection 97

3.2.4 Effect of the Time Correlation of the Error on the Smoothed Measurements 99

3.2.5 Inter-Frequencies Error Correlation 100

3.2.6 Error Correlation over Two Reference Receivers 101

3.3 Results on Noise and Multipath Errors Characterization 102

3.3.1 Experimental Set-up Description... 102

3.3.2 Noise and Multipath on Different Signals.. 106

3.3.3 MLA Calibration on L5 111

3.3.4 Smoothing Efficiency 115

3.3.5 Assessment of I-Free RMS... 121

3.3.6 Averaged Noise and Multipath... 123

3.3.7 Synthesis of the Results.. 124

3.4 $\sigma pr\ gnd$ Computation 125

3.4.1 Synthesis of the $\sigma pr\ gnd$ Calculation Process... 126

3.4.2 Day-to-Day Repeatability... 127

3.4.3 Statistical Uncertainty Inflation.. 131

3.4.4 Error Correlation between Reference Receivers 134

3.4.5 Long Term Error Variation (Seasonal Effects) 136

3.4.6 Ground multipath model... 136

3.4.7 $\sigma pr\ gnd$ Results 136

3.5 Conclusions 139

4 Satellite Selection 141

4.1 Motivations and Objectives.. 141

4.2 Satellite Selection Methods 141

4.2.1 Optimal Solution 142

4.2.2 Modified Minimum GDOP 142

4.2.3 Lear's Simple Satellite Selection 142
4.2.4 Fast Satellite Selection Algorithm 143
4.3 Selected Methods for Simulation 145
4.4 Simulations Baseline 146
4.4.1 Airports Coordinates 146
4.4.2 DOP Analysis and Computational Load 147
4.4.3 Protection Level Computation 148
4.4.4 Geometry Screening Availability 148
4.5 Simulation Results 148
4.5.1 Dual Constellation 12 Satellite subset 148
4.5.2 Dual Constellation 15 Satellites Subset 159
4.6 Conclusions 168
5 GBAS Integrity 171
5.1 The GAST D Concept 173
5.1.1 Low Level Performance Requirements for Ground Monitors 174
5.1.2 Geometry Screening 176
5.1.3 SiS TTA 177
5.2 GAST D Integrity Monitoring 179
5.2.1 GAST D Monitors State-of-Art 179
5.2.2 GAST D Monitoring Challenges 193
5.2.3 GAST-D RAIM Baseline and Results 203
5.3 GAST-F Integrity Monitoring 214
5.3.1 GAST-F Monitoring Challenges 214
5.3.2 GAST-F Monitors Evaluation 215
5.3.3 GAST-F RAIM Baseline and Results 220
5.4 Conclusions 227
6 Conclusions and Future Works 229
6.1 Conclusions 229

6.2 Perspectives for Future Works ... 232

7 References ... 233

A. Civil Aviation Authorities and Requirements ... 241

A.1 Civil Aviation Authorities ... 241

A.1.1 International Civil Aviation Organization (ICAO) ... 241

A.1.2 Radio Technical Commission for Aeronautics (RTCA, Inc.) ... 241

A.1.3 European Organization for Civil Aviation Equipment (EUROCAE) ... 242

A.1.4 Federal Aviation Authority (FAA) and European Aviation Safety Agency (EASA) . 242

A.2 Phases of Flight ... 242

A.2.1 Approach ... 244

A.3 Performance Based Navigation (PBN) ... 246

A.4 Performance Navigation Criteria ... 248

A.4.1 Accuracy ... 249

A.4.2 Availability ... 249

A.4.3 Integrity ... 249

A.4.4 Continuity ... 250

A.5 Annex 10 Signal in Space Requirements ... 250

8.1 CAT II/III Requirements ... 252

B. GBAS Messages ... 255

B.1 Type 1 Message – Pseudorange Correction ... 256

B.2 Type 2 Message – GBAS Related Data ... 258

B.3 Type 11 Message – Pseudorange Corrections for 30 Seconds Smoothed Pseudorange 259

C. MC/MF GBAS Ground Multipath and Noise Model ... 261

C.1 Pattonville 50 Meters Case ... 261

C.2 Pattonville 100 Meters Case ... 263

C.3 Toulouse Blagnac Airport ... 265

C.3.1 03/04/2016 ... 265

C.3.2 06/04/2016 ... 270

C.3.3 09/04/2016 275

C.4 MLA Calibration on L5 279

C.5 Smoothing Efficiency 281

C.5.1 Pattonville Results 281

C.5.2 Toulouse Blagnac 03/04/2016 Results 284

C.5.3 Toulouse Blagnac 06/04/2016 Results 286

C.5.4 Toulouse Blagnac 09/04/2016 Results 288

C.6 Optimal Smoothing Constant 290

C.7 Assessment of I-Free RMS 292

C.8 Averaged Noise and Multipath 293

List of Figures

Figure 1 – GNSS signals frequency plan (www.navipedia.net/index.php/GNSS_signal) 37

Figure 2 – Positioning obtained through trilateration... 38

Figure 3 – Simplified ionospheric wave front model (Luo, et al., 2004) 45

Figure 4 – LOS multipath example 48

Figure 5 – NLOS multipath example 49

Figure 6 – Differential GNSS simplified scheme 54

Figure 7 – Block diagram of carrier smoothed code processing 56

Figure 8 – SBAS ionospheric corrections adapted from (Escher, et al., 2014) 62

Figure 9 – Global SBAS coverage map (gpsworld.com) 63

Figure 10 – Ground station facilities spread over Europe for EGNOS SBAS system 64

Figure 11 – GBAS Runway coverage 67

Figure 12 – Typical GBAS architecture 68

Figure 13 – Airborne measurement processing.. 72

Figure 14 – GBAS integrity risk allocation (ICAO, 2006) 74

Figure 15 – Timing diagram for differential processing below 200 ft. (Brenner, et al., 2010) 75

Figure 16 – service type, facility classification and airborne equipment classes (RTCA Inc.; DO253-C, 2008) . 81

Figure 17 – CMCs before (left) and after (right) phase ambiguity term compensation (each color represent a PRN) 93

Figure 18 – Pseudorange from one satellite, visible twice in a day 94

Figure 19 – Early-Late discriminator tracking of GPS satellites (RTCA Inc.; DO253-C, 2008).......................... 95

Figure 20 – Thermal noise standard deviation Vs. C/N_0 96

Figure 21 – Code Tracking Delay for One Path Multipath 97

Figure 22 – Antenna positions for data collection at Pattonville airport 103

Figure 23 – MLA antenna and reflector building in Pattonville airport... 104

Figure 24 – Toulouse Blagnac airport GBAS ground station (Ladoux, 2016)...................................... 105

Figure 25 – GPS L5 raw CMC time series for one satellite, with and without epoch continuity detection 106

Figure 26 – GPS L1 C/A, GPS L5 and I-Free Raw and 100 seconds smoothed CMCs for All Satellites Toulouse Blagnac RR1 107

Figure 27 – Galileo E1 C/A, E5a and I-Free Raw and 100 seconds smoothed CMCs for All Satellites Toulouse Blagnac RR1 109

Figure 28 – GPS and Galileo CMCs standard deviation for raw and smoothed cases on all signals 110

Figure 29 – Comparison between RMS and standard deviation for 100 s. smoothed GPS and Galileo signals . 112

Figure 30 – GPS L5 CMCs Mean Value (left) St. Deviation (right) Vs. Elevation Angle for All Satellites across Three Days 113

Figure 31 – Calibrated raw and 100 s smoothed CMCs for GPS signals on RR1 114

Figure 32– Calibrated raw and 100 s smoothed CMCs for Galileo signals on RR2 115

Figure 33 – Real Vs. theoretical smoothing reduction for GPS (a, c, e) and Galileo (b, d, f)........................... 116

Figure 34 – Autocorrelation function for GPS L1 and L5 for different satellites 117

Figure 35 – Autocorrelation function for Galileo E1 and E5a for different satellites 118

Figure 36 – Standard deviation comparison for different Smoothing constants for GPS and Galileo signals 120

Figure 37 – Real and theoretical I-free CMCs RMS comparison on GPS for PRN 3 (a) PRN 8 (b) and Galileo PR8 (c) and PRN 26 (d) 122

Figure 38 – RMS difference percentage distribution for GPS I-free (left) and Galileo I-free (right), each color represents a satellite 122

Figure 39 – Standard deviation comparison between empirical and theoretical value for GPS CMCs (a and c) and Galileo CMCs (b and d) 123

Figure 40 – Day-to-day autocorrelation functions for different elevation angles 128

Figure 41 – CMCs and autocorrelation functions for all satellites with elevation angle bigger than 80° 129

Figure 42 – Galileo CMCs for four consecutive days 130

Figure 43 – Statistical uncertainty effects on Galileo signals for one, four and nine days comparison 131

Figure 44 – Inflation factor for statistical uncertainty fir different number of samples 132

Figure 45 – Number of independent samples per bin comparison for GPS 133

Figure 46 – Number of independent samples per bin, with unique bin for elevation >80°, for GPS 134

Figure 47 – ρ coefficients as function of n and r 135

Figure 48 – $\sigma pr\ gnd$ values for GPS and Galileo signals for 100 seconds smoothed case 137

Figure 49 – $\sigma pr\ gnd$ values for GPS and Galileo signals for 30 seconds smoothed case 137

Figure 50 – $\sigma pr\ gnd$ values for GPS and Galileo signals for 300 seconds smoothed case 138

Figure 51 – Fast satellite selection sky subdivision example (Zhang, et al., 2008) 145

Figure 52 – Number of Satellites for all the simulated epochs and airports and 12 satellites subset in red 149

Figure 53 – Histogram of satellites number across all airports and epochs with percentage of use of satellite selection for subset 12 149

Figure 54 – VDOP values across all epochs and airports for all the methods and for all-in-view satellites 150

Figure 55 – HDOP values across all epochs and airports for all the methods and for all-in-view satellites 151

Figure 56 – GAST-D VPL computed across all the epochs and airports for three selection methods and all-in-view satellites 153

Figure 57 – GAST-D LPL computed across all the epochs and airports for three selection methods and all-in-view satellites 154

Figure 58 – GAST D $Svert$ values across all epochs and airports for three methods and all-in-view satellites 154

Figure 59 – GAST D $Svert2$ values across all epochs and airports for three methods and all-in-view satellites 155

Figure 60 – I-Free VPL across all epochs and airports for three methods and all-in-view satellites 157

Figure 61 – I-Free LPL across all epochs and airports for three methods and all-in-view satellites 157

Figure 62 – I-Free $Svert$ values across all epochs and airports for three methods and all-in-view satellites 158

Figure 63 – I-Free $Svert2$ values across all epochs and airports for three methods and all-in-view satellites 158

Figure 64 – Number of satellites for all the epochs and airports and 15 satellites subset in red 160

Figure 65 – Histogram of satellites number across all airports and epochs with percentage of use of satellite selection for subset 15 160

Figure 66 – VDOP values across all epochs and airports for all the selection criteria and for all-in-view satellites 161
Figure 67 – HDOP values across all epochs and airports for all the selection criteria and for all-in-view satellites 162
Figure 68 – GAST D VPL for all the epochs and airports for all the analyzed methods and all-in-view satellites 163
Figure 69 – GAST D LPL for all the epochs and airports for all the analyzed methods and all-in-view satellites 164
Figure 70 – GAST D $Svert$ computed for all the epochs and airports for all the analyzed methods and all-in-view satellite 164
Figure 71 – GAST D $Svert2$ computed for all the epochs and airports for all the analyzed methods and all-in-view satellites........ 165
Figure 72 – I-Free VPL for all the epochs and airports for all the analyzed methods and all-in-view satellite .. 166
Figure 73 – I-Free LPL for all the epochs and airports for all the analyzed methods and all-in-view satellites . 166
Figure 74 – I-Free $Svert$ computed for all the epochs and airports for all the analyzed methods and all-in-view satellites........ 167
Figure 75 – I-Free $Svert2$ computed for all the epochs and airports for all the analyzed methods and all-in-view satellites........ 167
Figure 76 GBAS standards to support CAT III operations (ICAO NSP, 2010)........ 172
Figure 77 – GAST-F fallback modes example........ 173
Figure 78 – Derived limit case Pmd requirement for ranging source monitor (ICAO NSP, 2010)........ 175
Figure 79 – General Pmd requirement for ranging source monitors in range domain 175
Figure 80 – Example of monitor performances Vs. Pmd requirements 176
Figure 81 – Timing diagram derivation for below 200 ft. processing derived from (SESAR JU, 2011)........ 178
Figure 82 – Threat Model A: Digital failure 179
Figure 83 – Threat Model B: Analog failure mode........ 180
Figure 84 – Threat Model C: Analog and digital failure mode. 180
Figure 85 – Acceleration induced differential range error 185
Figure 86 – simulated ionospheric delay (left) and related smoothing time variant filter response........ 190
Figure 87 - Pmd performances for DSIGMA........ 191
Figure 88 – Ionospheric delay on two different RRs 192
Figure 89 – example of stationary front for possible worst case geometry (Lee, et al., 2011)........ 194
Figure 90 – IGM test statistic for Houston airport (ICAO NSP WGW/WP 16, 2014) 196
Figure 91 – Simulation of maximum induced delay for an ionospheric front impacting the aircraft but no the GS 198
Figure 92 – Ionospheric induced range error for different ionospheric angle 199
Figure 93 – Point along the approach used to derive DRAIM performances........ 204
Figure 94 – DRAIM Pmd of ionospheric front induced error for GPS Optimal 24 and $\Delta v = 70\ m/s$ for all airports 208

Figure 95 – DRAIM Pmd for ionospheric front induced error for GPS 31 Satellites and $\Delta v = 70\ m/s$ for all airports 209
Figure 96 – DRAIM Pmd for ionospheric front induced error for GPS optimal 24 and $\Delta v = 35\ m/s$ for all airports 210
Figure 97 – DRAIM Pmd for ionospheric front induced error for GPS 31 Satellites and $\Delta v = 35\ m/s$ for all airports 211
Figure 98 – DRAIM Pmd for ionospheric front induced error for GPS optimal 24 and $\Delta v = 0\ m/s$ for all airports 212
Figure 99 – DRAIM Pmd for ionospheric front induced error for GPS 31 satellites and $\Delta v = 0\ m/s$ for all airports 213
Figure 100 – Timing diagram derivation for below 200 ft. processing with PRC update rate at 2.5 seconds 216
Figure 101 – Pmd values for different accelerations and K-values for new metric........ 218
Figure 102 – integrity messages scheme........ 219
Figure 103 – DRAIM Pmd for an ionospheric front induced error for GPS & Galileo Optimal 24 and $\Delta v = 70\ m/s$ for all airports........ 223
Figure 104 – DRAIM Pmd for an ionospheric front induced error for GPS 31 satellites and Galileo Optimal 24 and $\Delta v = 70\ m/s$ for all airports........ 224
Figure 105 – DRAIM Pmd for an ionospheric front induced error for GPS & Galileo Optimal 24 and $\Delta v = 35\ m/s$ for all airports........ 225
Figure 106 – DRAIM Pmd for an ionospheric front induced error for GPS 31 satellites and Galileo Optimal 24 and $\Delta v = 35\ m/s$ for all airports........ 226
Figure 107 – Typical phases of flight (Cassel, et al., 1995)........ 243
Figure 108 – Phases of flight and GNSS augmentation (Montloin, 2011)........ 245
Figure 109 – Total system error components (Martineau, 2008)........ 248
Figure 110 – “ILS look-alike method”........ 253
Figure 111 – Autoland method........ 254
Figure 112 – GPS L1 C/A, GPS L5 and I-Free raw and smoothed CMC for all satellites Pattonville 50 m. case 262
Figure 113 – Raw (left) and 100 s. smoothed (right) CMC standard deviation for GPS L1, L5 and I-Free combinations Pattonville 50 m. case........ 263
Figure 114 – GPS L1 C/A, GPS L5 and I-Free for raw and smoothed CMCs for all satellites Pattonville 100 m. case........ 264
Figure 115 – Raw (left) and 100 s. Smoothed (right) CMCs Standard Deviation for GPS L1, L5 and I-Free Combinations Pattonville 100 m. case........ 265
Figure 116 – GPS L1 C/A, GPS L5 and I-Free raw and 100 seconds smoothed CMCs for all satellites Toulouse Blagnac RR1 03/04/2016........ 266
Figure 117 – GPS L1 C/A, GPS L5 and I-Free raw and 100 seconds smoothed CMCs for all satellites Toulouse Blagnac RR2 03/04/2016........ 267

Figure 118 – Galileo E1, Galileo E5a and I-Free raw and 100 seconds smoothed CMCs for all satellites Toulouse Blagnac RR1 03/04/2016 268
Figure 119 – Galileo E1, Galileo E5a and I-Free raw and 100 seconds smoothed CMCs for all satellites Toulouse Blagnac RR2 03/04/2016 269
Figure 120 – GPS L1 C/A, GPS L5 and I-Free raw and 100 seconds smoothed CMCs for all satellites Toulouse Blagnac RR1 06/04/2016 271
Figure 121 – GPS L1 C/A, GPS L5 and I-Free raw and 100 seconds smoothed CMCs for all satellites Toulouse Blagnac RR2 06/04/2016 272
Figure 122 – Galileo E, Galileo E5a and I-Free raw and 100 seconds smoothed CMCs for all satellites Toulouse Blagnac RR1 06/04/2016 273
Figure 123 – Galileo E1, Galileo E5a and I-Free raw and 100 seconds smoothed CMCs for all satellites Toulouse Blagnac RR2 06/04/2016 274
Figure 124 – GPS L1 C/A, GPS L5 and I-Free raw and 100 seconds smoothed CMCs for all satellites Toulouse Blagnac RR1 09/04/2016 275
Figure 125 – GPS L1 C/A, GPS L5 and I-Free raw and 100 seconds smoothed CMCs for all satellites Toulouse Blagnac RR2 09/04/2016 276
Figure 126 – Galileo E1, Galileo E5a and I-Free raw and 100 seconds smoothed CMCs for all satellites Toulouse Blagnac RR1 09/04/2016 277
Figure 127 – Galileo E1, Galileo E5a and I-Free raw and 100 seconds smoothed CMCs for all satellites Toulouse Blagnac RR1 09/04/2016 278
Figure 128 – Comparison between RMS and standard deviation for Pattonville 50 m (left side) and 100 m (right case). 279
Figure 129 – Calibrated raw and 100 s smoothed CMCs for GPS L5 and I-Free for Pattonville 50 m. case 280
Figure 130 – Calibrated raw and 100 s smoothed CMCs for GPS L5 and I-Free for Pattonville 100 m. case ... 281
Figure 131 – Real Vs. theoretical smoothing gain for GPS L1 C/A, GPS L5 and GPS I-Free for Pattonville 50 m (left side) and 100 m (right side) 282
Figure 132 – Autocorrelation function for GPS L1 C/A and L5 for satellite PRN 1 (a, b) and 24 (c, d) on Pattonville 50 m 283
Figure 133 – Autocorrelation function for GPS L1 C/A and L5 for satellite PRN 9 (a, b) and 25 (c, d) on Pattonville 100 m 284
Figure 134 – Real Vs. theoretical smoothing gain for GPS (left side) and Galileo (right side) signals for Toulouse Blagnac 03/04/2016 on RR1 285
Figure 135 – Real Vs. theoretical smoothing gain for GPS (left side) and Galileo (right side) signals for Toulouse Blagnac 03/04/2016 on RR2 286
Figure 136 – Real Vs. theoretical smoothing gain for GPS (left side) and Galileo (right side) signals for Toulouse Blagnac 06/04/2016 on RR1 287
Figure 137 – Real Vs. theoretical smoothing gain for GPS (left side) and Galileo (right side) signals for Toulouse Blagnac 06/04/2016 on RR2 288

Figure 138 – Real Vs. theoretical smoothing gain for GPS (left side) and Galileo (right side) signals for Toulouse Blagnac 09/04/2016 on RR1 289
Figure 139 – Real Vs. theoretical smoothing gain for GPS (left side) and Galileo (right side) signals for Toulouse Blagnac 09/04/2016 on RR2 290
Figure 140 – Standard Deviation Comparison for Different Smoothing Constants for GPS L1, GPS L5 and I-free on Pattonville 50 m (left side) and Pattonville 100 m (right side)........ 291
Figure 141 – Real and theoretical I-free CMCs RMS comparison for satellite PRN 1 (left) and PRN 8 (right) Pattonville 50m 292
Figure 142 – Real and theoretical I-free CMCs RMS comparison for satellite PRN 1 (left) and PRN 8 (right) Pattonville 100m 292
Figure 143 – RMS difference percentage distribution for GPS I-free for Pattonville 50 m (left side) and 100 m (right side), each color represents a satellite 292
Figure 144 – Standard deviation comparison between empirical and theoretical value for GPS CMCs (a, c) and Galileo CMCs (b, d) 03/04/2016........ 293
Figure 145 – Standard deviation comparison between empirical and theoretical value for GPS CMCs (a, c) and Galileo CMCs (b, d) 06/04/2016........ 294
Figure 146 – Standard deviation comparison between empirical and theoretical value for GPS CMCs (a, c) and Galileo CMCs (b, d) 09/04/2016........ 295

List of Tables

Table 1 – Comparison between Klobuchar and NeQuick models 43

Table 2 – Ionospheric gradient parameters (ICAO NSP, 2015) 45

Table 3 – Thermal noise standard deviation for DLL and PLL (Julien O., 2011/2012) 47

Table 4 – SiS performance requirements (ICAO, 2006) 51

Table 5 – GNSS Signals for Civil Aviation (ARINC Engineering Services, 2004) and (GJU-GALILEO Joint Undertaking, 2010) 53

Table 6 – $Kffmd$ Values 76

Table 7 – Kmd Values 77

Table 8 – Vertical alert limit 78

Table 9 – Lateral alert limit 78

Table 10 – Ground reference receiver error allocation model 82

Table 11 – Summary of LAAS SIS residual errors (McGraw, et al., 2000) 83

Table 12 – Airborne thermal noise and interference error model parameters 84

Table 13 – $\sigma pr\ gnd$ bound values for all analyzed signals for GPS and Galileo 139

Table 14 – GDOP values for different number of satellite at high elevation for a simulated study (Zhang, et al., 2008) 144

Table 15 – Airports coordinates used in simulation 147

Table 16 – VDOP percentile at 95, 99 and 99.9 % for 12 satellites subset 151

Table 17 – HDOP percentile at 95, 99 and 99.9 % for 12 satellites subset 151

Table 18 – Computational time, in seconds, for all methods with 12 satellites subset 152

Table 19 – Geometry screening availability for all the selection methods with 12 satellites and all in view case 155

Table 20 – Geometry screening availability for all selection methods and all in view case 159

Table 21 – VDOP percentile at 95, 99 and 99.9 % for 15 satellites subset 161

Table 22 – HDOP percentile at 95, 99 and 99.9 % for 15 satellites subset 162

Table 23 – Computational time, in seconds, for all methods with 15 satellites subset 163

Table 24 – DISGMA test metric standard deviation (ICAO NSP, 2016) 190

Table 25 – Difference speed limit for CCD detection 195

Table 26 – Airport latitude, longitude and runway heading for DRAIM simulation 203

Table 27 – ionospheric front induced range error (m) 205

Table 28 – Percentage of epoch with a not sufficient Pmd for GAST-D 214

Table 29 – Acceleration detected with $Pmd = 10 - 9$ for different K-values 218

Table 30– Percentage of epoch with a not sufficient Pmd for GAST-F 227

Table 31 – Decision height and visual requirements (ICAO, 2001) 246

Table 32 – SiS performance requirements (ICAO, 2006) 251

Table 33 – Alert limit associated to the typical operations (ICAO, 2006) 252

Table 34 – SiS performance requirements for various phases of aircraft operation 254

Table 35 – LAAS VHF Data Broadcast (VDB) messages and broadcast rate (DO-246D, 2008)....................... 255
Table 36 – GBAS message type required for each service level... 256
Table 37 – Message type 1 format 257
Table 38 – Message Type 2 format... 258
Table 39 – Additional data block 3 259
Table 40 – Message Type 11 format... 260

Table of Acronyms

AAD	**Aircraft Accuracy Designator**
ADB	**Additional Data Block**
AMD	**Airframe Multipath Designator**
ABAS	**Aircraft Based Augmentation System**
APV	**Approach with Vertical Guidance**
ARAIM	**Advanced Receiver Integrity Monitoring**
ARNS	**Aeronautical Radio Navigation Services**
ATM	**Air Traffic Management**
C/A	**Coarse Acquisition**
CCD	**Code Carrier Divergence**
CMC	**Code Minus Carrier**
CNS	**Communication Navigation Surveillance**
DF	**Divergence Free**
DGNSS	**Differential GNSS**
DH	**Decision Height**
DRAIM	**Differential-Receiver Autonomous Integrity Monitoring**
DSIGMA	**Dual Solution Ionosphere Gradient Monitoring Algorithm**
EGNOS	**European Geostationary Navigation Overlay Service**
ESA	**European Space Agency**
FAA	**Federal Aviation Administration**
FAS	**Final Approach Segment**

FASLAL	**FAS Lateral Alert Limit**
FAST	**Facility Approach Service Type**
FASVAL	**FAS Vertical Alert Limit**
FD	**Fault Detection**
FDE	**Fault Detection and Exclusion**
FTE	**Flight Technical Error**
GAD	**Ground Accuracy Designator**
GAST	**GBAS Service Type**
GBAS	**Ground Based Augmentation System**
GFC	**GBAS Facility Classification**
GLONASS	**GLObal'naja NAvigacionnaja Sputnikovaja Sistema**
GLS	**GBAS Landing System**
GNSS	**Global Navigation Satellite System**
GPIP	**Glide Path Intersection Point**
GPS	**Global Positioning System**
HAL	**Horizontal Alarm Limit**
HPL	**Horizontal Protection Level**
IATA	**International Air Transport Association**
ICAO	**International Civil Aviation Organization**
IF	**Ionosphere Free**
IGM	**Ionosphere Gradient Monitor**
ILS	**Instrumental Landing System**
LAAS	**Local Area Augmentation System**

LAL	**Lateral Alarm Limit**
LOS	**Line Of Sight**
LPL	**Lateral Protection Level**
LTP	**Landing Threshold Point**
MC	**Multi Constellation**
MF	**Multi Frequency**
MT	**Message Type**
NLOS	**Non-Line Of Sight**
OACI	**l'Organisation de l'Aviation Civile Internationale**
PA	**Precision Approach**
PBN	**Performance Based Navigation**
PRC	**PseudoRange Correction**
PSE	**Path Steering Error**
PVT	**Position Velocity and Time**
RAIM	**Receiver Autonomous Integrity Monitoring**
RNAV	**Area Navigation**
RNP	**Required Navigation Performance**
RR	**Reference Receiver**
RRC	**Range Rate Correction**
SARPs	**Standard And Recommended Practices**
SBAS	**Satellite Based Augmentation System**
SC	**Single Constellation**
SESAR	**Single European Sky ATM Research**

SF	**Single Frequency**
SiS	**Signal in Space**
SQM	**Signal Quality Monitor**
TEC	**Total Electron Content**
TTDAB	**Time-to-detect And Broadcast**
TC	**Tropospheric Correction**
TSE	**Total System Error**
TTA	**Time-To-Alert**
U.S.	**United States**
VAL	**Vertical Alarm Limit**
VDB	**VHF Data Broadcast**
VPL	**Vertical Protection Level**
WAAS	**Wide Area Augmentation System**
WP	**Working Package**

1 Introduction

1.1 Background and Motivations

The civil aviation is the transport sector having experienced, during the last tens of years, the largest growth in term of passengers, tonnes of transported goods and number of trips. According to the International Civil Aviation Organization (ICAO), the number of transported passenger in 2012 was 2.9 billion, and will reach 3.6 billion by the end of 2016 according to International Air Transport Association (IATA). Tonnes of freight transported also need to be added to this data to provide a complete and accurate point of the situation of the civil aviation traffic demand.

To provide an efficient response to this trend, the entire system, comprising airplane, airports, air traffic management (ATM) systems need to improve or innovate their services to make operations more efficient and at the same time as safe as possible. In this scope, the creation of flexible routes for the approach and landing operation can bring a lot of benefits to the ATM segment, permitting also cleaner and less noisy operation.

The main system used to provide accurate guidance for the approach and landing, for the CAT III operations, is the Instrumental Landing System (ILS). Despite its capabilities to provide accurate guidance in the vertical and lateral axes, there are some limitations that make this system no longer the optimal choice for such operations, such as the fact that it can only provide information for straight-in trajectories. This condition limits, nowadays, the creation of different and flexible routes that permit to increase the number of operations-per-hour (take-off and landing) or to avoid to fly over city centres. Moreover this system is considered expensive since it has to be installed at each runway end to cover all approach routes. In order to develop new flexible routes another system, able to provide the same services as the ILS, must be found.

Nowadays, most of the civil aviation aircrafts are equipped with Global Navigation Satellite System (GNSS) receivers (90% of aircrafts according to EUROCONTROL Survey (Roelandt, 2014)) and it is recognized as a key technology in providing accurate navigation services with a worldwide coverage. GNSS concept was defined by the International Civil Aviation Organization (ICAO) in (ICAO, 2006).

To use GNSS within the CNS (Communications, Navigation, and Surveillance)/ATM system, a stand-alone core constellation needs to be augmented to meet requirements specified by ICAO (ICAO, 2006) in terms of accuracy, integrity, availability and continuity. Therefore, several augmentation systems have been developed for this purpose:

- GBAS (Ground Based Augmentation System)
- SBAS (Satellite Based Augmentation System)

- ABAS (Aircraft Based Augmentation System).

Among them, GBAS is considered as a very attractive system since it provides navigation services, with a level of performance comparable with the ILS currently used (Felux, et al., 2013). It uses the Differential GNSS principle to improve the performance of stand-alone GNSS in order to reach the accuracy required (ICAO, 2006). Nevertheless, accuracy is not the only parameter required to use a GNSS system for civil aviation: integrity must be provided as well. To provide the required integrity, GBAS is composed of a ground station able to monitor the presence of a variety of threats on the received GNSS signal. It includes several receivers, each one generating pseudorange measurements, with the aim to elaborate pseudorange corrections that have to be transmitted to the airborne receiver. An associated integrity message is generated by the ground station providing system and correction integrity information. Using this information, the user receiver is able to correct its own measurements and to exclude some of them in case of the presence of anomalous errors, thus guarantying the required integrity level.

Currently (as of 2016), GBAS has been certified for CAT I precision approaches, and some projects are ongoing to develop a concept for reaching CAT II/III requirements. This explains the interest of Civil Aviation, since GBAS may then become an alternative to classical ILS and MLS equipment which are currently the only means to achieve CAT II/III precision approaches.

In order to classify the GBAS services, the acronym GAST (GBAS Approach Service Type) has been created. Nowadays GAST-C is the service corresponding to the CAT I precision approach service, and it is the only one certified, using single constellation and single frequency core system. Two levels of service are under development to provide guidance for CAT II/III precision approach: GAST-D and GAST-F. The first one corresponds to a single constellation and single frequency GBAS as for the GAST C service, the main difference being the use of a double smoothing constant and the split of the responsibility for the integrity monitoring between ground station and airborne receivers. The GAST F service instead relies on dual constellation and dual frequencies GBAS; however the processing and monitoring schemes for this latter service are still under development.

1.1.1 SESAR Project

Contrary to the United States, Europe does not have a single sky, one in which air navigation is managed at the European level. Furthermore, European airspace is among the busiest in the world with over 33,000 flights (SESAR, 2009) on busy days and high airport density. This makes air traffic control even more complex.

The EU Single European Sky is an ambitious initiative launched by the European Commission in 2004 to reform the architecture of European air traffic management. It proposes a legislative approach to meet future capacity and safety needs at a European rather than a local level.

The key objectives of the Single European Sky Advanced Research (SESAR) project are to (SESAR, 2009):

- Restructure European airspace as a function of air traffic flows
- Create additional capacity
- Increase the overall efficiency of the air traffic management system

Then, the major elements of this new institutional and organizational framework ATM in Europe consist of:

- Separating regulatory activities from service provision, and the possibility of cross-border ATM services.
- Reorganizing European airspace that is no longer constrained by national borders.
- Setting common rules and standards, covering a wide range of issues, such as flight data exchanges and telecommunications.

Furthermore, the activities in the CNS domain constitute a significant level of investment within the SESAR program and are included in the Work Package 15 (WP15) named "*Non-Avionic CNS System* Work package". It addresses CNS technologies development and validation also considering their compatibility with the Military and General Aviation user needs.

In WP 15 the sub-task 15.3 is dedicated to the NAVIGATION. Navigation systems developments in SESAR focus on the evolution of GNSS-based navigation technologies which will be developed to fulfil navigation performance supporting RNP (Required Navigation Performance) based operations as defined and validated in the operational projects of the program.

The SESAR work program integrates operational projects, which define new PBN (Performance Based Navigation) procedures and concepts, with the technical projects, which develop the Navigation tools and systems according to the operational needs, which are validated by the operational projects. For the underlying navigation sensor and system developments, SESAR projects aim to define the medium and long term GNSS baseline including the expected configuration of constellations, signals and augmentation systems (GBAS/ABAS/SBAS). This will drive the further developments within the program covering evolution from single constellation/single frequency (GPS L1 C/A) to multi-constellation/multi-frequency (GPS L1/L5 and Galileo E1/E5).

This PhD project is included inside this part of the SESAR project and more precisely in the *WP 15.3.7 "Multi GNSS CAT II/III GBAS"*.

1.2 Objectives and Contributions

1.2.1 Objectives

As mentioned in the section above, current GBAS is based on GPS and GLONASS constellations and provides precision approach service down to Category I (CAT-I) using a single protected signal (GPS L1 C/A). The evolution of GBAS towards Multi-Constellation (MC) and Multi-Frequency (MF) is expected to provide better performance and robustness as well as the availability of new services. Several expected improvements (ICAO NSP, 2010) are listed below:

- The development of a Multi-Constellation GBAS service will provide additional ranging sources that will permit to improve the availability of the service (improvement of the satellites geometry). Moreover, the presence of a larger number of satellites permits to increase the continuity of service in case of local atmospheric anomalies, such as ionospheric scintillation. This issue could be solved with the MC GNSS implementation because with more satellites in view, it would be much less likely that scintillation would result in loss of service. So, the availability of additional ranging sources and frequencies will improve the operational robustness.
- The implementation of a second constellation, Galileo, will increase the continuity of service because in a case of total constellation failure, the entire system can rely on the other constellation ranging sources.
- Future satellites will provide signals on multiple frequencies which allow to form combinations that remove the ionospheric delay from the measurement. Thanks to this properties MC/MF GBAS is expected to overcome the integrity problems experienced by GAST-D for ionosphere monitoring (Thales, 2006).
- New signals will increase the robustness against unintentional interference and will improve the accuracy.

Despite the advantages listed above, a series of challenges and key issues have to be considered and solved before the system may be used. These include:

- deriving system-level requirements,
- selection of the optimal MF processing mode,
- defining VHF Data Broadcast (VDB) transmission and format of the transmitted message from the GBAS VDB unit (Beck, et al.)
- management of dual constellation at ground and aircraft sides,
- analysis and characterization of Galileo fault modes,
- ground subsystem monitoring and technology,

- airborne performance and certification,
- operational impact,
- standardization, validation and certification authorities' involvement.

In the frame of this thesis some of these points have been investigated or analyzed.

The selection of the optimal processing mode assumes that the performance of new signals and DF combinations are known in order to estimate the system accuracy for any possible mode. On this topic, the errors affecting the PseudoRange Corrections (PRC) have been analyzed. The objective is to derive new models that permit to characterize the ground performances considering the impact of new signals or combinations. The analysis has also considered the impact of different smoothing time constants and the impact of the inter-frequencies correlation and the correlation across Reference Receivers (RR).

The increased number of available satellites, jointly with the presence of a second frequency, increases the number of corrections to broadcast from the ground station to the airborne receiver. Moreover, a further limitation can be represented by the limited number of channels available in an embedded receiver. A possible solution to this limitation is the implementation of a satellite selection algorithm. Other proposed solution regards the broadcast of correction at a lower rate or the modification of the current VDB message structure. In this thesis, an overview of satellite selection methods proposed in literature has been done and for some of them, the predicted availability and the Dilution of Precision (DOP) have been calculated and compared with the all-in-view solution.

Using new signals, and relying on DF combinations, one aspect that is impacted is the integrity monitoring. All monitors developed so far are in fact intended to work on Single Frequency (SF) using GPS L1 C/A as measurement. The use of new signals may require a modification of the current monitors or an assessment of new integrity performances. Moreover with an increased number of satellites, and a second frequency, the number of corrections to broadcast increases a lot. Possible solutions to increase the messages capacity consider to change the current processing mode, based on the broadcast of corrections with 2 Hz frequency, for a lower PRC and RRC update rate. The impact of all these changes have to be analyzed on all existing monitors to derive new performances according to the used processing scheme. It has to be considered that GAST-D, for instance is still under validation due to lack of integrity performances in monitoring ionosphere anomalies. The objectives in this part is to analyze and propose a solution to improve the monitoring under GAST-D. The solution proposed may be used also under GAST-F service whenever one of the two frequency will not be available, relying in this case on two constellations. The impact of a lower update rate is analyzed as well.

1.2.2 Original Contributions

The main contributions of this thesis are summarized below and detailed all along this report.

- Analysis of PRC residual errors (noise and multipath) using real airport data for the new signals (GPS L5 and Galileo E1, E5a and for the I-free combination).
- Code Minus Carrier calibration process for L5 band measurements on the BAE ARL-1900 antenna
- Impact of different smoothing time constant on all signals and combination previously analyzed
- Derivation of the inter-frequencies correlation impact on I-free combination
- Computation of the $\sigma_{pr\,gnd}$ for all signals and combinations, and comparison with GAD curves proposed for GPS L1 C/A in the frame of GAST-C service development
- Degradation of the VDOP and HDOP when using a satellites subset, 12 and 15 satellites
- Analysis of the availability for a DC GBAS when subset is used for SF and I-free combinations
- Estimation of the feasibility of a lower PRC and RRC update rate on the acceleration monitor
- Analysis of the performances in using RAIM to monitor atmospheric anomalous conditions not covered by the current GAST-D monitor scheme.
- Analysis of the performances of RAIM for a DC/SF GBAS (GAST-F with a lost frequency) for the same ionosphere anomalous conditions defined for GAST-D.

1.3 Dissertation Organization

The thesis is organized in the following way. Chapter 2 introduces the main principles of GNSS introducing the error affecting the pseudorange measurement and causing an error on the computed position solution. The requirement to use GNSS in civil aviation are then introduced followed by the description of the main augmentation systems proposed so far: ABAS, SBAS and GBAS. A last section is entirely dedicated to the GBAS, the architecture, the messages and the integrity monitoring are presented in this section for GAST-C service. GAST-D and DC/DF GBAS, known as GAST-F are presented finally.

Chapter 3 concerns the analysis of the noise and multipath affecting the PRC at the ground station. In the first section, the methodology adopted to derive information about these two errors and all the analysis done are presented. In the following, the results for each analysis are shown. The last section of this chapter introduces the methodologies followed to compute the $\sigma_{pr\,gnd}$ values starting from a limited set of empirical data.

Chapter 4 introduces the satellites selection methods found in literature and chosen to be analyzed. The simulation baseline is then introduced before providing the results for two subset sizes: 12 and 15 satellites. Results are given in term of VDOP and HDOP for the all-in-view and the analyzed methods in order to have an idea about the loss of accuracy. Then the predicted availability is obtained by comparing the VPL and LPL with the related alert limit. The chapter will conclude on the interest to apply a satellite selection algorithm.

Chapter 5 is dedicated to the integrity monitoring. The first section introduces the main differences that exists between the concepts of GAST-C and D to derive the airworthiness. The following section introduces the monitors' state-of-art for GAST-D. Then the challenges that are still active in the monitoring of the ionosphere anomalies, for GAST-D, are presented. The last part of the section proposes a solution to improve the integrity performances and the results obtained applying this solution. Another section is dedicated to the GAST-F challenges in the integrity monitoring domain. The impact of a different processing mode, with a lower PRC and RRC, on the excessive acceleration monitor is analyzed. Finally the same monitor solution proposed for GAST-D is applied to a particular GAST-F scenario, loss of one of the two frequencies, SF/DC GBAS case under the same conditions.

Chapter 6 provides the conclusion derived from the analysis of results obtained in the previous chapter and the perspectives for future works.

In the appendix A the civil aviation authorities and requirements are presented to help the understating of concepts introduced in chapter 2. Appendix B provides details about the GBAS messages structure. Appendix C shows the results of chapter 3 for all analyzed days and airports location.

2 GNSS in Civil Aviation

2.1 GNSS Background

The Global Navigation Satellite System (GNSS) is a concept developed by the ICAO (International Civil Aviation Organization) and more precisely by the FANS (Future Air Navigation Systems) committee.

"GNSS. A worldwide position and time determination system that includes one or more satellites constellations, aircraft receivers and system integrity monitoring, augmented as necessary to support the required navigation performance for the intended operation" (ICAO, 2006)

It is part of the CNS/ATM concept (Communication Navigation Surveillance/Air Traffic Management) which was also established by ICAO in 1983 but adopted in 1991. The latter was intended as a basis for the implementation of new technologies, such as communications by satellites and data transmissions, and its operational plan was adopted by ICAO in 2003 and remains set around the world. PVT Computation and Pseudorange Measurement.

2.1.1 GNSS Signals

The aim of this part is to briefly present the different signals that are available for a civil aviation.

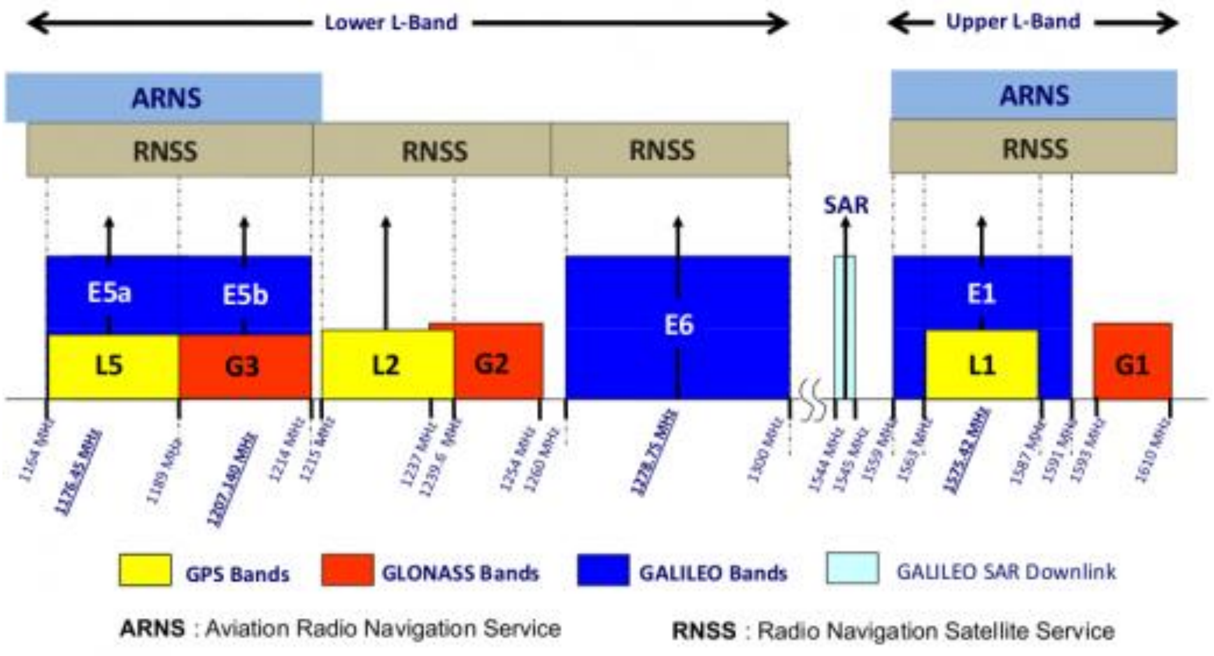

Figure 1 – GNSS signals frequency plan (www.navipedia.net/index.php/GNSS_signal)

In Figure 1 the signals that are available for three different constellations, GPS, Galileo and GLONASS are shown according to the used frequency. They are:

- GPS L1 C/A, L2 and L5
- Galileo E1, E5a, E5b and E6
- GLONASS G1, G2 and G3

More details about the signals used in civil aviation will be given in section 2.2.1

2.1.2 PVT Computation and Pseudorange Measurement

In a GNSS system, the user's position is computed based on the knowledge of the distances between the satellites and receiver antennas, known as ranges. A GNSS receiver estimates the satellite/user range by measuring the travel time of a signal emitted by the satellite and reaching the user, and then multiplying it by the speed of light (thus assuming travel through a vacuum).

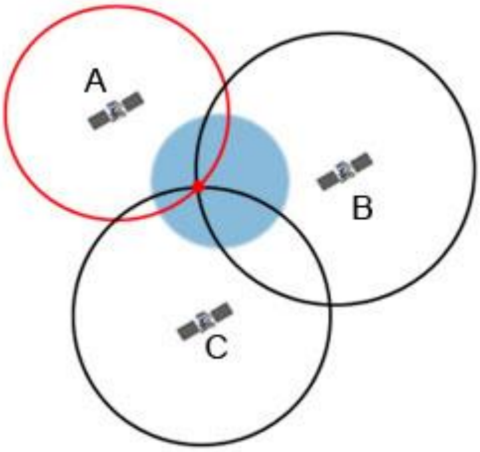

Figure 2 – Positioning obtained through trilateration

As highlighted by Figure 2, it is theoretically possible to compute the 3-D user position based on three range measurements. In particular, knowing the satellites position (x_s, y_s, z_s) and the distance r, it is possible to solve a system formed as:

$$r = \sqrt{(x_s - x_u)^2 + (y_s - y_u)^2 + (z_s - z_u)^2} \qquad \text{Eq. 2.1}$$

Where the sub-index s stands for satellite and u stands for user.

The mechanism used by a GNSS system to measure the satellite/user range is however not fully compatible with Equation Eq. 2.1. Indeed, the user-satellite distance is in fact measured by comparing the emission and reception times of the transmitted signal. This assumes a common time scale between satellites and user receiver which is not the case in the design of satellite positioning systems to date (Kaplan, et al., 2006). Because of the presence of an offset between the satellite and receiver time, the actual receiver measurement includes a time bias. It is therefore called a pseudorange and can be modelled as follows:

$$\rho = c[(T_u + \Delta t_u) - (T_s + \Delta t_s)] \qquad \text{Eq. 2.2}$$

Where:

- $(T_u + \Delta t_u)$ is the reception time in the receiver system time, which can be decomposed into:
    - T_u: the reception time in the GNSS system time (UTC time or GPS/ Galileo /Beidou time)
    - Δt_u is the receiver time offset with respect to the GNSS time scale
- $(T_s + \Delta t_s)$ is the emission time in the satellite system time with:
    - T_s: the emission time in the GNSS system time

Equation Eq. 2.2 can be rewritten as:

$$\rho = c[(T_u - T_s) + (\Delta t_u - \Delta t_s)] \qquad \text{Eq. 2.3}$$

And knowing that the term $c(T_u - T_s)$ represents the true distance r between satellite and user

$$\begin{aligned}\rho &= r + c(\Delta t_u - \Delta t_s) \\ &= \sqrt{(x_s - x_u)^2 + (y_s - y_u)^2 + (z_s - z_u)^2} + c(\Delta t_u - \Delta t_s)\end{aligned} \qquad \text{Eq. 2.4}$$

The satellite and receiver clock offset are not the only sources of error affecting the pseudorange measurement: a series of error due to the propagation channel and the ability of the receiver to synchronize with the received signal are present on the pseudorange, leading to the following model:

$$\rho = r + c(\Delta t_u - \Delta t_s) + E \qquad \text{Eq. 2.5}$$

Details on the errors affecting the pseudorange measurement, E will be given in Eq. 2.10.

Before computing the user position, the errors affecting the measurement must be corrected in order to obtain the most accurate solution to the problem. Beside the correction of some of the propagation errors affecting the pseudorange, the term Δt_s can also be corrected at user level thanks to the accurate monitoring and prediction of the satellite clock bias made by the GNSS ground infrastructure. On the other hand, Δt_u cannot be corrected a priori as it is receiver dependent. However, Δt_u being common to all measurements, it can be estimated as the fourth unknown (with the 3D position parameters) of the PVT solution. This means that the position and the receiver clock bias can be computed with at least four measurements from 4 different satellites.

2.1.3 The Geometry Aspect

Before describing the errors affecting the pseudorange measurement and consequentially the computed position accuracy, it is useful to introduce the notion of satellite geometry and its impact on the position computation. Indeed, according to the satellite positions viewed by the receiver, the computed position accuracy, can vary a lot. This link between satellite geometry and position accuracy is captured by the Dilution Of Precision (DOP) value (Kaplan, et al., 2006).

$$\sqrt{\sigma_x^2 + \sigma_y^2 + \sigma_z^2 + \sigma_{\Delta t_u}^2} = GDOP \times \sigma_{UERE} \qquad \text{Eq. 2.6}$$

Where:

- $\sigma_x^2, \sigma_y^2, \sigma_z^2, \sigma_{\Delta t_u}^2$ represent the accuracy of the estimated solution on the three axis, x, y and z and on the receiver clock offset
- σ_{UERE} is the pseudorange error factor (Kaplan, et al., 2006)

This quantity is linked to the elevation and azimuth angles of all satellites with respect to the user location. It can be computed based on the G matrix as (Kaplan, et al., 2006):

$$G_i = [-\cos(El_i)\cos(Az_i) \quad -\cos(El_i)\sin(Az_i) \quad -\sin(El_i) \quad 1] \qquad \text{Eq. 2.7}$$

Then the DOP is computed as

$$H = (G^T \cdot G)^{-1} \qquad \text{Eq. 2.8}$$

$$DOP = \sqrt{H_{1,1}^2 + H_{2,2}^2 + H_{3,3}^2 + H_{4,4}^2} \qquad \text{Eq. 2.9}$$

The larger the DOP is, the less accurate is the computed position and time (for a given set of pseudoranges).

2.1.4 Measurement Model and Error Budget

In GNSS, a fundamental role is played by the pseudorange measurement. As seen in section 0, the pseudorange measurements generated by the receiver include an error term originating from multiple sources. These errors can be divided into four main categories:

- Delays induced by the propagation of the signal through the atmosphere
- Multipath
- Receiver synchronization errors and in particular thermal noise
- Satellite clock offset correction error

From a given GNSS signal, a receiver can typically generate two types of pseudorange measurements: the code and carrier phase measurements, which are originating from 2 means of synchronizing the receiver with the satellite signal. Expliciting all the sources of measurements' errors, these pseudorange measurements made by a receiver u for a given satellite i at epoch k can be modelled as:

$$\rho^i(k) = r_u^i(k) + c\left(\Delta t_u(k) - \Delta t_s^i(k)\right) + I^i(k) + T^i(k) + D_{multi,PR}^i(k) + \eta_{PR}^i(k) \qquad \text{Eq. 2.10}$$

$$\phi^i(k) = r_u^i(k) + c\left(\Delta t_u(k) - \Delta t_s^i(k)\right) - I^i(k) + T^i(k) + N^i\lambda + D_{multi,\phi}^i(k) + \eta_\phi^i(k) \quad \text{Eq. 2.11}$$

Where:

- ρ^i is the code pseudorange measurement in meters
- ϕ^i is the phase pseudorange measurement in meters
- r_u^i is the geometrical distance between the receiver and the satellite i in meters
- I^i is the ionospheric propagation delay in meters
- T^i is the tropospheric propagation delay in meters
- N^i is the phase ambiguity term
- λ is the wavelength related to the used frequency
- D_{multi}^i is the code pseudorange measurement error induced by multipath propagation, it is different on the code and phase measurement
- η_{PR}^i is the code phase thermal noise error
- η_ϕ^i is the phase offset thermal noise error
- Δt_u is the offset between the GNSS system time and the receiver time
- Δt_s^i is the offset between the GNSS system time and the i^{th} satellite time

Other error sources, like satellite and receiver real-valuated carrier hardware biases and wind-up error, are voluntary omitted because there are not critical errors.

In the following sections, the error models will be presented.

2.1.4.1 Ionospheric delay

The ionosphere is a medium located between 50 and 1000 km above the earth surface. When the sun rays pass through this region, they ionize a portion of the gas and this releases free electrons. The electrons influence the propagation of the signal in the ionosphere (Leick, 1995).

Ionospheric error is the most severe error affecting GNSS measurements since it can create large propagation delays (with respect to propagation through a vacuum). It is very complex to model and therefore it is difficult to predict the delay so as to correct a priori the measurements. The ionosphere introduces a group delay and a phase advance to the GNSS signal that both have the same magnitude.

2.1.4.1.1 Nominal ionospheric error

As the ionosphere is a dispersive medium, the propagation velocity of GNSS signals through the ionosphere depends on their carrier frequency and the ionosphere's total electron content (TEC, in e/m²) integrated along the LOS (Line Of Sight). This TEC represents the number of free electrons in a 1 m² column along the LOS. It can be modelled as expressed in (Leick, 1995):

$$TEC = \int_{LOS\,path} N_e . dS \qquad \text{Eq. 2.12}$$

With N_e the local electron density expressed in units of electron per cubic meters.

The ionospheric delay model is used to represent the total error affecting pseudorange measurements due to the propagation of the signal through the ionosphere. The group delay can be approximated at the first order (Leick, 1995) as:

$$I^k \approx \frac{40.3}{f^2} TEC \ (m) \qquad \text{Eq. 2.13}$$

Where:

- f is the carrier frequency of the GNSS signal

To compensate the ionospheric effect on the GNSS measurement, the Klobuchar or NeQuick model (which parameters are computed by the GNSS system and transmitted to the user) can be used. The ionospheric delay can be also estimated using dual frequency measurement combinations as it is frequency dependent. More details about the estimation of the ionospheric delay using dual frequency measurements will be provided in section 3.2.

2.1.4.1.2 Klobuchar and NeQuick Models

Klobuchar model can be found in (ARINC Engineering Services, 2004) or (Arbesser-Ratsburg, 2006). It is a thin shell ionosphere model represented by 8 coefficients. It is used as a correction model of the ionospheric delay and a basis for ionosphere correction by the GPS system. Indeed, the eight coefficients are computed by the GPS ground infrastructure and transmitted to the users through the GPS navigation message.

In the case of Galileo stand-alone service, a more recent model is used which is called the NeQuick algorithm (GJU-GALILEO Joint Undertaking, 2010). It is supposed to have better performance than the Klobuchar algorithm and is assumed to be able to correct 70% of the ionospheric delay when operating on E5a, E5b, and E1 frequencies (Egis avia, 2010).

A trade-off has to be found between the percentage ionospheric correction and the complexity of the computations required. The following table which summarizes the two models main characteristics extracted from (Egis avia, 2010) has to be considered with regards to the operational application aimed by the receiver using these models.

Table 1 – Comparison between Klobuchar and NeQuick models

	Klobuchar	**NeQuick**
Model Type	Single Layer Model	Electron Density Model
Percentage of Ionospheric Error Estimated Over the World During the Year	50 % of Error Estimated	70 % of Error Estimated
Iono Effect Covered	Ionospheric Delay	Ionospheric Delay
Constellation Concerned	GPS	Galileo
Accuracy	Long Term (> 1 year)	Seasonal (4 Months)
Seasonal Variations	No	Yes
Large Scale Space Variations	Medium	Good Except near Equator
Reactivity	Iono parameters broadcasted every 12.5 minutes Iono information updated once every day (Best Case) or every 6 days (Worst Case)	Iono parameters broadcasted every 1.64 seconds in F/NAV message and every 0.328 seconds in I/NAV message Iono coefficients updated by ground segment every 24 hours Disturbance flags updated by ground segment every 100 minutes
Complexity	Simple Cosine Function: Low Complexity	Epstein Formulation of different Layers and Seasonal Variations, Sunspot Number: High Complexity

2.1.4.1.3 Abnormal behaviour

Some phenomena occurring in the ionosphere are not represented by the previous models. As they may have a huge impact on the pseudorange errors, it is useful to present them. The state of the ionosphere is a function of intensity of solar activity, magnetic latitude, local time, and other factors. The possibility of extremely large ionosphere spatial gradients was originally discovered through studies done during ionosphere storm events. Several phenomena like ionospheric storms, plasma bubble or ionospheric scintillation can be responsible for these gradients.

The **solar activity** produces large variations in the particle and electromagnetic radiation incident upon the earth and these disturbances, when affecting the ionosphere, are known as ionospheric storms. An ionospheric storm tends to generate large disturbances in ionospheric density distribution and in total electron content; in case of ionospheric storm, the models showed before are not valid to have a good estimation of the ionospheric delay. In particular it is possible to see in (Thales, 2006) that the solar flux, having an impact on the TEC, has a cycle period of about 11 years.

Plasma bubble is a plasma density depletion region and is most prominent at night time in the equatorial ionosphere. This phenomenon can be responsible for another anomaly called irregular TEC gradient.

Ionospheric scintillation (Luo, et al., 2004) manifests itself as rapid changes of the phase and amplitude of the signal. Scintillation is caused by the passage of the signal through a region of small scale irregularities in electron density. The irregularities influence the refractive index which in turn causes a time variation in phase (phase scintillation) and also scattering of the signal (cycle slips and even loss of lock). As it was already said, irregularities in the ionosphere can be produced by several phenomena which appear prominently in different area. Ionospheric scintillation occurs primarily in equatorial and high-latitude regions. Although it can occur at all latitudes, mid-latitudes are typically affected only during large magnetic storms which would be more prevalent during periods of solar maximum. Different measures can be defined for quantifying the amount of ionospheric scintillation. The most common is the amplitude scintillation index which can be expressed as:

$$S_4 = \sqrt{\frac{\langle I^2 \rangle - \langle I \rangle^2}{\langle I \rangle^2}}$$

Where I is the signal intensity and the angle brackets indicate averaging over a time interval.

Ionospheric gradient are modelled as a linear front moving at constant speed (m/s) and characterized by its gradient (mm/km). The linear gradient model shown is defined by three parameters: velocity, gradient width (w), and gradient slope (g). The total delay difference (D) is then given by: $D = wg$ (Luo, et al., 2004).

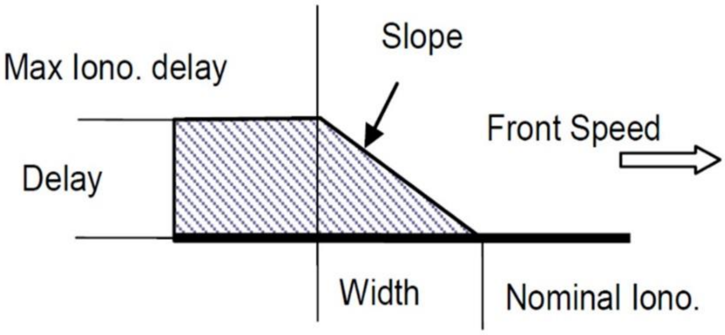

Figure 3 – Simplified ionospheric wave front model (Luo, et al., 2004)

The parameters modelling an ionospheric front have been studied for several years, using data provided by SBAS systems like the Wide Area Augmentation System (WAAS). The last updated parameters were presented during the ICAO Navigation Safety Panel (NSP) Ionospheric Gradient Monitor (IGM) Ad-Hoc group meeting held on 6th February 2016 (ICAO NSP, 2015).

Table 2 – Ionospheric gradient parameters (ICAO NSP, 2015)

$Slope$	$v < 750\ m/s$	$\leq 500\ mm/km$
	$750 \leq v \leq 1500\ m/s$	$\leq 100\ mm/km$
$Width$		$25 - 100\ km$
$Delay$		$\leq 50\ m$

These parameters are used to model an ionospheric front in the establishment of the ionosphere monitor performances.

2.1.4.2 Tropospheric delay

Troposphere is a non-dispersive medium that goes from the earth surface to about 50 km. It causes a delay in signal propagation due to air pressure, water-vapour and temperature. It is easier to model efficiently the impact of troposphere on the GNSS signal propagation (and thus to correct it) than that of the ionosphere. The UNB3 model used in civil aviation GPS receivers to correct the tropospheric delay can be found in (RTCA, Inc., 2006). Moreover, for civil aviation Galileo receivers, it is specified in (EUROCAE WG-62, 2007) that the Galileo receiver shall apply a tropospheric correction which is at least as good as the one defined for UNB3. Consequently, this model is a reference for both GPS and Galileo receivers.

$$T^i = -\left(d_{hyd} + d_{wet}\right).m(El_i) \qquad \text{Eq. 2.14}$$

Where:

- d_{hyd} is the estimated vertical range delay (i.e. for a satellite at 90° elevation angle) induced by gases in hydrostatic equilibrium in meters
- d_{wet} is the estimated vertical range delay caused by water vapour in meters
- El_i the satellite elevation angle
- $m(El_i)$ is a mapping function that scales the delays to the actual satellite elevation angle

d_{hyd} and d_{wet} are computed using the receiver height and five meteorological parameters: pressure P (mbar), temperature T, water vapor pressure e (mbar), temperature lapse rate β (K/m), and water vapor lapse rate λ (dimensionless).

Further details about the values needed to compute the tropospheric delay are given in (RTCA, Inc., 2006)

2.1.4.3 Satellite Clock Errors

The pseudorange measurements of GNSS receivers are biased by the lack of synchronization between the satellite and user clocks.

The satellite clock bias with respect to the GNSS system time is monitored by the GNSS control segment and transmitted to the users through the GNSS navigation message. The correction of the satellite clock offset for GPS and Galileo satellites is provided to the user through 4 terms, to be applied according to (ARINC Engineering Services, 2004) and (GJU-GALILEO Joint Undertaking, 2010):

$$\Delta t^i = a_{f0} + a_{f1}(t - t_{oc}) + a_{f2}(t - t_{oc})^2 + \Delta t_r \qquad \text{Eq. 2.15}$$

Where:

- a_{f0}, a_{f1} and a_{f2} are the polynomial coefficient provided for any satellite in the navigation data message. They represent the clock offset, the clock drift and the clock drift rate.
- t is the GPS system time in seconds and t_{oc} is the clock data reference time
- Δt_r is the relativistic correction

  $$\Delta t_r = F\, e\sqrt{A} \sin E_k$$

  The orbit parameters $e, \sqrt{A}, E_k$ are given in the navigation message or may be computed as in (ARINC Engineering Services, 2004). F is a constant$-4.442807633 \cdot 10^{-10}\ s/\sqrt{m}$.

2.1.4.4 Inter-frequency Biases

In addition to the dispersive ionospheric delay, the path of different signals from the same satellite at different frequencies may be subject to small biases created by RF components (antennae, filters, amplifiers) of the satellite or receiver, known as Inter Frequency Biases (IFB). The group delay T_{gd} expresses the magnitude of the satellite Inter-Frequencies Bias (IFB) for the L1/L2 signals combination in the GPS system. The receiver component of the IFB is only present on the L2 measurement, in fact by definition the IFB component on L1 is zero because the system time used by GPS receivers comes from the L1 C/A code (Holaschutz, et al., 2008). In order to take into account the same delay on L5 measurement another parameter, the Inter-Signals Correlation (ISC) is broadcast so that

$$(\Delta t_{sv})_{L5} = \Delta t_{sv} - T_{gd} - ISC_{L5}$$

2.1.4.5 Noise

Thermal noise is created by the receiver RF front-end. It is classically modelled as an additive white Gaussian noise. It affects the captured signal and therefore degrades the synchronisation capability of the receiver, and hence, the pseudorange measurements accuracy. The impact of thermal noise on the code and phase pseudorange is different, as illustrated in Table 3.

Table 3 – Thermal noise standard deviation for DLL and PLL (Julien O., 2011/2012)

	Thermal noise standard deviation (σ)
Code Pseudorange	$\approx 1\, m$
Phase Pseudorange	$\approx 0.001\, m$

2.1.4.6 Multipath

Multipath represents the non-direct path of one or more signals to reach the antenna. This multipath will mix with the direct LOS signal and will degrade the ability of the receiver to get synchronized with the direct signal (the only one representative of the true satellite/receiver range). It can lead to errors of different magnitude on the pseudorange measurement due to the excess of path of a reflected signal. This is represented in the following figure.

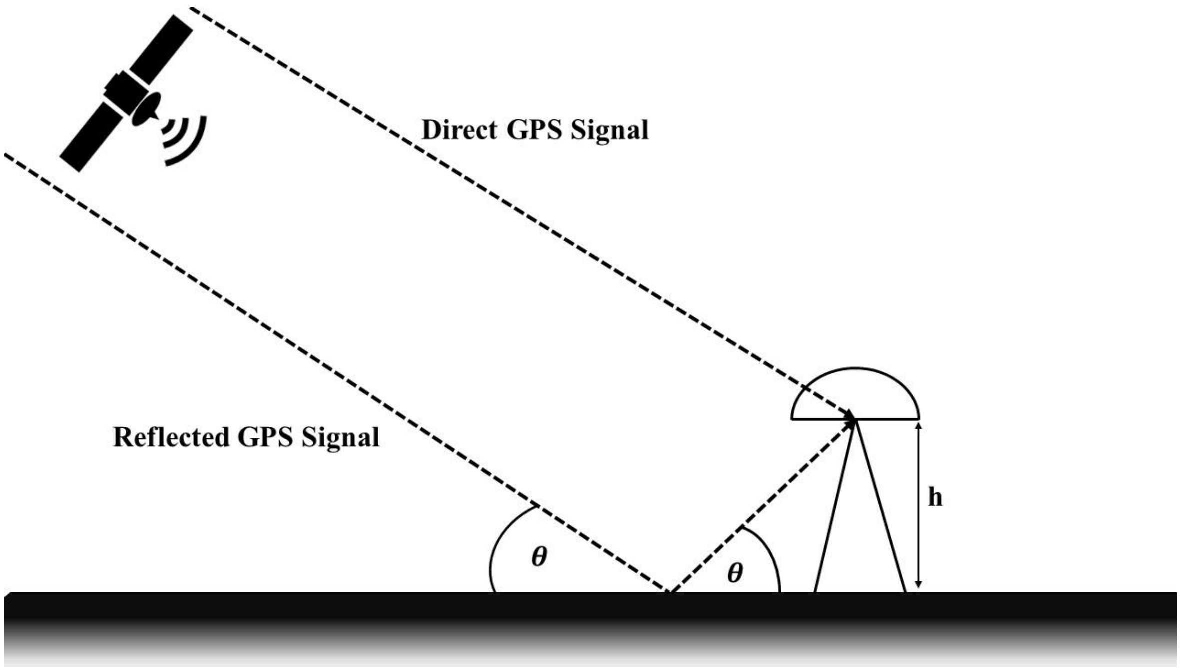

Figure 4 – LOS multipath example

The worst case pseudorange measurement error due to multipath interference from a reflected signal of the same amplitude as the direct signal is typically 150 meters for GPS L1 C/A code. However, most receivers, and new signals waveforms, are designed to produce smaller errors than this (Groves, et al., 2013).

The NLOS reception condition is a special case of multipath in which the direct signal (LOS) is blocked and only reflections are received by the receiver. This condition is typical of the urban environment, where the presence of buildings may block the direct signal and increase the probability to receive a NLOS signal. In civil aviation this phenomenon can occur at airport level, during the taxi operations near to the aerostation buildings.

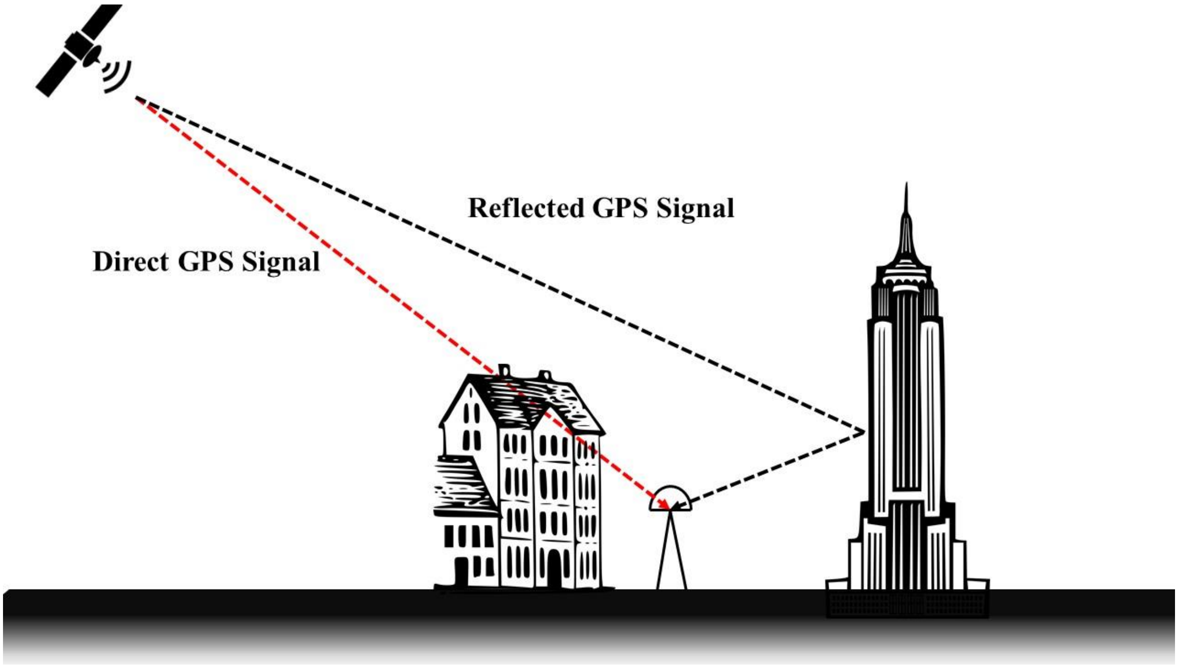

Figure 5 – NLOS multipath example

In this case, the receiver will most likely get synchronized with the strongest reflected GNSS signal. The pseudorange measurement will therefore be biased by a value equal to the additional path due to the reflection. This kind of error is always positive and it is potentially unlimited. The strength of NLOS signals varies greatly. They can be very weak, but can also be nearly as strong as the directly received signals. NLOS reception and multipath interference sometimes occur together. The most obvious case is when the direct signal from a particular satellite is blocked and multiple reflected signals are received. In this case, the combined ranging error may be thought of as the sum of an NLOS error due to the strongest reflected signal and a multipath error due to the additional reflected signals interfering with the strongest signal (Groves, et al., 2013).

2.1.4.7 Interference

Interference occurs when any undesired signal interferes with the reception of the GNSS signals of interest. Due to low power levels of the GNSS signals, GNSS receivers are susceptible to unintentional and intentional interference in their frequency bands. Even if a large number of mitigation techniques have been investigated to improve the performance of the GNSS receivers, civil aviation system may remain vulnerable.

Whereas all signals occupy protected bands, L5/E5a signals at 1176.45 MHz are exposed to interference by other aeronautical system pulsed emitters, especially distance measuring equipment (DME) and tactical air navigation (TACAN) systems. They operate in the frequency band between 960 MHz and 1215 MHz which are part of the aeronautical radio navigation services (ARNS) band. Emissions from these systems degrade the signal-to-interference plus noise ratio (SINR), cause tracking loops of receivers to fail and make the E5 decoding process more difficult than decoding L1, E1 (Thales, 2006).

Different methods can be used in order to mitigate this type of interference like pulse blanking or notch filtering or other more advanced methods (Thales, 2006).

Some of the interference can be intentional to GNSS signals, it is then called jamming. Indeed, it has been reported that low power jammers (personal privacy devices) can deny GPS/GBAS operation as reported in (Grabowski, 2012).

The three main unintentional interference types to be accounted for in the ARNS are:

- Carrier Wave interferences on all bands.
- Wideband interferences on all bands.
- Pulsed Interferences.
- Wideband jammers.

When some interfering signal is superimposed to the received useful signal, this may have the following three impacts on the pseudo range measurements (Martineau, 2008):

- The measurements are affected by some additional noise
- One or several measurements are affected by a bias (divergence of measurement)
- Some or all of the measurements are no longer available (loss of tracking)

2.2 Civil Aviation Applications

According to (ICAO, 2006), the combination of GNSS elements and a fault-free GNSS user receiver shall meet a series of defined Signal-in-Space (SiS) requirements. The concept of a fault-free user receiver is applied only as a means of defining the performance of combinations of different GNSS elements. The fault-free receiver is assumed to be a receiver with nominal accuracy and time-to-alert performance. Such a receiver is assumed to have no failures that affect the integrity, availability and continuity performance.

Table 4 – SiS performance requirements (ICAO, 2006)

Typical Operation	Accuracy Horizontal 95%	Accuracy Vertical 95%	Integrity	Time-to-Alert	Continuity	Availability
En-Route	*3.7 km*	*N/A*	$1 - 10^{-7}/h$	*5 min*	$1 - 10^{-4}/h$ *to* $1 - 10^{-8}/h$	*0.99 to 0.99999*
En-Route Terminal	*0.74 km*	*N/A*	$1 - 10^{-7}/h$	*15 s*	$1 - 10^{-4}/h$ *to* $1 - 10^{-8}/h$	
Initial Approach, Intermediate Approach, Non-Precision Approach, Departure	*220 m*	*N/A*	$1 - 10^{-7}/h$	*10 s*	$1 - 10^{-4}/h$ *to* $1 - 10^{-8}/h$	*0.99 to 0.99999*
Approach Operations with Vertical Guidance (APV-I)	*16 m*	*20 m*	$1 - 2 \cdot 10^{-7}/app$	*10 s*	$1 - 8 \cdot 10^{-6}/15\ s$	*0.99 to 0.99999*
Approach Operations with Vertical Guidance (APV-II)	*16 m*	*8 m*	$1 - 2 \cdot 10^{-7}/app$	*6 s*	$1 - 8 \cdot 10^{-6}/15\ s$	*0.99 to 0.99999*
Category I Precision Approach	*16 m*	*4 m ~ 6 m*	$1 - 2 \cdot 10^{-7}/app$	*6 s*	$1 - 8 \cdot 10^{-6}/15\ s$	*0.99 to 0.99999*

It is possible to see from the previous table that to use GNSS in civil aviation, defined levels of accuracy, continuity, integrity and availability must be met. The three requirements are defines as:

- *"The continuity of a system is the ability of the total system (comprising all elements necessary to maintain craft position within the defined area) to perform its function without interruption during the intended operation. More specifically, continuity is the probability that the specified system performance will be maintained for the duration of a phase of operation, presuming that the system was available at the beginning of that phase of operation"* (ICAO, 2006)
- *"Integrity is a measure of the trust that can be placed in the correctness of the information supplied to the total system. Integrity includes the ability of a system to provide timely and valid warnings to the user (alerts) when the system must not be used for the intended operation."* (ICAO, 2006)

- *"The availability of GNSS is characterized by the proportion of time the system is to be used for navigation during which reliable navigation information is presented to the crew, autopilot or other system managing the flight of the aircraft."* (ICAO, 2006)

Stand-alone GNSS in their current forms are, however, not able to meet the integrity requirement because of their failure rate. They have a failure rate, GPS $10^{-6}\,per\ year$ (GPS SPS, 2008) and GLONASS $10^{-4}\,per\ year$ (Heng, 2012), that does not permit to meet the continuity and the integrity requirements without an active monitoring system. Moreover the accuracy provided by GPS SiS (GPS SPS, 2008) and GLONASS SiS (Heng, 2012) is not meeting the accuracy requirements for operations like Approach operations with Vertical Guidance II (APV-II) and Category I (CAT I) precision approach.

In order to use GNSS to provide navigation guidance, the accuracy and the integrity must be improved. In the next sections the techniques used to improve the accuracy and the monitors or algorithms used to provide and improve integrity information will be presented.

2.2.1 GNSS Signals for Civil Aviation

In Figure 1 GNSS signals are presented. It is possible to see that they are located in the specific frequency bands named Radio Navigation Satellite Services (RNSS). Some of this signals are located into the ARNS (Aeronautical Radio Navigation Service) bands too, ARNS bands are reserved for aeronautical systems and particularly protected from in-band interference by regulation authorities. In the previous figure, we can observe that two different ARNS bands are occupied by GNSS signals, the 960-1215 MHz band and the 1559-1610 MHz band.

We will focus on the concerned signals which are:

- GPS L1 C/A
- GPS L1C
- GPS L5
- Galileo E1
- Galileo E5a

The characteristic of this signals are listed in Table 5:

Table 5 – GNSS Signals for Civil Aviation (ARINC Engineering Services, 2004) and (GJU-GALILEO Joint Undertaking, 2010)

Constellation	**Signal**	**Modulation**	**Code Length (ms)**	**Chip rate (Mcps)**	**Naviagtion Data (sps)**	**Secondary Code Length**
Galileo	E1B	CBOC (6,1,1/11)	4092	1.023	250	NO
	E1C		4092	1.023	Pilot	Primary x 25 (100 ms)
	E5A-I	QPSK(10)	10230	10.23	50	Primary x 20 (20 ms)
	E5A-Q		10230	10.23	Pilot	Primary x 100 (100 ms)
	E5B-I	QPSK(10)	10230	10.23	250	Primary x 4 (4 ms)
	E5B-Q		10230	10.23	Pilot	Primary x 100 (100 ms)
GPS	L1 C/A	BPSK(1)	1023	1.023	50	NO
	L1C-I	TMBOC(6,1,4/33)	10230	1.023	100	NO
	L1C-Q		10230	1.023	Pilot	1800 bits
	L5-I	QPSK(10)	10230	10.23	1000	NH-10 (10 bits)
	L5-Q		10230	10.23	Pilot	NH-20 (20 bits)

2.2.2 Accuracy Improvement

In 1.1.2, the errors affecting the pseudorange measurement have been described. Estimating and correcting some of these errors using an appropriate model is the normal practice for a stand-alone GNSS receiver. This correction procedure works quite well for an error source that is not dependent on the environment and is well modelled like the satellite clock offset. Other error sources like the ionospheric and tropospheric delays may not be fully corrected because the model itself is an approximation that does not consider all atmospheric parameters needed to compute the true delay. Moreover the used parameters are chosen according to a model and not according to the on-site conditions. Finally, for some error sources like noise and multipath it is not possible to provide a compensation value.

To improve the accuracy of the pseudorange measurement, two main techniques can be used:

- Differential Corrections
- Smoothing Technique

2.2.2.1 Differential Corrections

A way to further improve the correction of errors like ionosphere, troposphere and ephemeris errors, is Differential GNSS (DGNSS). This technique takes advantages of the spatial and temporal correlation under nominal condition of these errors. Their estimation, using a ground station at known position, is more accurate than using generic models as seen in the previous section for ionosphere and troposphere.

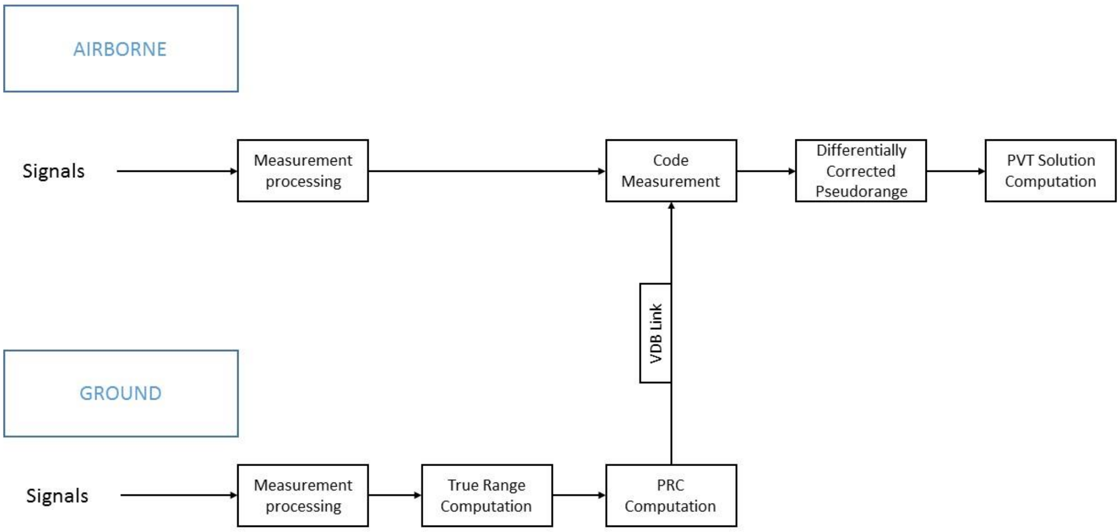

Figure 6 – Differential GNSS simplified scheme

The differential process uses the perfect knowledge of a reference station coordinates and satellite position to remove the true pseudoranges from the computed pseudorange leaving only the errors in the computed corrections, which can be used as corrections by the airborne receiver in the vicinity. The computation of the true pseudoranges is based on the satellites position computed using the ephemeris, which introduces the ephemeris error in the correction.

It is possible to write the pseudorange measurement as:

$$\rho_B = r_B + dr_B + \varepsilon_B \qquad \text{Eq. 2.16}$$

Where:

- dr_B represents the spatially and time correlated errors (ionosphere, troposphere and clock terms).
- ε_B represents the non-correlated errors (multipath and noise terms).

The corresponding PseudoRange Correction (PRC) can be computed by a reference station by removing the true range satellite-user from the pseudorange measurement on the ground is:

$$PRC = \rho_B - \hat{r}_B = dr_B + e_B + \varepsilon_B \qquad \text{Eq. 2.17}$$

Where:

- $\hat{r}_B$ is the computed user-satellite range using ephemeris to compute the satellite position
- e_B is the error introduced by using the ephemeris to compute the satellites positon and consequentially the user-satellite range

In a same way, the user (or airborne) pseudorange measurement is described by:

$$\rho_A = r_A + dr_A + \varepsilon_A \qquad \text{Eq. 2.18}$$

Where:

- dr_A is the spatially correlated delays and errors (ionosphere, troposphere and clock terms).
- ε_A is the non- correlated delays and errors (multipath and noise terms).

Finally the corrected measurement on the airborne side can be written as:

$$\rho_A - PRC \;\; = r_A + (dr_A - dr_B) - e_B + \; (\varepsilon_A - \; \varepsilon_B) \qquad \text{Eq. 2.19}$$

Where:

- $dr_A - dr_B$ is the residual error corresponding to the spatially correlated errors which should be at least partially cancelled.
- $\varepsilon_A - \; \varepsilon_B$ is the non-correlated error term provided by the ground and airborne functions.

The level of improvement of the accuracy is, however, related to two main parameters:

- Horizontal separation between the user and the ground station
- Correction time latency

Distance between the ground station and the user impacts the accuracy of the PRC since the spatial correlation of the errors in the PRC decreases with the increasing of the distance. The time latency, between the computation of the corrections and their application at the user side, is also a critical parameter. The corrections have to be applied in the shortest time delay to obtain the best accuracy improvement. As for the baseline distance, the time latency is related to the desired accuracy level.

2.2.2.2 *Smoothing Technique*

Certain non-correlated error sources such as those due to thermal noise or multipath cannot be removed by the differential correction process.

To reduce the error induced by these error sources the carrier smoothing technique can be used. Different techniques have been presented in the literature using single frequency or dual frequency combinations of phase and code measurements (Hwang, et al., 1999). The general scheme of the smoothing process is:

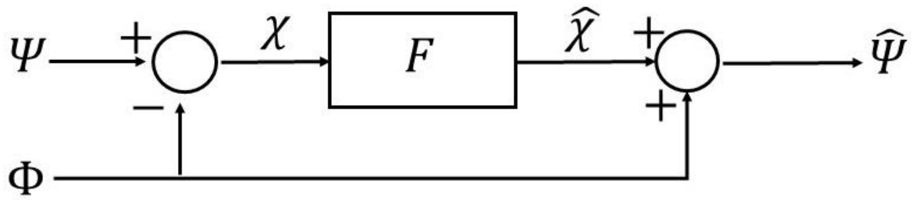

Figure 7 – Block diagram of carrier smoothed code processing

In Figure 7 the terms are

- Ψ is the code measurement combination
- Φ is the phase measurement combination
- χ is the Code Minus Carrier (CMC)
- $\hat{\chi}$ and $\hat{\Psi}$ are the smoothed CMC and pseudorange measurement
- F is the Hatch filter (Hatch, 1982).

The commonly used Hatch filter formula is:

$$\hat{\chi}^i(k) = \frac{1}{n}\Psi^{\mathrm{i}}(k) + \frac{n-1}{n}\left[\hat{\chi}^i(k-1) + \left(\phi^i(k) - \phi^i(k-1)\right)\right] \qquad \text{Eq. 2.20}$$

Where:

- i refers to any satellite in view
- k is the current epoch.
- n is a counter that goes from 1 to the chosen filter time constant for any according to the smoothed epochs. Reached its maximum value it remains constant.

The forms of the code and phase combinations differentiate the techniques proposed in the literature (Hwang, et al., 1999). In the next part of this section, the Single Frequency (SF), Divergence-Free (D-Free) and Ionosphere-Free (I-Free) smoothing techniques will be presented in details, highlighting the main advantages and drawbacks for each one. Some error sources like clock bias on satellite and receiver, tropospheric delay will not be considered because they are common on the code and phase measurement and therefore they are not impacted by the smoothing filter (Hwang, et al., 1999).

2.2.2.2.1 Single Frequency Smoothing

In this technique, the code and phase combination is equal to the difference between the code and phase measurement on a single frequency. Considering the code and phase equations Eq. 2.10 and Eq. 2.11 it is possible to determine the terms affecting the Code-Minus-Carrier (CMC) measurement.

$$\chi = 2I - N + (\eta_\rho - \eta_\phi) \qquad \text{Eq. 2.21}$$

η_ρ and η_ϕ are two terms representing the noise and multipath errors affecting the code and phase measurement. After filtering the CMC, the ionospheric term becomes:

$$\hat{\chi} = 2\,F\,(I) - N + F(\eta_\rho - \eta_\phi) \qquad \text{Eq. 2.22}$$

Where:

- F is the filter response as function of the selected filter time constant.

In particular the term $2\,F\,I$ can create problem whenever a time varying ionospheric delay is present. This effect appears especially on low-elevation satellites. N being constant, it will not be affected by the filter. After the smoothing of the CMC, the phase measurement is added.

$$\hat{\psi} = \hat{\chi} + \phi = r + (2\,F - 1)I + F\eta_\rho + (1 - F)\eta_\phi \qquad \text{Eq. 2.23}$$

Analyzing the previous equation, it is possible to highlight that it is now affected by some errors having different properties than the raw code measurement. The code noise and multipath term is now impacted by the smoothing filter, and assuming that it is statistically independent sample to sample its standard deviation may be considered as (Hwang, et al., 1999):

$$\hat{\sigma}_{noise\,\&\,multi} = \sigma_{noise\,\&\,multi}\sqrt{\frac{T}{2\tau}}$$

Where:

- T is the sampling output interval
- τ is the smoothing filter time constant

Using a value of the smoothing filter bigger than the measurement output interval (ex. 100s in the GBAS or SBAS system), the standard deviation of noise and multipath can be strongly reduced.

The main drawback of this technique is represented by the ionospheric term, $(2F - 1)I$. Let us consider the ionospheric delay as a bias plus ramp part.

$$I = I_0 + I_d t$$

It is possible to show that in presence of a time varying ionospheric delay ($I_d \neq 0$), the filter introduces an error equal to $2\tau I_d$ (Hwang, et al., 1999). This technique, in presence of a varying ionospheric delay, creates a divergence term proportional to the used smoothing constant and the delay itself.

In order to use the smoothed measurement under this condition in a differential GNSS system, the ground and airborne smoothing filters must be in steady state condition using the same filter time constant. In (RTCA Inc. DO245-A) the steady state is considered reached after 360 seconds of continuous operations for 100 seconds smoothing constant. This requirement can limit the satellites availability after acquisition of re-acquisition or carrier phase cycle slip.

2.2.2.2.2 D-Free CMC

A way to solve the previous problem of the single frequency smoothing under particular ionospheric conditions is the use of dual frequencies measurement. The divergence-free (D-Free) technique uses two phase measurements coming from different frequencies to compute the phase measurement combination.

$$\Phi = \phi_1 - \frac{2}{\alpha}(\phi_1 - \phi_5) \qquad \text{Eq. 2.24}$$

Where:

- ϕ_1 is the phase measurement on L1
- ϕ_5 is the phase measurement on L5
- $\alpha = 1 - \frac{f_1^2}{f_5^2}$, f_1 and f_5 are the carrier frequencies of the used signals

The CMC is then computed as:

$$\chi = \rho_1 - \phi_1 + \frac{2}{\alpha}(\phi_1 - \phi_5) \qquad \text{Eq. 2.25}$$

It is possible to demonstrate that thanks to the phase combination, the CMC is no longer affected by any ionospheric term. Replacing the code and phase measurement model in Eq. 2.25 it is possible to obtain.

$$\chi = (I_1 + \eta_{\rho 1}) - \left(-I_1 + N_1 + \eta_{\phi 1} - \frac{2}{\alpha}\left(-(I_1 - I_5) + (N_1 - N_2) + (\eta_{\phi 1} - \eta_{\phi 5})\right)\right) \qquad \text{Eq. 2.26}$$

Where:

- I_1 and I_5 are the ionospheric delay respectively on L1 and L5 measurement
- $\eta_{\phi 1}$ and $\eta_{\phi 5}$ are noise and multipath errors on the phase measurement according to the used frequency

Considering the relationship between the ionospheric delay and the frequency of the received signal

$$I_1 = \frac{I}{f_1^2}; \qquad I_5 = \frac{I}{f_5^2} \qquad \text{Eq. 2.27}$$

It is possible to derive the following relationship

$$I_1 - I_5 = \left(1 - \frac{f_1^2}{f_5^2}\right) I_1 = \alpha\, I_1 \qquad \text{Eq. 2.28}$$

Replacing the term found in equation Eq. 2.28 in equation Eq. 2.26 and simplifying the common terms obtaining:

$$\chi = \left(I_1 + \eta_{\rho 1}\right) - \left(I_1 + N_{15} + \eta_{\phi 15}\right) = \eta_{\rho 1} - \left(N_{15} + \varepsilon_{\phi 15}\right) \qquad \text{Eq. 2.29}$$

Where:

- $N_{15} = N_1 - \frac{2}{\alpha}(N_1 - N_5)$
- $\eta_{\phi 15} = \eta_{\phi 1} - \frac{2}{\alpha}\left(\eta_{\phi 1} - \eta_{\phi 5}\right)$

The CMC as shown in Eq. 2.29 is not affected by the ionospheric delay term. After the filter, it becomes:

$$\hat{\chi} = F\eta_{\rho 1} - N_{15} - F\eta_{\phi 15} \qquad \text{Eq. 2.30}$$

As for the single frequency case, the last step is the addition of the phase measurement to the CMC.

$$\widehat{\psi} = \hat{\chi} + \Phi = F\,\eta_{\rho 1} - F\eta_{\phi 15} + r + I_1 + \eta_{\phi 15} = r + I_1 + F\,\eta_{\rho 1} + (1 - F)\eta_{\phi 15} \qquad \text{Eq. 2.31}$$

The analysis of the residual error shows that the noise and multipath affecting the code measurement has the same properties as in the single frequency case, the same error on the phase can be considered as negligible.

The ionospheric delay is no longer impacted by the smoothing filter and its value is the same as the one present on the code measurement, and it will appear in the corrections sent to the user. This technique solves the problem of the filter steady state, but in case of an ionospheric threat, the system cannot be used due to the spatial decorrelation of the ionospheric delay between ground and airborne system.

2.2.2.2.3 I-Free CMC

The ionosphere-free (I-Free) technique uses two code and two phase measurements coming from two different frequencies to remove the ionospheric delay also from the smoothed code measurement. The code and phase combinations are built in this way:

$$\Psi = \rho_1 - \frac{1}{\alpha}(\rho_1 - \rho_5) \qquad \text{Eq. 2.32}$$

$$\Phi = \phi_1 - \frac{1}{\alpha}(\phi_1 - \phi_5) \tag{Eq. 2.33}$$

Forming the CMC it is possible to see that the ionospheric delay is not present:

$$\begin{aligned}\chi = (I_1 + \eta_{\rho 1}) - \frac{1}{\alpha}\left((I_1 - I_5) + (\eta_{\rho 1} - \eta_{\rho 5})\right) \\ - \left(-I_1 + N_1 + \eta_{\phi 1} - \frac{1}{\alpha}\left(-(I_1 - I_5) + (N_1 - N_5) + (\eta_{\phi 1} - \eta_{\phi 5})\right)\right)\end{aligned} \tag{Eq. 2.34}$$

Knowing the relationship between ionospheric delay and frequency of the received signal in Eq. 2.28 it is possible to simplify the common terms obtaining:

$$\begin{aligned}\chi = (I_1 + \eta_{\rho 1}) - I_1 - \frac{1}{\alpha}\left(+(\eta_{\rho 1} - \eta_{\rho 5})\right) \\ - \left(-I_1 + N_1 + \eta_{\phi 1} + I_1 - \frac{1}{\alpha}\left((N_1 - N_5) + (\eta_{\phi 1} - \eta_{\phi 5})\right)\right)\end{aligned} \tag{Eq. 2.35}$$

The remaining terms can be written as

$$\chi = \eta_{\rho 15} - (N_{15} + \eta_{\phi 15}) \tag{Eq. 2.36}$$

Where:

- $\eta_{\rho 15} = \eta_{\rho 1} - \frac{1}{\alpha}(\eta_{\rho 1} - \eta_{\rho 5})$
- $\eta_{\phi 15} = \eta_{\phi 1} - \frac{1}{\alpha}(\eta_{\phi 1} - \eta_{\phi 5})$
- $N_{15} = N_1 - \frac{1}{\alpha}(N_1 - N_5)$

As for the D-Free case the ionospheric delay is not present in the CMC, after the filter the CMC is

$$\hat{\chi} = F\varepsilon_{\rho 15} - F(N_{15} + \varepsilon_{\phi 15}) \tag{Eq. 2.37}$$

Adding the phase combination as in Eq. 2.11 the smoothed code measurement is:

$$\hat{\psi} = \hat{\chi} + \phi = r + F\varepsilon_{\rho 15} + (1 - F)\varepsilon_{\phi 15} \tag{Eq. 2.38}$$

It is possible to notice that in the smoothed code measurement, represented above, the ionospheric delay is not present at all. This condition brings a lot of benefits in the GBAS system in term of reduced, or totally absent, monitoring activity of the ionospheric threat.

However, the use of two code measurements leads to an increased standard deviation value of the code measurement, without considering the smoothing impact on it.

$$\sigma_{I-Free} = \sqrt{\left(1-\frac{1}{\alpha}\right)^2 \sigma_{\rho 1}^2 + \frac{1}{\alpha^2}\sigma_{\rho 5}^2 + \left(\frac{2}{\alpha}-\frac{2}{\alpha^2}\right) Cov(\rho_1, \rho_5)} \qquad \text{Eq. 2.39}$$

The total variance of the I-Free code measurement is therefore bigger than the single frequency or the D-Free code measurement, because they use a single code measurement. Considering the frequency of GPS L1 and GPS L5, or for Galileo E1 and E5a, the value of α is -0.7933. Assuming that the standard deviations of the raw code measurements have the same values and there is no covariance between the measurements, the standard deviation of the I-Free is 2.5583 times bigger than $\sigma_{\rho 1}$.

2.2.3 Integrity Improvement

To use GNSS in civil aviation it is not enough to simply improve the accuracy over the standalone system. The knowledge of the position integrity must be provided as well (Kaplan, et al., 2006)

2.2.3.1 Navigation Threats

In (EU-U.S , 2012) navigation threats are defined as:

"all possible events (i.e. of natural, systemic or operational nature) that can drive the computed navigation solution to deviate from the true position, regardless of whether a specific fault can be identified in one of the navigation systems or not."

Based on the previous definition the following threats have been identified (EU-U.S , 2012):

- Satellite Clock and Ephemeris
- Signal deformation
- Code-Carrier incoherence
- Satellite antenna bias
- Ionosphere anomalous condition
- Troposphere anomalous condition
- Noise and multipath

In order to guarantee the integrity against these threats, in augmentation systems different typologies of monitor have been developed. They will be presented in 2.3.3 and in 5.2.1

2.2.3.2 Threats Monitoring

Over the years different ways to provide integrity information have been developed, referred to as augmentation systems. The augmentation systems are classified as:

- Satellite Based Augmentation System (SBAS)
- Ground Based Augmentation system (GBAS)
- Aircraft Based Augmentation System (ABAS)

Details about each one of these augmentation system will be provided in the next sections

2.2.4 Augmentation Systems

2.2.4.1 SBAS

SBAS is a civil aviation safety-critical system that covers wide-area or regional areas through the use of geostationary satellites which broadcast augmentation information to the airborne GNSS receiver. SBAS provides a series of information with the aim to improve the accuracy and the integrity of the computed PVT. The accuracy is improved thanks to the broadcast of differential corrections computed by the ground segment for all satellites:

- Satellite clock/time errors
- Ephemeris errors
- Ionospheric corrections computed for a series of points forming a grid. The user can then use these values to assess, by interpolation, its appropriate correction (Escher, et al., 2014). In Figure 8 it is possible to see how the ionospheric delay is computed, for an aircraft, using the closest values in a grid.

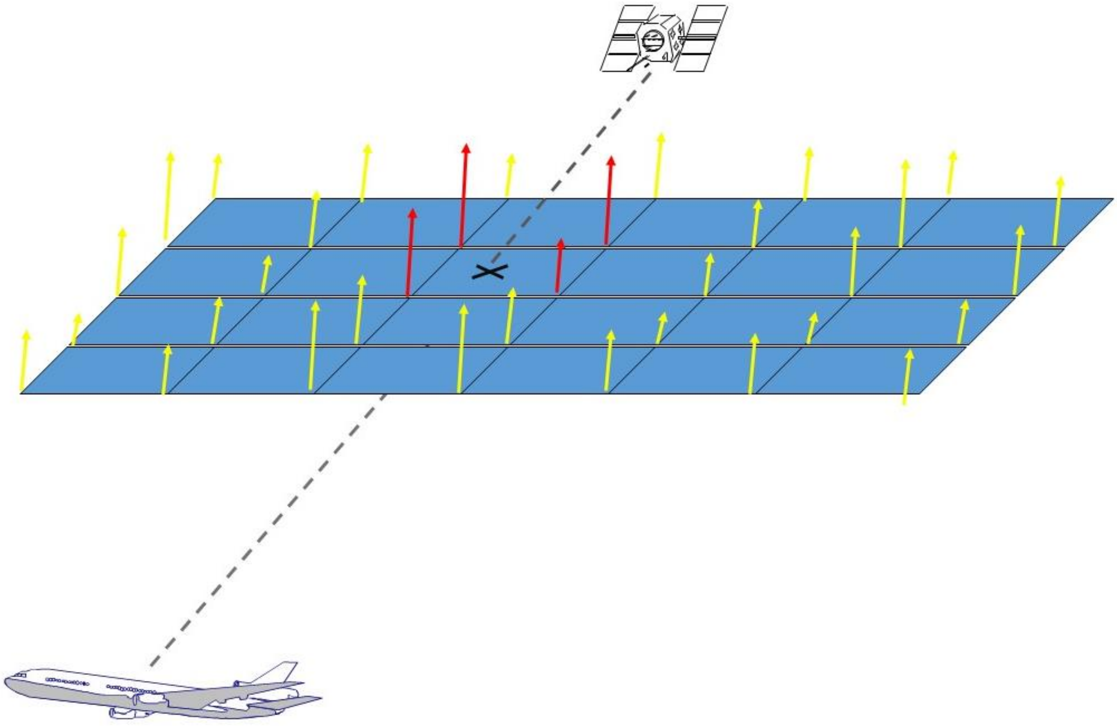

Figure 8 – SBAS ionospheric corrections adapted from (Escher, et al., 2014)

The integrity information is provided by the ground segment through the provision of appropriate assessment of the provided differential corrections and the monitoring of potential Signal-in-Space (SiS) failure. SBAS ground stations thus encompass a series of monitors are present (Van Dyke, et al., 2003):

- Signal Distortion Monitor (SDM), also mentioned as Signal Quality Monitor (SQM)
- Code-Carrier Divergence (CCD)
- Ephemeris Error Monitor
- Step or ramp accelerations monitor

The integrity is thus guaranteed by the ground segment relying also on the following elements:

- Tests carried out by and interference monitor
- Parallel processing chains enabling data checks
- Position monitor installed jointly with the ground station to check that the protection level truly overbound the position error

Due to the use of similar monitor between SBAS and GBAS, more details about the monitors will be provided in the next sections about GBAS integrity monitor.

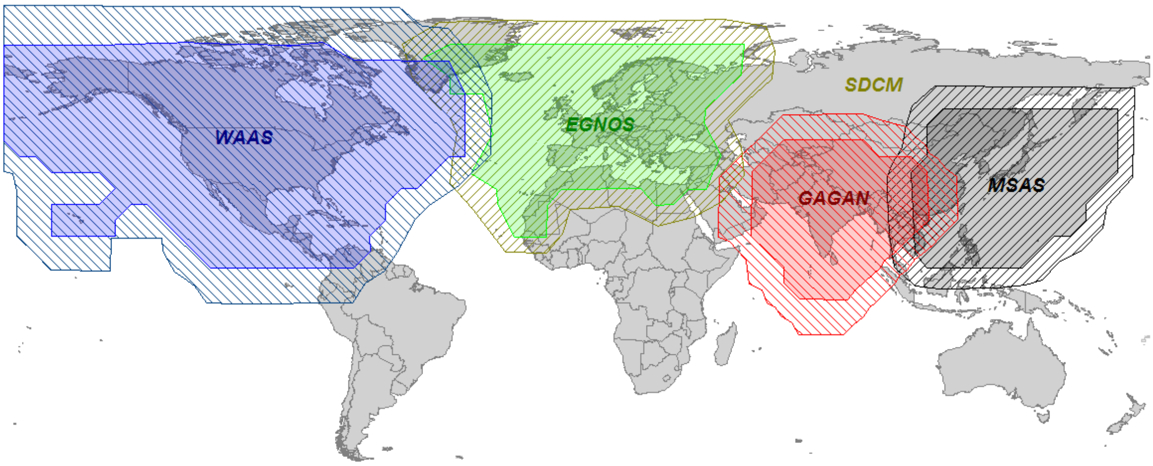

Figure 9 – Global SBAS coverage map (gpsworld.com)

The main parts of the system architecture are

- Space segment, GNSS constellations and the geostationary satellites (GEO) with navigation payloads in charge of transmitting a GPS-like carrier signal with the SBAS information.
- Support segment comprising all the elements needed to support the correct operation and maintenance of the SBAS: configuration control, performance evaluation, maintenance and development, help desk, etc.

- User segment comprising all the user equipment needed to receive and use the SBAS information.
- Ground segment comprising all the ground elements in charge of the provision of the SBAS navigation message. The main purpose of the ground segment is to generate and uplink the augmentation signal that will be broadcast by the GEO satellite. To achieve this objective different ground facilities with different tasks are used:
    - Monitoring Station Network: Its purpose is to collect data from the satellites that must be augmented. This is performed by a network of GNSS receivers.
    - Processing Facility Center: It is in charge of processing the data provided by the Monitoring Station Network to generate the messages to be broadcasted to the satellites.
    - GEO Satellite Control Center: It is in charge of generating the signal with the message provided by the Processing Facility Center and up-linking it to the GEO satellites.
    - Communication Layer: It interconnects the different elements of the Ground Segment.

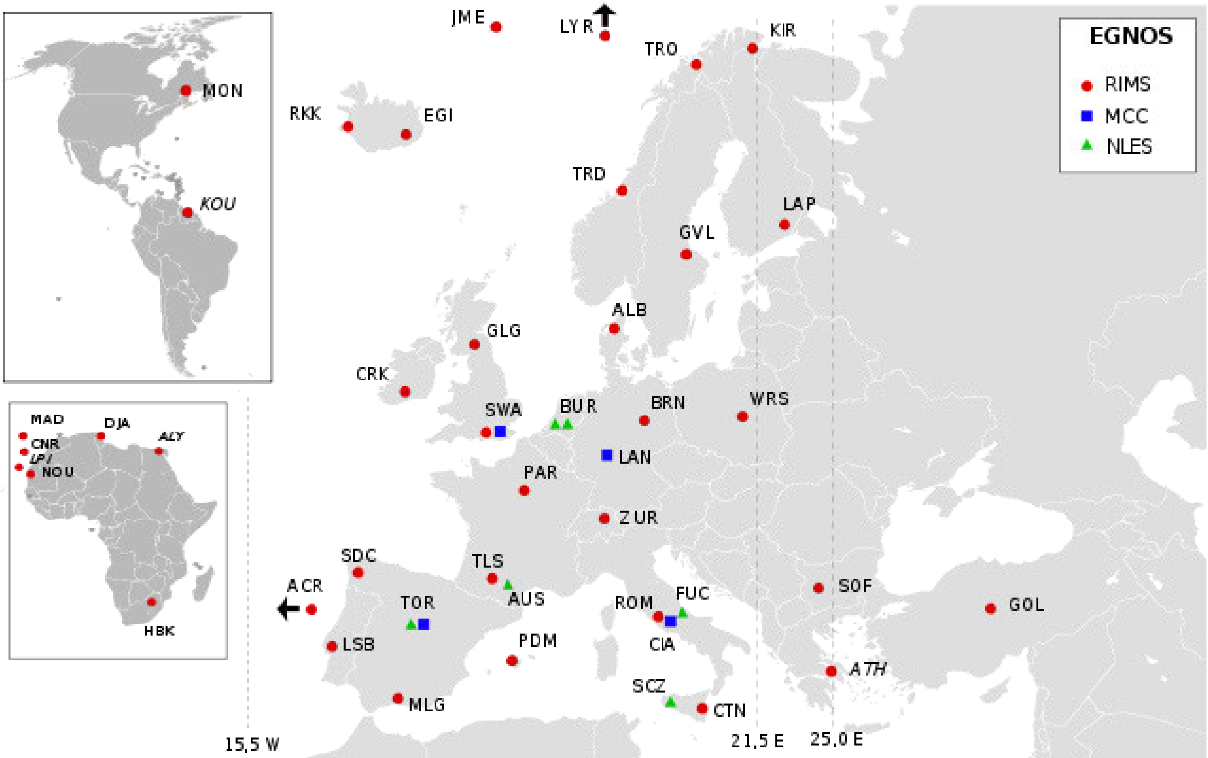

Figure 10 – Ground station facilities spread over Europe for EGNOS SBAS system

Considering the limitation of the number of ground control stations and operation costs, it is thought that the best performance level that can currently be attained by the SBAS corresponds to ICAO APV I or II (Table 4) performance approaches (Escher, et al., 2014).

CAT I approaches with VAL = 35m and recommendations in ICAO Annex 10 are built to exploit the high accuracy of the American satellite-based augmentation system WAAS. This operation would provide a significant operational benefit compared to the existing APV operations, mainly because of the decision height of 200 ft..

2.2.4.2 ABAS

An ABAS is basically a system that augments and/or integrates the information obtained from the GNSS elements only with information available on board the aircraft (Escher, et al., 2014). The scope of the system is to provide information about the integrity and to improve the accuracy of the GNSS solution.

The information about integrity are provided using:

- RAIM (Receiver Autonomous Integrity Monitoring), this algorithm uses redundant GNSS measurement to derive integrity information
- AAIM (Aircraft Autonomous Integrity Monitoring) this technique integrates the redundant GNSS information with other information present on-board the aircraft as the inertial information.

The accuracy of the GNSS solution is improved integrating the GNSS information with the ones coming from the other sensors present on-board the aircraft. Data fusion mainly allow to improve the accuracy and the continuity if the service (Escher, et al., 2014).

Nowadays, around 70% of European flights are made by aircraft equipped with GPS and RAIM (Rees, 2009).

2.2.4.3 GBAS

The last augmentation system described is the GBAS. Being the main focus of this thesis, a detailed description is given in section 2.3

2.3 GBAS

To provide an accurate guidance for the approach and landing phases, up to CAT III service level, the ILS (Instrumental Landing System) has been used so far. Nevertheless, with the increase of the civil aviation traffic volume and airport surfaces, this system is no longer representing an optimal means to provide guidance to the aircrafts. The main drawbacks of the ILS are in fact:

- One installation required on each runway end and
- Only straight-in approach and landing signal guidance.
- Removal of the ILS sensitive area
- Reduced separation minima according to wake turbulence (ICAO PANS ATM)

ICAO, in order to find a system more flexible than ILS, able to provide guidance not only for the straight–in trajectory, has identified GNSS as a technology with the potential to replace it. As explained in 2.2.2 and 2.2.3 GNSS stand-alone service cannot meet the accuracy and integrity requirement. In order to meet ICAO standards an augmented system must be used to improve performances.

GBAS is a civil aviation safety-critical system that supports local augmentation of the GNSS constellation by providing enhanced levels of service that support all phases of approach, landing, departure and surface operations. While the main goal of GBAS is to provide integrity assurance, it also increases the accuracy with position errors standard deviation below 1 m for 95% if time (Kaplan, et al., 2006). Signals from GNSS satellites are received by the Reference Receivers at the GBAS-equipped airport, which calculates pseudorange errors using these signals. Then GBAS Ground Facility (GF) averages these errors on each pseudorange measurement to create for each satellite a PRC and RRC. The GF creates a message to broadcast the corrections. Other messages are created to broadcast integrity parameters, approach path and information related to the used approach service. Finally all the correction messages are sent to a VHF data broadcast (VDB) transmitter.

Despite the similitude with SBAS, there are some important differences. The area coverage is one of the main difference between GBAS and SBAS, typically GBAS covers a radius of 50 Km in order to support precise approach operations while SBAS covers wide areas as an entire continent. The GBAS coverage for each runway end is defined in (ICAO, 2006) and (RTCA Inc. DO245-A).

- *laterally, beginning at 140 m (450 ft.) each side of the landing threshold point/fictitious threshold point (LTP/FTP) and projecting out ±35 degrees either side of the final approach path to 28 km (15 NM) and ±10 degrees either side of the final approach path to 37 km (20 NM); and*
- *vertically, within the lateral region, up to the greater of 7 degrees or 1.75 promulgated glide path angle (GPA) above the horizontal with an origin at the glide path interception point (GPIP) to an upper bound of 3000 m (10 000 ft.) height above threshold (HAT) and 0.45 GPA above the horizontal or to such lower angle, down to 0.30 GPA, as required, to safeguard the promulgated glide path intercept procedure. The lower bound is half the lowest decision height supported or 3,7 m (12 ft.), whichever is larger.*

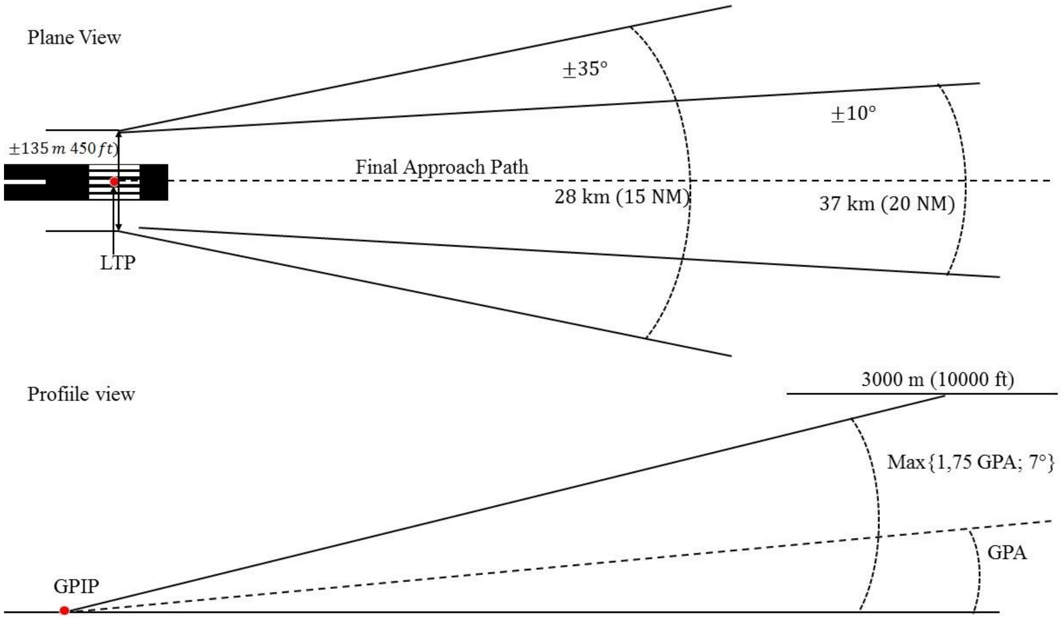

Figure 11 – GBAS Runway coverage

The horizontal distance of 37 km must be increased considering that the position of the GBAS ground station may be located anywhere in the airport area. Typical coverage values are 45/50 km.

The coverage is not the only difference, the way to compute and provide corrections represents an important difference as well. In GBAS corrections are scalar values computed for any satellites with a limited validity in time and space, relying on the correlation properties in time and space of certain error sources.

2.3.1 GBAS Architecture

A typical GBAS architecture is represented in Figure 12.

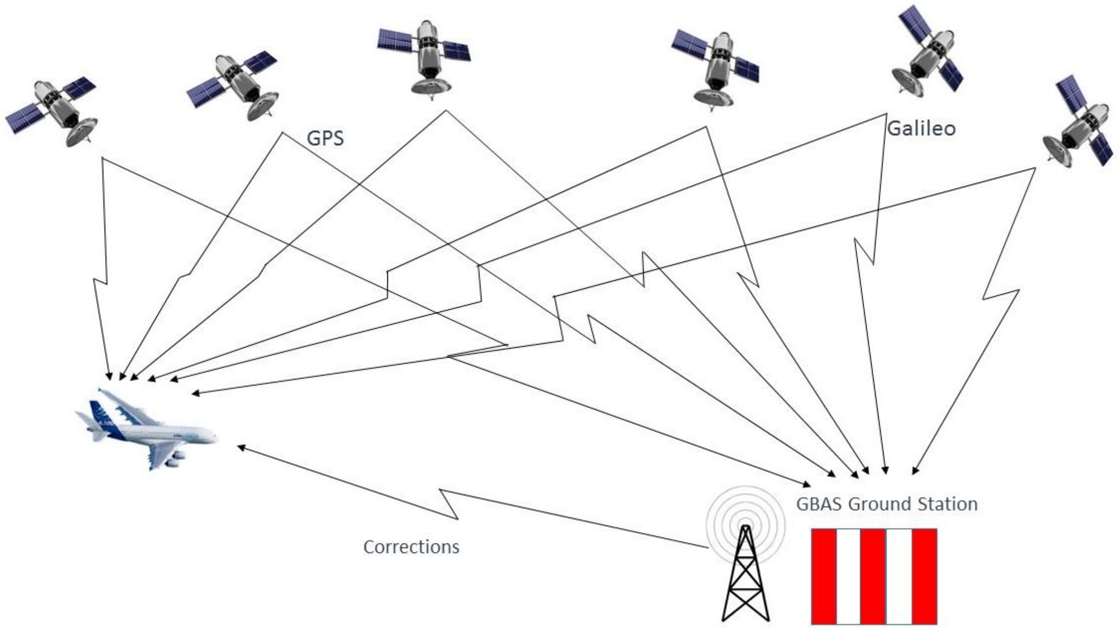

Figure 12 – Typical GBAS architecture

The main components of a GBAS system, as seen in Figure 12, are

- Ground station, equipped with a series of receivers
- User segment, typically corresponding to an aircraft
- Space segment (GNSS core constellations)

2.3.1.1 Ground Station

A typical GBAS ground station is composed by the following components:

- 2 to 4 GNSS Reference Receivers and their respective geographically separated antennas;
- A VHF data broadcast (VDB) transmitter;
- A monitor system;
- Ground processing unit.

It can be considered as the subsystem playing the major role in GBAS system. Its main purposes are:

- reception and decoding of signals-in-space;
- Computation of the differential corrections to the carrier-smoothed pseudoranges;
- Integrity monitoring;
- Generation and broadcasting of GBAS messages.

2.3.1.2 User Segment

The user segment of a GBAS system corresponds to all aircrafts equipped with a GBAS receiver and all the avionics necessary to use the information provided. The main function of this subsystem are (ICAO, 2006):

- To receive and decode the GNSS satellites signal(s) and GBAS correction messages;
- To determine the aircraft position;
- To assess the availability of the service;
- To compute deviations from the desired flight path calculated from the Final Approach Segment (FAS) data;
- To provide guidance signals and integrity information.

2.3.1.3 Space Segment

The space segment is represented by all the GNSS constellations that are operational or under development. It will be seen in the following of the work that according to the selected service one or more constellations can be used to reach the scope of GBAS.

2.3.2 GBAS Measurements Processing

2.3.2.1 Ground measurement processing

As said in the previous section, the GBAS ground section is in charge of computing the PRC and Range-Rate Corrections (RRC) and broadcast them to any user present in the coverage area (RTCA Inc. DO245-A). The entire process to compute the PRC and the RRC can be split in two main blocks:

1. Smoothing of the pseudorange
2. Computation of the PRC and RRC

The different possible processes for the smoothing have been already shown in 2.2. In the following, the process for the computation of the correction will be shown.

The first measurement to analyse is the received pseudorange measurement considering that more than one reference receiver is present at the ground.

$$\rho_m^i = r_m^i + \Delta t^i + \Delta t_m + I^i + T^i + \eta_m^i \qquad \text{Eq. 2.40}$$

Where m indicates one of the RR at ground station, considering the short distance between RRs in nominal condition the ionospheric and tropospheric delay are assumed to have the same values on different RRs.

Using the navigation message and the procedures described in (ARINC Engineering Services, 2004) and (GJU-GALILEO Joint Undertaking, 2010), each reference receiver can compute the satellites position and, knowing its own position, the geometrical range; r_m^i. The latter can be removed from the received pseudorange measurement, and Eq. 2.40 becomes

$$PRCt_m^i = \rho_m^i - r_m^i = \Delta t^i + \Delta t_m + I_m^i + T_m^i + \eta_m^i + e_m^i \qquad \text{Eq. 2.41}$$

e_m^i is the error caused by ephemeris error on satellite i and receiver m.

This kind of error is not listed in section 0 and in the previous equation because it cannot be classified as a *measurement* error, but rather as a *computation* error. It must be taken into account when the satellites position is computed because of errors in using ephemeris. This error denotes the difference between the real satellite position and the one computed by any user using the ephemeris into the line-of-sight vector. It is reasonable to approximate this error as similar for all the RR because it is function of the user-satellite vector, being this distance bigger than 20000 km and the RRs distance in the order of tens of meters.

The right terms in equation Eq. 2.41 can be divided in two main categories:

1. Errors correlated between aircraft and ground station including the tropospheric and ionospheric delay, the satellite clock bias and the ephemeris error.
2. Uncorrelated Errors including the two remaining error sources considered, multipath, noise as well as the receiver clock bias.

In order to limit the magnitude of the corrections and to reduce the size of the transmitted message, the receiver clock average is estimated and removed from the final PRC of each RR.

$$\widetilde{\Delta t_m} = \frac{1}{N}\sum_{i=1}^{N} PRCt_m^i \qquad \text{Eq. 2.42}$$

Where:

N is the number of satellites used by all receivers to compute the PRC

The estimated receiver clock offset differs from the real one, Δt_m by the following term.

$$\widetilde{\Delta t_m} = \Delta t_m + \frac{1}{N}\sum_{i=1}^{N}\left(\Delta t^i + I^i + T^i + \varepsilon^i + \eta_m^i\right) \qquad \text{Eq. 2.43}$$

Defining

$$t_m = \frac{1}{N}\sum_{i=1}^{N}\left(\Delta t^i + I^i + T^i + \varepsilon^i + \eta_m^i\right) \qquad \text{Eq. 2.44}$$

The first four terms inside the brackets, in Eq. 2.44, are highly correlated for all the reference receivers. Being errors common to all PRCs their impact on the user's position is negligible. They will be estimated jointly with the user's receiver clock offset as the fourth unknown of the PVT solution and then corrected. The last term in Eq. 2.44 is the only term that impacts the user's position accuracy, Eq. 2.44 can be rewritten as:

$$t_m = \kappa + \frac{1}{N}\sum_{i=1}^{N} \eta_m^i \qquad \text{Eq. 2.45}$$

Where $\kappa = \frac{1}{N}\sum_{i=1}^{N} t^i + I^i + T^i + \varepsilon^i$

Removing the estimated receiver clock offset from the $PRCt_m$ of all satellites and same RR gives:

$$PRC_m^i = PRCt_m^i - \widetilde{\Delta t_m} = t^i + I^i + T^i + \eta_m^i + \varepsilon^i - t_m \qquad \text{Eq. 2.46}$$

The corrections can now be averaged over the M reference receivers at ground in order to obtain the final PRC to be broadcasted to the user.

$$PRC^i = \frac{1}{M}\sum_{\mathrm{m}=1}^{M} PRC_m^i \qquad \text{Eq. 2.47}$$

The effect of averaging the corrections of each RR has the following impact on the PRC (RTCA Inc. DO245-A).

$$PRC^i = \Delta t^i + T^i + I^i + \varepsilon^i - \frac{1}{\mathrm{M}}\sum_{m=1}^{M} t_m + \frac{1}{M}\sum_{\mathrm{m}=1}^{M} \eta_m^i \qquad \text{Eq. 2.48}$$

Replacing the estimated receiver clock t_m with the one in Eq. 2.45, the actual PRC computed by the ground system is:

$$PRC^i = \Delta t^i + T^i + I^i + \varepsilon^i - \kappa - \frac{1}{M}\sum_{m=1}^{M} \frac{1}{N}\sum_{\mathrm{i}=1}^{N} \eta_m^i + \frac{1}{M}\sum_{\mathrm{m}=1}^{M} \eta_m^i \qquad \text{Eq. 2.49}$$

The terms $\Delta t^i + T^i + I^i + \varepsilon^i$ are spatially and temporally correlated between the ground station and the airborne receiver. The term κ has been already descripted, being common to all satellites is removed compensating for the receiver clock offset. The last terms are the ground error contribution to the corrected pseudorange.

The problem seen in 2.2 for the ionospheric delay after the smoothing process is not considered in the previous equation for the PRC computation.

The Range Rate Corrections (RRC) is the rate of change of corrections in time and as for the PRC, it is sent from the ground station to the user. It is computed as

$$RRC^i(k) = \frac{PRC^i(k) - PRC^i(k-1)}{\Delta T} \qquad \text{Eq. 2.50}$$

The index k represents the reference epochs of each PRC and RRC, ΔT is the correction interval; defined for the GBAS ground segment to be 0.5 seconds.

2.3.2.2 Airborne measurement processing

The corrected pseudorange measurements are computed in two main steps:

1. Smoothing of the raw pseudorange measurement
2. Application of the PRC and RRC and other corrections to obtain the corrected pseudorange measurement.

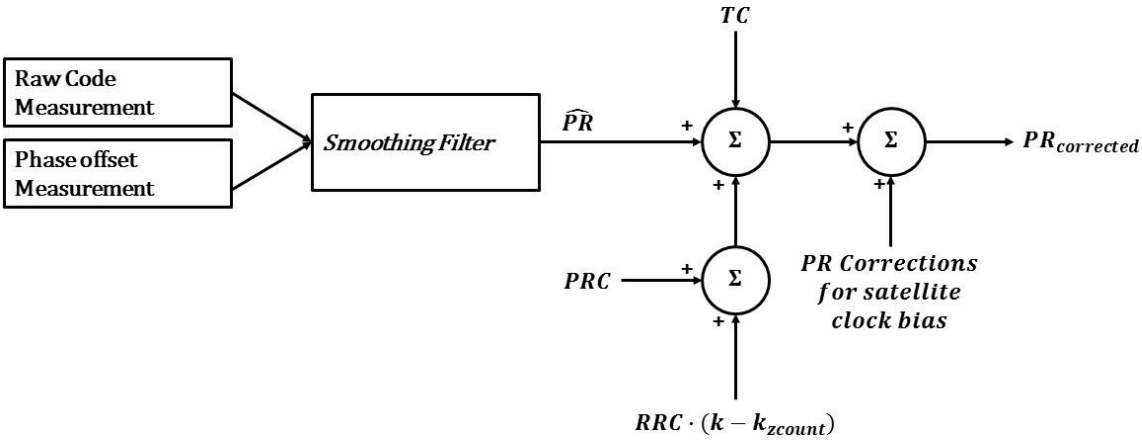

Figure 13 – Airborne measurement processing

The smoothing process is the same as explained in section 2.2. Once that the measurements have been smoothed, according to the scheme proposed in Figure 13, the corrected pseudorange may be computed

$$\rho^i_{corrected}(k) = \rho^i_{smooth}(k) + PRC^i + RRC^i \cdot (k - t_{zcount}) + TC^i + c \cdot \Delta t^i(k) \qquad \text{Eq. 2.51}$$

Where:

- ρ^i_{smooth} is the smoothed pseudorange from i^{th} satellite
- $k$indicates the current epoch
- t_{zcount} is the time of applicability of the PRC
- Δt^i is the satellite clock correction as in equation Eq. 2.15

- TC^i is the tropospheric correction for the i^{th} satellite taking into account the different height between the aircraft and the ground station.

The tropospheric corrections is computed as (RTCA Inc. DO245-A):

$$TC^i = N_R\, h_0 \frac{10^{-6}}{\sqrt{0.002 + sin^2(\theta_i)}} \left(1 - e^{-\frac{\Delta h}{h_0}}\right) \qquad \text{Eq. 2.52}$$

Where:

- N_R is the refractivity index contained in the message type 2 (Appendix B.2)
- Δh is the height of the aircraft above the GBAS reference point
- θ_i is the elevation angle of the satellite for which the correction is computed
- h_0 is the tropospheric scale height from message type 2 (Appendix B.2)

The tropospheric correction is common to all the GBAS services, its uncertainty is given by (RTCA Inc. DO245-A)

$$\sigma_{tropo} = \sigma_{N_R} \frac{h_0 10^{-6}}{\sqrt{0.002+sin^2(\theta_i)}} \left(1 - e^{-\frac{\Delta h}{h_0}}\right) \qquad \text{Eq. 2.53}$$

Where:

- σ_{N_R} is the refractivity uncertainty transmitted in message type 2 (Appendix B.2)

2.3.3 GBAS Integrity Monitoring

The integrity monitoring process in GBAS, for GAST C service (2.3.4.1), relies on two complementary processes:

- Computation of a protection level in order to bound the maximum vertical and horizontal error
- Monitor of all ranging sources to detect possible biases on measurement done at the ground station

The entire integrity risk must be allocated between the two processes

2.3.3.1 Risk Allocation

The GBAS system has to implement a series of monitors able to meet the requirement stated in (RTCA Inc.; DO253-C, 2008) a Signal in Space (SiS) integrity risk of 2×10^{-7} per approach for CAT I approach operation. This risk is allocated between the ground sub-system monitors and the protection level according to (ICAO, 2006) and it is represented in Figure 14.

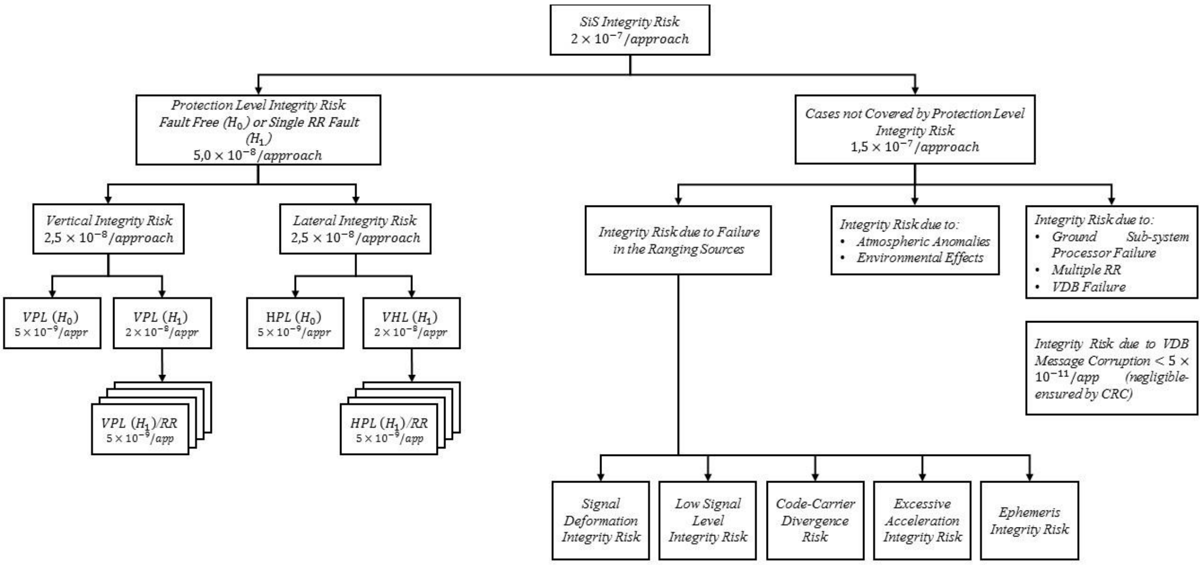

Figure 14 – GBAS integrity risk allocation (ICAO, 2006)

As it is possible to see, the majority of the allocation, 75%, is given to the cases not covered by the protection levels computed under fault-free (H_0) and faulty (H_1) condition. This integrity risk is then split in ranging source faults and ground subsystem faults. The ranging fault failure allocation has to take into account for the following threats: signal deformation, low signal level, code-carrier divergence, excessive acceleration and ephemeris error. The ephemeris integrity risk is ensured by the ephemeris position bound (RTCA Inc. DO245-A) and the VDB message corruption allocation is based on the level of integrity ensured by the Cyclic Redundancy Checks (CRC).

The detection of a fault is not the only process permitting to reach an integrity requirement. It is also important to broadcast the alarm in a certain time. In GBAS, this time is defined as Time To Alert (TTA) and it is stated that its maximum values does not have to exceed 3 seconds when MT 1 is broadcast. In Figure 15, it is possible to see the time subdivision phases between the onset of an error and the broadcast of the alarm.

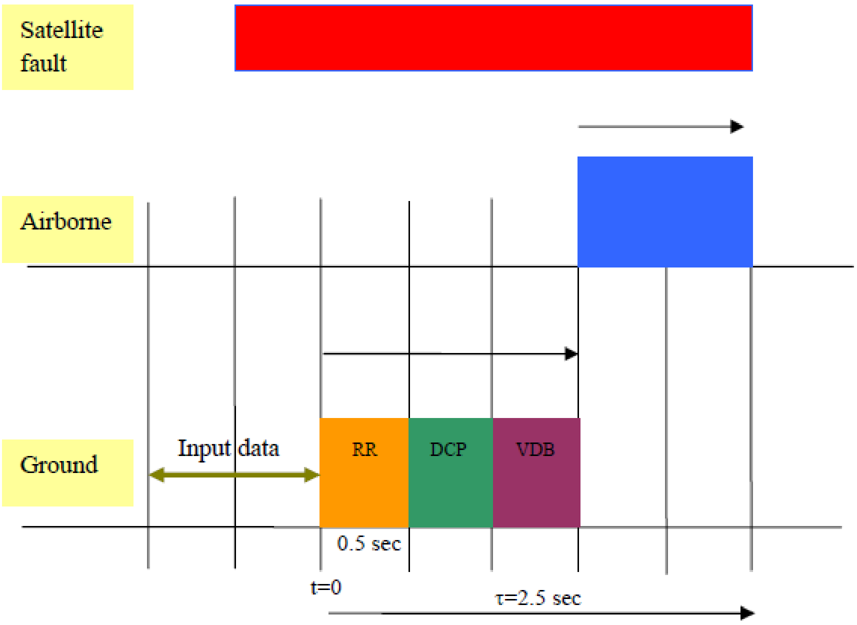

Figure 15 – Timing diagram for differential processing below 200 ft. (Brenner, et al., 2010)

In the Figure 15 the fault onset is at $t = -0.5$ s. After 0.5 s, the first faulted measurement is received. A total time of 1.5 seconds is considered as the time to process the measurement and to broadcast the messages to the airborne subsystem. A margin of 1 s is considered, corresponding to the delay of missing two messages. Summing the previous time values the total, from the fault onset to the received message containing an alarm, is 3 seconds as in (ICAO, 2006).

2.3.3.2 Protection Level

The signal-in-space vertical and lateral protection levels (VPL and LPL) are upper confidence bounds on the error in the position relative to the aircraft position defined as (ICAO, 2006):

$$VPL = \max\{VPL_{H0}; VPL_{H1}\} \quad \text{Eq. 2.54}$$

$$HPL = \max\{HPL_{H0}; HPL_{H1}\} \quad \text{Eq. 2.55}$$

VPL_{H0} and LPL_{H0} are the protection level assuming the fault free hypothesis, H_0, they can be computed as follow:

$$VPL_{H0} = K_{ffmd}\sqrt{\sum_{i=1}^{N} S_{vert,i}^2\,\sigma_i^2} + D_V \quad \text{Eq. 2.56}$$

$$LPL_{H0} = K_{ffmd}\sqrt{\sum_{i=1}^{N} S_{lat,i}^2\,\sigma_i^2} + D_L \quad \text{Eq. 2.57}$$

Where:

- The index i refers to one of the N satellites in view
- K_{ffmd} is the multiplier (unitless) determining the probability of fault free missed detection (ICAO, 2006) depending on the number of reference receiver at the ground station M and the probability of fault-free missed detection:

Table 6 – K_{ffmd} Values

$\boldsymbol{K_{ffmd}}$			
M=1	**M=2**	**M=3**	**M=4**
6.86	**5.762**	**5.810**	**5.847**

- $\sigma^{(i)} = \sqrt{\sigma_{pr\ gnd}^{2}{}^{(i)} + \sigma_{pr\ air}^{2}\,(i) + \sigma_{tropo}^{2}{}^{(i)} + \sigma_{iono}^{2}{}^{(i)}}$; The detail of each of these terms will be provided according to the analyzed GBAS service (details in 2.3.3).
- $S_{vert,i} = S_{3,i} + S_{1,i} * tg(GPA)$, S is the projection matrix of the three coordinates x,y,z and the receiver clock offset, computed as:

$$S = (G^T \cdot W \cdot G)^{-1} \cdot G^T \cdot W \qquad \text{Eq. 2.58}$$

G is the observation matrix composed by four columns and N rows as the number of visible satellites. Each row of the matrix is:

$$G_i = [-\cos(El_i)\cos(Az_i) \quad -\cos(El_i)\sin(Az_i) \quad -\sin(El_i) \quad 1] \qquad \text{Eq. 2.59}$$

The reference coordinates frame is defined such that x is along track positive forward, y is cross-track positive left in the local level tangent plane and z is the positive up and orthogonal to x and y (ICAO NSP WGW/Flimsy29, 2010). This statement is respected computing the East-North-Up (ENU) coordinates of each satellite and then performing a rotation on the z axis of (90°-α); α is the heading of the runway used for the landing

- $S_{lat} = S_{2,i}$
- GPA is the Glide Path Angle
- W is the inverse of the least square weighting matrix:

$$W = \begin{bmatrix} \sigma_1^2 & 0 & 0 & 0 \\ 0 & \sigma_2^2 & 0 & 0 \\ 0 & 0 & \ddots & 0 \\ 0 & 0 & 0 & \sigma_N^2 \end{bmatrix}^{-1} \quad S_{apr\ lat,i} = S_{2,i}$$

- D_V and D_L represent the vertical and lateral projection difference between the position solution computed using two different smoothing constants. They are set at zero if only one smoothing constant is used.

VPL_{H1} and LPL_{H1} represent the protection level under H1 hypothesis, presence of a fault on one of the reference receivers.

$$VPL_{H1} = \max_j\{VPL_{Apr\ H1}(j)\} + \mathrm{D_V}$$

$$LPL_{H1} = \max_j\{LPL_{Apr\ H1}(j)\} + \mathrm{D_L}$$

Where the index m indexes the M reference receivers at the ground.

$$VPL_{Apr\ H1}(j) = |B_{j\ apr\ vert}| + K_{md}\ \sigma_{Apr\ vert\ H1} \qquad \text{Eq. 2.60}$$

$$LPL_{Apr\ H1}(j) = |B_{j\ apr\ lat}| + K_{md}\ \sigma_{Apr\ lat\ H1} \qquad \text{Eq. 2.61}$$

- K_{md} is the multiplier (unitless) which determines the probability of missed detection for a faulted ground subsystem. Its value is given in the following table according to the number of reference receiver at the ground.

Table 7 – K_{md} Values

K_{md}			
M=1	**M=2**	**M=3**	**M=4**
Not Used	**2.935**	**2.898**	**2.878**

- $B_{j\ Apr\ Vert} = \sum_{i=1}^{N} S_{Apr\ vert,i} B(i,j)$
- $B_{j\ Apr\ Lat} = \sum_{i=1}^{N} S_{Apr\ lat,i} B(i,j)$
- $B(i,j)$ is a value expressed in meters for the i^{th} satellite and the j^{th} reference receiver as expressed in message type 1 (B.1). It is the difference of the averaged correction from the M reference receivers and the averaged corrections computed excluding the j^{th} receiver.

$$B_j^i = PRC^i - \frac{1}{M-1}\sum_{\substack{j=1 \\ j\neq m}}^{M} PRC_j^i \qquad \text{Eq. 2.62}$$

- $\sigma_{i\ H1}^2 = \left(\frac{M(i)}{U(i)}\right)\sigma_{pr\ gnd}^2(i) + \sigma_{pr\ air}^2\ (i) + \sigma_{tropo}(i) + \sigma_{iono}(i)$; as for the fault free case details about the terms composing the total sigma will be provided in the next sections according to the GBAS serviced described. $U(i)$ is the number of reference receiver used to compute the correction for the i^{th} source not considering the j^{th} receiver at ground.

The values of VPL and LPL are then compared with the alert limit computed according the GBAS service in use and the altitude of the aircraft from the LTP, for VPL, and the horizontal distance for the LPL. The alert limits are computed according to (ICAO, 2006).

Table 8 – Vertical alert limit

Height above LPT/FTP of aircraft position translated onto the final approach path (feet)	**Vertical Alert Limit (meters)**
$H \leq 200$	$FASVAL$
$200 < H \leq 1340$	$0.02925\,H(ft) + FASVAL - 5.85$
$H > 1340$	$FASVAL + 33.35$

Table 9 – Lateral alert limit

Horizontal distance of aircraft position from the LTP/FTP as translated along the final approach path (meters)	**Lateral Alert Limit (meters)**
$D \leq 873$	$FASLAL$
$873 < D \leq 7500$	$0.0044\,D(m) + FASLAL - 3.85$
$H > 7500$	$FASLAL + 29.15$

The values of FASVAL and FASLAL cannot be bigger than 10 meters.

2.3.3.3 Ground Monitors

This section introduces the monitors that are used in GBAS to detect some of threats presented in 2.2.3.1.

It has to be said that, even if they are presented according to their main role, some monitors can perform detection for more than one threat. CCD can detect payload divergence and ionospheric fronts as well. In other cases a single threat can be monitored by more than one monitor to improve the integrity performances, this could be the case of ionospheric front that can be detected by CCD and Excessive Acceleration.

2.3.3.3.1 Signal Quality Monitor (SQM)

The Signal Deformation threat is a fault condition in the GPS satellite that causes the broadcast C/A code to be distorted so that the correlation peaks used for tracking in the airborne system and the ground system are deformed. The extent of the deformation depends on the receiver bandwidth and the resulting tracking error depends on where the correlator points used for code tracking are located (along the correlator peak). The SQM is based on the analysis of the correlator outputs, two metrics, defined in (Enge, et al., 2000)and (Mitelman, 2004), they are used to detect:

- peaks deformation,
- peaks flatness
- close-in multi-peaks

2.3.3.3.2 Low Signal Level Monitor

According to (Pullen, et al., 2007) this kind of threat is managed by the Signal Quality Monitor.

2.3.3.3.3 Code-Carrier Divergence (CCD) Monitor

The code-carrier incoherence threat is a fault condition that causes the excessive divergence of the two broadcast signals, the phase and the code measurement.

A Code Carrier Divergence fault may cause a differential ranging errors in one or both of the following:

1. the aircraft and ground filter designs are not identical
2. the aircraft and ground filters start at different times

Both of these cases can result in a difference between the transient responses of the filters in the presence of a CCD event.

The monitor works by analyzing the rate of change of two consecutive CMC smoothed with two cascaded first order low pass filters (Jiang, et al., 2015). Details about this monitor are given in section 5.2.1.3

2.3.3.3.4 Excessive Acceleration Monitor

The Excessive Acceleration (EA) threat is a fault condition in a GNSS satellite that causes the carrier (and code in unison) of the broadcast signal to accelerate excessively. Possible causes could be the most likely fault of a satellite clock, or an undesired acceleration in the satellite position domain due to unscheduled manoeuvre. The threat space is 1-dimensional and corresponds to all possible accelerations.

The range acceleration error limit is the maximum for any satellite measured over any 3-epoch interval for any point within the coverage area in (Brenner, et al., 2010). Details about this monitor are given in section 5.2.1.4

2.3.3.3.5 Ephemeris Error/ Failure Monitoring

The Ephemeris Error threat is a fault condition that causes the broadcast ephemeris parameters to provide an excessive satellite position errors perpendicular to the ground subsystem’s line of sight to the satellite. Different types of ephemeris errors have been identified. They concern about errors for wrong ephemeris upload or unexpected manoeuvres that are not seen from any ground stations. A last case is represented by unchanged ephemeris after a manoeuvre. This brief description focuses on the core case. Additional corner cases may exist depending on the specific design of the ground subsystem monitoring.

According to (ICAO NSP WGW/Flimsy29, 2010) there are several methods to monitor the possible ephemeris error:

1) Use of a ground monitor. Different kind of monitors are available in order to monitor the different threats (ICAO NSP WGW/Flimsy29, 2010)
2) Computation of the ephemeris error bound. This method is similar to the protection level seen in section 2.3.3.2 a series of parameters are used for the ephemeris error bound:
    - $P_{e,j}$ is the ephemeris decorrelation parameter for the j^{th} ranging source in message type 1 (Appendix B.1)
    - $K_{md\ e,j}$ is the broadcast ephemeris missed detection multiplier from message type 2 (Appendix B.2)

As for the protection level, the VEB and LEB do not have to overcome the VAL and LAL limit.

2.3.4 GBAS Approach Service Type

A GBAS station may provide multiple types of approach service simultaneously to many users who may have different operational objectives. To facilitate the interoperability between users, and consistent predictable performances, the airborne and the ground subsystem performance requirements are organized into matched sets that are intended to be used in conjunction. These sets are referred collectively as GBAS Approach Service Type (GAST). Then, for each subsystem, the required performance referring to the Ground Facility Classification (GFC) and the Airborne Equipment Classification (AEC) are defined (RTCA Inc.; DO253-C, 2008). The relationship between the GAST and the other two sets of performance can be seen in the next figure.

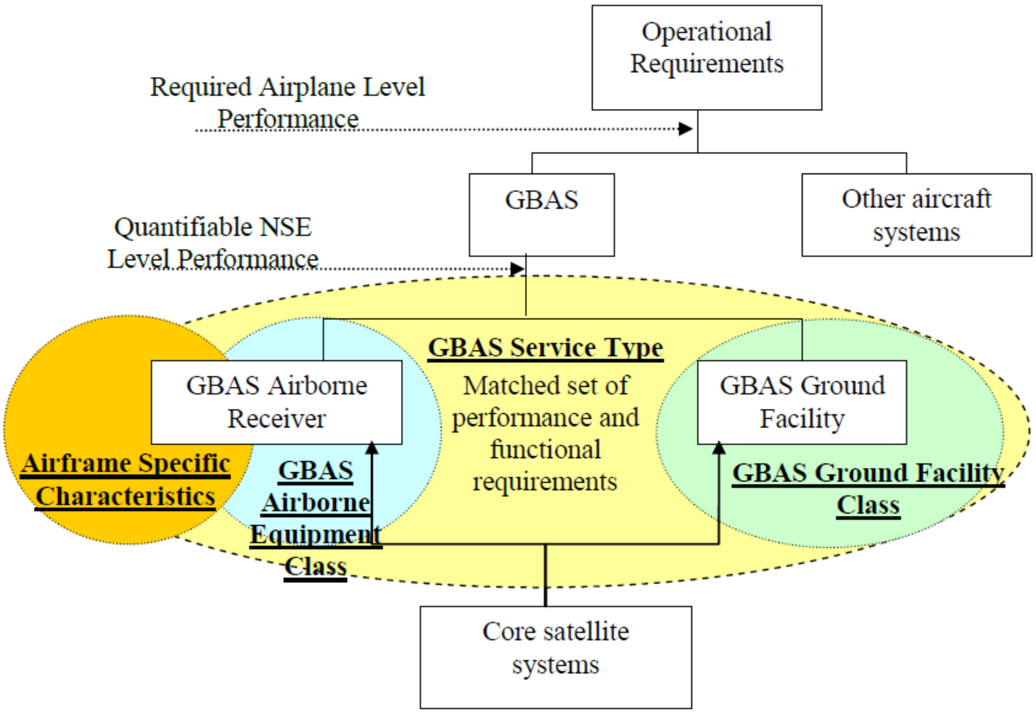

Figure 16 – service type, facility classification and airborne equipment classes (RTCA Inc.; DO253-C, 2008)

Nowadays three GAST levels are described in (ICAO, 2006): A, B and C. the first two levels provide the accuracy level for the APV I and APV II service, GAST C is the one providing guidance for the approach phase until the CAT I decision height of ILS. These three levels are the only ones approved by the civil aviation authorities. The requirement for a fourth level are described in (ICAO NSP WGW/Flimsy29, 2010) and (RTCA Inc.; DO253-C, 2008), it is named GAST D and it will provide guidance for the approach and landing phase for the equivalent CAT III ILS. This service has not been still validated due to some integrity issue. A last service, analyzed in this thesis is GAST F. The aim of this service is, as for GAST D, to provide CAT III ILS precision approach guidance. In the following part the main differences between those three service levels will be explained.

2.3.4.1 GAST-C

GAST C is the only validated GBAS Landing System (GLS) able to provide lateral and vertical guidance until the CAT I decision height point. The service relies on a single constellation core satellite constellation, GPS or GLONASS, using only single frequency measurement on L1 frequency.

The architecture and the message structure for this service is shown in appendix B, and they are almost similar for all the services.

The processing model for this service relies on the use of a smoothing constant of 100 seconds.

For each satellite it is possible to derive the error model estimating the errors impacting on each GBAS subsystem, ground station and aircraft, and considering the uncertainty on the troposphere and ionosphere correction computed at ground (RTCA Inc. DO245-A).

$$\sigma^{(i)} = \sqrt{\sigma_{pr\,gnd}^{2}{}^{(i)} + \sigma_{pr\,air}^{2}{}^{(i)} + \sigma_{iono}^{2}{}^{(i)} + \sigma_{tropo}^{2}{}^{(i)}}$$

The ground station pseudorange error model is determined by the contribution of the receiver noise and multipath, the model is represented by the following formula.

$$\sigma_{gnd}(\theta) = \begin{cases} a_0 + a_1 e^{-\frac{\theta}{\theta_c}} & ,\theta \geq 35° \\ \sigma_{MAX} & ,\theta < 35° \end{cases} \qquad \text{Eq. 2.63}$$

Where:

- θ is the elevation angle of the satellite under analysis

The other coefficient are defined in the next table for three levels of accuracy: Ground Accuracy Designator (GAD) A-B-C (RTCA Inc. DO245-A).

Table 10 – Ground reference receiver error allocation model

Accuracy Designator	a_0 (m)	a_1 (m)	θ_c **(deg)**	σ_{max}
GAD-A	0.50	1.65	14.3	--
GAD-B	0.16	1.07	15.5	--
GAD-C	0.15	0.84	15.5	0.24

These coefficients are computed from the analysis of the receiver noise and multipath on a receiver.

Another term must be added to the standard deviation computed in Eq. 2.63 in order to compute the $\sigma_{PR\,gnd}$, which takes into account the decorrelation of atmospheric and ephemeris errors, due to the distance between the user and the ground station that affects the SIS error. In (McGraw, et al., 2000) an upper bound of this error has been computed, they are represented by the following formula.

$$\sigma_{SIS}(\theta) = \sqrt{a_2^2 + a_3^2\, F_{PP}(\theta)^2} \qquad \text{Eq. 2.64}$$

F_{PP} is the obliquity factor for ionospheric error

$$F_{PP}(\theta) = \left[1 - \left(\frac{R_e \cos(\theta)}{R_e + h_I}\right)^2\right]^{\frac{1}{2}} \qquad \text{Eq. 2.65}$$

Where:

- R_e is the earth radius 6378.1363 km
- h_I is the ionospheric shell height; 350 km

The values of a_2 and a_3 are given in the next table.

Table 11 – Summary of LAAS SIS residual errors (McGraw, et al., 2000)

Error source	**GAD-A,B**		**GAD-C**	
	$a_2\ (m)$	$a_3\ (m)$	$a_2\ (m)$	$a_3\ (m)$
Troposphere	--	0.02	--	0.007
Ionosphere	--	0.02	--	0.007
Data link latency	0.05	--	0.01	--
Ephemeris	0.02	--	0.01	--
Ground-to-airborne multipath	0.02	--	0.02	--
Reference RCVR relative survey	0.05	--	0.03	--
Total RSS	0.08	0.03	0.04	0.01

The value of $\sigma_{PR\ gnd}$ ca be computed using the following formula

$$\sigma_{PR\ gnd} = \sqrt{\frac{\sigma_{gnd}^2}{M} + \sigma_{SIS}^2} \qquad \text{Eq. 2.66}$$

M is the number of RR present at the ground station.

The airborne error contribution is defined in (RTCA Inc. DO245-A) as the combination of two error sources, receiver noise and interference and multipath.

$$\sigma_{PR\ air} = \sqrt{\sigma_{noise}^2 + \sigma_{MP}^2} \qquad \text{Eq. 2.67}$$

The noise and interference contribution can be computed using the following formula according to the performance of the receiver defined by the Aircraft Accuracy Designator (AAD) for two levels; A and B.

$$\sigma_{noise} = a_0 + a_1 e^{-\frac{\theta}{\theta_c}}\ , 5° < \theta < 90° \qquad \text{Eq. 2.68}$$

The values of the coefficients are listed in the next table

Table 12 – Airborne thermal noise and interference error model parameters

Accuracy Designator	a_0 (m)	a_1 (m)	θ_c (deg)
AAD-A	0.15	0.43	6.9
AAD-B	0.11	0.13	4.0

The multipath error contribution was developed starting from a measurement test campaign and re-assessed in (Murphy, et al.).

$$\sigma_{MP} = 0.13 + 0.53e^{-\frac{\theta}{10°}} \qquad \text{Eq. 2.69}$$

The tropospheric residual error uncertainty has been already shown in equation Eq. 2.53, the ionospheric residual error uncertainty is instead given in (ICAO NSP WGW/Flimsy29, 2010):

$$\sigma_{iono} = F_{PP} \times \sigma_{vig} \times (x_{air} + 2 \times 100 \times v_{air}) \qquad \text{Eq. 2.70}$$

Where:

- σ_{vig} is a parameter transmitted in message type 2 (B.2) indicating the maximum not monitored ionosphere vertical gradient
- v_{air} is the horizontal aircraft speed
- x_{air} is the horizontal slant distance between aircraft and LGF

The model of the residual error for GAST C impact the computation of the protection levels in the monitor.

The monitoring process for this service follows what explained in section 2.3.3, the responsibility for the integrity is entirely allocated to the ground subsystem.

2.3.4.2 GAST-D

As said in the introduction GAST D is the fourth GBAS service, it is still under validation but standards and recommended practices (SARPs) may be found in the proposed amendment to ICAO Annex 10 (ICAO NSP WGW/Flimsy29, 2010) and in (RTCA Inc.; DO253-C, 2008). The service aims at providing accuracy for the approach and landing phase like CAT III ILS. It relies on a single satellite constellation, GPS or GLONASS, and single frequency measurement, L1. In order to achieve this result, a series of differences exists between GAST C and D (ICAO NSP WGW/Flimsy29, 2010).

- Addition of low level monitor performance for the ground subsystem;
- Addition of ionospheric monitoring and use of 30 seconds smoothed corrections in the airborne equipment supported by additional information from the ground subsystem.

- Additional ionosphere monitoring required by the ground subsystem
- An additional siting requirement for the ground subsystem in order to limit the distance between the LTP and the ground station
- Addition of B-values monitoring in the airborne equipment to address residual risk not bounded by the H1 protection level hypothesis
- Additional airborne geometry screening requirement
- Additional protection level parameters that are based on overbounding without consideration for rare anomalous ionospheric condition which are covered by airborne monitoring.
- Addition of a ground subsystem design integrity risk requirement

GAST D has a series of new innovations aimed to improve the integrity of the system. In this section the main difference for the processing scheme and the accuracy model will be presented, all the new monitors required and the new integrity concept will be presented in detail in 5.

In GAST C the corrected pseudorange are computed using the PRC and RRC smoothed with a time constant of 100 seconds. In order to make the PRC and RRC less susceptible to the build-up of the ionospheric delay, a shorter time constant is used in GAST D: 30 seconds (DO-246D, 2008). Furthermore, the simultaneous use of **30 second and 100 second smoothed pseudoranges** allows the airborne equipment to monitor the existence of ionospheric gradients thanks to the comparison between the position solutions computed with the corrected pseudoranges smoothed with the two constants. This differences, in the lateral and vertical domain, D_L and D_V are monitored by the **Dual Solution Ionospheric Gradient Monitor Algorithm (DSIGMA)**. Additionally to this new monitor the **airborne-CCD** is employed at all times in order to allow detection of ionospheric gradients before the airplane reaches the ground subsystem or starts using the differential corrections. **In GAST D the airborne is responsible to detect anomalous ionosphere conditions.**

Despite the new airborne monitors, improved monitoring capabilities are also required for the ground subsystem. A new monitor called **Ionospheric Gradient Monitor (IGM)** has been developed, jointly with a new siting criteria and new requirement for the ranging source error detection. The **siting criteria** limits the distance between a ground subsystem reference point and any LTP located in the covered area to 5 km. This constraints is necessary to bind the maximum decorrelated ionospheric error (ICAO NSP WGW/Flimsy29, 2010).

To improve the monitor of the ground station errors a new monitor based on the **B values** (5.2.1.6), sent in message type 1, is used. A single reference receiver fault can affect multiple, if not all, satellite correction and integrity information. Such a “fault” can be due to actual reference receiver hardware failure or excessive multipath on one or more satellites. For GAST C, the ground subsystem is required to monitor metrics relating to the B-value estimates used to characterize reference receiver fault errors, and transmit those B-values that are accepted to the aircraft in MT-1. Also for GAST C, airborne monitoring is indirectly provided by the requirement to compute position domain protection levels under H1 hypothesis from the broadcast B-values and compare them to corresponding alert limits. While this ground and airborne monitoring is effective in detecting reference receiver faults within the GAST C protection level integrity allocations, additional airborne monitoring is needed for GAST D to mitigate single reference failure effects as defined in (RTCA Inc. DO245-A). For GAST D, the airborne equipment must also monitor the impact single reference receiver fault errors on total GBAS NSE performance and mitigate conditions which are unacceptable given the aircraft's unique landing characteristics and the operation to be performed. The monitor test statistic is formed by combining the vertical and lateral B-value derivations and the 30/100 sec smoothed position solutions difference. The airborne equipment's knowledge of the specific geometry used in the final position solution allows it to be the most efficient judge of whether an apparent reference receiver failure will result in hazardous misleading information or not (ICAO NSP WGW/Flimsy29, 2010).

To compensate the low level monitor performance expressed in the pseudorange domain and basic position accuracy performance requirements, the user must have knowledge of how the position solution is computed and how the errors are projected from the range domain to the position domain. Airborne equipment may be required to do additional **geometry screening** to reject geometries that rely too much on a single satellite range.

GAST D systems must be able to demonstrate equivalence with GAST C performance requirements. The airborne equipment will achieve this using new broadcast parameters in place of those required for GAST C. These parameters will be set by the ground subsystem to provide protection level integrity of a 100 second smoothed position solution. New airborne algorithms will calculate additional errors that would be introduced in a 30 second position solution, using corrections from the Type 11 message (B.3), and apply the necessary corrections to extend protection level integrity to the 30 second position solution. These new parameters, have the same meaning as for GAST C. The main difference is that they do not include any inflation to take into account possible ionospheric anomalies since monitors are present on the aircraft.

- $\boldsymbol{K_{md\ e\ D,GPS}}$ **and** $\boldsymbol{K_{md\ e\ D,GLONASS}}$.
- $\boldsymbol{\sigma_{vig,D}}$.
- $\boldsymbol{P_D}$
- $\boldsymbol{\sigma_{pr\ gnd\ 100}}$, $\boldsymbol{\sigma_{pr\ gnd\ 30}}$
- $\boldsymbol{D_V}$ **and** $\boldsymbol{D_L}$ projection in the vertical and lateral domain of the difference between the 100 s and 30 s smoothed solution

All the others parameters are considered as for the GAST C service.

The main difference between the previous parameters and the ones used for GAST C is the absence of inflation values to cover possible ionospheric decorrelated error. Also, two $\sigma_{pr\ gnd}$ are used. The first value $\sigma_{pr\ gnd\ 100}$ is used to compute the σ_i used in equation Eq. 2.56 and Eq. 2.57when GAST D is active, while the value of $\sigma_{pr\ gnd\ 30}$ is used to compute the weight matrix W.

2.3.4.3 GAST-F

Despite the development of the GAST D service to provide CAT III accuracy level, GAST D is still vulnerable to anomalous ionospheric condition. The presence of anomalous ionospheric conditions could lead to the following cases (Milner, 2014):

- Service outages from detected gradients and scintillation
- Difficulty to meet availability and continuity requirements in some regions
- Integrity monitoring validation difficulties

Other GAST D drawbacks are related to possible vulnerability to interference or jamming on the single frequency L1 or unavailability under critical geometries due to degraded constellation.

In order to find a solution to the drawbacks of GAST D, the European Commission, through the SESAR (Single European Sky and ATM Research) project, has funded the 15.3.7 Working Package (WP) in charge of developing the concept for a Multi Constellation (MC) and Multi Frequency (MF) GBAS service. The new service is denoted as GAST F and it will rely on the use of dual constellation: GPS and Galileo and dual frequency measurements on L1 and L5 frequencies. The signals used will be (Milner, 2014)

- GPS L1 C/A (maintain legacy)
- Galileo E1
- GPS L5
- Galileo E5a (interoperability with GPS L5 and decision by EUROCAE)

Potential future development of the GAST F may include the use of GPS L1C signal, as well as the use of GLONASS or Beidou constellation. Possible development to triple frequency is also considered.

The main differences introduced by GAST F may be summarized in the following points.

- The use of a second constellation leads to an increased number of PRC and RRC to broadcast, the current VDB structure limits this number to 20. Two possible ways to solve the problem are: use of a satellite selection algorithm or modification of the VDB requirement. Moreover, if a new combination is used, the related PRC must be broadcast together with the exiting one for 100 and 30 seconds in order to maintain interoperability between the services
- Dual frequency measurement allow to use combinations like D-Free and I-Free. The use of this new measurement combination requires the study of the performance of the noise and multipath

error at the ground and airborne side and the selection of the optimal measurement processing mode.

- A study to verify the applicability of existing monitors to the new signals and if needed, the development of new monitoring algorithms to meet the integrity requirement have to be done as well.
- Evaluation of error sources like ionosphere, multipath and interference on the new signals has to be done to verify if the threat model defined for GPS L1 C/A can be retained as valid or need to be modified.

3 MC/MF GBAS Ground Multipath and Noise Model

In section 2.3.4.3 the GAST F concept has been presented. It is developed on the basis of a multi-constellation (GPS and Galileo) multi-frequency (L1/L5 and E1/E5a) GBAS. In order to assess which processing mode or modes have to be selected for the GAST F solution, the error models for the new signals must be developed taking into account the impact of the antenna and receiver, both on the ground and airborne sides.

3.1 Objectives and Motivations

Dual frequency techniques have been investigated in literature by (Hiroyuki, 2007) and (Hwang, et al., 1999), leading to two smoothing algorithms, Divergence Free (D-free) and Ionosphere Free (I-free) smoothing, which were presented in section 2.2.2.2. The differences between the two algorithms relate to the level of mitigation of the ionospheric delay and the resulting noise inflation of the final observables.

These techniques can thus be used to mitigate the ionosphere and provide Cat II/III services when the GAST D service would be unavailable (under ionospheric gradient conditions or under poor geometry conditions). The SESAR 15.3.7 project is developing the GAST F concept through the investigation of these processing methodologies. In order to assess accurately the performance which may be achieved, the error model for the new signals and new combinations must be determined. It is important to determine this at the raw pseudorange level before addressing the impact of smoothing. Furthermore, different smoothing time constants and correction update rates are being considered within the SESAR framework which will require newly characterised models completing those presented within the MOPS, SARPs and (RTCA Inc. DO245-A). In addition, new GAST F constraints regarding the antenna environment for the ground installation and on the tracking configuration on the receiver may be defined which would modify the impact of noise and multipath on the measurement.

The scope of this chapter is to analyze the error characteristics of the pseudorange correction (PRC) sent by the ground station. In particular, there is a lack of information about performance on the correction using the L5/E5a signals as well as the I-free techniques.

3.2 Methodology to Characterize Noise and Multipath at the Ground Station

In order to evaluate the performance of the ground station, which can indirectly affect the entire GBAS system availability, the PRC must be analysed, particularly its uncorrelated errors. According to 2.3.2 , the PRC is composed of:

$$PRCt^i = \rho^i - r^i = \Delta t^i + t_{RRs} + I^i + T^i + \eta^i + \varepsilon^i \qquad \text{Eq. 3.1}$$

Where t_{RRs} is a term including the error obtained from the receivers clock offset removal from the PRCs (section 2.3.2)

Details about the errors are given in section 2.1.4.

The terms Δt^i(satellite clock error), I^i(ionospheric delay), T^i(tropospheric delay) and ε^i(ephemeris error) in Eq. 3.1 are highly correlated between the airborne and ground measurements, and thus are highly reduced when the PRC are applied. On the contrary, the two remaining terms t_{RRs} and η_m^i being uncorrelated are not removed. The reference receivers clock error t_{RRs} is common to all the PRCs. This means that this error will be projected in the airborne clock state when the position is computed (RTCA Inc. DO245-A). The remaining term η_m^i, representing the noise and multipath terms, is not correlated between ground and airborne side. This term, contrary to the others, add an error to the corrected pseudorange at the airborne level. For this reason it has to be evaluated in order to derive the ground impact on the measurement errors.

3.2.1 The CMC: a Useful Combination to Evaluate Noise and Multipath

To extract information about the noise and multipath affecting the PRC, the Code Minus Carrier (CMC) can be used. It is shown in (Rotondo G., et al., 2015) that the main contribution to the CMC is provided by these two error sources. Considering the model of code and phase measurement in Eq. 2.10 and in Eq. 2.11, and removing the common terms, the CMC components for a given satellite are:

$$CMC_{SF} = 2 \cdot I - N\,\lambda + \eta_\rho - \eta_\phi \qquad \text{Eq. 3.2}$$

For simplicity, the satellite superscript index i has been dropped from the notation in the following. It is possible to see that the main error sources in the CMC are the ionospheric delay I, the phase ambiguity term N and the noise and multipath term affecting the code η_ρ and phase η_ϕ.

The ionospheric delay can be removed using dual frequency measurement combination. In the case of SF measurement, it is possible to estimate the ionospheric delay using DF data from a nearby station. Knowing the phase measurement model, the ionospheric delay can be computed differencing the phase measurement on two frequencies:

$$\phi_1 - \phi_5 = -(I_1 - I_5) + (N_1\lambda_1 - N_5\lambda_5) + (\eta_{\phi 1} - \eta_{\phi 5}) \qquad \text{Eq. 3.3}$$

The indices 1 and 5 refer to the two frequencies employed. Considering the relationship between the phase and the ionospheric delay given in Eq. 2.27 it is possible to derive the ionospheric delay on one of the two frequency as:

$$\phi_1 - \phi_5 = -(\alpha\, I_1) + (N_1\lambda_1 - N_5\lambda_5) + (\eta_{\phi 1} - \eta_{\phi 5}) \qquad \text{Eq. 3.4}$$

- $\alpha = 1 - \frac{f_1^2}{f_5^2}$

It is possible to derive the ionospheric delay by multiplying all the terms by $-\frac{1}{\alpha}$.

$$-\frac{1}{\alpha}(\phi_1 - \phi_5) = I_1 - \frac{1}{\alpha}(N_1\lambda_1 - N_5\lambda_5) - \frac{1}{\alpha}(\eta_{\phi 1} - \eta_{\phi 5}) \qquad \text{Eq. 3.5}$$

It is possible to rewrite the previous equation in the following way

$$\frac{f_5^2}{f_1^2 - f_5^2}\,(\phi_1 - \phi_5) = I_1 + \frac{f_5^2}{f_1^2 - f_5^2}\Big((N_1\lambda_1 - N_5\lambda_5) + (\eta_{\phi 1} - \eta_{\phi 5})\Big) \qquad \text{Eq. 3.6}$$

As it is possible to note in Eq. 3.6 differencing the phase measurement on two frequencies and multiplying it by $\frac{f_5^2}{f_1^2 - f_5^2}$ it is possible to obtain the ionospheric delay affected by:

- Phase ambiguity difference $N_1\lambda_1 - N_5\lambda_5$
- Noise and multipath affecting the phase measurement $\eta_{\phi 1} - \eta_{\phi 5}$

The noise and multipath affecting the phase measurement, for its magnitude, can be considered negligible as shown in (Rotondo G., et al., 2015). Eq. 3.6 can be rewritten as:

$$\hat{I}_1 = \frac{f_5^2}{f_1^2 + f_5^2}\,\big((\phi_1 - \phi_5) - (N_1\lambda_1 - N_5\lambda_5)\big) \qquad \text{Eq. 3.7}$$

In the same way the estimated ionospheric delay on L5 is given as:

$$\hat{I}_5 = \frac{f_1^2}{f_5^2 + f_1^2}\,\big((\phi_5 - \phi_1) - (N_5\lambda_5 - N_1\lambda_1)\big) \qquad \text{Eq. 3.8}$$

The ionospheric delay estimated in Eq. 3.7 or in Eq. 3.8 is still not representing the true delay because it is affected by the phase ambiguity difference term multiplied by the frequency factor. Relying on the property of the phase ambiguity, to be a constant value over continuous data and, it is removed from Eq. 3.7 or Eq. 3.8 by subtracting the averaged value. Cycle slips must be monitored as well. The methodology to remove the phase ambiguity term from the estimated ionospheric delay is presented in section 3.2.1.1

In case of DF data from the receiver under analysis, the D-Free and I-Free combinations (sections 2.2.2.2.2 and 2.2.2.2.3) can be used.

$$CMC_{D-Free\,1} = \rho_1 - \phi_1 + \frac{2}{\alpha}(\phi_1 - \phi_5) \qquad \text{Eq. 3.9}$$

$$CMC_{D-Free\ 5} = \rho_5 - \phi_5 + \frac{2}{\beta}(\phi_5 - \phi_1) \qquad \text{Eq. 3.10}$$

$$CMC_{I-Free} = \rho_1 - \frac{1}{\alpha}(\rho_1 - \rho_5) - \phi_1 + \frac{1}{\alpha}(\phi_1 - \phi_5) \qquad \text{Eq. 3.11}$$

Where:

- $\beta = 1 - \frac{f_5^2}{f_1^2}$

It is demonstrated in (2.2.2.2) that the ionospheric delay is no longer present using the previous combinations.

The last term to remove from the previous CMC combinations is the phase ambiguity for the SF case or a term representing a combination between the phase ambiguity on L1 and L5 measurement;

- D-Free, $N_{15} = N_1\lambda_1 - \frac{2}{\alpha}(N_1\lambda_1 - N_5\lambda_5)$
- I-Free, $N_{15} = N_1\lambda_1 - \frac{1}{\alpha}(N_1\lambda_1 - N_5\lambda_5)$

Knowing that the phase ambiguity is a constant value over time for continuous measurement, it is possible to remove it from a continuous CMC time series, by removing its average value. This method is possible because the multipath and noise are considered to be zero mean distribution errors over long periods. At least one hour of consecutive data are required. The methodology adopted is presented in section 3.2.1.1

Once that the phase ambiguity has been removed from the CMC, it is representative of only noise and multipath, as it is possible to demonstrate.

$$CMC_{SF} = \eta_\rho - \eta_\phi \qquad \text{Eq. 3.12}$$

$$CMC_{D-Free\ 1} = \eta_{\rho 1} - \eta_{\phi 1} + \frac{2}{\alpha}(\eta_{\phi 1} - \eta_{\phi 5}) \qquad \text{Eq. 3.13}$$

$$CMC_{D-Free\ 5} = \eta_{\rho 5} - \eta_{\phi 5} + \frac{2}{\beta}(\eta_{\phi 5} - \eta_{\phi 1}) \qquad \text{Eq. 3.14}$$

$$CMC_{I-Free} = \eta_{\rho 1} - \frac{1}{\alpha}(\eta_{\rho 1} - \eta_{\rho 5}) - \eta_{\phi 1} + \frac{1}{\alpha}(\eta_{\phi 1} - \eta_{\phi 5}) \qquad \text{Eq. 3.15}$$

The CMC, after the compensation of the phase ambiguity and the removal of the ionospheric delay, is composed of the noise and multipath term affecting the code and the phase measurement. Considering the magnitude of these error on the two measurement provided in Table 3.

It is possible to assess that the multipath and noise on the phase measurement provide a negligible contribution to the CMC when the same error on code measurement is present. The previous equations can be rewritten as:

$$CMC_{SF} \approx \eta_{\rho} \qquad \text{Eq. 3.16}$$

$$CMC_{D-Free\ 1} \approx \eta_{\rho 1} \qquad \text{Eq. 3.17}$$

$$CMC_{D-Free\ 5} \approx \eta_{\rho 5} \qquad \text{Eq. 3.18}$$

$$CMC_{I-Free} \approx \eta_{\rho 1} - \frac{1}{\alpha}\left(\eta_{\rho 1} - \eta_{\rho 5}\right) \qquad \text{Eq. 3.19}$$

3.2.1.1 Phase Ambiguity Removal

As mentioned in 3.2.1, the CMC average value (over a long period), or the averaged ionospheric delay; has to be subtracted from the CMC to remove the phase ambiguity. In the next figure it possible to see that the CMCs from each satellite is affected by a constant bias.

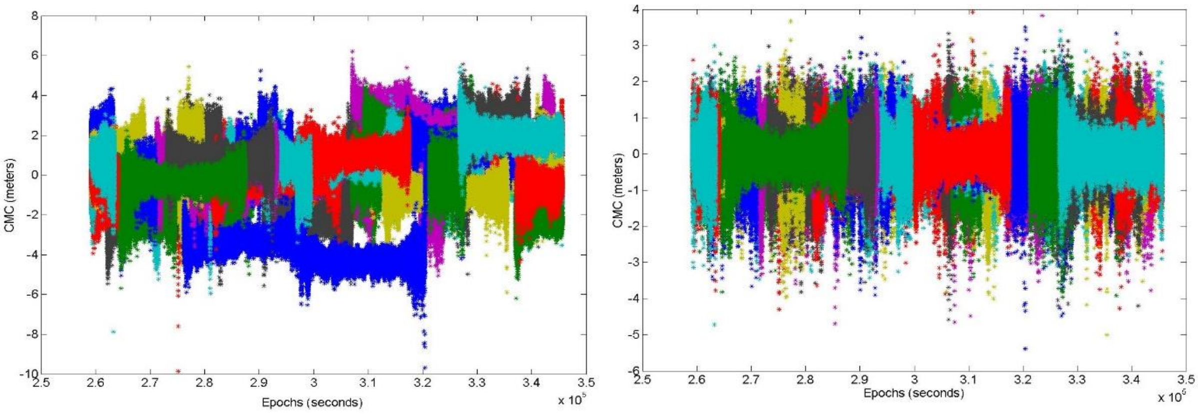

Figure 17 – CMCs before (left) and after (right) phase ambiguity term compensation (each color represent a PRN)

In case of discontinuity in measurement epochs, the average value has to be computed and removed from each continuous slice of measurement. This is because the phase ambiguity term is different in any group of continuous data.

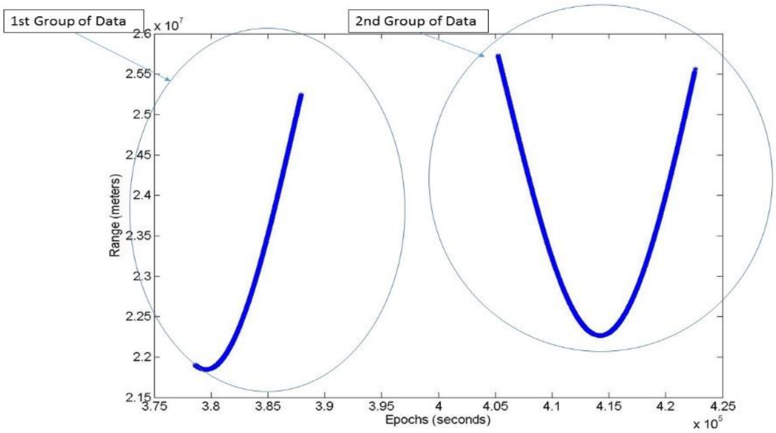

Figure 18 – Pseudorange from one satellite, visible twice in a day

Another condition that has to be treated is the detection of cycle slips on phase measurement. Cycle slip can occur for low elevation satellites and results in an offset on the phase due to a change in the phase ambiguity without a loss of the PLL tracking. This means that no time discontinuity is detected just checking the epochs difference. Cycle slips are monitored comparing the predicted phase measurement, computed using Doppler measurement (Kannemans, 2003), with the real one as:

$$\phi_{pred}(k) = \phi(k-1) + \frac{\big(d(k-1) + d(k)\big)}{2} \cdot \Delta T \qquad \text{Eq. 3.20}$$

Where:

- ϕ is the phase measurement in cycles
- k indicates the epochs
- d is the doppler measurement in Hz (cycles/s)
- ΔT is the measurement interval

The predicted phase measurement is then compared to the real one to detect possible cycle slips.

$$\nu_{test}(k) = \left|\phi(k) - \phi_{pred}(k)\right| \qquad \text{Eq. 3.21}$$

If in any epochs, the value of ν_{test} is bigger than 0.5 (Kannemans, 2003), a cycle slip is detected and the time series of CMC is split in sub-groups.

In order to have a realistic evaluation of the CMCs the groups of data must be longer than one hour in order to assume the multipath error as zero mean. The averaging of data groups smaller than one hour can, in fact, compensate partially the multipath.

3.2.2 Impact of Modulation on Noise and Multipath

The main objective of this section is the comparison between the noise and multipath affecting GPS L1 C/A, GPS L5, GALILEO E1 and GALILEO E5a. Thanks to the difference of modulations used performances are expected to be different. Noise and multipath affecting the I-free combination will be analyzed as well.

Details about the signals modulation and frequencies used are provided in Table 5.

It is possible to estimate the performance of the different modulations (BPSK(1), BPSK(10) and CBOC(1,1)) regarding their inherent resistance to thermal noise using the formula provided in (Betz, et al., 2000). Error characteristics depend on the RF front-end filter bandwidth BW, the chip spacing C_S, the carrier to noise density ratio $\frac{C}{N_0}$, the one-sided bandwidth of the DLL and the integration time.

For a civil aviation receiver the allowed values of BW and C_S are defined in (RTCA Inc.; DO253-C, 2008). For GPS L5 and Galileo E1 and E5a signals constraints are still under development. In Figure 19 the tracking constraint for GPS satellites are shown.

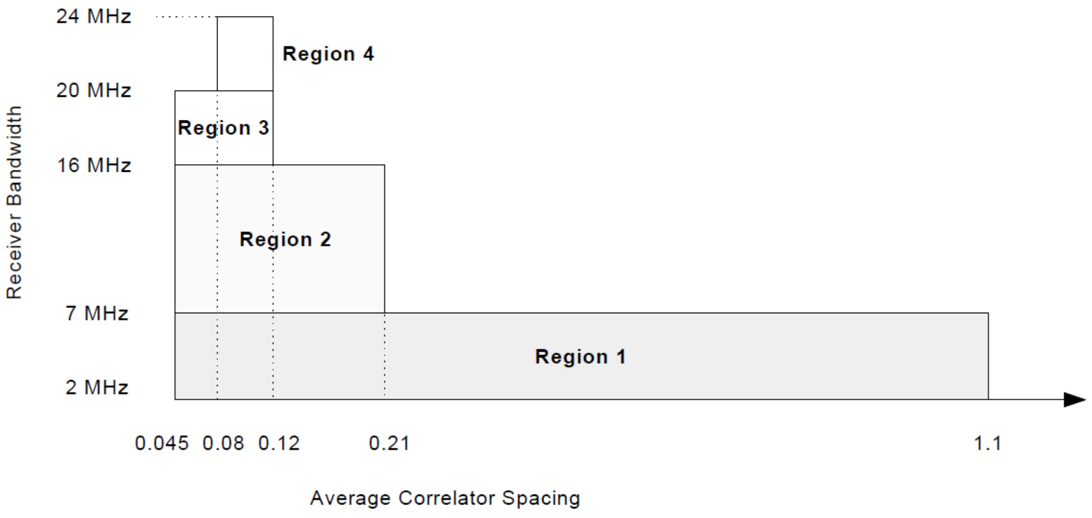

Figure 19 – Early-Late discriminator tracking of GPS satellites (RTCA Inc.; DO253-C, 2008)

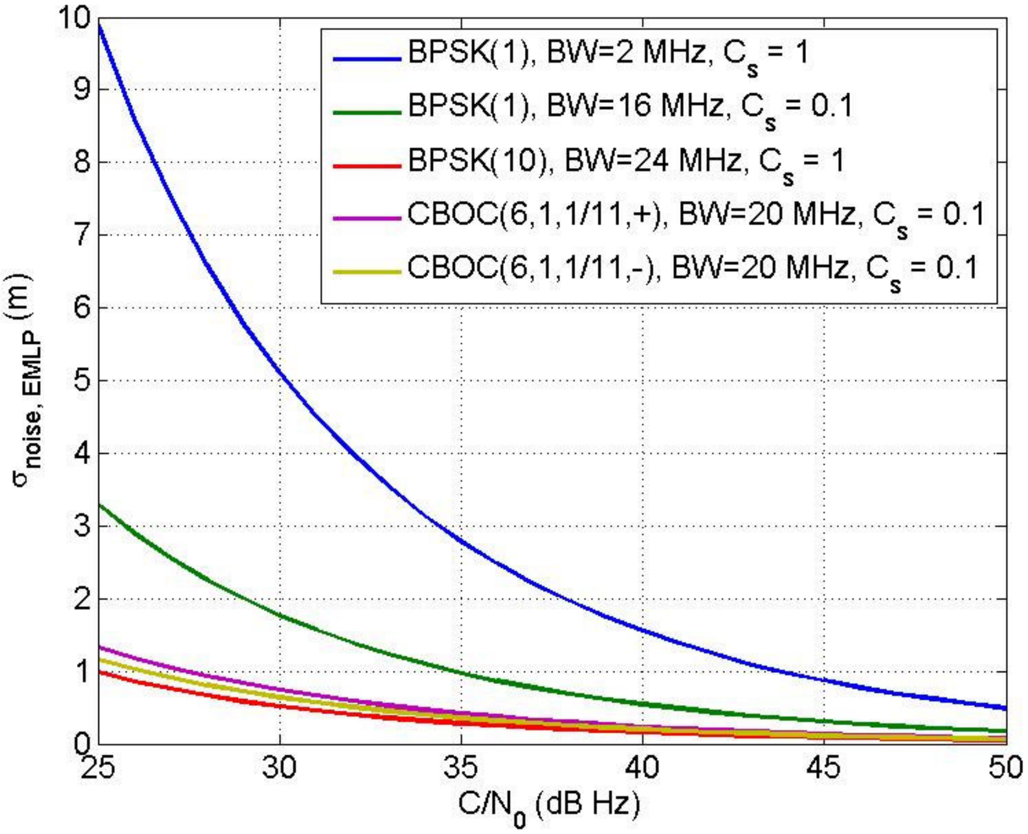

Figure 20 – Thermal noise standard deviation Vs. C/N_0

In Figure 20, the one-sided equivalent rectangular bandwidth of the DLL is equal to 1 Hz and the integration time is 20 ms. The early-late spacing is chosen to be characteristic of an expected civil aviation airborne receiver. In the next figure, the code tracking error 2.1.4.5 in presence of a single multipath with half amplitude and a varying delay (usually called the Multipath Error Envelope) is shown for different configurations.

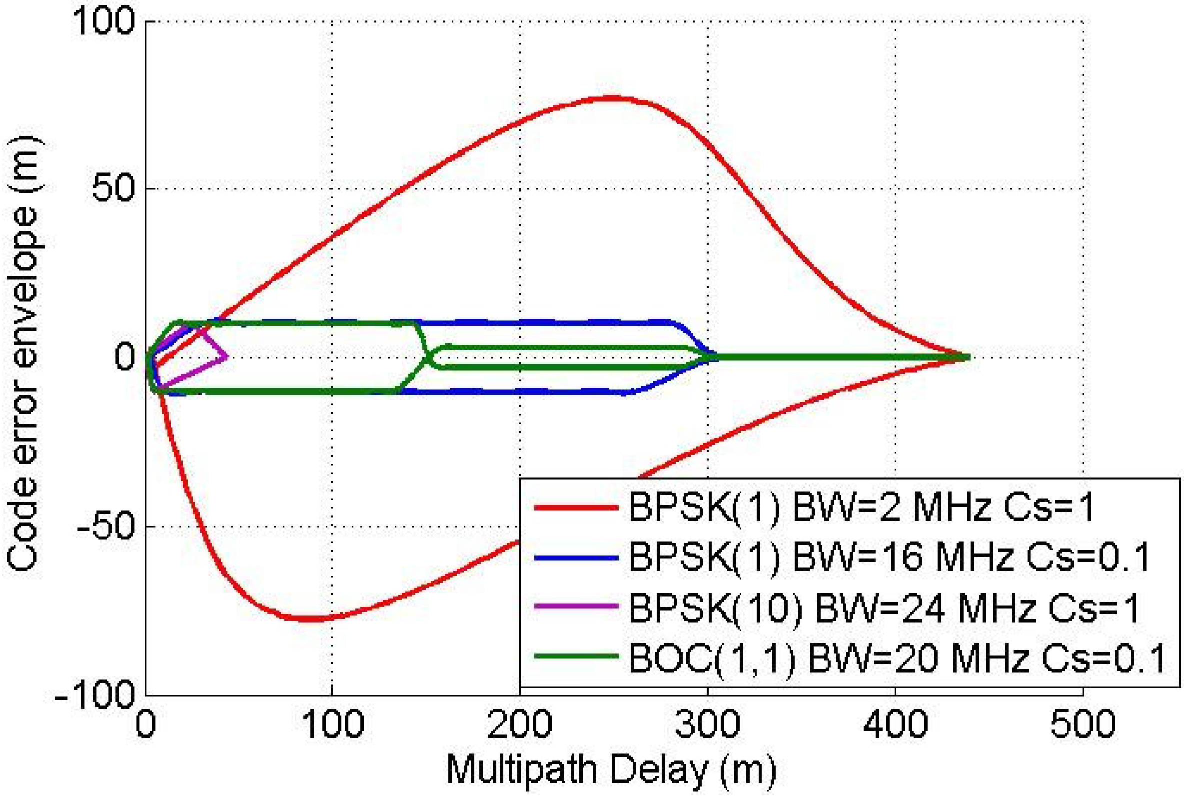

Figure 21 – Code Tracking Delay for One Path Multipath

As seen in Figure 20 and Figure 21, the BPSK (10) modulation, used for GPS L5 and GALIELO E5a, is expected to provide better performance than the BPSK (1) (GPS L1 C/A) for the thermal noise impact and multipath tracking error performance. The BOC (1,1), used for Galileo E1, is also expected to provide better performance than BPSK(1) used for GPS L1 C/A due to the different modulation and the used bandwidth and chip space. In particular, it is expected to have a lower standard deviation for the noise component.

Note, that the receiver configurations used to estimate the performance shown in the two previous figures are not representative of a real GBAS configuration, they were just used to compare the modulation performance.

3.2.3 Residual Biases Detection

The usual error model for the noise and multipath error on the pseudorange measurements is a centered normal distribution with zero mean. For this reason, the standard deviation or the variance are usually used for its parameter representation. In case of biases affecting the CMC, the mean value is not zero. The error model using only the standard deviation then cannot be realistic.

$$\sigma(El) = \sqrt{E\left|x_i(El) - E|x_i(El)|\right|^2} \qquad \text{Eq. 3.22}$$

For a limited series, the previous equation can be rewritten as:

$$\sigma(El) = \sqrt{\frac{1}{N}\sum_{n=1}^{N}\big(x_n(El) - \mu(El)\big)^2} \qquad \text{Eq. 3.23}$$

Where:

- $x_n(El)$ is the n^{th} sample present in the series within an elevation bin centred on El composed by N samples
- μ is the mean value of the series

Using the Root Mean Square (RMS) the mean value is not removed, so any unmodelled term present on the CMC can be seen when compared with the standard deviation. The equation to compute the RMS is:

$$RMS(El) = \sqrt{\frac{1}{N}\sum_{n=1}^{N}(x_n(El))^2} \qquad \text{Eq. 3.24}$$

Considering the error model as normal distribution $N(bias(El), \sigma(El))$ it can be rewritten as:

$$\begin{aligned} RMS(El) &= \sqrt{\frac{1}{N}\sum_{i=1}^{N}(b(El) + \eta_i(El))^2} = \sqrt{b^2(El) + \frac{1}{N}\sum_{i=1}^{N}\big(\eta_i(El)^2 + 2b(El)\eta_i(El)\big)} \\ &\cong \sqrt{b^2(El) + \frac{1}{N}\sum_{i=1}^{N}\eta_i(El)^2} = \sqrt{b^2(El) + \sigma^2(El)} \end{aligned} \qquad \text{Eq. 3.25}$$

Where:

- η is a variable with normal distribution and zero mean $N(0, \sigma(El))$
- $b(El)$ is a constant value.

Neglecting biases in the CMC is less forgiving for the I-free combination, since the biases on each frequencies will be combined into a potentially larger bias. For the I-Free combination, the RMS equation is:

$$RMS_{I-Free}(El) = \sqrt{\begin{array}{c}\left(1-\frac{1}{\alpha}\right)^2 \left(b_{L1}^2(El)+\sigma_{L1}^2(El)\right) + \frac{1}{\alpha^2}\left(b_{L5}^2(El)+\sigma_{L5}^2(El)\right) \\ + \left(\frac{2}{\alpha}-\frac{2}{\alpha^2}\right)\left(b_{L1}(El)b_{L5}(El)+Cov(\eta_{L1},\eta_{L5})\right)\end{array}} \quad \text{Eq. 3.26}$$

An important term to note in Eq. 3.26 is $b_{L1}(El)b_{L5}(El)$. If they have the same sign, the total RMS will be lower than the uncorrelated case because they will be multiplied by a negative factor ,$\left(\frac{2}{\alpha}-\frac{2}{\alpha^2}\right)$, and the same case happens if the cross-covariance of the errors is positive. In case of opposite signs of the bias or negative covariance, the total RMS will increase.

To check if residual biases, not modelled as noise and multipath are present on the PRCs the comparison between the standard deviation and the RMS is done.

3.2.4 Effect of the Time Correlation of the Error on the Smoothed Measurements

In section 2.2.2.2, the smoothing algorithms are presented for SF and DF cases. The standard deviation of noise and multipath components after the smoothing filter are provided in (Hwang, et al., 1999), and reminded in the following equations.

$$\sigma_{SF} \cong \sigma_{D-Free}(El) = \sigma_{L1/L5}(El)\sqrt{\frac{T}{2\tau}} \quad \text{Eq. 3.27}$$

$$\sigma_{I-Free}(El) = \sqrt{\left[\left(1-\frac{1}{\alpha}\right)^2 \sigma_{L1}^2\,(El) + \frac{1}{\alpha^2}\sigma_{L5}^2(El)\right]\frac{T}{2\tau}} \quad \text{Eq. 3.28}$$

Eq. 3.27 and Eq. 3.28 are valid if the errors present on the measurement can be modelled as white noise. If time correlation is present, the effect of the smoothing will not respect the previous formula. In the case of RMS analysis, only the noise term (and not the bias) is impacted by the smoothing process. Starting from Eq. 3.25.

$$RMS_{smooth}(El) = \sqrt{b^2(El) + \sigma^2(El)\frac{T}{2\tau}} \quad \text{Eq. 3.29}$$

To estimate the presence of time-correlated errors, the efficiency of the smoothing can be checked. The efficiency can be defined as the Ratio between the smoothed CMC standard deviation and the raw one. It should be equal to the smoothing factor:

$$\frac{\sigma_{D-Free\,smooth}}{\sigma_{D-Free\,raw}} = \frac{\sigma_{I-Free\,smooth}}{\sigma_{I-Free\,raw}} = \sqrt{\frac{T}{2\tau}} \quad \text{Eq. 3.30}$$

Where $\sigma_{I-Free\ raw} = \sqrt{\left(1-\frac{1}{\alpha}\right)^2 \sigma_{L1}^2\ (El) + \frac{1}{\alpha^2}\sigma_{L5}^2(El)}$

The same comparison cannot be done on the RMS due to the difficulty in computing the exact contribution of the noise and the multipath.

3.2.4.1 Impact of Different Smoothing Constants

The presence of time correlation on the pseudorange errors raises the need to analyze the impact of the smoothing algorithm using different values of the smoothing constant. The choice of the values of the smoothing constant determines the noise reduction. Logically the choice of a bigger smoothing time can be desirable in order to further reduce the error levels. However, it must be considered that to reach the expected performance of the smoothing process, it is necessary to wait for the smoothing filter convergence. For the GBAS case in (ICAO, 2006), it is recommended to wait 360 seconds before reaching steady state performance if a smoothing time constant of 100 s. This constraint already impacts the availability of the measurements (after acquisition, re-acquisition or smoothing filter re-initialisation). However, the use of dual constellation having a positive impact on the availability, a trade-off between PRC accuracy and availability may be ultimately required.

The values of time constants that will be analyzed are:

- 30 seconds (GAST D MT11)
- 100 seconds (GAST C/D MT1)
- 300 seconds
- 500 seconds
- 1000 seconds

3.2.5 Inter-Frequencies Error Correlation

This analysis regards the evaluation of inter-frequency error correlation. This analysis is particularly interesting because it impacts directly the RMS value of the I-Free. It is known that one of the bigger drawbacks of this technique is the increased noise level caused by the combination of two code measurements. However, if some correlation between noise and multipath on the two frequencies exists, it can reduce the RMS or standard deviation of the I-Free measurement. Looking at Eq. 3.26 is possible to see that an important role is played by the following term.

$$\left(\frac{2}{\alpha}-\frac{2}{\alpha^2}\right)[b_{L1}(El)b_{L5}(El) + Cov(\eta_{L1},\eta_{L5})]$$

Knowing that the value of α is -0.7933, using L1 and L5 measurements, the constant term in the first brackets is -5.6995. A positive cross-covariance of the noise errors and the presence of biases with the same sign will result in a reduction factor in the RMS formula computation. In order to analyze the impact of the biases and the covariance of the noise on the two measurement, a comparison between the measured RMS_{I-Free} and a theoretical $RMS_{I-Free,theory}$, where no inter-frequency correlation is considered, is done. The RMS of the theoretical I-Free is obtained as:

$$RMS_{I-Free,theory} = \sqrt{\left(1-\frac{1}{\alpha}\right)^2 RMS_{L1}^2 + \frac{1}{\alpha^2} RMS_{L5}^2} \qquad \text{Eq. 3.31}$$

The model used to compute the theoretical RMS considers neither any combination of the bias on measurement nor an inter-frequency covariance between the noises. The same analysis can be done for the standard deviation in order to obtain information about the only noise covariance on measurement.

$$\sigma_{I-Free,theory} = \sqrt{\left(1-\frac{1}{\alpha}\right)^2 \sigma_{L1}^2 + \frac{1}{\alpha^2} \sigma_{L5}^2} \qquad \text{Eq. 3.32}$$

As for the RMS analysis the value of the $\sigma_{I-Free,theory}$ is compared with the one obtained from the empirical data. Differences between the two sigma are due to non-zero values of the covariance between the errors on the two analyzed frequencies. The covariance contribution is

$$\left(\frac{2}{\alpha}-\frac{2}{\alpha^2}\right)[Cov(\eta_{L1},\eta_{L5})]$$

As for the RMS, positive values of covariance may reduce the σ_{I-Free} of the empirical data.

In order to have a mathematical estimation of the difference between the standard deviation estimated as in Eq. 3.32 and the one obtained from the empirical data the percentage of reduction or augmentation will be computed for all satellites.

$$difference\ (\%) = \left(\frac{RMS_{I-free,empirical} - RMS_{I-free,theory}}{RMS_{I-free,empirical}}\right) * 100 \qquad \text{Eq. 3.33}$$

3.2.6 Error Correlation over Two Reference Receivers

The analysis explained up to now takes into account only one RR at a time. In GBAS however, the ground station is composed of multiple RRs. In particular, for GAST-D service, the number must be at least four. The advantage of having more than one station is a reduction of the standard deviation value of the uncorrelated error sources like the noise. The improvement on the accuracy is not the only advantage. Having four stations also permits to monitor the PRCs to determine if a fault occurred on one RR (5.2.1.6) or to improve the monitoring of ranging error source like ionosphere fronts (5.2.1.8).

To compute the averaged CMC, a simple mean between the CMCs from two stations at the same epoch is made. In theory, if errors are not correlated over the two RRs, the sigma of the averaged CMC should be:

$$\sigma_{gnd\ AV} = \frac{\sqrt{\sigma^2_{gnd\ RR1} + \sigma^2_{gnd\ RR2}}}{2} \qquad \text{Eq. 3.34}$$

Where $\sigma_{gnd\ AV}$ is the standard deviation of the averaged CMCs.

In case of correlated errors Eq. 3.34 becomes

$$\sigma_{gnd\ AV} = \frac{\sqrt{\sigma^2_{gnd\ RR1} + \sigma^2_{gnd\ RR2} + 2cov(RR1, RR2)}}{2} \qquad \text{Eq. 3.35}$$

Where cov is the covariance of the two series.

The aim of this analysis is to check if the empirical sigma ground is similar to the one shown in Eq. 3.34. On the contrary if differences between the theoretical sigma (Eq. 3.34) and the empirical one exist, the covariance between errors on the two receivers must be investigated. The analysis is done only for the smoothed CMCs because in any GBAS ground station the averaging of the PRCs is done after the smoothing process.

In order to have a mathematical estimation of the difference between the standard deviation estimated as in Eq. 3.34 and the one obtained from the empirical data the percentage of reduction or augmentation will be computed for all satellites.

$$difference\ (\%) = \left(\frac{|\sigma_{gnd,empirical} - \sigma_{gnd,AV}\ |}{\sigma_{gnd,AV}}\right) * 100 \qquad \text{Eq. 3.36}$$

3.3 Results on Noise and Multipath Errors Characterization

In this section the results obtained analysing the properties of the CMCs on different signals and combinations will be shown.

3.3.1 Experimental Set-up Description

Two different set-ups have been analyzed:

- Pattonville Airport, Nov-Dec 2014
- Toulouse Blagnac Airport, April 2016

3.3.1.1 Pattonville Airport

For the analysis of multipath and noise, the data collection has been done by Thales Avionics at Pattonville airport in Germany. The antenna used was a BAE-ARL1900 and the receiver was a Septentrio PolaRx4. Data were collected at 1 Hz on two frequencies, L1 and L5, for three days for different antenna positions as shown in the next figure. The antenna used in the data collect is the one proposed in (Lopez, 2008) as reference antenna for GBAS ground stations and also mentioned in the literature as Multipath Limiting Antenna (MLA).

Figure 22 – Antenna positions for data collection at Pattonville airport

Since the scope of this study is to analyse the noise and multipath in an environment similar to an airport, the configurations used are therefore 100 and 50 meters away from a nearby building. The choice to analyze also the data collection done at 50 meters distance point has been done to evaluate the properties of the antenna in rejecting the non-nominal multipath error.

Figure 23 – MLA antenna and reflector building in Pattonville airport

For each configuration, two days have been selected and analyzed:

- 50 meters case; 19-20/11/2014
- 100 meters case; 01-02/12/2014

The signals were recorded on two frequencies, L1 and L5 bands for GPS constellation. Signals on E1 and E5a bands were recorded for Galileo satellites. Galileo CMC has not been analyzed since only three satellites were in orbit at the data collection time.

3.3.1.2 Toulouse Blagnac Airport

For the data collection done in Toulouse airport, two MLA antennas, BAE ARL-1900, and two Septentrio PolaRX receivers were used (Ladoux, 2016). This permits to analyze also the error correlation across two receivers to determine the standard deviation reduction due to the PRC averaging. The antennas have been installed in the proximity of the existing GBAS GAST-C station in order to simulate an airport scenario with no near obstacles.

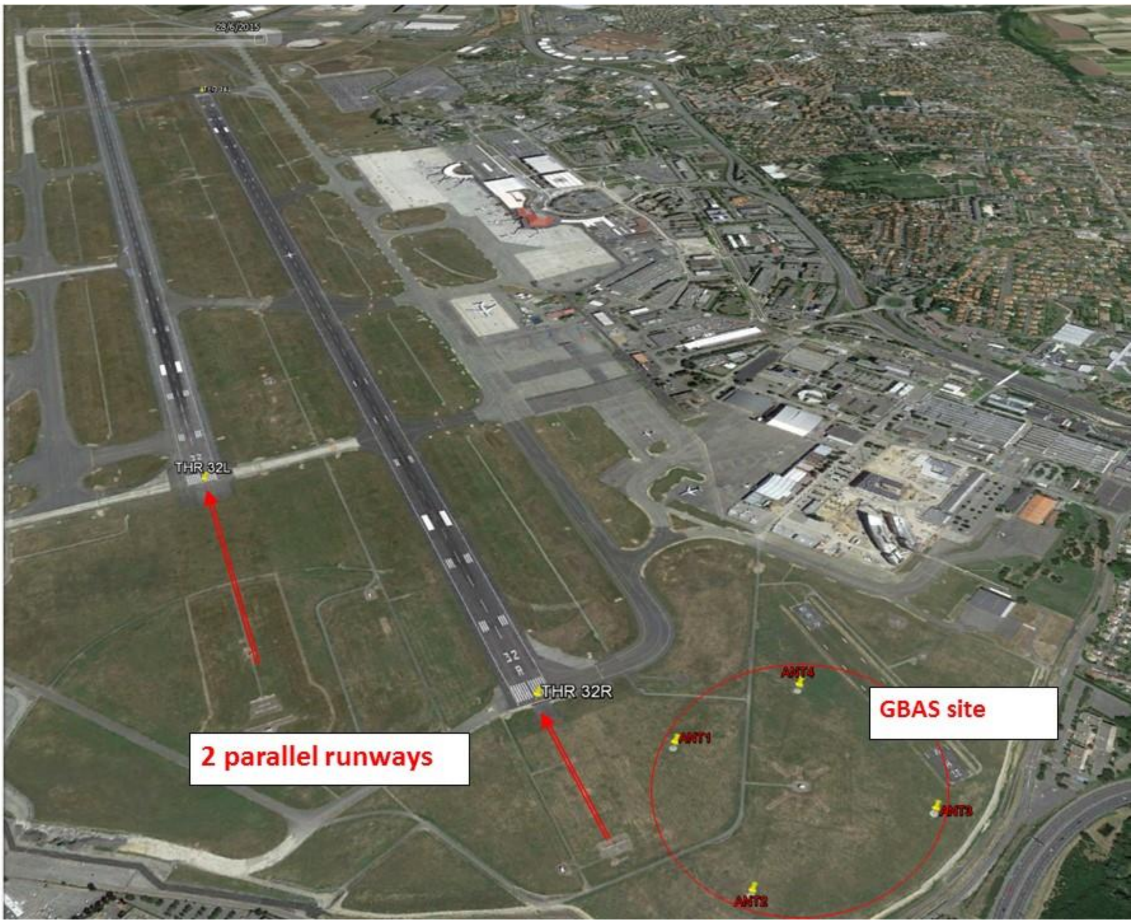

Figure 24 – Toulouse Blagnac airport GBAS ground station (Ladoux, 2016)

The main difference with the Pattonville airport data collection is the absence of a fix obstacles in the proximity of the antennas in Toulouse. Blagnac airport is used for commercial aviation. This means that a series of large aircrafts land, move and take-off on the airport. Moreover, on the airport is also present the Airbus plant executing flight test on different aircraft models, including the A380, the largest commercial aircraft. These conditions create a scenario totally different from the first one, where Pattonville airport is used only as base for a helicopter rescue service. The presence of landing and departing aircraft, as well as aircraft waiting in the "hold position" can be an additional source of multipath error.

The campaign has been performed for ten full days, from 02/04/2016 to 10/04/2016. The signals collected were GPS L1 C/A, GPS L5, Galileo E1 and E5a. There were 9 Galileo satellites in orbit at the time of the collect. However, due to an issue in the conversion of the binary file to RINEX format, Galileo satellite PRN 30 will not be used.

During this data collection, there were an issue related to a lack of data during from 1 to 3.5 seconds after each hour. Being an hourly data collection this lack of data seems related to the saving process of the previous hour ".LOG" file. If the scheme presented in 3.2.1.1 to remove phase ambiguity is used, the averaged CMC is computed hourly and removed from the related CMCs segment. This way to proceed is good to be sure that phase ambiguity residual term, present on the CMC, has the same value throughout each hour segment. At the same time, using this methodology, there is the risk to compensate the multipath affecting the CMC by averaging the CMC over short time windows. In Figure 24 it is possible to see the effects of using or not the time continuity check.

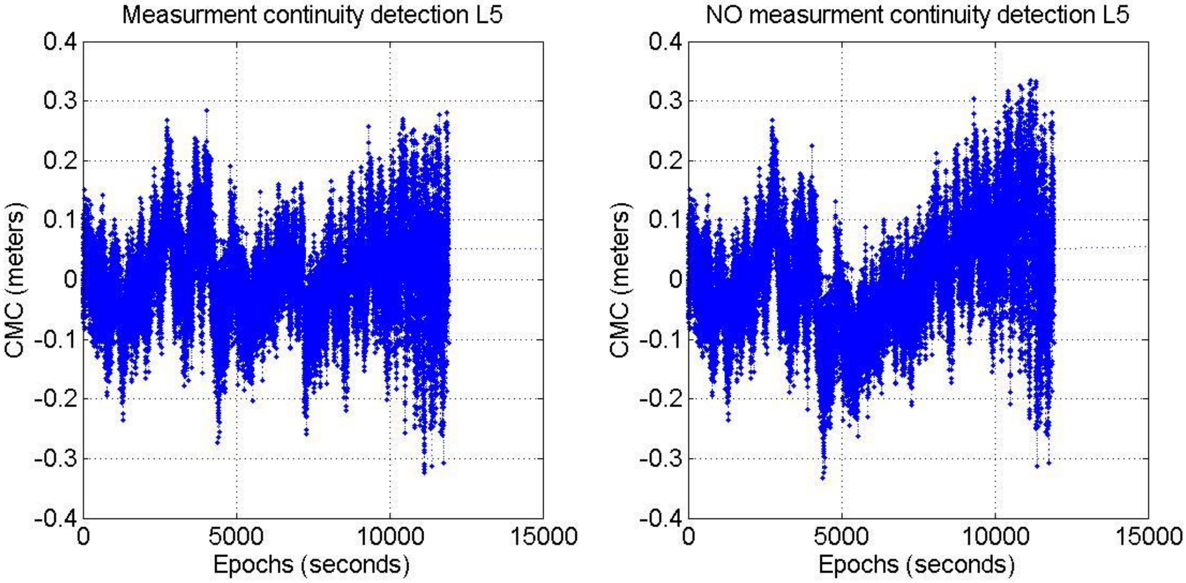

Figure 25 – GPS L5 raw CMC time series for one satellite, with and without epoch continuity detection

In order to obtain a realistic analysis the time continuity check has not been used for this analysis.

3.3.2 Noise and Multipath on Different Signals

To avoid the repetition of similar figures for all the analyzed cases the results will be shown for only one day of data collection done at Toulouse airport. This location has been selected because is the one with the highest number of visible Galileo satellites. The selected day is 02/04/2016. Results concerning Pattonville and all additional days are provided in appendix C.

This section analyses the noise and multipath on different measurement or combinations:

- D-Free GPS L1 C/A
- D-Free GPS L5
- D-Free Galileo E1,
- D-Free Galileo E5a
- I-Free for GPS and Galileo

The next three plots show the raw CMC, L1 and L5 D-Free and I-Free, for the one day out of the 4 analysed and for the RR1. In this case there are 12 satellites transmitting the GPS L5 signal each one represented by a different colour (due to the limited colours on MATLAB sometime colours repetition occur).

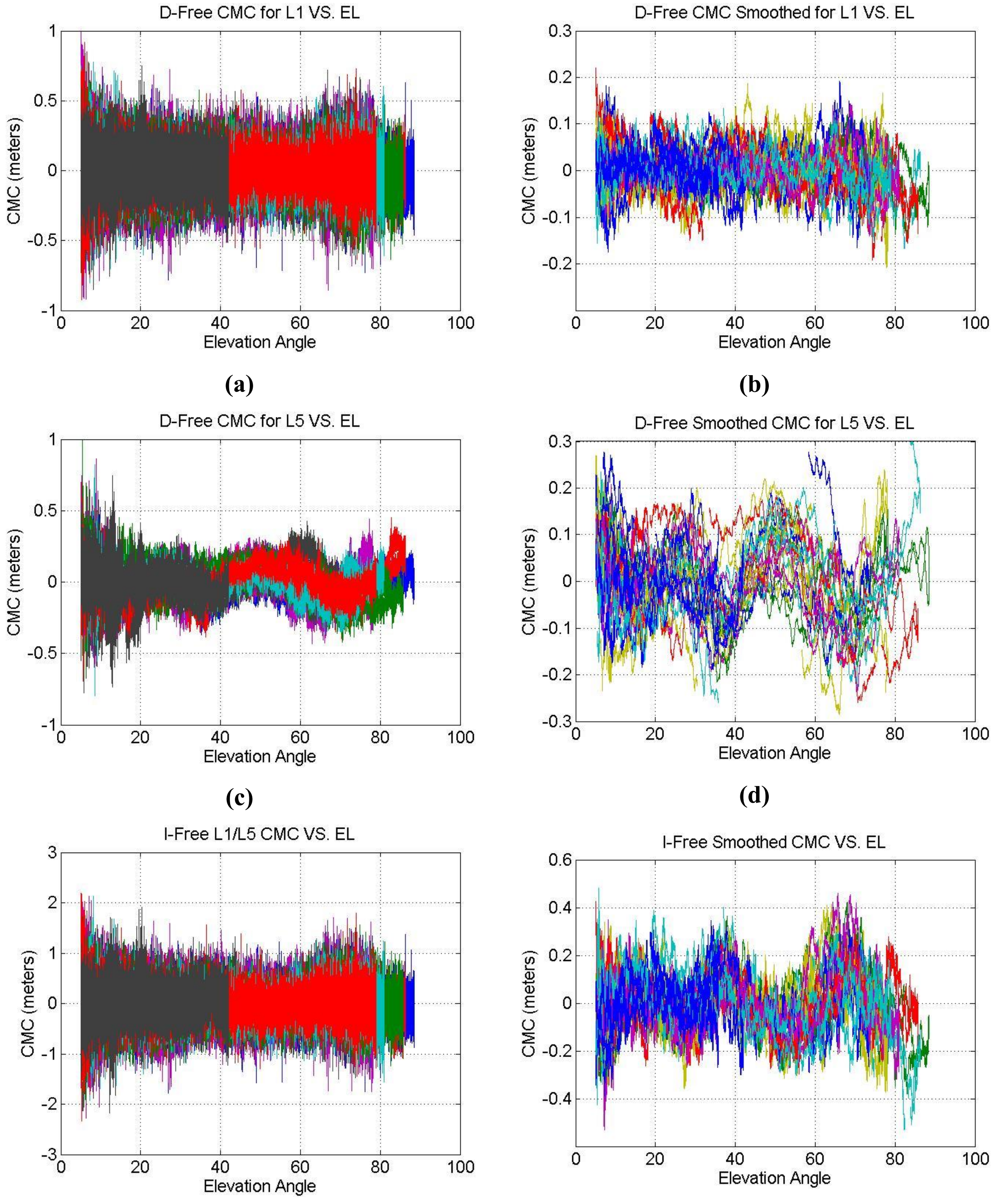

(a) **(b)**

(c) **(d)**

(e) **(f)**

Figure 26 – GPS L1 C/A, GPS L5 and I-Free Raw and 100 seconds smoothed CMCs for All Satellites Toulouse Blagnac RR1

In Figure 26 (a) and (b) the CMCs for GPS L1 C/A signals, from all the satellite in view, are shown. It is possible to note that in both the cases there is also no elevation dependency, except for values from

5° to 10° elevation angle. A slightly increased level of noise is present at around the 70° elevation angle. This in particular is caused by a reduction of the antenna gain around this elevation angle (Lopez, 2008).

In Figure 26 (c) and (d) the GPS L5 CMCs are shown. The raw CMCs show a lower level of noise than the same CMCs on GPS L1.Some elevation dependent oscillations, not modelled as noise or multipath or ground multipath (Montloin, 2014), are visible on the raw CMCs. The smoothed CMCs confirm the presence of these oscillations. Possible causes will be investigated in section 3.3.3.

Finally in Figure 26 (e) and (f) the CMCs for the I-free combination show, as expected, an increased noise level than the previous cases. As for the GPS L1 case the raw CMCs seem to have no elevation dependency from 10° to 90°. The oscillations seen on GPS L5 CMCs are visible only on the smoothed CMCs, Figure 26 (f), with an opposite sign.

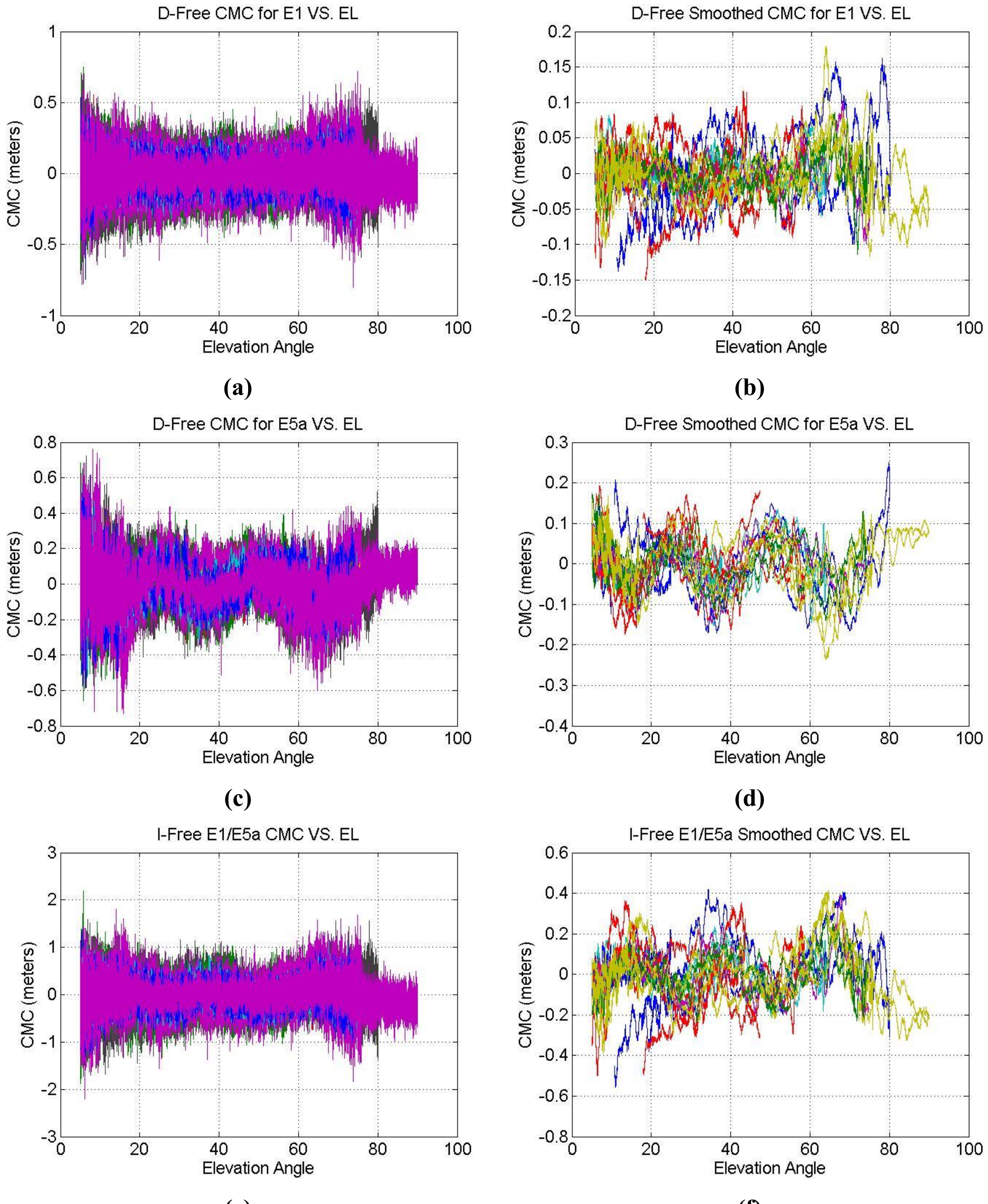

(a) **(b)**

(c) **(d)**

(e) **(f)**

Figure 27 – Galileo E1 C/A, E5a and I-Free Raw and 100 seconds smoothed CMCs for All Satellites Toulouse Blagnac RR1

Figure 27 (a) and (b) show the noise and multipath affecting the Galileo E1 signals. As for the GPS L1 case the CMCs seem to have no elevation dependency for both the cases.

In Figure 27 (c) and (d) the CMCs for GLILEO E5a are shown. As for GPS L5 the same oscillations are visible. The noise level seems to be a bit lower than Galileo E1 CMCs. The smoothed CMCs emphasize the oscillations visible on the raw CMCs.

The last couple of plots, Figure 27 (e) and (g), show the impact of the noise and multipath on I-free combination. The noise level is bigger than the E1 or E5a cases. Oscillations are only visible on smoothed CMCs, probably due to the higher level of noise on the raw case.

The next figures investigates the standard deviation of the measurements as a function of the satellite elevation. The CMCs used to compute the standard deviation, in each elevation angle bin, are the ones from all satellites having and elevation angle comprised between ± 0.5° from the reference elevation angle.

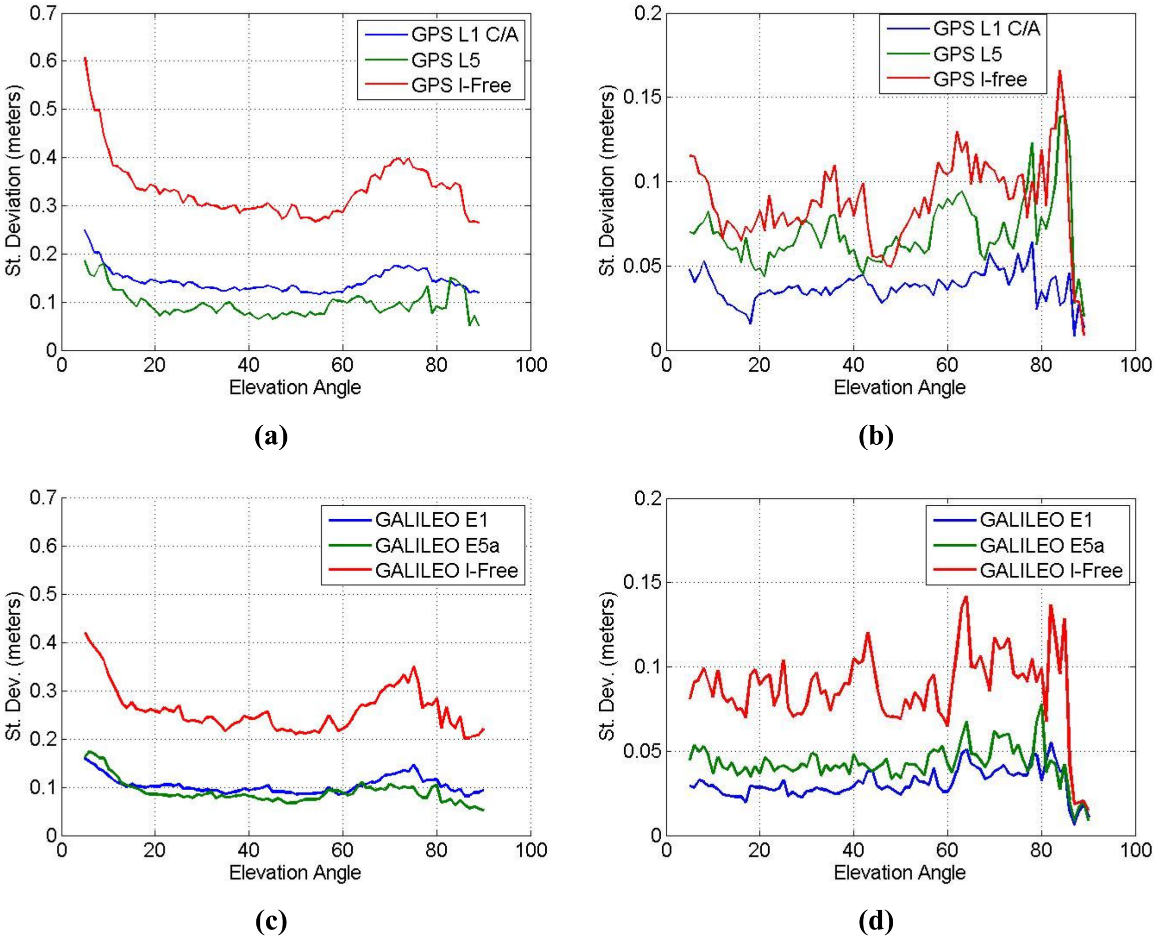

(a) **(b)**

(c) **(d)**

Figure 28 – GPS and Galileo CMCs standard deviation for raw and smoothed cases on all signals

Figure 28 shows the performance of GPS and GALILEO signals. Comparing the performance between the raw cases, (a) and (c), and the smoothed cases, (b) and (d), it is possible to see that for the smoothed CMC the performance of L5 band measurements are worse than L1 band measurement. This result is at the opposite of what was seen in 3.2.2. Performance of the GALILEO E1 signal with its BOC modulation is better than the one of the GPS L1 C/A as expected. The performance on the smoothed CMC are similar due to reduction of the noise level provided by the low pass filter. The I-free combination, as seen from the CMCs figures, is the one with the highest standard deviation for both the cases.

3.3.3 MLA Calibration on L5

The aim of this analysis is to identify possible residual biases on the smoothed CMCs. The detection is done comparing the RMS and the standard deviation computed on the same data set.

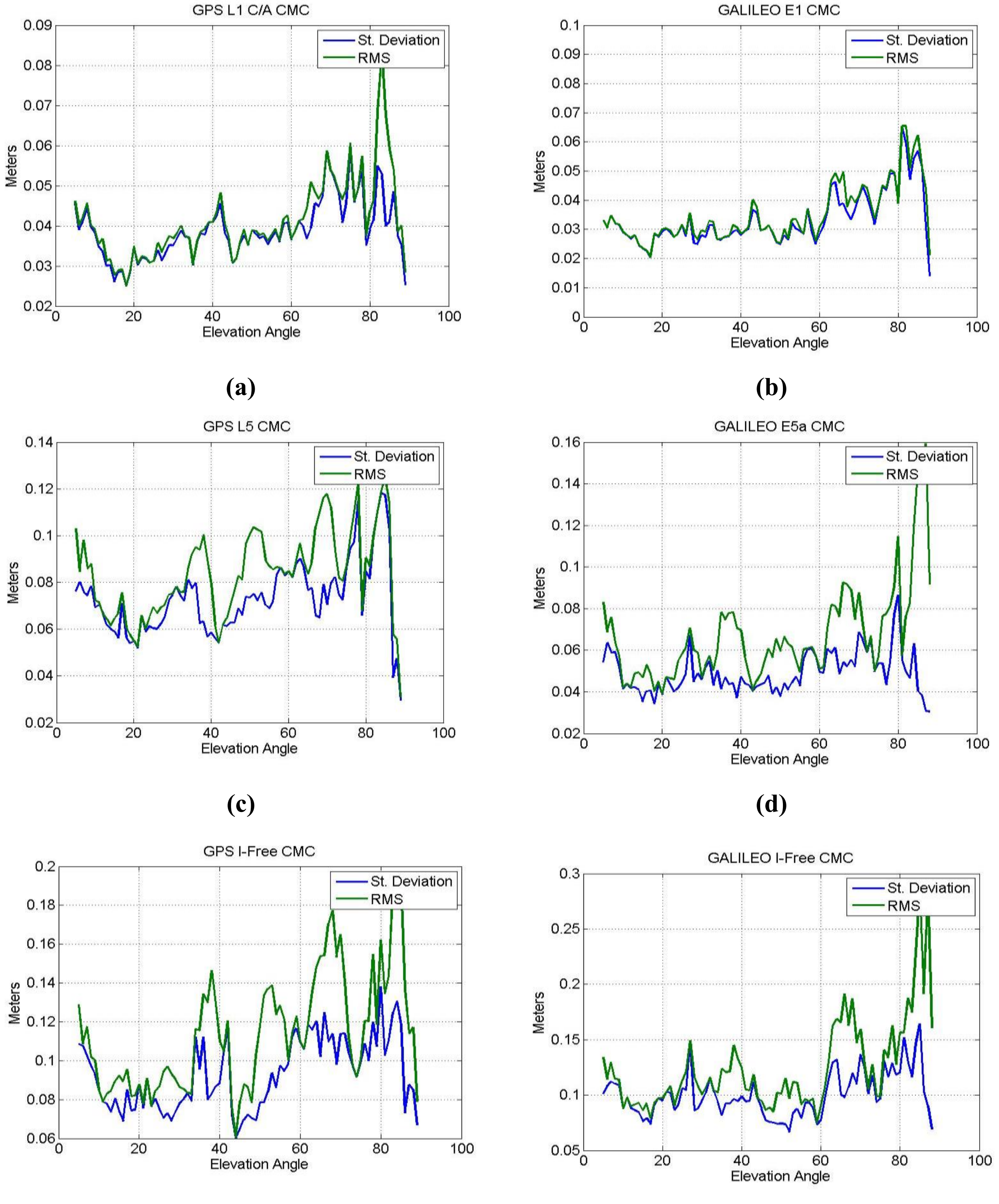

(a) (b) (c) (d) (e) (f)

Figure 29 – Comparison between RMS and standard deviation for 100 s. smoothed GPS and Galileo signals

It is possible to see, from Figure 29, that the RMS and the standard deviation on L5 band signals and on the I-Free combinations are different. This points toward the presence of a bias.

The errors present on the CMC are modelled for long time series as:

- a distribution with zero mean and elevation dependent standard deviation for noise
- an elevation dependent bias different for each satellite for multipath

Looking at Figure 26 and Figure 27 (d, f) in 3.3.2, it is possible to see that the biases are in fact slowly varying oscillations common to all satellites with various azimuths and with a common elevation dependency. This type of bias is not due to ground multipath because its oscillation have a different elevation angle dependency (Montloin, 2014) . The cause of these oscillations is attributed to an antenna bias. No such similar oscillations are present on data recorded with a different antenna (Circiu, et al., 2015).

According to (Lopez, 2008), it has been seen that some code and phase delay may occur on this antenna type. It is nevertheless possible to derive the code minus phase delay, and calibrate the data as described in (Lopez, 2008) for the GPS L1 band. It is proposed to follow the same methodology for calibrating the L5 band CMC and the I-Free CMC.

In order to remove the possible calibration error from the GPS L5 CMC, the following methodology has been used.

1. Computation of the CMC for all satellites across all the analyzed days using different smoothing time constants
2. Binning of the CMC by elevation angle
3. Computation of the CMC mean value for each elevation bin
4. Choice of the most appropriate smoothing constant to compute the calibration values
5. Interpolation of the calibration values using spline method to create calibration values with a 0.1° resolution

The results of the calibration are given in the following figures.

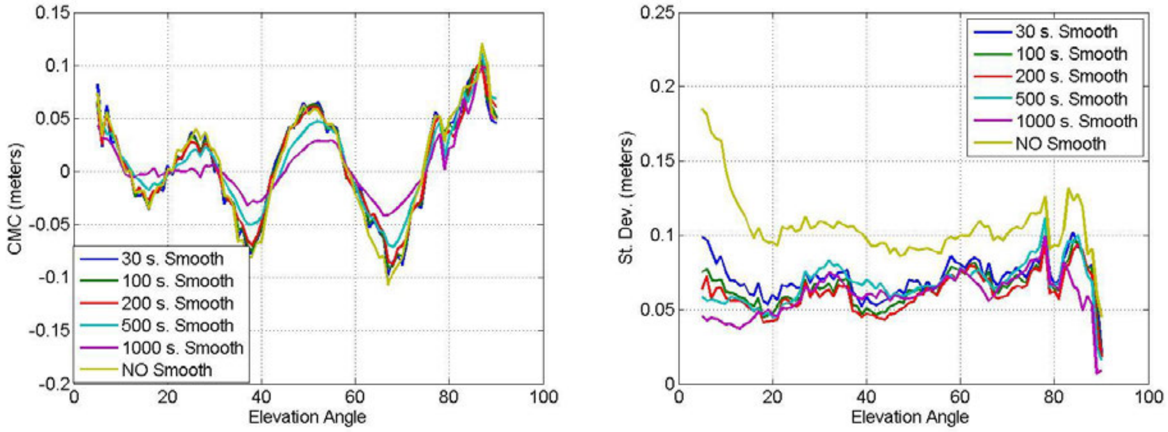

Figure 30 – GPS L5 CMCs Mean Value (left) St. Deviation (right) Vs. Elevation Angle for All Satellites across Three Days

Analysing the two previous figures, it is possible to see that the use of long smoothing time constant reduces the elevation dependent oscillating biases observed in Fig 36. Recall that the goal of the smoothing process is to reduce the standard deviation of the CMC, and shall not remove biases. The most appropriate CMC to use is the 100 seconds smoothed since it has an acceptable accuracy as stated by the analysis of the standard deviation and does not cut the values around the peak.

The application of the calibration values to the raw and smoothed CMCs brings the following benefits on GPS L5, Galileo E5a and I-Free CMCs.

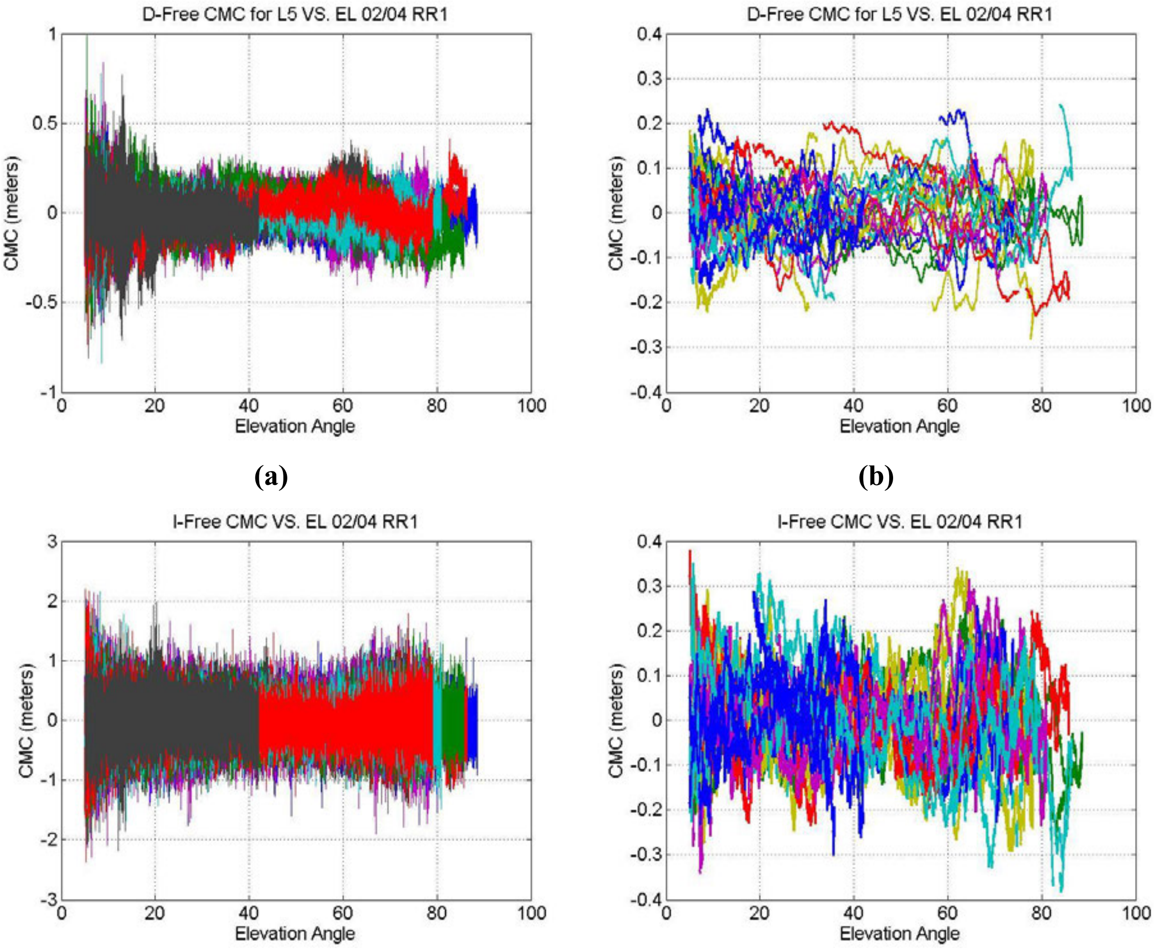

(a) **(b)**

(c) **(d)**

Figure 31 – Calibrated raw and 100 s smoothed CMCs for GPS signals on RR1

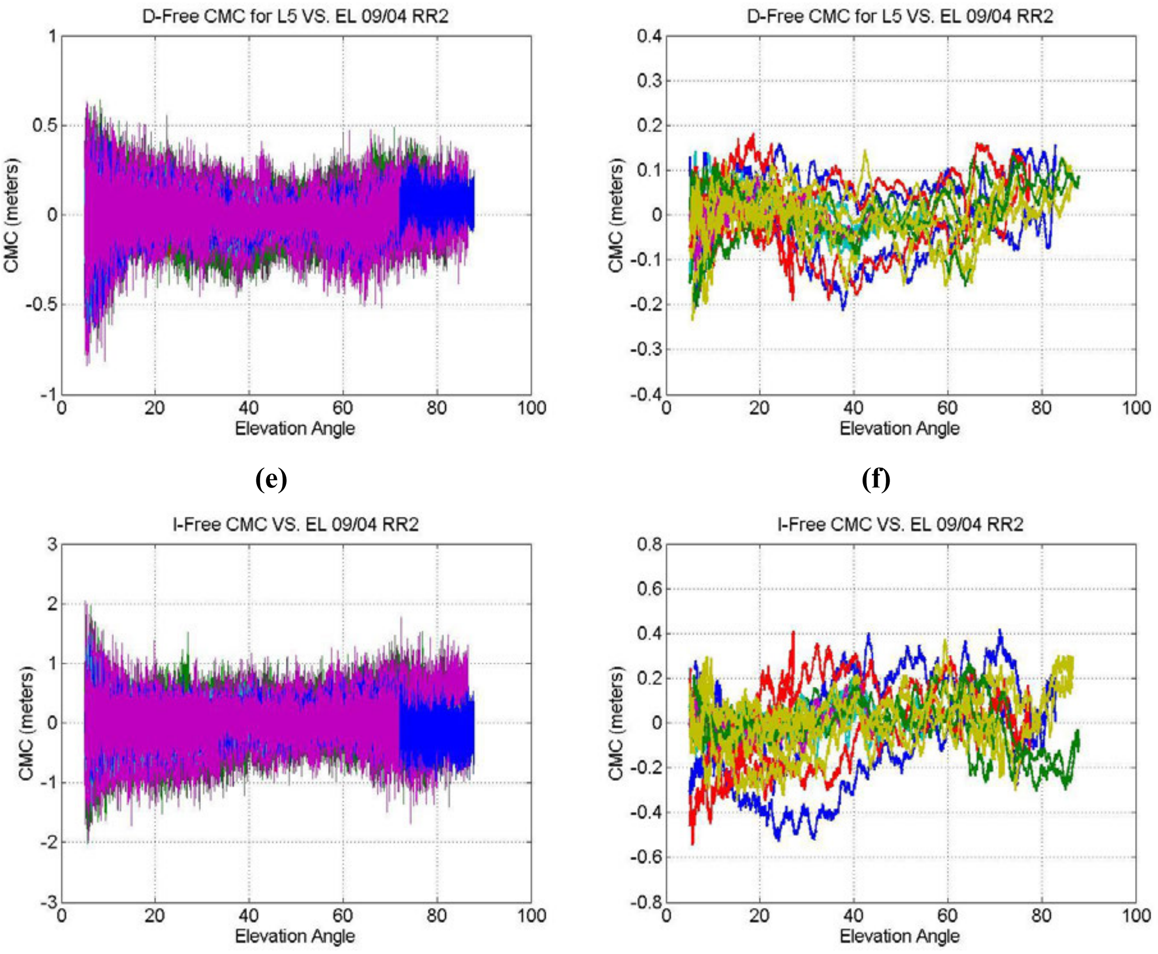

(e) **(f)**

(g) **(h)**

Figure 32– Calibrated raw and 100 s smoothed CMCs for Galileo signals on RR2

It is possible to see on Figure 32 that the calibrated CMCs are no longer affected by any elevation-dependent bias. The effects of the calibration on the other days produce the same results as for the one shown in the Figure 32. For all results in the following of the thesis the calibrated ones will be used.

3.3.4 Smoothing Efficiency

This analysis aims at verifying the presence of time correlation on the errors affecting the CMCs. This analysis is done by examining the smoothing efficiency, comparing the ratio of the smoothed and raw CMCs standard deviation with the theoretical standard deviation reduction recalled in Eq. 3.30. The values of the smoothing reduction will be shown for only one day for each data collection case because results provide similar results across days. The smoothing constant used is 100 seconds.

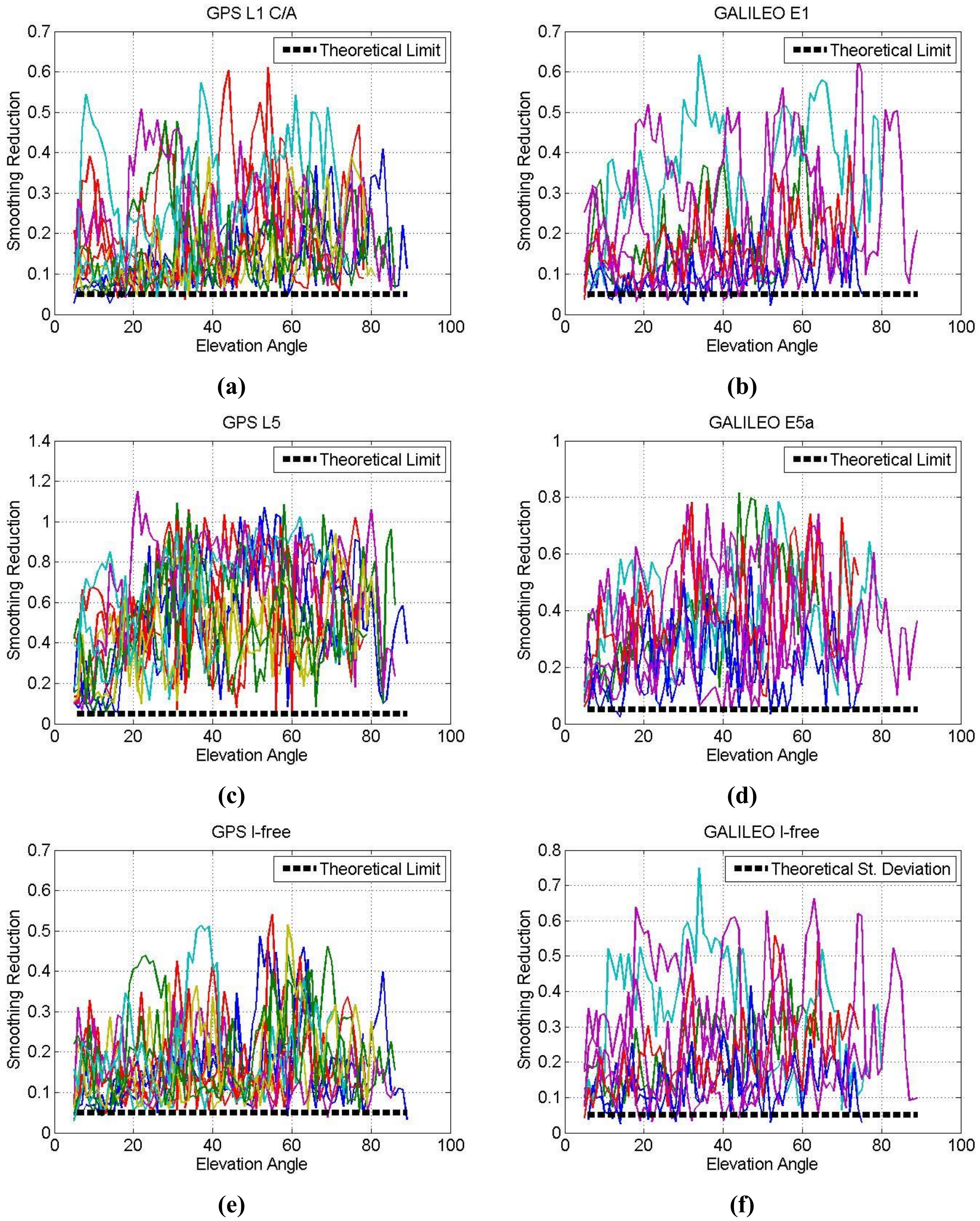

(a) (b)

(c) (d)

(e) (f)

Figure 33 – Real Vs. theoretical smoothing reduction for GPS (a, c, e) and Galileo (b, d, f)

As it is possible to see from the study of Figure 33, the theoretical smoothing reduction (Eq. 3.30) is reached only in a few instances. In the majority of the cases, the value is higher than theory, which shows a certain degree of time correlation on the errors. The smoothing is more efficient on GPS L1 and Galileo E1 (reduction similar to the theoretical value), Figure 33 (a, b). On GPS L5 and Galileo E5a, the smoothing is less efficient than on L1 band measurement (the standard deviation reduction is not at the same level as expected by theory), Figure 33 (c, d). The reduction, due to the smoothing process, on the

I-Free CMCs seems to be a sort of average between the two previous cases since the values of the reductions are smaller than L5 band measurement but bigger the ones on L1 band, Figure 33 (e, f). In a few of epochs the value of the smoothing reduction is smaller than the theory, this effect is caused by rapid changes of the deterministic components similar to jumps.

In order to have a better understating of the results obtained in the previous analysis, the following figures display the autocorrelation function for the CMCs of some satellites. This analysis can be useful to identify the correlation time of noise and multipath which could be the cause of the smoothing inefficiency in certain cases.

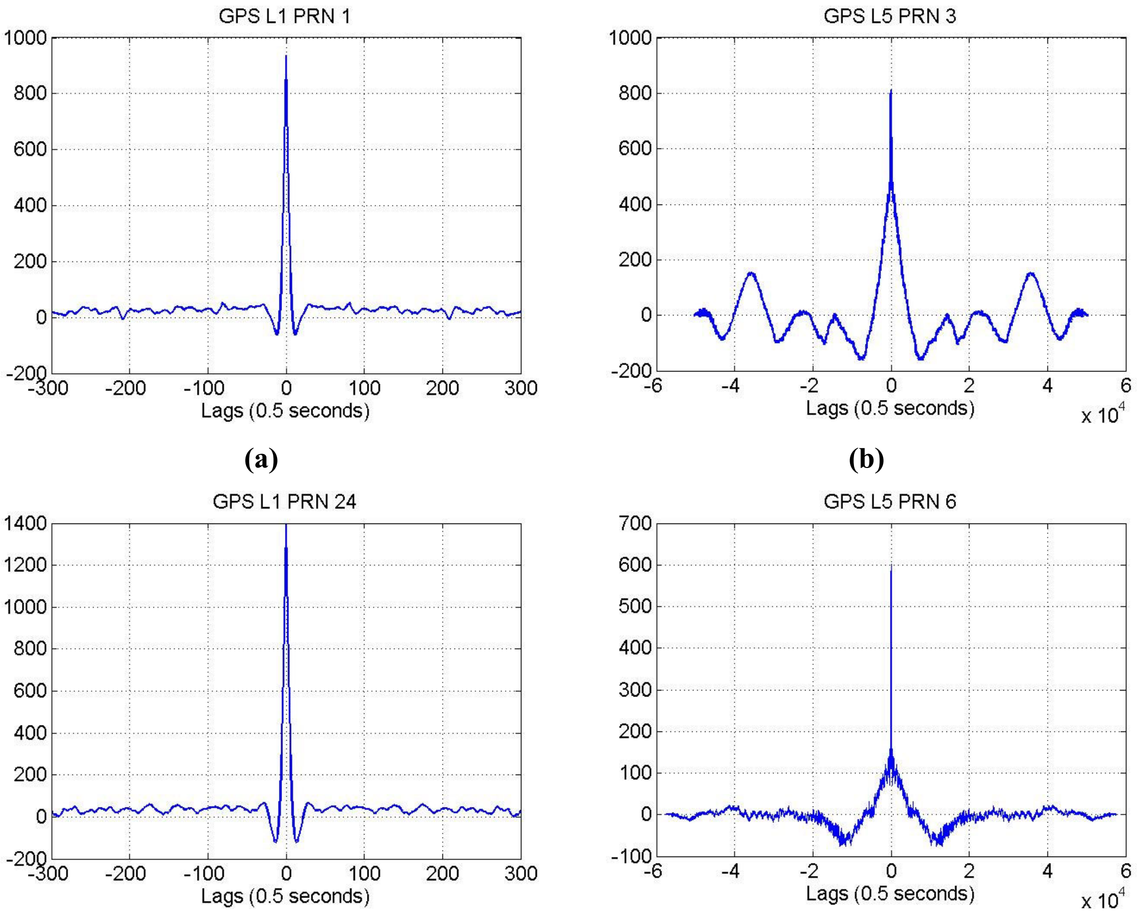

(a) **(b)**

(c) **(d)**

Figure 34 – Autocorrelation function for GPS L1 and L5 for different satellites

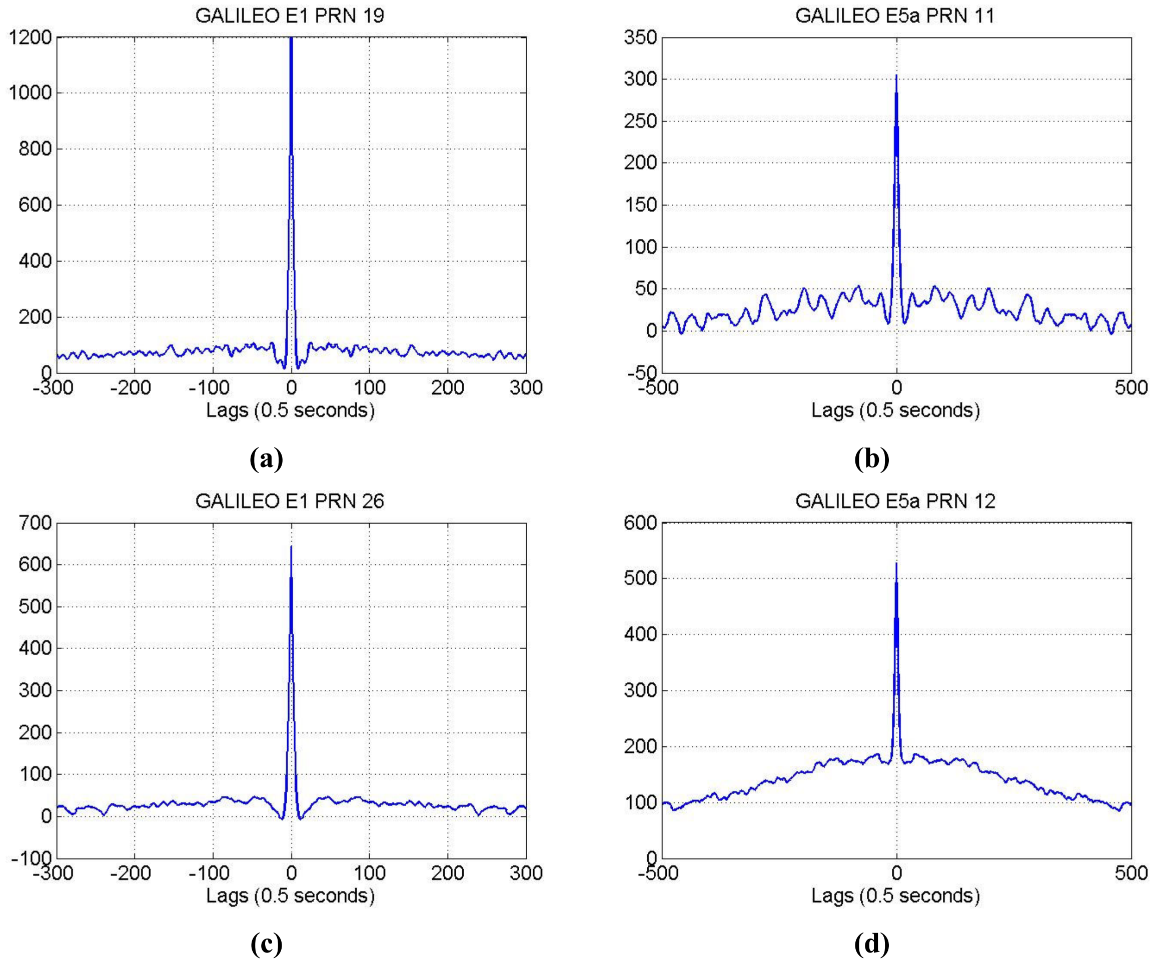

Figure 35 – Autocorrelation function for Galileo E1 and E5a for different satellites

The complete analysis of the autocorrelation functions on the L1 and L5 band signals, Figure 34 and Figure 35, have given the following results:

- GPS L1 and Galileo E1 CMCs show a correlation period (computed at 10% of the main peak) comprised between 3 and 5 seconds (Figure 34Figure 35 a, c). Some cases of low smoothing efficiency are possibly due to a not optimal choice of the elevation angle bin (presence of a low number of samples for some satellites).

- The correlation function on GPS L5 and Galileo E5a point out a series of correlation periods too spread out in order to estimate a unique value. Figure 34 and Figure 35 (b, d) only show results for two satellites, the complete analysis is shown in appendix C.5. In some cases, the correlation period is higher than the smoothing filter constant. This condition leads to a low level of smoothing efficiency.

The results of the autocorrelation function confirm what has been seen from the smoothing gain figures. The smoothing is more efficient on L1 band measurement than on L5. The cause of this difference could be the multipath errors present on L5 and E5a CMCs. It is good to remind that the antenna used in all the data collection is optimized to work on the L1 band. Another error source on L5 could be the residual calibration errors.

3.3.4.1 Optimal Smoothing Constant

In the previous section, it has been seen that the errors affecting the CMC are correlated in time and this property acts as if the smoothing is less efficient than what expected in theory. A possible way to improve the efficiency of the smoothing is the choice of a longer smoothing time constant. In particular, the smoothing constant has to be bigger than the correlation time to obtain a good smoothing efficiency. In the next figures the averaged standard deviation over all satellites and days will be shown for different smoothing constant. The analysis will be done for each signal band, L1 and L5, and for the I-free combination separately.

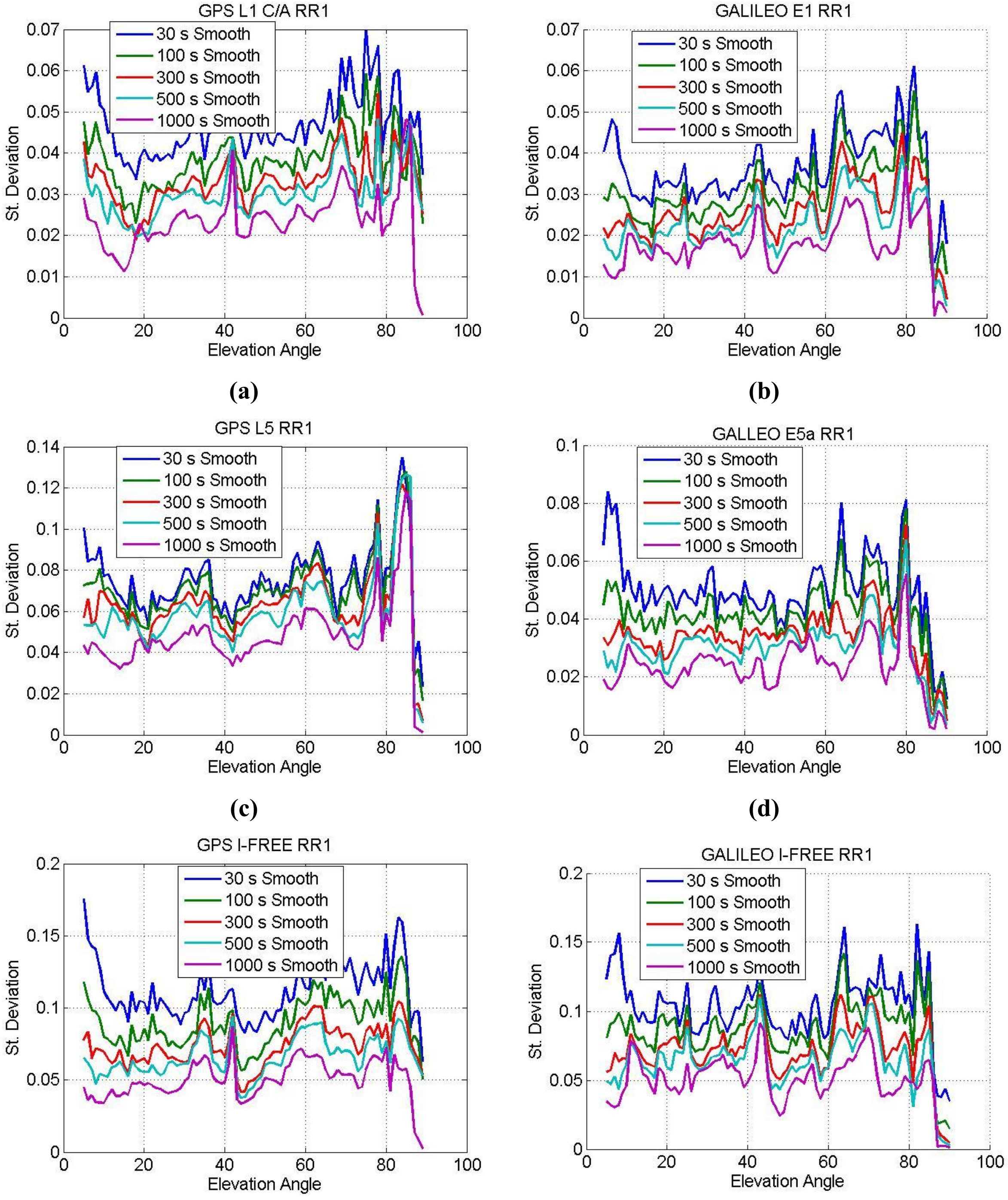

(a) (b)

(c) (d)

(e) (f)

Figure 36 – Standard deviation comparison for different Smoothing constants for GPS and Galileo signals

Examining the Figure 36, it is possible to observe that the use of longer smoothing time constant brings advantages in term of standard deviation reduction. The choice of an optimal smoothing constant is, however, related also to the time that the filter needs to reach the steady state. Considering also the results obtained in the previous section the choice of the optimal smoothing constant is also related to the correlation time of each signal.

For the D-free combination relying on L1 band signals it is possible to see, from Figure 36 (a, b), that 100 seconds could represent already an optimal choice. The use of longer smoothing time constants brings small advantages in term of standard deviation reduction, at the same time a bigger smoothing constant increases the time to wait for the filter to reach the steady state.

The analysis of the smoothing reduction on D-free combination relying on L5 band measurement, Figure 36 (c, d), leads in some cases to different results than L1. The standard deviation reduction, related to the used smoothing time constant, sometimes in not decreasing with the increasing of the time constants. 1000 seconds is the only smoothing constant that reduces significantly the standard deviation, but this constant adds an important constraint in term of satellite availability. In some cases the use of 300 seconds seems to be a good compromise between standard deviation reduction and time to reach steady state performance. The choice of the optimal smoothing constant is quite challenging due to the different results obtained from the autocorrelation functions analysed in the previous section.

The final part of this analysis assesses the I-free combination. The standard deviation of these CMCs is higher than the D-free one for this combination due to the use of the two code measurement 2.2.2.2. Examining the (e, f) plots in Figure 36 it is possible to see that 300 seconds as smoothing constant provides good results in term of standard deviation reduction.

As final results, the proposed smoothing constant are

- 100 seconds for L1 band SF or D-free combination, considering the results for L5 band measurement and I-free combination 300 seconds can be also proposed in order to have the same smoothing on both frequencies.
- 300 seconds for L5 band SF or D-free combination (1000 provides lower STD but impacts the system availability)
- 300 seconds for I-free combination

In case of unique smoothing constant for a flexible system, 300 seconds seems to be a reasonable choice. The use of dual constellation GBAS can partially compensate the constraints introduced by a longer smoothing constant with the increased number of visible satellites.

3.3.5 Assessment of I-Free RMS

The following analysis aims to verify the presence of some degrees of correlation between the errors on the two analysed frequency measurements. The comparison is done between the theoretical standard deviation, computed as in Eq. 3.32, and the one computed from the empirical data.

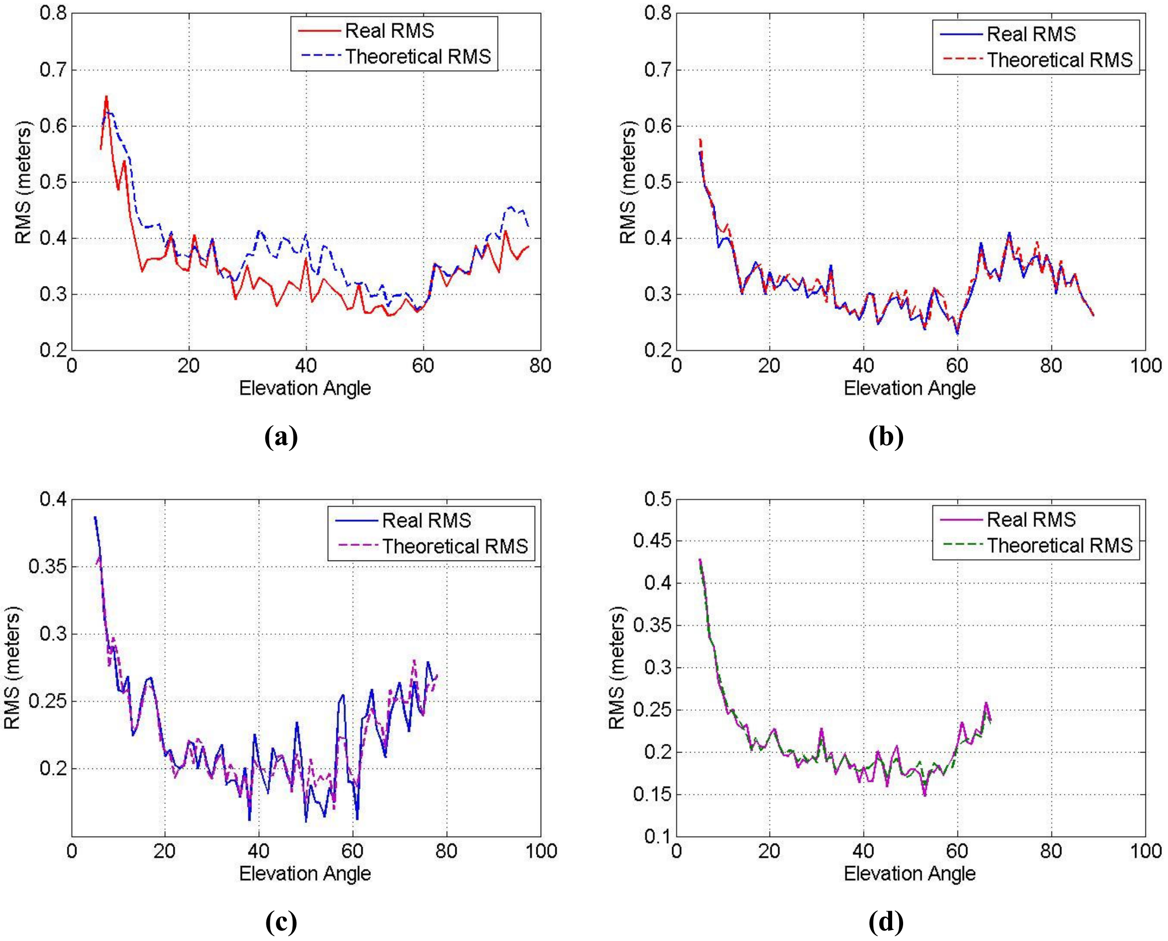

Figure 37 – Real and theoretical I-free CMCs RMS comparison on GPS for PRN 3 (a) PRN 8 (b) and Galileo PR8 (c) and PRN 26 (d)

The differences between the theoretical model and the real standard deviation, obtained from the I-free CMCs, are very small. In order to have a better analysis than in Figure 37, the standard deviation difference percentage between the two standard deviations, as in Eq. 3.33 will be computed.

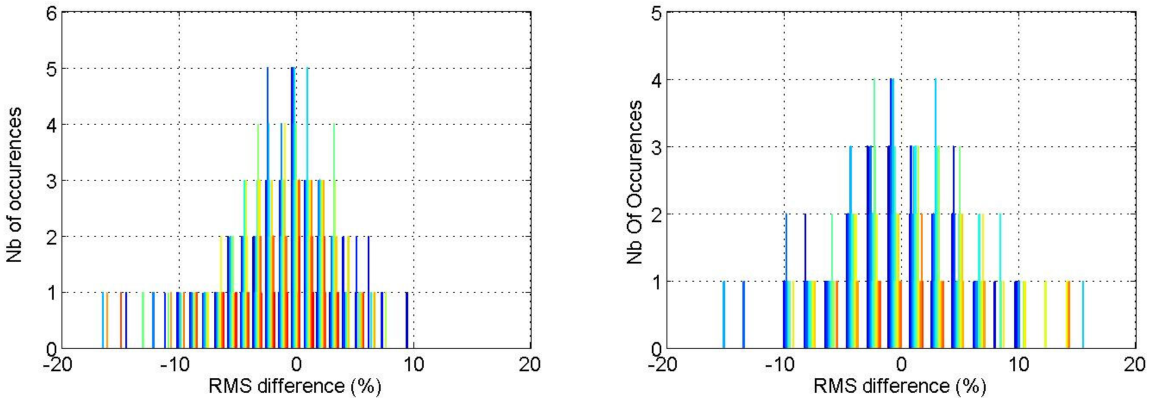

Figure 38 – RMS difference percentage distribution for GPS I-free (left) and Galileo I-free (right), each color represents a satellite

Analyzing Figure 38 it is possible to see that the differences between the theoretical and empirical RMS, are limited for almost all the cases around 10% of the theoretical value. In case of positive values the empirical I-free standard deviation is bigger than the theoretical model given in Eq. 3.31. According to those results an inflation value of the I-free standard deviation, computed from the standard deviation of L1 and L5 band measurements, may be useful to bind the empirical one. For this scope analysis, of more data are needed to derive a reliable inflation coefficient.

3.3.6 Averaged Noise and Multipath

In this section the results of averaging the CMCs of two antennas are shown. The main interest is the comparison between the standard deviation computed as in Eq. 3.34 and the one obtained from the empirical data where the error receiver correlation effects are present.

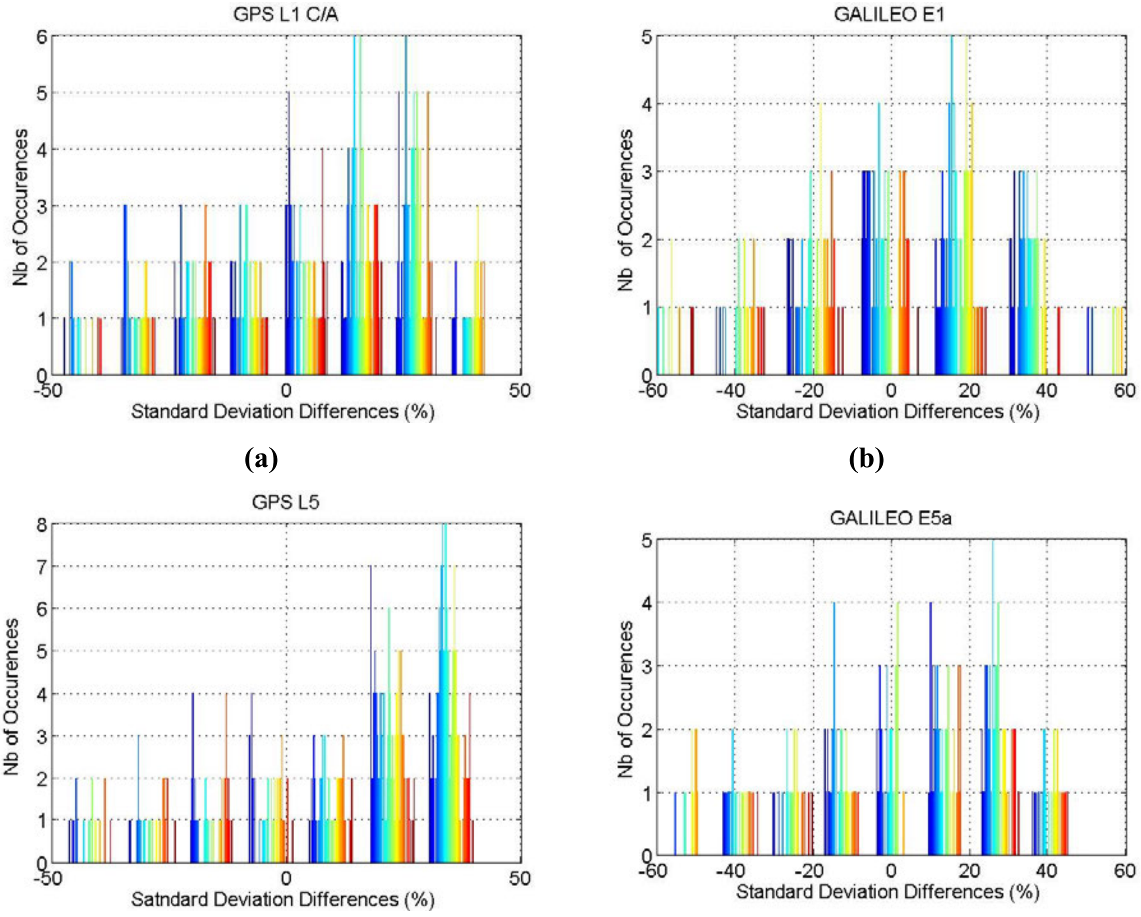

(a) **(b)**

(c) **(d)**

Figure 39 – Standard deviation comparison between empirical and theoretical value for GPS CMCs (a and c) and Galileo CMCs (b and d)

The analysis of Figure 39 shows that the real standard deviation value is quite often different than the theoretical one. This result leads to the conclusion that some degrees of, positive or negative, correlation between the noise and multipath on the CMCs from the two RRs exist.

This results impact the computation of the $\sigma_{pr\ gnd}$ in the next section.

3.3.7 Synthesis of the Results

Section 3.3 has shown the results obtained by analyzing the noise and multipath error affecting the PRC from a ground station. A lot of interest for this analysis relies on the performance of signals for which there is a lack of information:

- GPS L5
- Galileo E1
- Galileo E5a
- I-free combination for GPS and Galileo signals

The results could be synthesized by the following bullets

- The measurement on the L5 band, BPSK(10) modulation (GPS L5 and Galileo E5a), were expected to provide better performance than GPS L1 measurements that are modulated as BPSK(1). The results confirm this statement for the raw data. However, for the smoothed measurements the performance of L5 measurements are worse than the ones on L1. The cause of worse than expected performance on the L5 band measurement may also be the result of the antenna employed. The BAE ARL-1900 was developed to work only on L1 band. Other works have shown that smoothed L5 band measurements have lower standard deviation than GPS L1 C/A PRC (Circiu, et al., 2015)
- The CBOC modulation, adopted for Galileo E1, provides better performance than GPS L1 C/A, confirming what is expected by theory.
- The comparison between standard deviation and RMS has permitted to directly identify residual biases affecting the CMCs. Noise and multipath are expected to be “zero-mean” over a long period (more than one hour), and also when all satellites are analyzed together. The RMS differs from standard deviation if a bias is present. In this case a problem related to the calibration of L5 band measurement has been found. To solve this issue a calibration procedure has been followed to calibrate the CMCs.
- To compute the standard deviation reduction due to the smoothing process, noise and multipath errors on measurements are considered as decorrelated in time in literature (Hwang, et al., 1999). Relying on this property standard deviation of smoothed errors can be easily computed. The analysis of the smoothing efficiency has shown that time correlation exists and that its effect is

to make smoothing less efficient than what expected by theory. This effect especially impacts L5 band measurements for which the correlation time overcomes hundreds of seconds for certain cases. Possible causes of this correlation could be residual errors not compensated by the calibration.

- Because the results obtained in the previous section, an analysis about different smoothing time constants has been done. The results show that 100 seconds is an optimal choice for L1 band measurement since time correlation of the errors on measurement from this band is lower than 10 seconds. To obtain good performance from L5 band measurement a constant of 1000 seconds could be used, however, this impacts too much the measurement availability. A time constant of 300 seconds seems to be a good trade-off between accuracy improvement and availability of the system. For the I-free combination the same constant as for L5 could be maintained. The longer smoothing constant could be used only for dual constellation, thanks to the presence of a bigger number of satellites which will compensate for the decreased availability of the measurements during the smoothing convergence period of the smoothing filter.
- Presence of correlation between errors on the two used frequency has been observed. This condition is particularly important because it can impact the I-free standard deviation. Results show a weak inter-frequencies correlation of noise and multipath that should require to inflate the I-free standard deviation computed as in Eq. 3.31 to bound empirical results
- The last analysis has focused on the correlation of the errors between RRs. This analysis directly impacts the computation of the $\sigma_{pr\ gnd}$ standard deviation and a model similar to the GAD. In details if positive degrees of correlation exists between RRs the standard deviation estimated from the empirical data must be inflated to take it into account. From the results it is possible to note, for almost all cases, positive correlation between RRs.

3.4 $\sigma_{pr\ gnd}$ Computation

The scope in analyzing the noise and multipath affecting the ground measurement is to compute the $\sigma_{pr\ gnd}$ (2.3.3.2) and compare it with the GAD curves for which the model parameters are shown in Table 10. This analysis is useful because it permits to estimate the accuracy of the new signals and combinations. The value of $\sigma_{pr\ gnd}$ is computed, in this thesis, starting from the standard deviation obtained from the empirical data. In literature (Circiu, et al., 2015) another method has been proposed to compute the same parameter, using B values (5.2.1.6). Since this value is computed for any new GBAS ground installation it has to be computed relying on a short time window (nominally three days). Even if more than one day of data collection is available their use is sometimes misleading. For the GPS case, in fact, the CMCs show a repetition of the track for each satellite. This effect is caused by the similarity between GPS satellites revolution period and the earth's one. Each user can see a satellite in almost the same position, elevation and azimuth angle, each 24 hours.

3.4.1 Synthesis of the $\sigma_{pr\ gnd}$ Calculation Process

To compute the $\sigma_{pr\ gnd}$ starting from empirical data recorded for a limited duration the following methodology can be followed (Pervan, et al., 2005).

1. Selection of the number of days to use according to the Day-to-Day repeatability of certain error sources and according to the used constellation.
2. Inflation for statistical uncertainty due to limited number of samples
   $$\sigma_{s,m} = \delta * \sigma_m$$
   Where:
   - σ_m is the standard deviation of the PRC computed for all satellites on RR m
   - δ is an inflation factor taking into account for the statistical uncertainty, details will be given in 0
3. Inflation for correlation between receivers
   $$\sigma_{sc,m} = \beta_m * \sigma_{s,m}$$
   Where β_m is the inflation coefficient taking into account for correlation between RRs, details will be given in 3.4.4
4. Inflation for long-term variation
   $$\sigma_{sct,m} = \gamma_m * \sigma_{sc,m}$$
   Where γ_m is the inflation coefficient taking into account for long term variation (section 3.4.5)
5. Generation of the composite sigma for all ground receivers
   $$\sigma_{comp} = \sqrt{\frac{\sum_{m=1}^{M} \sigma_{sct,m}^2}{M}}$$
6. Combination of the composite sigma with the bound for ground multipath reflection
   $$\sigma_{pr\ gnd}^{I} = \sqrt{\sigma_{comp}^2 + \sigma_{MP}^2}$$
   σ_{MP} is the contribution of the ground multipath to the value of $\sigma_{pr\ gnd}$ (section 3.4.6)
7. Inflation of the $\sigma_{pr\ gnd}$ as function of the distance between the ground station and the airborne receiver
   $$\sigma_{pr\ gnd}^{II} = \sqrt{{\sigma_{pr\ gnd}^{I}}^{2} + \sigma_{Sys}^2}$$
   σ_{Sys} is defined in section 2.3.4.1, Eq. 2.64. For the current analysis the value of a_3 referred to the ionosphere are not considered due to the presence of airborne monitors.

Details about the inflations factors and about the selections of used days will be given in the next sections.

3.4.2 Day-to-Day Repeatability

In order to verify if CMCs from the same satellite are similar for consecutive days the following analysis is done.

- Creation of a vector composed by CMCs, from all satellites of the same day, for a defined elevation angle bin. It is very important to respect the satellite order for any daily vector.
- Creation of vectors composed by the reference day and one of the following days. For example

  $$\left[CMC_{(El),day1}, CMC_{(El),day2}\right]$$

  Also a vector composed by twice the replica of the CMC from the first day is created as the reference for a simulated day-to-day repetition.
- Comparison of the autocorrelation functions for all the day combinations to detect the daily correlation of the CMCs.

For the analysis of day-to-day correlation on GPS signals the 02/04/2016 has been used as reference day. The 03/04/2016-06/04/2016 and 10/04/2016 have been used as comparison days. Any vector is composed by the CMCs from all satellites with elevation angle comprised in $\pm$ 1° from the reference elevation angle.

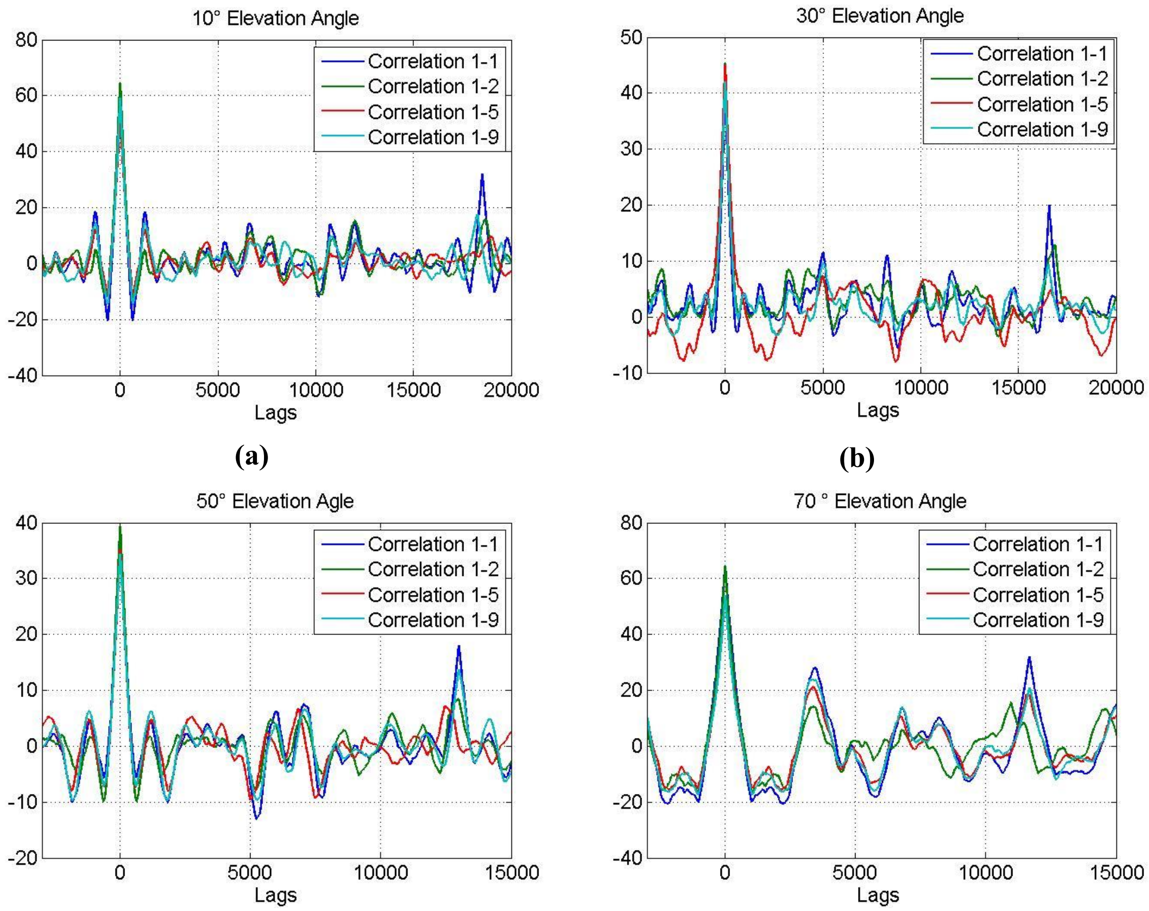

(a) **(b)**

(c) **(d)**

Figure 40 – Day-to-day autocorrelation functions for different elevation angles

Figure 40 shows the autocorrelation function for CMCs vectors comparing the first day with the other three days. The number of samples for each day are related to total number of samples that are available for all satellites in a single day. For example in Figure 40 (a) there are almost 20000 samples. The blue line in all the plots represent a simulation of perfect day-to-day correlation, a side peak is visible at the points where the simulated second day epochs CMCs starts. The other lines are compared to this line to derive the errors correlation degrees. From the analysis of Figure 40 (a, b), c, d it is possible to see that the errors show some degrees of correlation between days.

A particular case is represented by the elevation angles bigger than 80°. Due to the low number of satellites passing at this elevation the autocorrelation function is distorted and is not possible to have an analysis of day-to-day correlation. A possible solution to increase the number of samples is to create a unique bin for all elevation angles bigger than 80°.

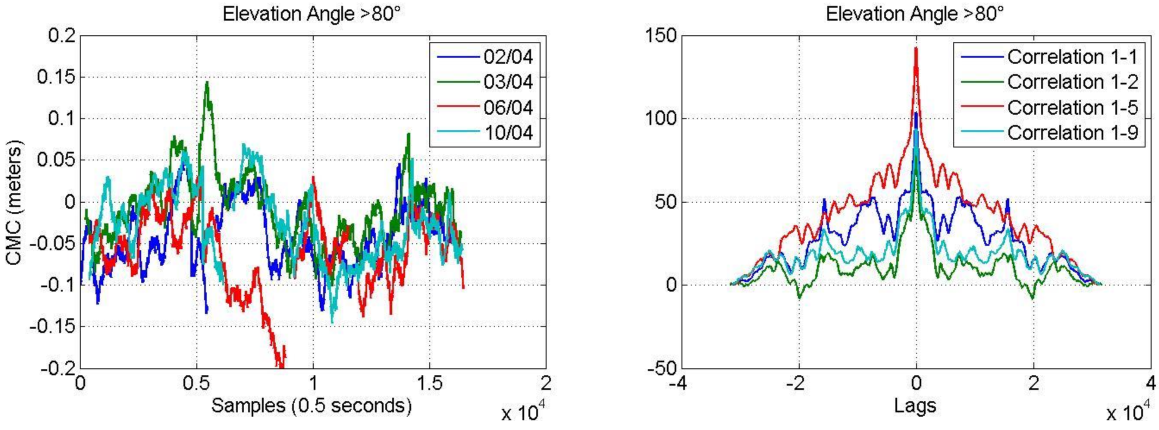

Figure 41 – CMCs and autocorrelation functions for all satellites with elevation angle bigger than 80°

Day-to-day repeatability analysis for elevation angle >80° (Figure 41 - right) does not permit to estimate correctly if a daily correlation exists. In order to obtain this information it is possible to rely on the simple CMC plot (Figure 41 - left). It is possible to see that the CMCs have the same shape across different days.

As result of this analysis, for GPS satellites case, in order to consider all possible CMCs variations (red line in Figure 41 – left) it has been decided to use all days available. However to cope with the statistical uncertainty issue the number of total samples will be divided by the number of used days.

A different case is represented by Galileo satellites. Any user can see a Galileo satellite in the same position in the sky each 10 sideral days. This condition leads to observe, each day, different satellites passing in an elevation bin. The difference is also related to the number of satellites. In Figure 42 it is possible to observe that for four consecutive days the CMCs are always different. This property is verified for ten days.

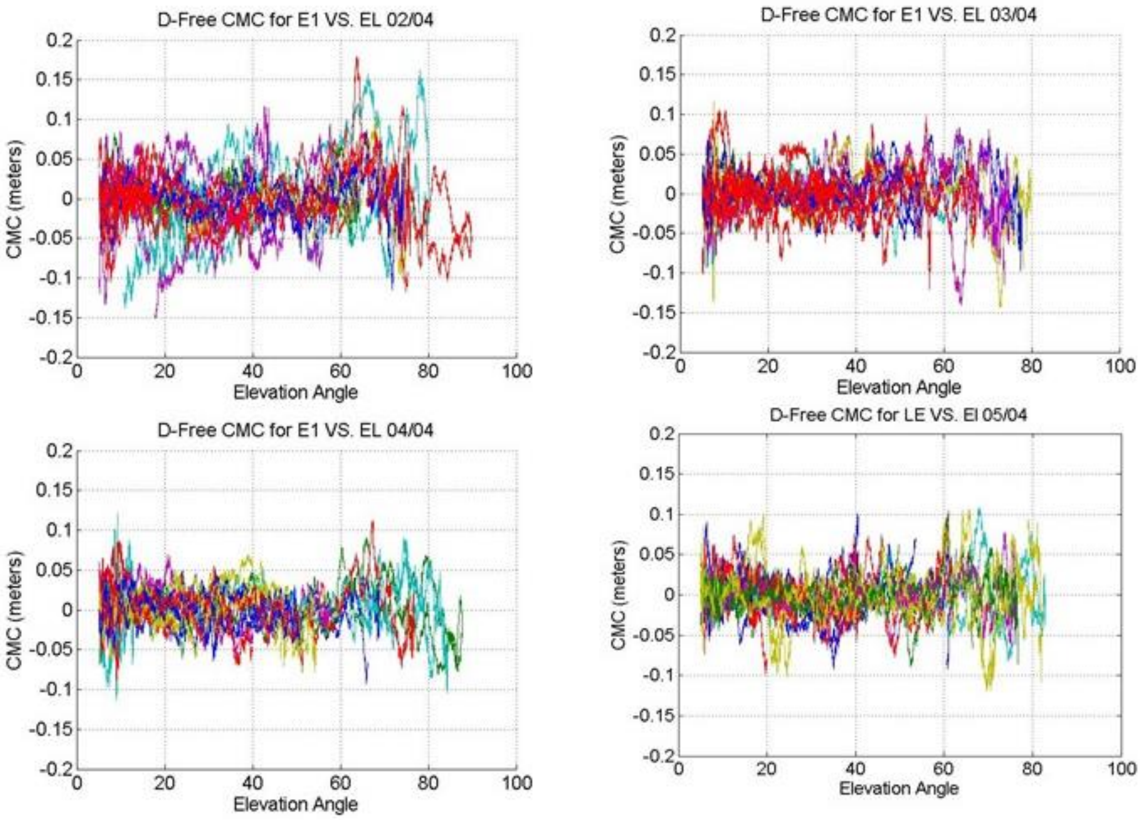

Figure 42 – Galileo CMCs for four consecutive days

Due to the difference between Galileo and GPS repetition period, it is possible to use up to ten days consecutive of Galileo CMCs for the $\sigma_{pr\,gnd}$ computation. Two intervals will be used to check the impact of the statistical uncertainty on the $\sigma_{pr\,gnd}$ derivation.

In order to analyze the impact of using one or more days to derive the $\sigma_{pr\,gnd}$ Figure 43 shows the impact for the Galileo constellation case.

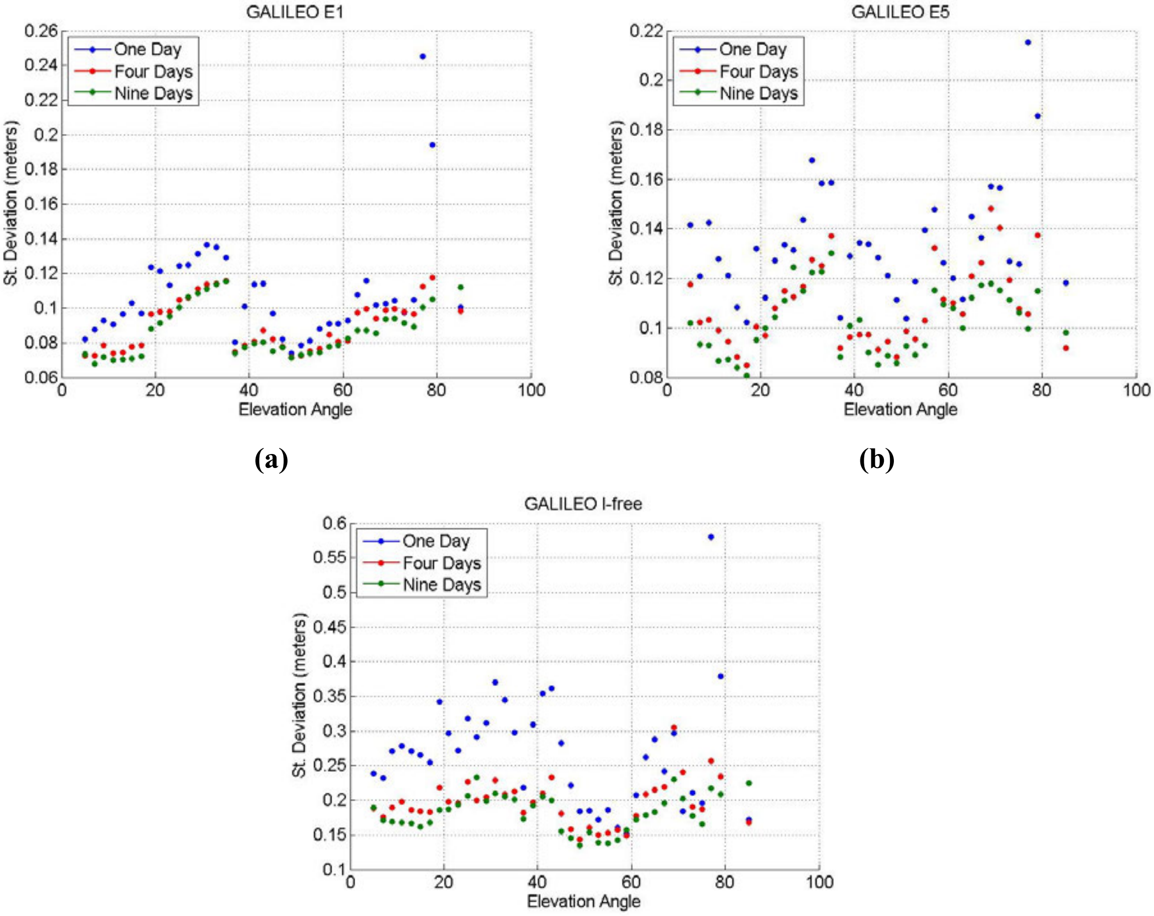

(a) **(b)**

(c)

Figure 43 – Statistical uncertainty effects on Galileo signals for one, four and nine days comparison

Results in Figure 43 show that relying on a big number of independent samples it is possible to obtain a lower standard deviation value. A low number of samples is, in fact inflated due to the statistical uncertainty as explained in the next section. This explain why the selection of the number of days to use and the bin size is quite important.

3.4.3 Statistical Uncertainty Inflation

As seen in 3.4.2, due to the day-to-day repeatability of certain error sources and due to limited time window used to estimate the $\sigma_{pr\ gnd}$, the number of samples available in each elevation angle bin will be limited, especially for the GPS case. The computed standard deviation s, from a limited number of samples, is related to the standard deviation computed from an infinite number of samples (σ) by the following relationship.

$$\Pr\left\{q_{\frac{\alpha}{2}} < \frac{ks^2}{\sigma^2} < q_{1-\frac{\alpha}{2}}\right\} = 1 - \alpha \qquad \text{Eq. 3.37}$$

Where:

- q_p is the quantile function of a chi square distribution with k degrees of freedom
- k is determined by $n-1$, with n number of samples
- $1-\alpha$ is the confidence interval

The previous equation can be rewritten as

$$\Pr\left\{\frac{ks^2}{q_{1-\frac{\alpha}{2}}} < \sigma^2 < \frac{ks^2}{q_{\frac{\alpha}{2}}}\right\} = 1-\alpha \qquad \text{Eq. 3.38}$$

Considering a confidence interval of 99.9%, Figure 44 shows the inflation factor $\delta = \sqrt{\frac{k}{q_{\frac{\alpha}{2}}}}$ that applied to s permits to estimate the upper bound of σ. δ is not dependent from the reference receiver since the same CMC length, consequentially the same number of independent samples, is used for both the RRs.

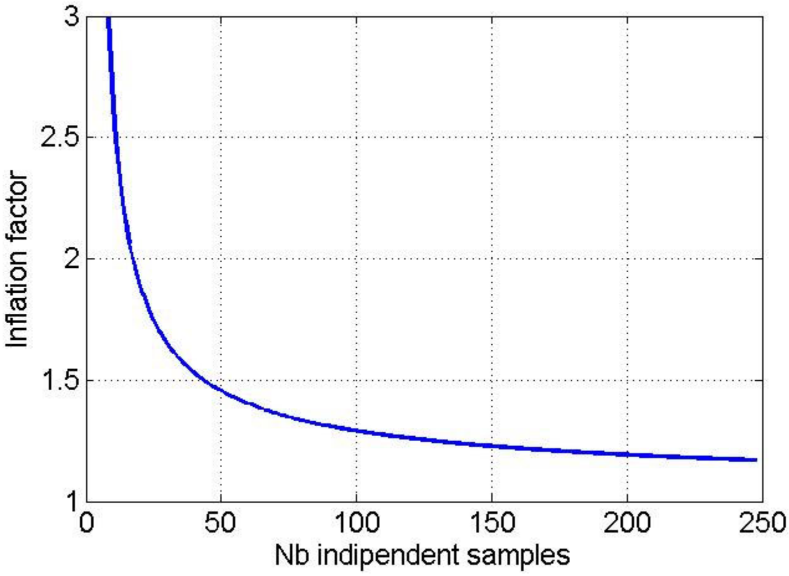

Figure 44 – Inflation factor for statistical uncertainty fir different number of samples

$$\sigma_{s,m} = \delta * \sigma_m \qquad \text{Eq. 3.39}$$

Where:

- σ_m is the standard deviation estimated from the empirical data for the m^{th} RR
- $\sigma_{s,m}$ is the standard deviation inflated to take in to account for the confidence interval due to the limited number of samples

It is clear that the choice of the bin width influences the estimation of the $\sigma_{pr\,gnd}$ since a bigger bin contains more samples. In order to estimate the optimal elevation angle bin to use three values have been analyzed:

- ± 0.5° with an elevation angle resolution of 1°
- ± 1.0° with an elevation angle resolution of 2°
- ± 2.5° with an elevation angle resolution of 5°

Knowing that the time correlation on raw GPS L1 C/A and Galileo E1 is lower than 10 seconds an independent sample is counted each 100 seconds of data. This permits to take into account the effect of 100 seconds smoothing filter on the time correlation of smoothed measurement. For L5 band measurements it is impossible to define a unique correlation value, therefore the same value obtained for L1 band measurements will be used. Moreover, it has to be reminded that a calibration issue has been found on L5 band measurement which could impact the estimation of the real correlation time.

Figure 45 shows the number of independent samples for each of the analyzed bin width for all CMCs on one day for GPS.

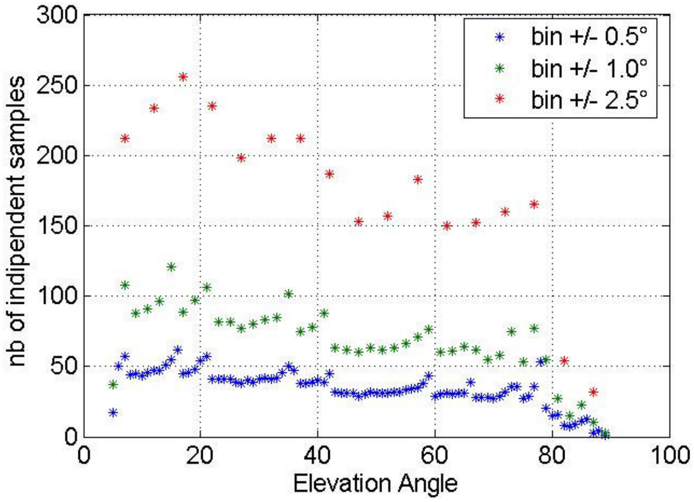

Figure 45 – Number of independent samples per bin comparison for GPS

Considering the result of Figure 45, and reminding that at the time of data collection only 12 satellites transmitting L5 band measurement were available, an elevation angle resolution of 2° will be used for GPS signals. The same analysis for Galileo case has not been done since more days will be used and more samples will be available. The same elevation angle bin as for GPS, however, will be used for Galileo.

For both constellations, to avoid a low number of samples for the elevation angles bigger than 80°, a unique bin with all the CMCs having an elevation >80° will be created.

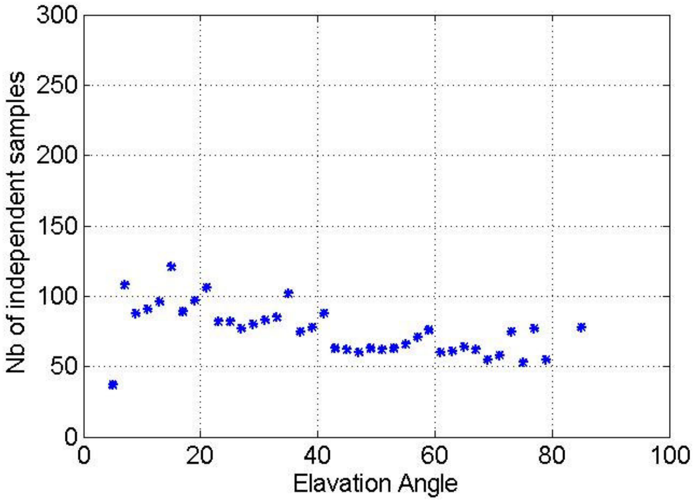

Figure 46 – Number of independent samples per bin, with unique bin for elevation >80°, for GPS

3.4.4 Error Correlation between Reference Receivers

In the computation of the VPL and LPL it is assumed that errors between ground receivers are uncorrelated. The value of $\sigma^2_{pr\ gnd}$ is in fact divided by the number of RRs present at ground. In reality it is possible, and it has been seen in 3.3.6, that some correlation between receivers exists, and even if small they have to be taken into account. To accommodate with the effect of errors correlation between receivers the value of the estimated empirical sigma must be inflated by a factor β.

$$\sigma_{sc,m} = \beta_m \cdot \sigma_{s,m} \qquad \text{Eq. 3.40}$$

Where:

- $\sigma_{sc,m}$ is the standard deviation taking into account also for RRs correlation
- β_m is the correlation coefficient

The value of β can be computed starting from the Pearson's correlation coefficient r using the Fischer transformation (Pervan, et al., 2005).

$$z = \ln\left(\frac{1+r}{1-r}\right) \qquad \text{Eq. 3.41}$$

If the errors on the two RRs follow a bivariate normal distribution z is assumed to follow a normal distribution (Pervan, et al., 2005).

$$z \sim N\left[\frac{1}{2}\ln\left(\frac{1+z}{1-z}\right), \frac{1}{\sqrt{n-3}}\right] \qquad \text{Eq. 3.42}$$

Where:

- n is the number of independent samples used to derive r

It is possible to compute z', corresponding to the 99.9% confidence interval point for the previous distribution. Using the cumulative distribution function (CDF) it is possible to find z'

$$z' = cdf\big(CI, \mu(z), \sigma(z)\big) \qquad \text{Eq. 3.43}$$

Obtained z' it is possible to compute ρ as:

$$\rho = \frac{\exp(2z') - 1}{\exp(2z') + 1} \qquad \text{Eq. 3.44}$$

The value of the coefficient β can be now computed for all the combinations of receiver pairs

$$\beta_m = \begin{cases} \sqrt{1 + \sum_{\substack{i=1 \\ i \neq m}}^{M} \rho_{mi}} & if\ \rho \geq 0 \\ 1 & if\ \rho < 0 \end{cases} \qquad \text{Eq. 3.45}$$

In the next figure some values of ρ are shown as function of n and r.

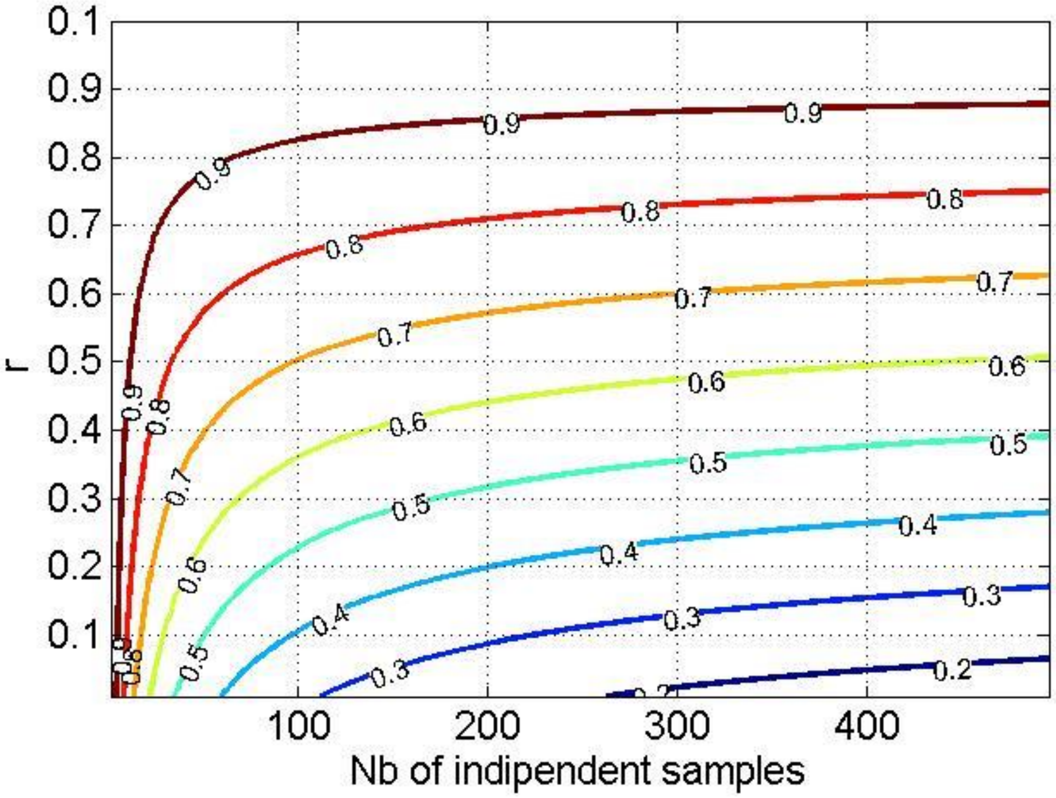

Figure 47 – ρ coefficients as function of n and r

3.4.5 Long Term Error Variation (Seasonal Effects)

A last effect related to the short duration of the data collection is the lack of information on long term variation, also defined as seasonal variation (Pervan, et al., 2005). To take into account for this kind of effect an inflation coefficient must be computed. Due to the lack of information about these variations a value of 1.14 is used as in (Pervan, et al., 2005).

$$\sigma_{sct,m} = \gamma_m * \sigma_{sc,m} \tag{Eq. 3.46}$$

Where $\sigma_{sct,m}$ takes into account the effect of seasonal variation plus the RRs correlation and the statistical uncertainty already considered in $\sigma_{sc,m}$

3.4.6 Ground multipath model

The ground-reflection multipath is a slow varying phenomenon that is hard to estimate with short time data analysis. In (Pervan, et al., 2005) is shown that this kind of error can be overbound by a zero mean Gaussian distribution with standard deviation as:

$$\sigma_{MP} \geq 1.05\left(\frac{D}{U}\right)\min[2h\sin(El)\,, d] \tag{Eq. 3.47}$$

Where:

- $\frac{D}{U}$ is the amplitude of the reflected signal relative to the direct
- h is the antenna height, a value of 2.5 meters has been selected for the computation of the $\sigma_{pr\ gnd}$
- d is half of the correlator spacing in meters

3.4.7 $\sigma_{pr\ gnd}$ Results

The main difference between Galileo and GPS constellation is the possibility to use more than one day, for Galileo case, for the computation of the $\sigma_{pr\ gnd}$ in order to have more independent samples. However, to compute the $\sigma_{pr\ gnd}$ for GPS case all days will be used and the number of independent samples will be divided by the number of used days. For Galileo, $\sigma_{pr\ gnd}$ will be computed relying on all available days as well, without dividing the number of independent samples.

In Figure 48 the $\sigma_{pr\ gnd}$ for GPS and Galileo CMC, smoothed with a 100 seconds filter, are shown

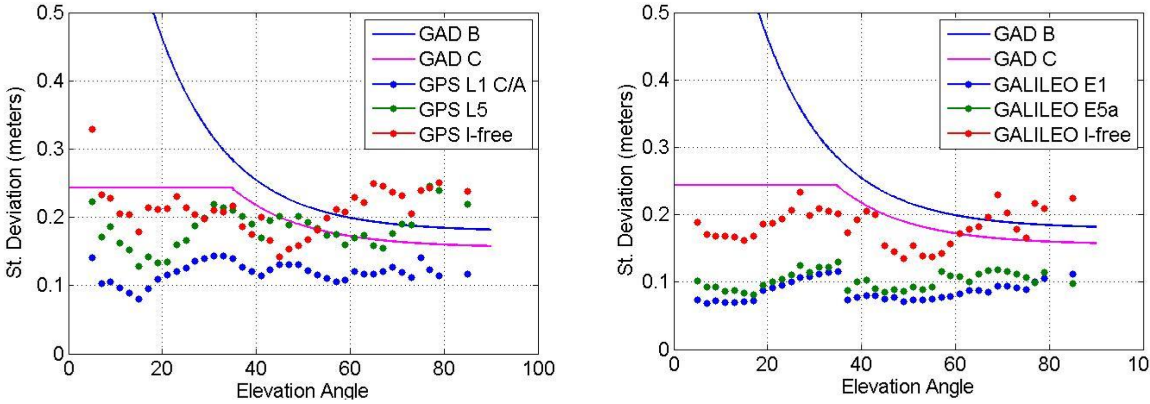

(a) **(b)**

Figure 48 – $\sigma_{pr\ gnd}$ values for GPS and Galileo signals for 100 seconds smoothed case

It is possible to see from Figure 48 that the $\sigma_{pr\ gnd}$ for GPS L1 and Galileo E1 is well below the GAD-C model for single RR. The results on the L5 band, for both constellations, are worse than L1 band ones. The possible cause is the calibration issue joint to the antenna non-optimization for multipath rejection on this band. For both frequencies Galileo provided better results than GPS. The I-Free case in the only case where GPS has better performance than Galileo

In Figure 49 results for 30 seconds smoothed CMC are shown. This time constant is used in GAST-D to improve detection of ionospheric errors. In literature no $\sigma_{pr\ gnd}$ values are provided for this case.

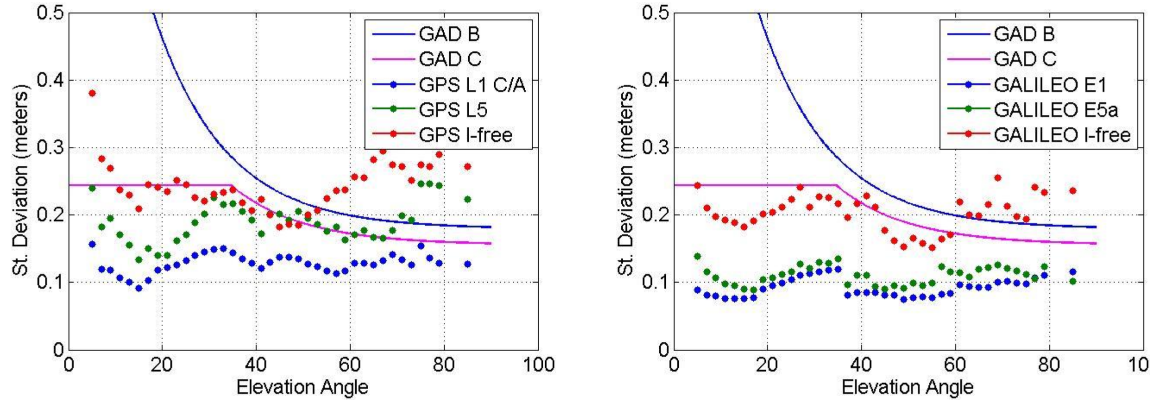

(a) **(b)**

Figure 49 – $\sigma_{pr\ gnd}$ values for GPS and Galileo signals for 30 seconds smoothed case

On all signals in Figure 49 it is possible to note a small increasing of the standard deviation compared with the one in Figure 48. Values of $\sigma_{pr\ gnd}$ for 30 seconds smoothed CMC show results very close to the one obtained for the 100 seconds smoothed case. Reminding that in theory the smoothing reduction is $\sqrt{\frac{T}{2\tau}}$, the values of 30 seconds smoothed CMC, compared to the 100 seconds ones, has to be $\frac{\sigma_{30}}{\sigma_{100}} =$

$\sqrt{\frac{200}{30}} = 1.8257$. Considering the time correlation of noise and multipath impacting the smoothing efficiency, as seen in 3.3.4, the previous values are not reached.

According to the results obtained in 3.3.4.1, an optimal choice for the smoothing constant can be the use of 300 seconds. Figure 50 shows the values of $\sigma_{pr\ gnd}$ for this time constant.

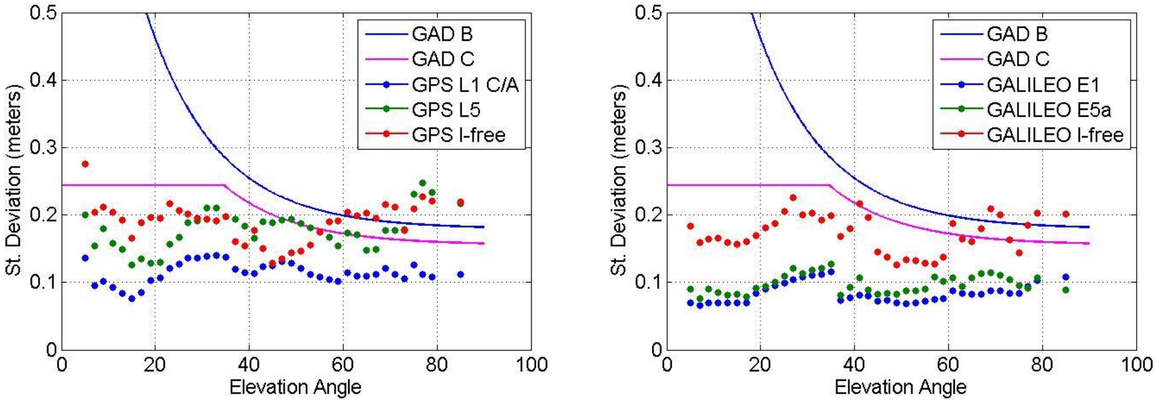

(a) **(b)**

Figure 50 – $\sigma_{pr\ gnd}$ values for GPS and Galileo signals for 300 seconds smoothed case

Results given in Figure 50 show how the use of a bigger smoothing constant brings benefits especially for L5 band measurement and for the I-free combination. The values of the $\sigma_{pr\ gnd}$, for all signals, are smaller than the one obtained for the 100 seconds case (Figure 48).

As final result of this analysis it is possible to propose values to bind the $\sigma_{pr\ gnd}$ and that can be used in simulation to estimate GBAS performances.

Table 13 – $\sigma_{pr\ gnd}$ bound values for all analyzed signals for GPS and Galileo

	Smoothing Constant		
	100 seconds	**30 seconds**	**300 seconds**
GPS L1 C/A	$0.15\ m$	$0.16\ m$	$0.14\ m$
Galileo E1	$0.12\ m$	$0.12\ m$	$0.12\ m$
GPS L5	$0.24\ m$	$0.26\ m$	$0.24\ m$
Galileo E5a	$0.13\ m$	$0.14\ m$	$0.13\ m$
GPS I-free	$0.26\ m$	$0.3\ m$	$0.24\ m$
Galileo I-free	$0.24\ m$	$0.26\ m$	$0.23\ m$

Values given in Table 13 can be used to perform simulations for integrity monitoring or protection level computation for GAST-D or GAST-F as well. It is good to remind that the main difference between GPS and Galileo $\sigma_{pr\ gnd}$ is provided by the statistical uncertainty inflation, bigger coefficient for GPS case. For Pattonville data collection has not been possible to compute the $\sigma_{pr\ gnd}$ due the presence of only one receiver, by the way considering the results are shown in appendix C it is expected to have similar values as for Toulouse data collection.

3.5 Conclusions

The aim of this chapter was to derive the impact of the errors affecting the PRC, in the specific noise and multipath. To derive information about these two errors the CMC has been used. The analysed signals are GPS L1 and L5 and Galileo E1 and E5a. Furthermore the I-free combination for both constellations has been analysed as well.

Some results have been already introduced in section 3.3.7, however it is good to remind the main outcomes:

- Bae ARL-1900 antenna used for both data collection, Pattonville and Toulouse Blagnac, is founded to be not adapted to work on L5 band. In particular a calibration issue has been identified, section 3.3.3, for which a CMC calibration process has been adopted to remove the biases from the data. After the removal of the calibration error the antenna provides worst performances for L5 band signals, GPS L5 and Galileo E5a, compared to GPS L1 or Galileo E1. This result is the opposite of the performances expected by theory.

- The noise and multipath inter-frequency correlation on L1 and L5 band measurement has been investigated. Results in 3.3.5 show that small positive and negative values of correlation exist between the two frequencies. Due to the variety of results, it was not possible to derive a unique value for this correlation. In some cases, the impact of negative correlation has led to values of I-free standard deviation higher than the one computed using the theoretical model in which the correlation is not considered. According to this results, the I-free standard deviation has to be inflated to bind possible negative correlation values.
- Having two reference receiver at ground, only for Toulouse data collection, the noise and multipath correlation between RRs has been investigated as well. As for the inter-frequencies correlation case, the results variety does not permit to estimate a unique value. However, the results are useful for the computation of the $\sigma_{pr\ gnd}$ model where correlation has to be considered.
- The last analysis aimed to derive the $\sigma_{pr\ gnd}$ and to compare it with the GAD curves. It is helpful to remind that this value differs from the standard deviation computed in section 3.3.2 because it is inflated to take into account different effects (3.4.1). The results show that the accuracy of the PRC for L1 band measurement is well below the most accurate GAD model (GAD-C). The use of a shorter (30 seconds) or a longer (300 seconds) smoothing constant does not bring relevant changes.
- For L5 band measurement, due to the antenna used, results are worse than for L1 band and are not bound by the same curve for GPS case. The use of 30 seconds smoothing constant does not bring any relevant change. The use of 300 seconds improves the performances for this band permitting to reach almost the same results as for L1 band measurement for Galileo signal and improving a lot for GPS one.
- The results for I-Free combination show that a dedicated bound must be derived for this combination. Being noisier than the SF combinations, the use of a big smoothing constant is the choice who lead to the better results. The issue found on L5 band measurement impacts the I-free combinations as well.

4 Satellite Selection

4.1 Motivations and Objectives

The use of two or more GNSS constellations and two frequencies in GAST-F produces several benefits, in terms of accuracy, integrity monitoring and system continuity. Despite the advantages in obtaining a larger number of measurements, there is at least one possible problem to cope with: the limited number of channels present in a GNSS receiver. The use of single frequency single constellation GBAS implies the tracking of up to 10-12 satellites. Considering the presence of a second constellation, this number can be doubled. It can be seen in the remainder of the chapter that 22 satellites may be visible at the same time, under defined circumstances, and this number must be also doubled if a second frequency is used. It is clear that any receiver, to work in dual constellation and dual frequency, need more than 44 channels to be sure that all satellites in view are tracked.

The problem of the number of visible satellites is, however, not only related to the number of channels in a receiver. In GBAS, another issue is represented by the maximum number of corrections that could be broadcasted through the VDB link. The correction message, as currently structured in GBAS GAST D, limits the number of corrections to 18. Considering the optimization of the message occupation, this number may increase to 27 (SESAR 15.3.7; WP3), which is considered as sufficient for GAST D. Considering the development of GAST F that uses a processing mode different from GAST D, and in order to maintain interoperability between the two GBAS services, the ground station must broadcast corrections for both GAST-D and F. Under these circumstances, the limit stated before must be split almost by two, even if, considering the redundancy of certain information present in the correction message, some space could be saved. Considering a possible limit of 15 corrections, there is a need to have a satellite selection algorithm in order to avoid accuracy problem when all satellites in view cannot be used.

Over the years, many methods were proposed to select a satellite subset instead of using all satellites in view in order to solve problems cited before. The choice of a satellite subset was focused on the search of the best subset in order to preserve the accuracy. The main parameter on which the search was focused on, was the DOP, also VDOP and HDOP, because it is the only index relating the accuracy to the constellation geometry.

4.2 Satellite Selection Methods

The algorithms presented in the next section were developed for the case of a subset having no more than four or five satellites. Their use to search a subset composed by a bigger number leads to an increase of the computational load in some cases, or to a non-optimal subset choice.

4.2.1 Optimal Solution

One of the main selection algorithms proposed in the past, is the optimal solution (Liu, et al., 2009). This algorithm computes the best value of GDOP trying all the possible satellite subset at the cost of a great computational load with the growth of the number of satellites in view. For example with 18 visible satellites and the search for a 12-satellite subset, the algorithm has to compute 18564 different GDOP values, the total amount being given by the following formula:

$$C_{12}^{18} = \frac{18!}{12!\,(18-12)!} = 18564$$

Using a 20-satellite subset out of 40 visible, the number increases to $1.38 \cdot 10^{11}$. It can thus be understood that this method works properly only for single constellation, when a low number of satellites is in view and a small satellite subset is searched for. Note that it is possible to use the same type of algorithm to optimize other DOP values, such as PDOP, HDOP or VDOP; also the protection level can be used as the optimization criterion.

4.2.2 Modified Minimum GDOP

An alternative method is the Modified Minimum GDOP. In this algorithm the first chosen satellite of the subset is the one with the highest elevation angle and the other satellites are searched as in the "optimal solution" case (Cryan, et al., 1992). This method reduces the computational burden in comparison with the "optimal solution" but the number of all possible combinations to be analysed can be still prohibitively large. Using the same example used for the optimal solution, 18 satellites available and a 12 satellites subset, and choosing the first as the one with the higher elevation angle the total amount of possible combination to be considered is 12376 and is given by:

$$C_{11}^{17} = \frac{17!}{11!(17-11)!} = 12376$$

It can be seen that the number of combinations to be analyzed is still very large.

4.2.3 Lear's Simple Satellite Selection

This technique, shown in (Cryan, et al., 1992), follows a defined procedure to choose the first three satellites and the last one is chosen minimizing the DOP value. The procedure works in the following manner:

- The first satellite is chosen finding the one with the highest elevation angle.
- The second is the one having an angle between the LOS (Line Of Sight) of the selected satellite and the LOS of the first satellite as close as possible to 90°.
- The third satellite chosen is the one that has the LOS perpendicular to the plane formed by the two previous satellites chosen.

- The last satellite is chosen to minimize the GDOP (Cryan, et al., 1992).

This technique has almost no computational load compared to the two previous methodologies. The main drawback of this method is that it was developed only for a four satellites subset and this is not enough for GBAS, even for single constellation and single frequency GBAS.

4.2.4 Fast Satellite Selection Algorithm

The main problem of the previous techniques is that they were developed to work better, in some cases to work only, with a 4 satellite subset and a limited number of satellites in view. When a larger number of satellites in the subset is searched, and there are a lot of satellites in view, the computational burden increases rapidly. Considering the scope of this analysis and the development of dual constellation dual frequency GBAS service, the number of satellites for the subset can be larger than ten. In order to overcome the problem of finding a subset with more than ten satellites without increasing too much the computational load, new algorithms were developed and are presented in the following.

The algorithm proposed in (Zhang, et al., 2008) is a good solution to the problem related with a subset bigger than 4 satellites. In this technique, a preliminary study with a simulated constellation was used to find the subset geometry with the best GDOP value starting from 4 and up to 15 satellites. From the result analysis, it is possible to see how the best GDOP varies according to the number of satellites selected at the zenith or near ($> 80°$) it and selecting the remaining according to their azimuth in order to have a homogenous distribution.

Table 14 – GDOP values for different number of satellite at high elevation for a simulated study *(Zhang, et al., 2008)*

		NUMBER OF SV AT THE ZENITH						
		1	2	3	4	5	6	7
SATELLITE SUBSET	4	3.3528						
	5	2.8169	2.7482					
	6	2.4953	2.2123	2.5466				
	7	2.281	1.8907	2.0108	2.4459			
	8	2.1279	1.6764	1.6892	1.91	2.3854		
	9	2.013	1.5233	1.4749	1.5884	1.8495	2.3451	
	10	1.9237	1.4084	1.3217	1.3741	1.528	1.8092	2.3163
	11	1.8523	1.3191	1.2069	1.221	1.3136	1.4877	1.7804
	12	1.7938	1.2477	1.1176	1.1061	1.1605	1.2733	1.4589
	13	1.7451	1.1892	1.0461	1.0168	1.0457	1.1202	1.2445
	14	1.7039	1.1405	0.9877	0.9454	0.9564	1.0054	1.0914
	15	1.6685	1.0993	0.939	0.8869	0.8849	0.9161	0.9766
	16	1.6379	1.0639	0.8977	0.8382	0.8265	0.8446	0.8873

The values of the GDOP shown in Table 14 are computed for a simulated constellation placing satellites at high elevation angle and the remaining equally spaced at low elevation angle. This study permits to establish how many satellites must be selected between the ones with the higher elevation angle before selecting the remaining ones following a defined algorithm.

The algorithm works in 4 steps:

1. Computation of the elevation and azimuth angle of all visible satellites.
2. According to the number of satellites of the subset, n, the number of satellites with the highest elevation angle is selected. Defined *p=number of satellite at zenith*; to find the *p* satellites with the highest elevation.
3. To divide the sky in $K = n - p$ equally-spaced in azimuth portions and group the satellites in each portions. It is possible to start the sky division from one particular direction or to select one satellite as reference and start from its azimuth. The satellite with the lowest elevation angle must be found and noted as S_{p+1}, it can be removed or used as reference for the group subdivision.
4. The fourth step is to combine one satellite from each k^{th} group with the others chosen in the second step. If there are more satellites in one or more groups, a GDOP computation for each

possible subset has to be done, the satellites that belong to the subset with minimum GDOP are selected for the solution computation. The total number of subset is:

$$T = C_1 \times C_2 \times \ldots \times C_{n-p} \qquad \text{Eq. 4.1}$$

Where:

- C_k is the number of satellites in the k^{th} group.

In Figure 51 an example of sky plot subdivision with high elevation angle satellites noted in green and the remaining satellites sort in groups. The satellite with the lowest elevation angle is coloured in red, it can be removed from the subsets or used as starting point of the groups subdivision.

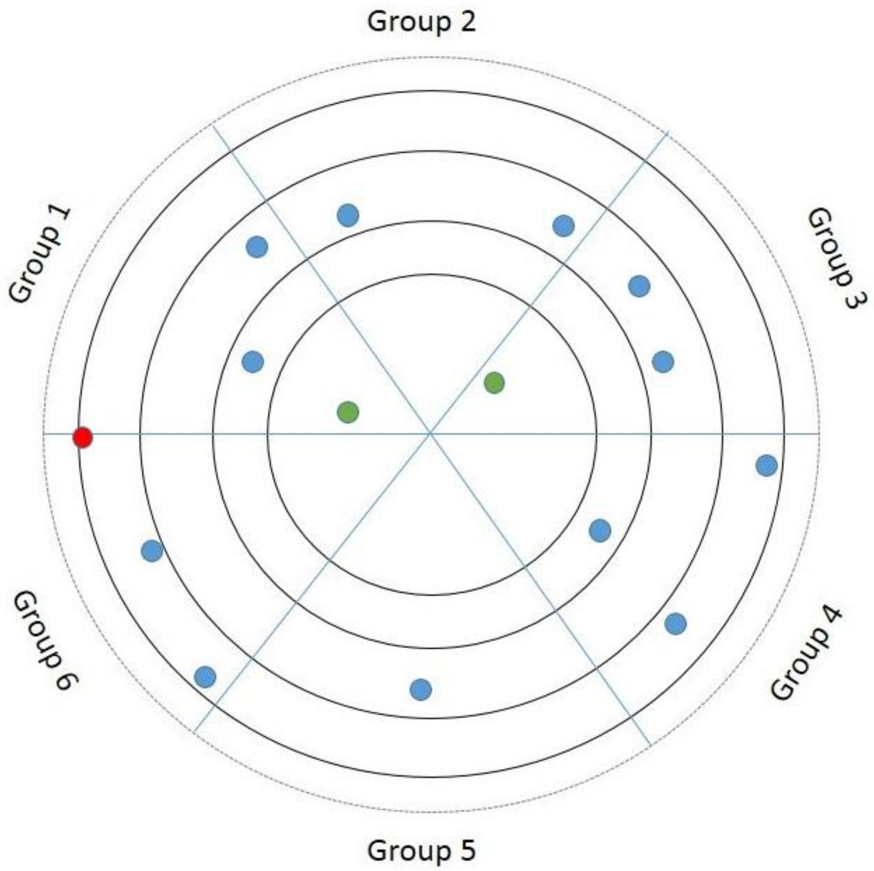

Figure 51 – Fast satellite selection sky subdivision example (Zhang, et al., 2008)

4.3 Selected Methods for Simulation

Considering the methods found in literature and the conditions of DF/DC GBAS, all methods developed to work properly for searching four or five satellites presented in section 4.2.1, 4.2.2 and 4.2.3 are not considered due to the high computational burden. However, the Optimal Solution method will be used to find the real best DOP value or protection level and to compare it with the other selection methods. The computational load of the optimal solution will be considered as well to compare it with the ones of other analyzed methods. The selection algorithm proposed in 4.2.4 is used to find the best subset due to its ability to find it without increasing too much the computational load. A last methods, even if is not a satellite selection algorithm is the selection of the n satellites with the highest elevation angle.

To summarize the selection algorithms or methods used for simulation are:

- Fast Satellite Selection; In order to make the algorithm faster, instead of computing the DOP for each combination, the satellite with the lower elevation angle will be systematically selected in each bin along with the satellites with high elevation angle.
- Maximum Elevation Angle; even if this is not an algorithm and it has not been presented before it will be used for its simplicity. The advantage of this method is to completely cancel the computational load. In this case, only the n highest elevation satellites are kept. The choice of the higher elevation satellites is determined by the analysis of the GAD and AAD model and as well as by the impact of the ionospheric delay and multipath on low elevation satellites. Analysing the GAD and AAD model, it is possible to see that the standard deviation of the residual errors is smaller for the satellite with higher elevation angle. The residual uncertainty of the tropospheric and ionospheric delay also shows a relationship between elevation angle and standard deviation values: the higher the elevation, the lower the standard deviation.
- Brute Force VPL (Optimal Solution); this is a modification of the optimal solution, where the optimization criteria is the VPL instead of the DOPs value. In the algorithm, a control also of the S_{vert} and S_{vert2} is done to be sure to find the lowest and valid protection level.

All the algorithms will be compared with the all-in-view condition to analyse also the accuracy loss or the protection level loss.

4.4 Simulations Baseline

In order to evaluate the impact in using a satellites subset instead of the whole set of satellites in view, a series of parameters have been computed across 18 airports for a simulated period of 10 days with 60 seconds resolution.

4.4.1 Airports Coordinates

The airports location used for the simulations are:

Table 15 – Airports coordinates used in simulation

Airport	**Latitude (°)**	**Longitude (°)**
Memphis	35.0424	-89.9767
Denver	39.8584	-104.667
Dallas	32.8964	-97.0376
Newark	40.6925	-74.1687
Washington	38.9445	-77.4558
Los Angeles	33.9425	-118.4081
Orlando	28.4289	-81.3160
Minneapolis	44.8805	-93.2169
Chicago	41.9796	-87.9045
Tacoma	47.1377	-122.4765
Anchorage	61.2167	-149.90
Bremen	53.0429	8.7808
Malaga	36.68	4.5124
Sydney	-33.9636	151.1859
Amsterdam	52.30907	4.763385
Rio	-22.8088	-43.2436
Peking	40.080109	116.584503
Johannesburg	-26.139099	28.246000

4.4.2 DOP Analysis and Computational Load

The concept of DOP has been already presented in 0. For this analysis the VDOP and HDOP of the satellite subsets and of the all-in-view situation will be analyzed.

$$H = (G^T \cdot G)^{-1} \qquad \text{Eq. 4.2}$$

$$VDOP = H_{3,3}; \;\; HDOP = \sqrt{H_{1,1}^2 + H_{2,2}^2} \qquad \text{Eq. 4.3}$$

A second type of parameter that helps to understand the computational load of each selection algorithm is the time spent to find the selected subset. The aim in analysing this parameters is just to have an index of the computational load of each method, it is however not representative of a real time implementation in an aircraft embedded subsystem.

4.4.3 Protection Level Computation

The previous parameters are not dependent on the simulated processing mode but only on the subset's satellite number. To take into account the possibility to use different processing modes, two subsections are present: GAST D and the I-Free processing mode. The parameters analyzed for each one are the Vertical Protection Level (VPL) and the Lateral Protection Level (LPL) computed as in (RTCA Inc.; DO253-C, 2008):

$$VPL = \max\{VPL_{H0}; VPL_{H1}\} \qquad \text{Eq. 4.4}$$

$$LPL = \max\{HPL_{H0}; LPL_{H1}\} \qquad \text{Eq. 4.5}$$

Details about the VPL and LPL are given in 2.3.3.2

Values of $\sigma_{pr\ gnd}$ are used according to results obtained in section 3.4

4.4.4 Geometry Screening Availability

The values of S_{vert} and S_{vert2} are also analyzed in order to simulate the impact of the subset on the geometry screening monitor 5.1.2. Details about S_{vert} are given in 2.3.3.2.

$$\max\{S_{vert}\} = \max_{\mathrm{i}}\{S_{3,i} + S_{1,i}\, tg(GPA)\} \qquad \text{Eq. 4.6}$$

S_{vert2} is the sum of the two biggest S_{vert}. The two parameters have to not exceed a limit dependent on the number of constellations used. The limit for a single constellation GBAS service is respectively 4 and 6. Considering the use of dual constellation in the simulations, they can be adapted to 2 and 3.

4.5 Simulation Results

4.5.1 Dual Constellation 12 Satellite subset

In this simulation, a dual constellation composed by the optimal 24 GPS and the optimal 24 Galileo constellations is simulated because these two constellations represent the baseline for the GAST-F service. The next figure shows the number of visible satellites across all the epochs and airports.

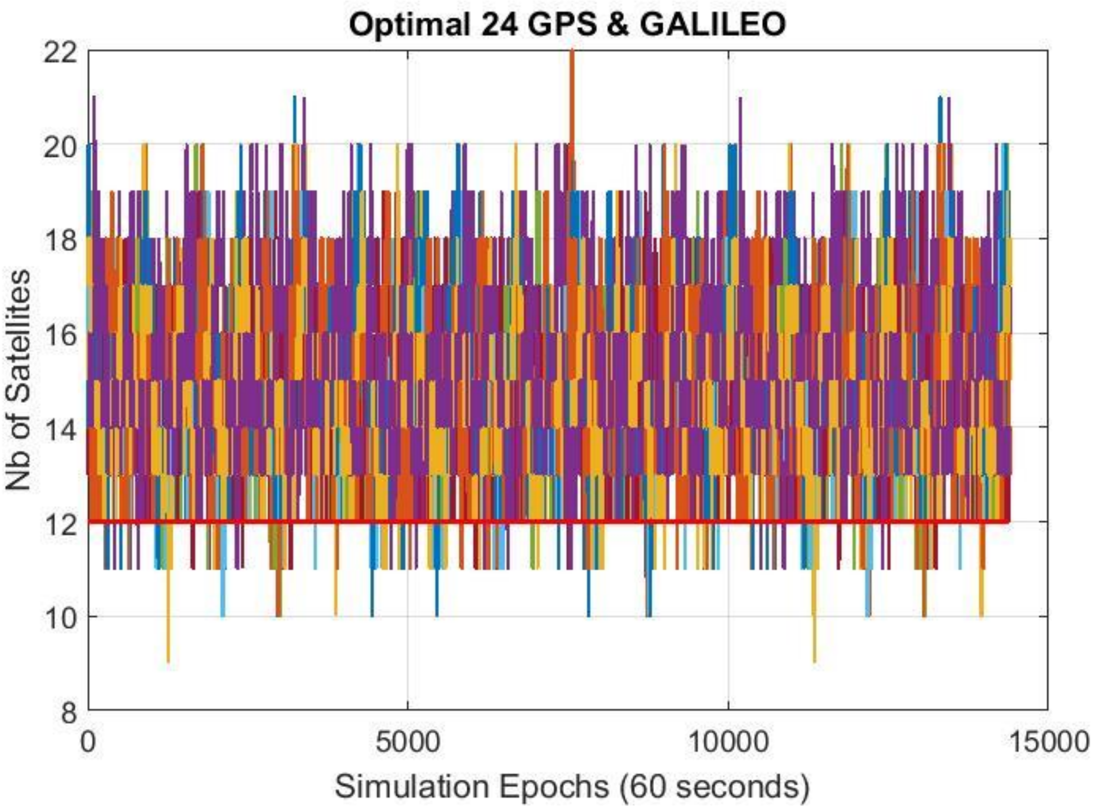

Figure 52 – Number of Satellites for all the simulated epochs and airports and 12 satellites subset in red

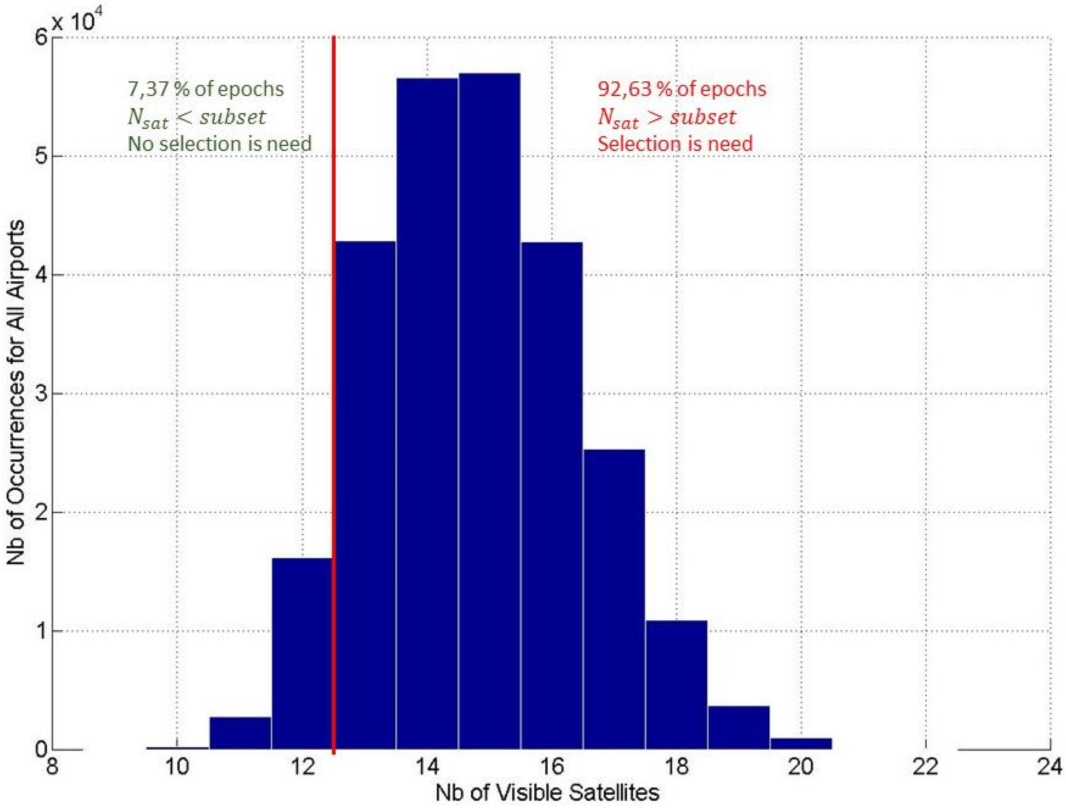

Figure 53 – Histogram of satellites number across all airports and epochs with percentage of use of satellite selection for subset 12

It is possible to see in the previous figures that for more than 92% of epochs, there are more satellites than the subset limit across all airport. Under this condition, the parameters computed for the all-in-view case and the ones computed using only a subset may be quite different. The computational load, due to a difference of 10 satellites in rare case between satellites in view and subset, is expected to be very high.

4.5.1.1 Impact of the Selection Method on the DOP Value

The values of the DOP, in the vertical and horizontal domain, provide a feedback about the accuracy that the all-in-view and the three selection algorithms are able to provide according to the number of satellite and their geometry in the sky. In Figure 54 and Figure 55 the values of VDOP and HDOP are shown.

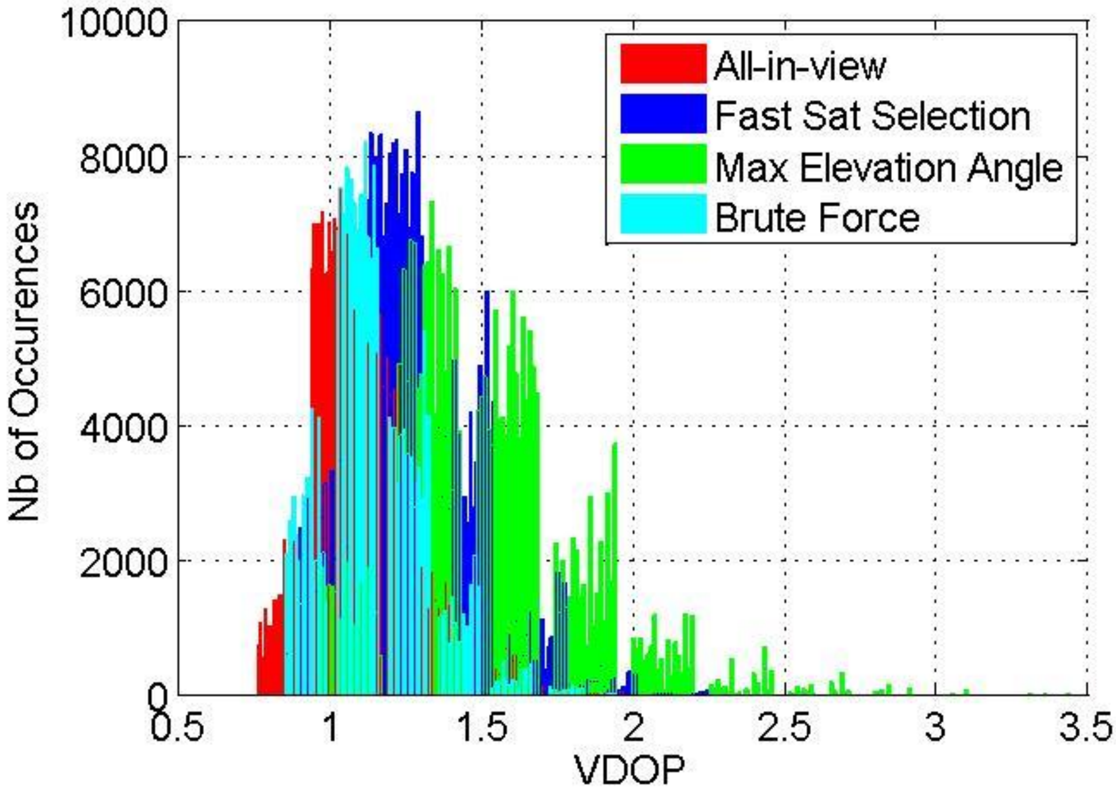

Figure 54 – VDOP values across all epochs and airports for all the methods and for all-in-view satellites

Table 16 – VDOP percentile at 95, 99 and 99.9 % for 12 satellites subset

	95 % VDOP	99 % VDOP	99.9% VDOP
All-in-view	1.4115	1.6099	1.9041
Fast Satellite Selection	1.6208	1.8551	2.1710
Maximum Elevation Angle	2.0411	2.4575	3.0718
Brute Force	1.4236	1.6180	1.9103

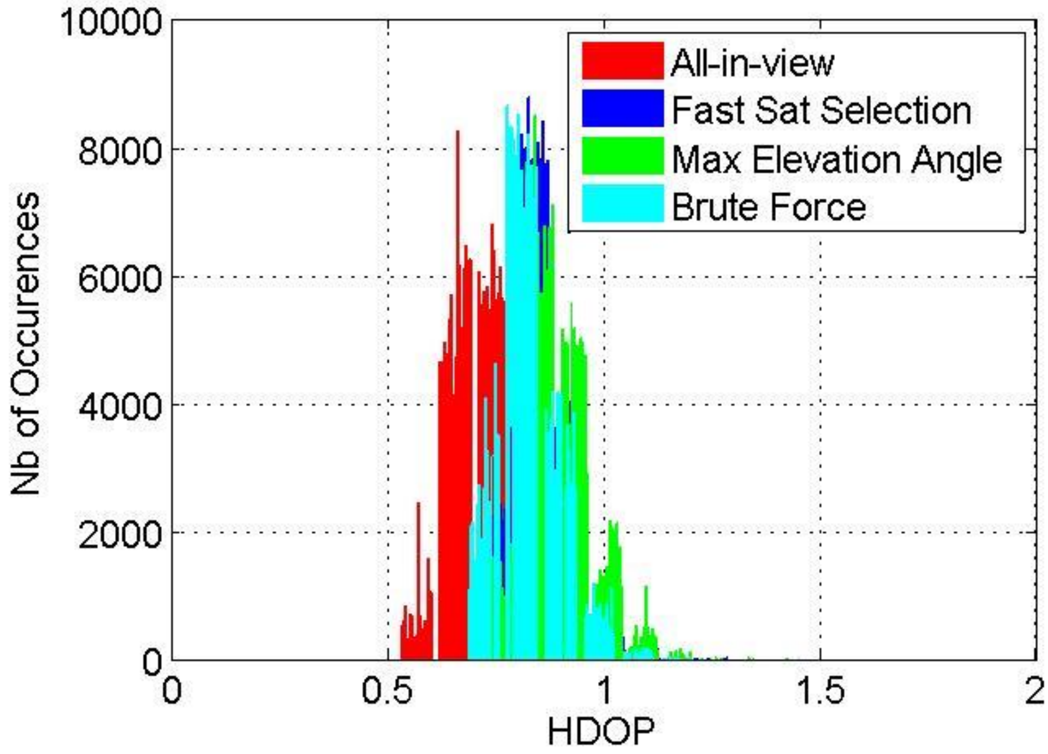

Figure 55 – HDOP values across all epochs and airports for all the methods and for all-in-view satellites

Table 17 – HDOP percentile at 95, 99 and 99.9 % for 12 satellites subset

	95 % HDOP	99 % HDOP	99.9% HDOP
All-in-view	**0.8758**	**0.9770**	**1.1125**
Fast Satellite Selection	**0.9760**	**1.0675**	**1.2383**
Maximum Elevation Angle	**1.0274**	**1.1182**	**1.3037**
Brute Force	**0.9547**	**1.0415**	**1.1935**

It is possible to see from the analysis of Figure 54, Figure 55, Table 16and Table 17 that, using a satellite subset, the DOP values are higher than for the all-in-view case. In particular, for the maximum elevation angle selection method, the VDOP values are clearly bigger than the other methods. The fast satellite selection and the brute force are able to provide values similar in magnitude to the all-in-view solution, the brute force methods seems in any case to provide slightly better results than the fast selection criteria.

In the next table, the average time to compute the previous parameters for one airport will be listed for all the three methods. The maximum time for each method will be listed as well in Table 18. This analysis aims to provide an insight of the computational load of each method.

Table 18 – Computational time, in seconds, for all methods with 12 satellites subset

	All-in-View	**Fast Satellite Selection**	**Max Elevation Angle**	**Brute Force**
Maximum Time	0.0604	0.1668	0.0537	119.14
Average Time	$6.3702 * 10^{-4}$	$1.5 * 10^{-3}$	$3.2416 * 10^{-4}$	0.8096

The brute force selection criteria is, as expected, the one with the highest computational load due to the number of combinations that has to be analyzed in order to find the best VPL. The other selection criteria require a computation time similar to the all-in-view case where no selection is done.

4.5.1.2 GAST D Protection Level

The simulated processing mode is the one used in GAST D, the sigma values for this service type are computed considering the model proposed in (RTCA Inc. DO245-A) and in (RTCA Inc.; DO253-C, 2008).

- the non-aircraft RMS error is computed considering results obtained in Table 10 and divided by $\sqrt{4}$ to consider the presence of four reference receivers at ground
- the airborne pseudorange performance are computed using the AAD model considering a B level (2.3.3), then it is multiplied by a factor of 1.3 in order to take into account the increased noise level related to the use of 30 seconds as smoothing constant instead of 100 seconds (Murphy, et al., 2010).
- the RMS of the aircraft multipath is computed as in the model given in Eq. 2.69
- the ionospheric and the tropospheric Residual Error are computed as in Eq. 2.70 and Eq. 2.52

D_V and D_L , represent the difference in the vertical and lateral domain between the 30 seconds and the 100 seconds smoothed solution. They are computed using a model proposed in (Wang, et al., 2014).

$$Th(D_V) = K_{fdD}\sqrt{\sum_{i=1}^{N} S_{Apr\,vert,i}^2\,\sigma_{D_R}^2} \qquad \text{Eq. 4.7}$$

$$Th(D_L) = K_{fdD}\sqrt{\sum_{i=1}^{N} S_{Apr\,lat,i}^2\,\sigma_{D_R}^2} \qquad \text{Eq. 4.8}$$

- $KfdD$, is the multiplier taking into account for the probability of false alarm. It is set at 5.5 considering a continuity risk of 4×10^{-8}
- $\sigma_{D_R} = F_{PP} \times \sigma_{vig} \times 140 \times V\_air$; Considering a value of $\sigma_{vig} = 4\,mm/km$ and a landing speed of the aircraft of $72\,m/s$, the previous model can be approximated to $\sigma_{D_R} = F_{PP} \times 0.04\,m$

The next figures show the VPL and LPL as in Eq. 4.4 and Eq. 4.5 and the values of S_{vert} and S_{vert2}. The aim of these two plots is to verify that at any epoch, the limit value of 10 meters is not exceeded by VPL or LPL, or the 2 and 3 limits are not overcome by S_{vert} and S_{vert2}.

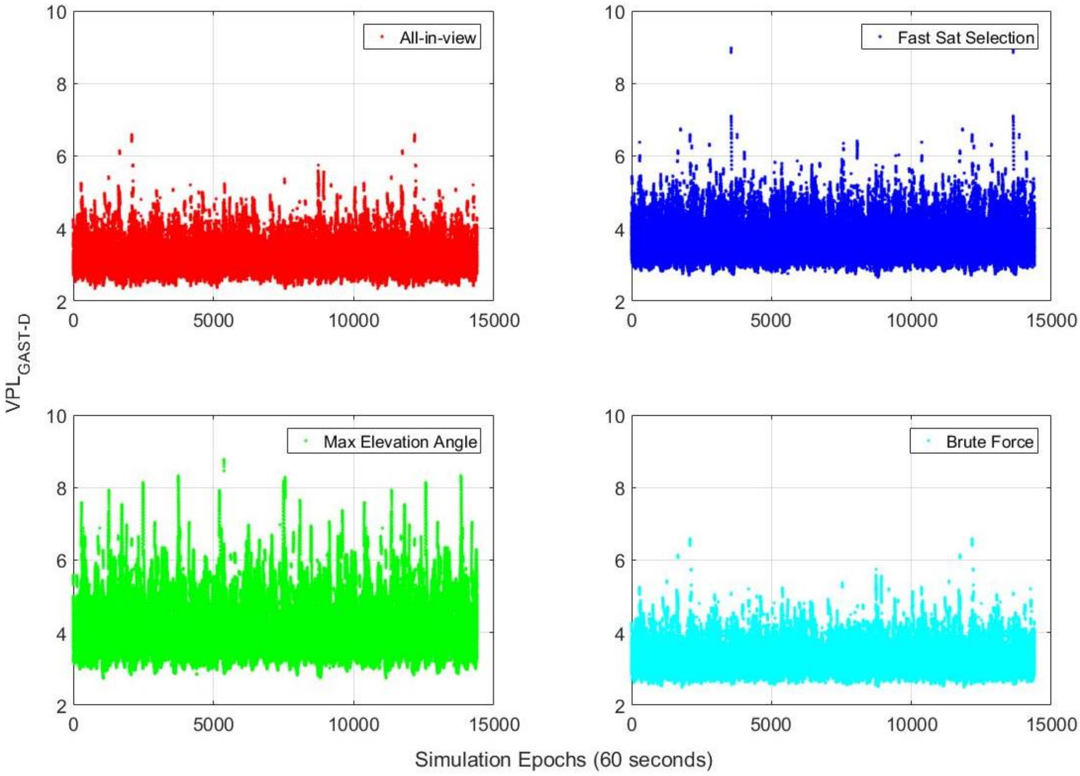

Figure 56 – GAST-D VPL computed across all the epochs and airports for three selection methods and all-in-view satellites

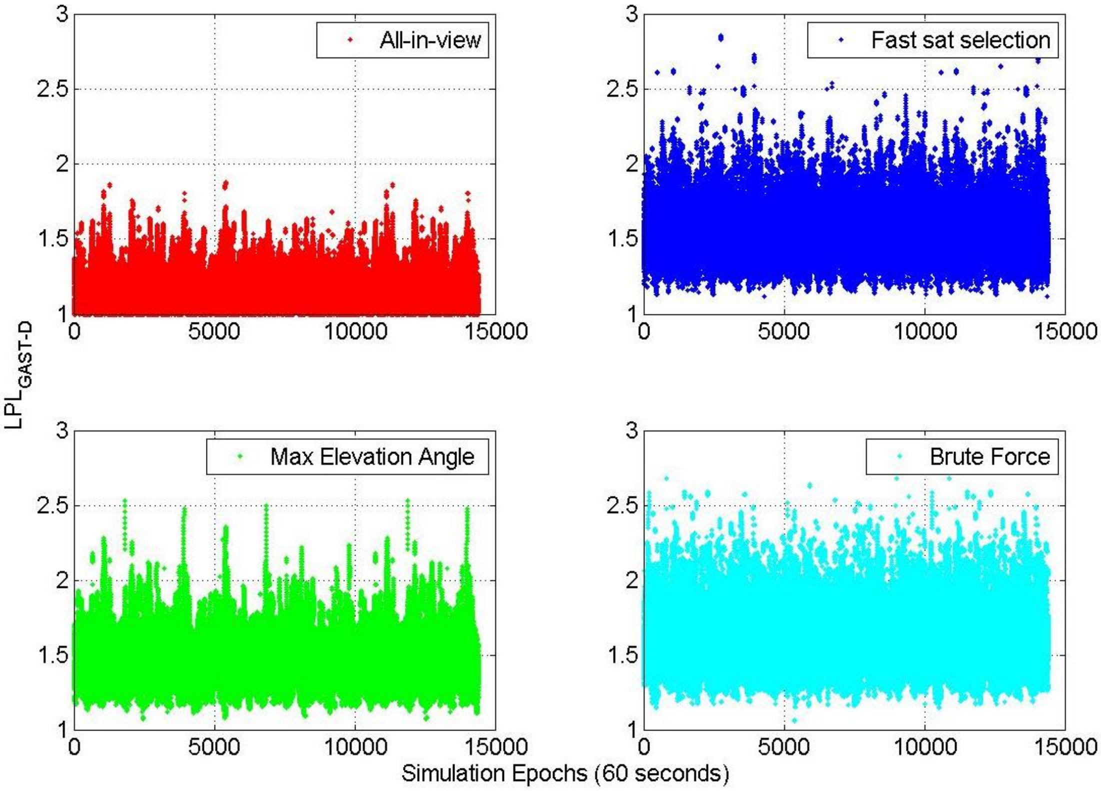

Figure 57 – GAST-D LPL computed across all the epochs and airports for three selection methods and all-in-view satellites

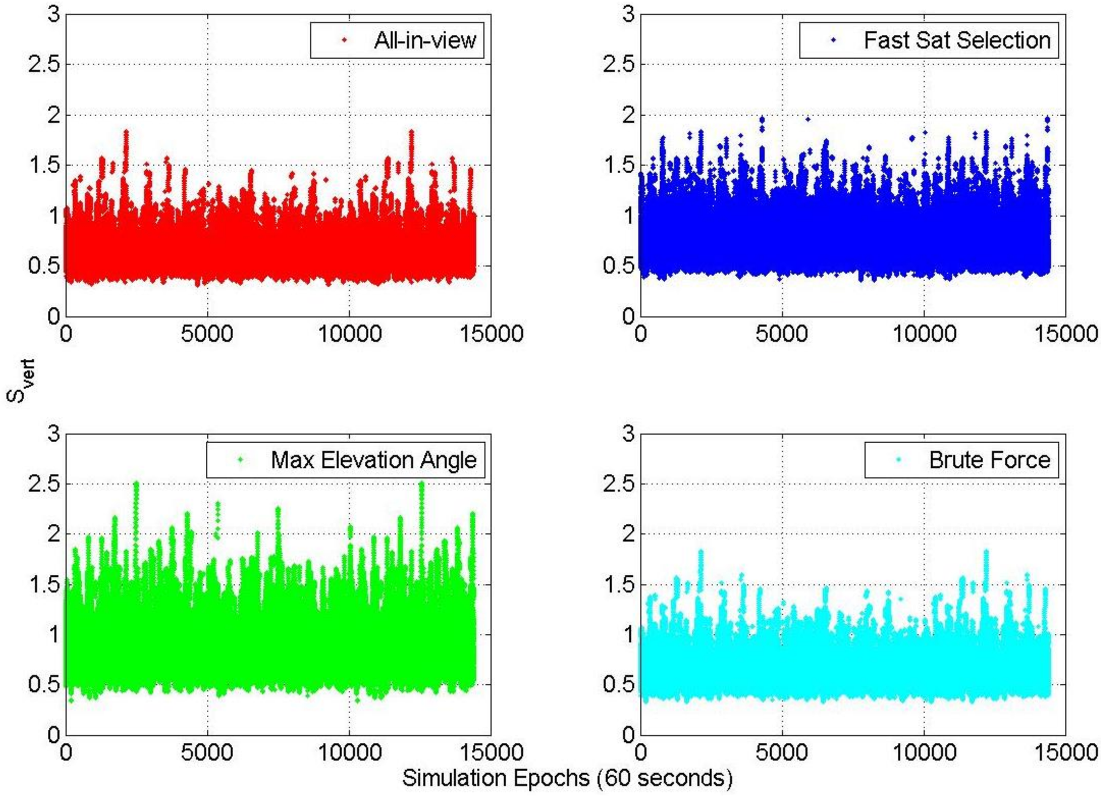

Figure 58 – GAST D S_{vert} values across all epochs and airports for three methods and all-in-view satellites

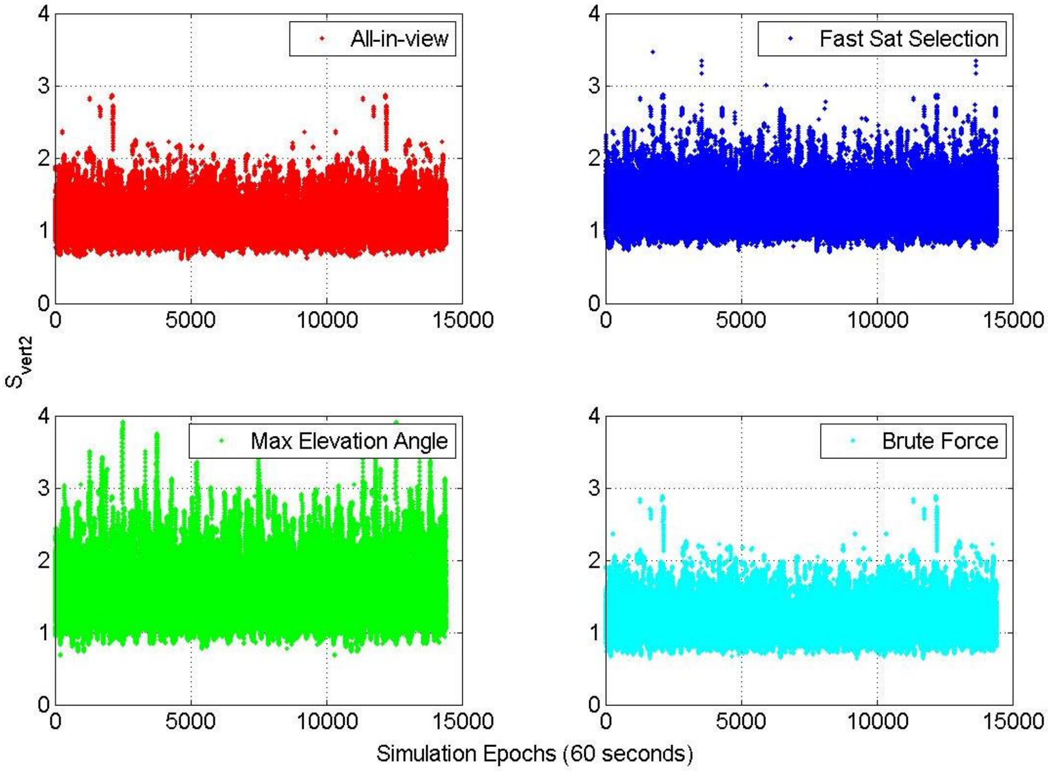

Figure 59 – GAST D S_{vert2} values across all epochs and airports for three methods and all-in-view satellites

As expected, the VPL provides larger values than the LPL. In both figures, the protection levels do not overcome the 10 meters limit, making the GAST D service available at all airports and at all epochs. The brute force algorithm is optimized to find the lowest VPL. This explains why at several epochs, the LPLs found by the brute force algorithm is higher than the ones found by the other two methodologies.

Table 19 – Geometry screening availability for all the selection methods with 12 satellites and all in view case

	VPL Availability	**LPL Availability**	**S_{vert} Availability**	**S_{vert2} Availability**
All-in-view	100 %	100 %	100 %	100 %
Fast Sat Selection	100 %	100 %	100 %	>99.999 %
Max Elevation Angle	100 %	100 %	99.92 %	99.79 %
Brute Force	100 %	100 %	100 %	100 %

The comparison between the three selection methods shows that the brute force algorithm is able to find the lowest VPL, the fast satellite selection finds geometries providing VPL values slightly larger than the brute force. This last provides, indeed, some geometry screening unavailability due to the overcoming of the S_{vert2} limit of 3. The use of geometries based on the selection of the satellites with the maximum elevation angle is the one providing the largest VPL values, moreover in several epochs the S_{vert} and S_{vert2} limits are overcome, making these epochs unavailable. In the horizontal domain the use of the maximum elevation angle criteria provide better result than the other two methodologies, the results are however good for all the three selection criteria.

4.5.1.3 I-Free Protection Level

In the frame of dual constellation and dual frequency GBAS research, a possible candidate for the processing mode is the I-Free (2.2.2.2.3). This mode permits to remove entirely the ionospheric delay from the code measurement at the cost of increased noise level, at the ground for the computation of the pseudorange correction and at the airborne level for the final position computation. To compute the protection level considering the use of this technique, there are no official formula as for the GAST D service, so the computation of these parameters will be done considering the results obtained in the analysis of the performance for noise and multipath at ground station level for L1 and L5. It has to be reminded that a calibration issue has been found n L5 band measurements and that it impacts also the I-free results. All the components taking into account the ionospheric delay for the computation of the protection level in GAST D will be removed for the I-Free protection level. The divergence terms, D_V and D_L, are set at zero because the double smoothing constant is not used in this case. The sigma ground will be inflated considering the use of the two frequencies, as well as the sigma airborne. The total sigma is:

$$\sigma_{tot\,I-Free}(i) = \sqrt{\sigma^2_{pr\,gnd\,I-Free,i} + \sigma_{tropo,i} + \sigma^2_{pr\,air\,I-Free,i}} \qquad \text{Eq. 4.9}$$

Where:

- $\sigma_{pr\,gnd\,I-Free}$ is defined using the bound defined in 3.4
- $\sigma_{pr\,air\,I-Free} = \sqrt{\sigma^2{}_{pr\,air\,L1}\left(1-\frac{1}{\alpha}\right)^2 + \sigma^2{}_{pr\,air\,L5}\,\frac{1}{\alpha^2}}$

Because lack of information about accuracy of L5 measurement at airborne side, $\sigma_{pr\,air\,L5}$ is assumed to have the same values as $\sigma_{pr\,air\,L1}$ computed relying on the AAD model (Table 12)

- $\sigma_{pr\,air\,I-Free} = \sigma_{pr\,air}\sqrt{\left(1-\frac{1}{\alpha}\right)^2 + \frac{1}{\alpha^2}}$

As for the previous case the protection level, the S_{vert} and S_{vert2} will be analyzed.

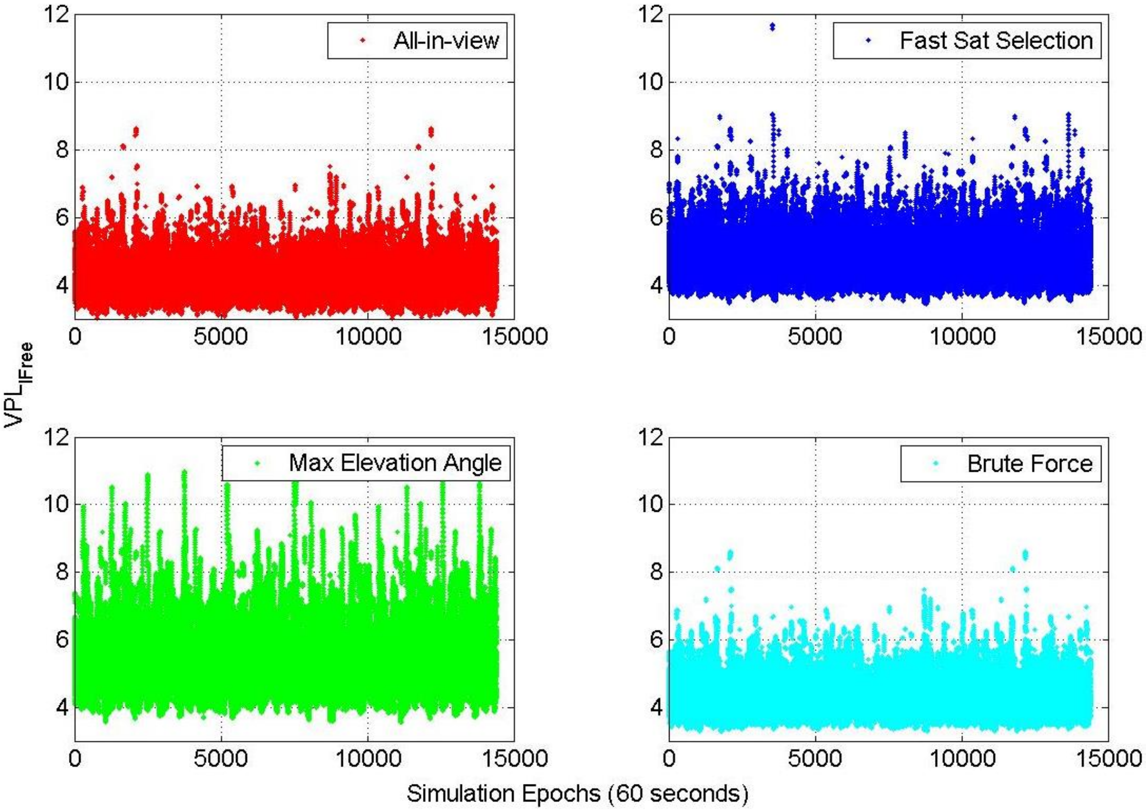

Figure 60 – I-Free VPL across all epochs and airports for three methods and all-in-view satellites

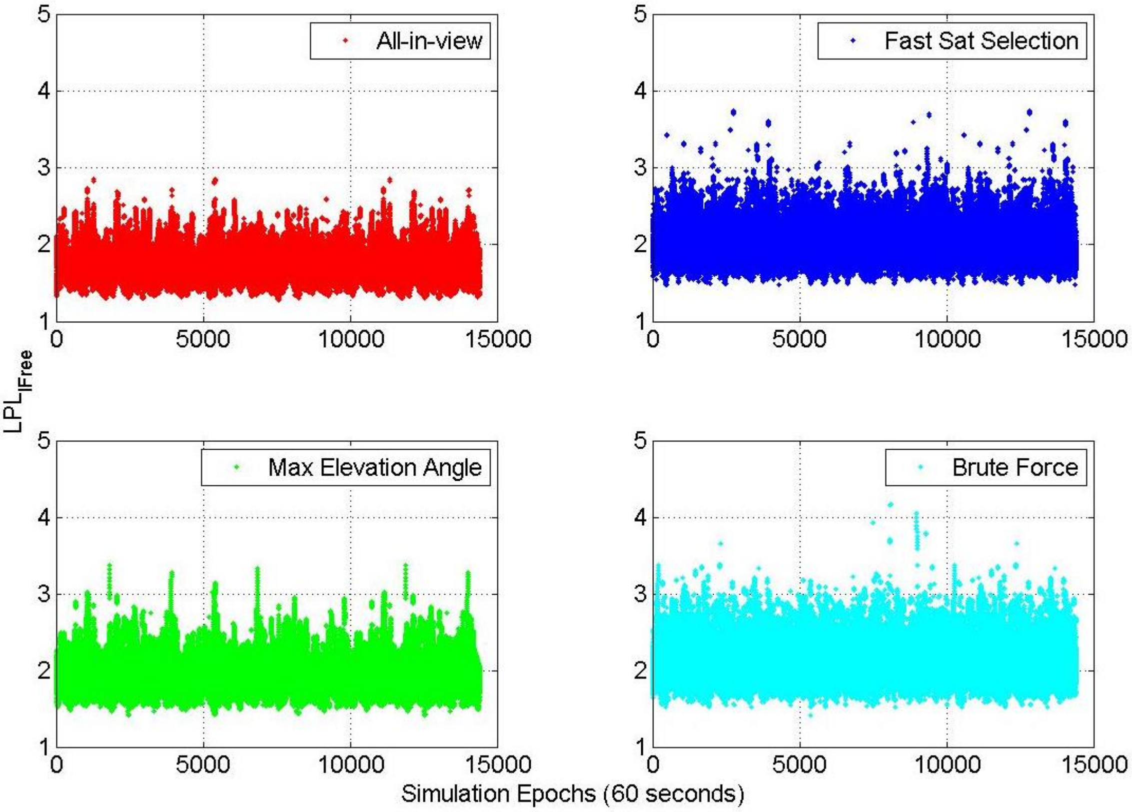

Figure 61 – I-Free LPL across all epochs and airports for three methods and all-in-view satellites

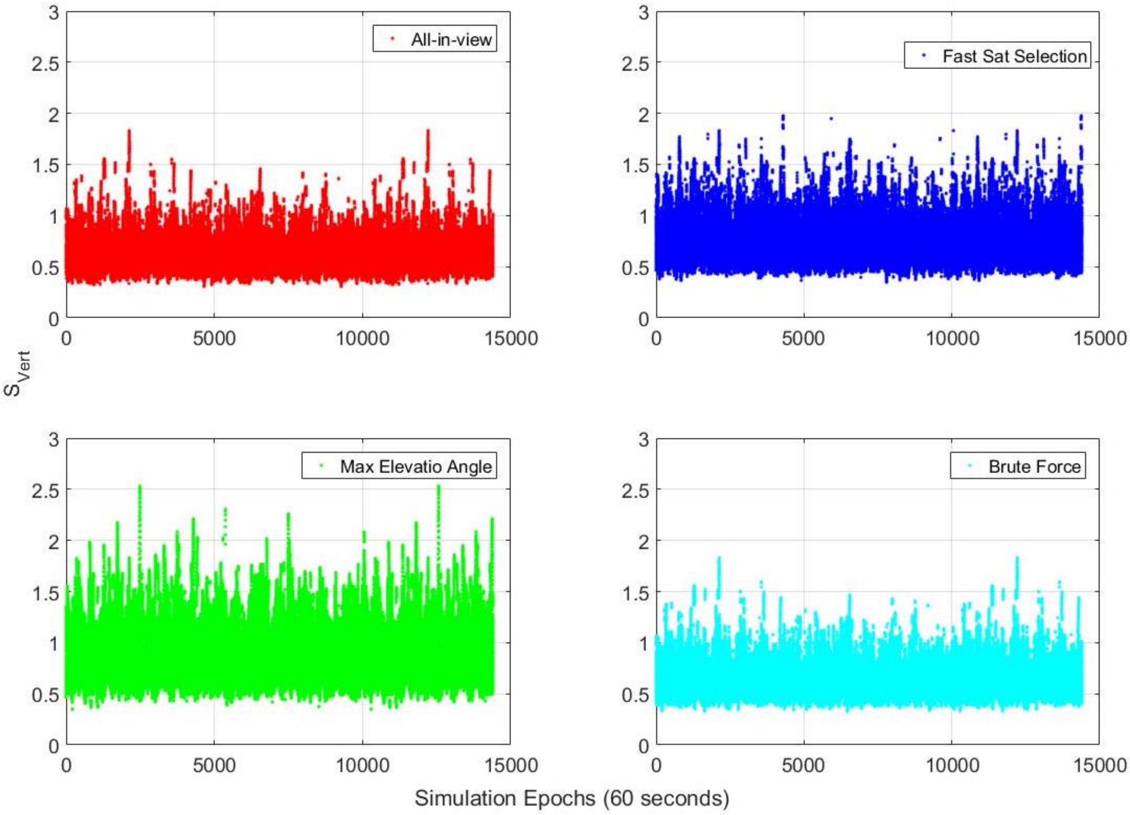

Figure 62 – I-Free S_{vert} values across all epochs and airports for three methods and all-in-view satellites

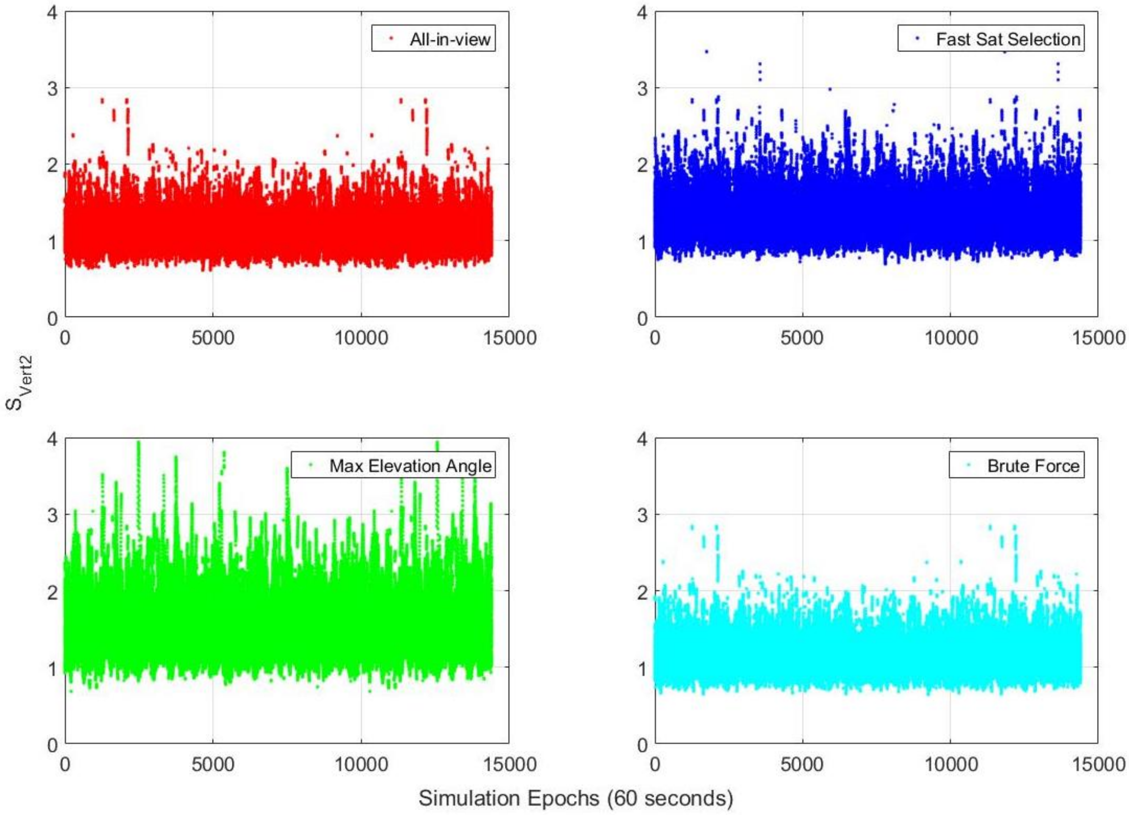

Figure 63 – I-Free S_{vert2} values across all epochs and airports for three methods and all-in-view satellites

Table 20 – Geometry screening availability for all selection methods and all in view case

	VPL Availability	**LPL Availability**	S_{vert} **Availability**	S_{vert2} **Availability**
All-in-view	100 %	100 %	100 %	100 %
Fast Sat Selection	> 99.999 %	100 %	100 %	99.91 %
Max Elevation Angle	99.92 %	100 %	99.91 %	99.78 %
Brute Force	100 %	100 %	100 %	100 %

The use of I-Free techniques, despite the absence of the sigma ionosphere value and the absence of the D_V or D_L in the protection level formula, generates values of VPL bigger than the GAST D case. This is because the value of standard deviation at ground and at airborne side are bigger than for GAST D. The fast satellite selection and the maximum elevation angle have values of VPL overcoming the alert limit of 10, leading to a system unavailability. The S values are as well as high fort the two methods, leading to unavailability in some epochs.

In particular the most critical conditions appear when the maximum elevation angle algorithm is used as selection method providing the lowest percentage of availability. The fast satellite selection method provides good performances and only in a few epochs the VPL exceeds the limit, as well as for the S_{vert} and S_{vert2} . The brute force algorithm is able to provide values of VPL almost similar to the all-in-view condition and does not exceed the 10 meters limit in any epoch, the percentage of availability for this method is 100 %.

4.5.2 Dual Constellation 15 Satellites Subset

In this simulation the same two constellations used in 4.5 are used, the only difference is the number of satellites used for the subset.

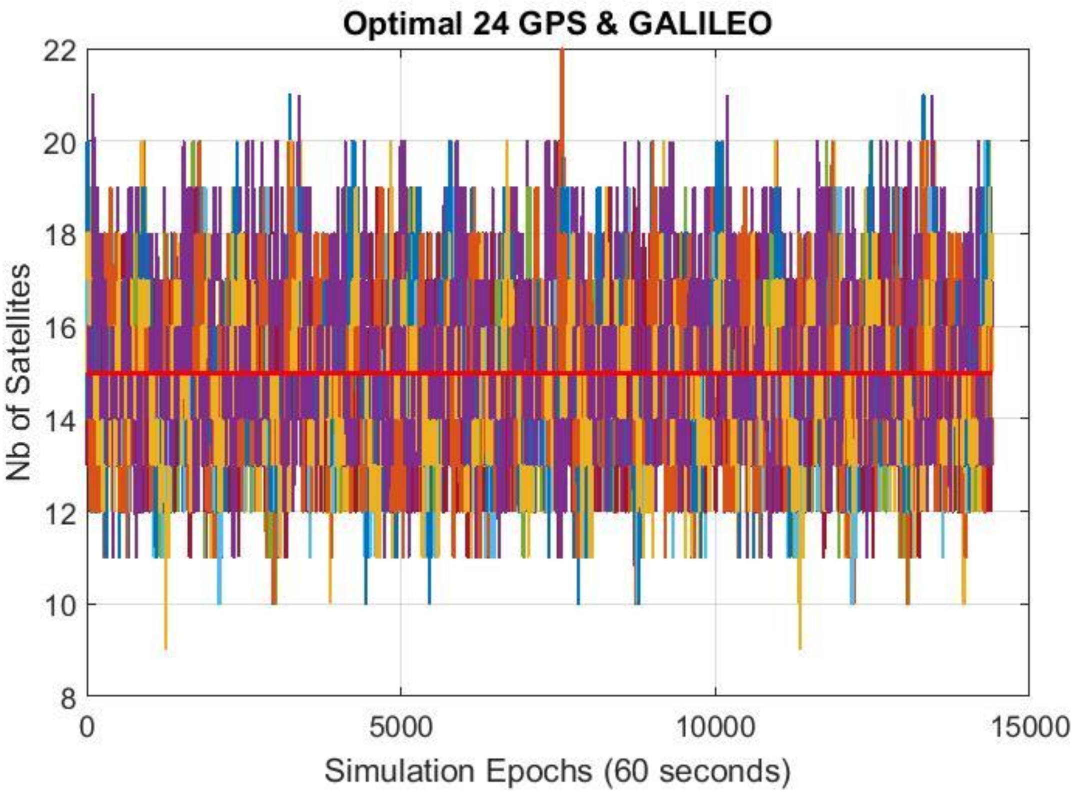

Figure 64 – Number of satellites for all the epochs and airports and 15 satellites subset in red

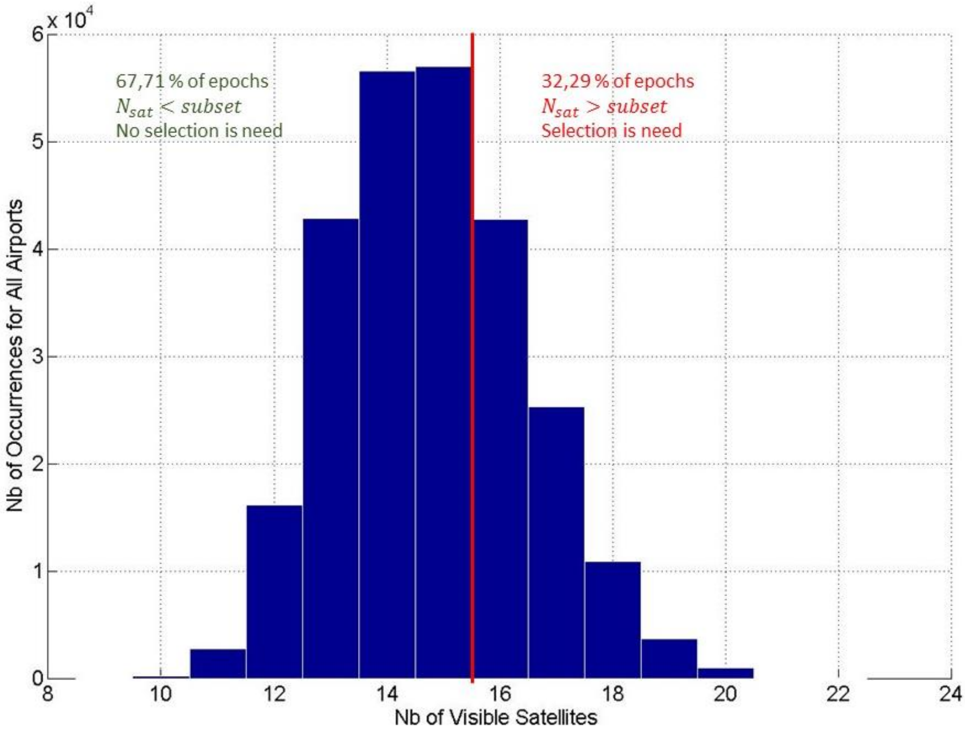

Figure 65 – Histogram of satellites number across all airports and epochs with percentage of use of satellite selection for subset 15

From the previous figures, it is possible to see that in 67.71 % of the epochs, for all the airports, there are less satellites in view than the subset limit. This will provide more similar results between the all-in-view and the subset parameters, reducing also the computational load due to the limited time of use of the algorithm and limiting the number of combinations to analyze per epoch thanks to the limited difference between satellites in view and subset dimension.

4.5.2.1 Impact of the Selection Method on the DOP Value

In the next figures the values of the DOP for the vertical and horizontal will be analyzed.

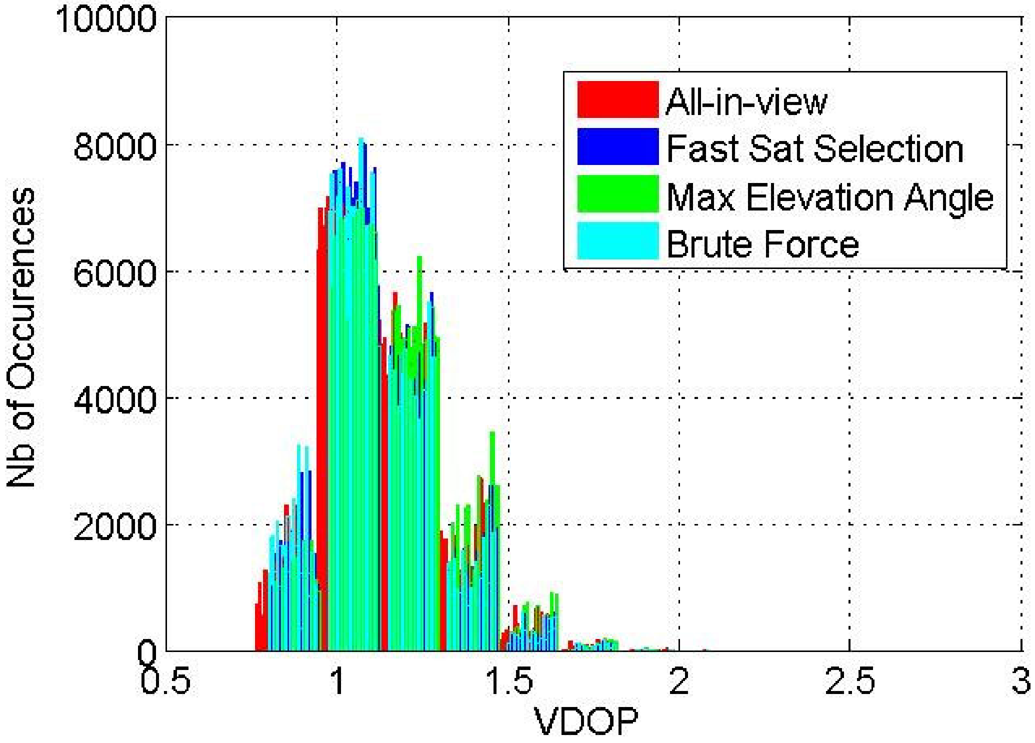

Figure 66 – VDOP values across all epochs and airports for all the selection criteria and for all-in-view satellites

Table 21 – VDOP percentile at 95, 99 and 99.9 % for 15 satellites subset

	95 % VDOP	**99 % VDOP**	**99.9% VDOP**
All-in-view	**1.4115**	**1.6099**	**1.9041**
Fast Satellite Selection	**1.4177**	**1.6121**	**1.9041**
Maximum Elevation Angle	**1.4668**	**1.6480**	**1.9129**
Brute Force	**1.4120**	**1.6099**	**1.9103**

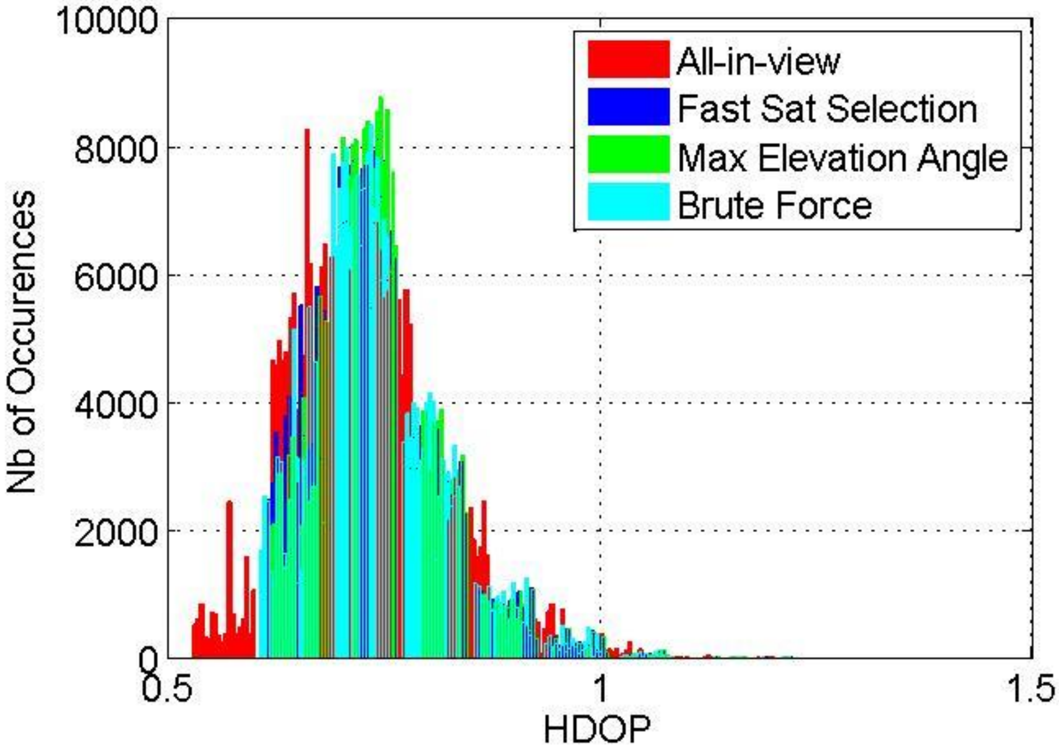

Figure 67 – HDOP values across all epochs and airports for all the selection criteria and for all-in-view satellites

Table 22 – HDOP percentile at 95, 99 and 99.9 % for 15 satellites subset

	95 % HDOP	99 % HDOP	99.9% HDOP
All-in-view	0.8758	0.9770	1.1125
Fast Satellite Selection	0.8760	0.9770	1.1125
Maximum Elevation Angle	0.8780	0.9773	1.1125
Brute Force	0.8760	0.9770	1.1125

Analyzing the DOP values, Figure 66, Figure 67, Table 21 – VDOP percentile at 95, 99 and 99.9 % for 15 satellites subset Table 21 and Table 22, it is possible to assess that the maximum elevation angle provides slightly degraded results compared to the other two methods. The other selection criteria provide results similar to the all-in view case.

The last analysis regards the computational time for each methods and for the all-in-view case.

Table 23 – Computational time, in seconds, for all methods with 15 satellites subset

	All-in-View	**Fast Satellite Selection**	**Max Elevation Angle**	**Brute Force**
Maximum Time	0.0243	0.2059	0.0591	4.125
Average Time	$5.2735 * 10^{-4}$	$8.2895 * 10^{-4}$	$7.4479 * 10^{-4}$	$7.8 * 10^{-3}$

The brute force selection criteria is, also when 15 satellites are selected as subset, the one with the highest computational load. Compared to the computation time for a subset with a size of 12 satellites, the maximum time for the brute force is very small. The other selection criteria have almost the same computational load as for the all-in-view case.

4.5.2.2 GAST-D Protection Level

In the next figures the VPL, LPL, S_{vert} and S_{vert2}, computed using the GAST D requirement, will be shown.

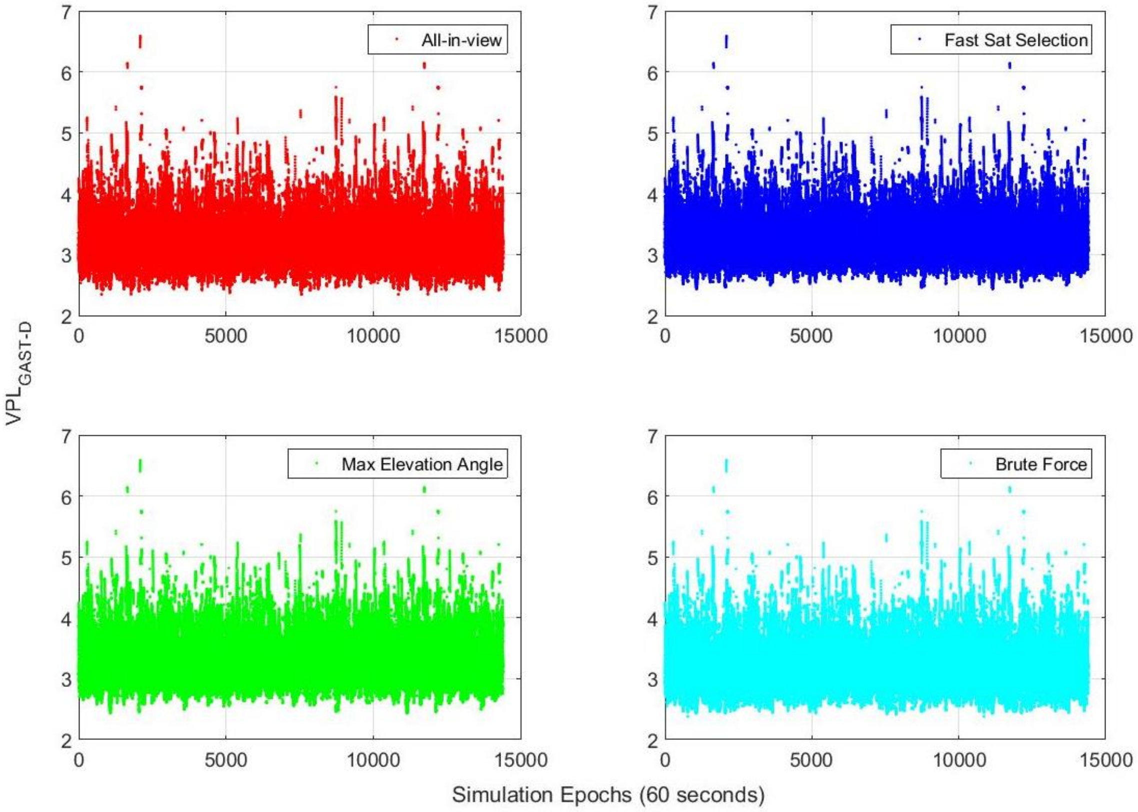

Figure 68 – GAST D VPL for all the epochs and airports for all the analyzed methods and all-in-view satellites

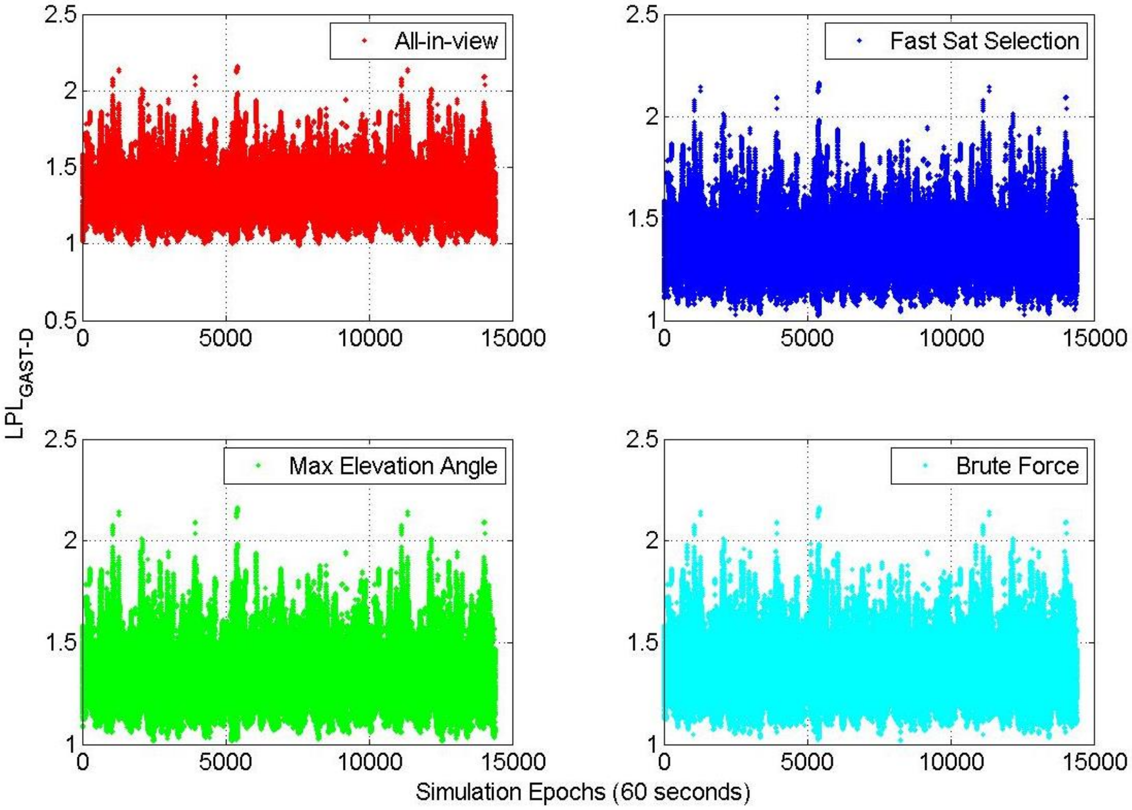

Figure 69 – GAST D LPL for all the epochs and airports for all the analyzed methods and all-in-view satellites

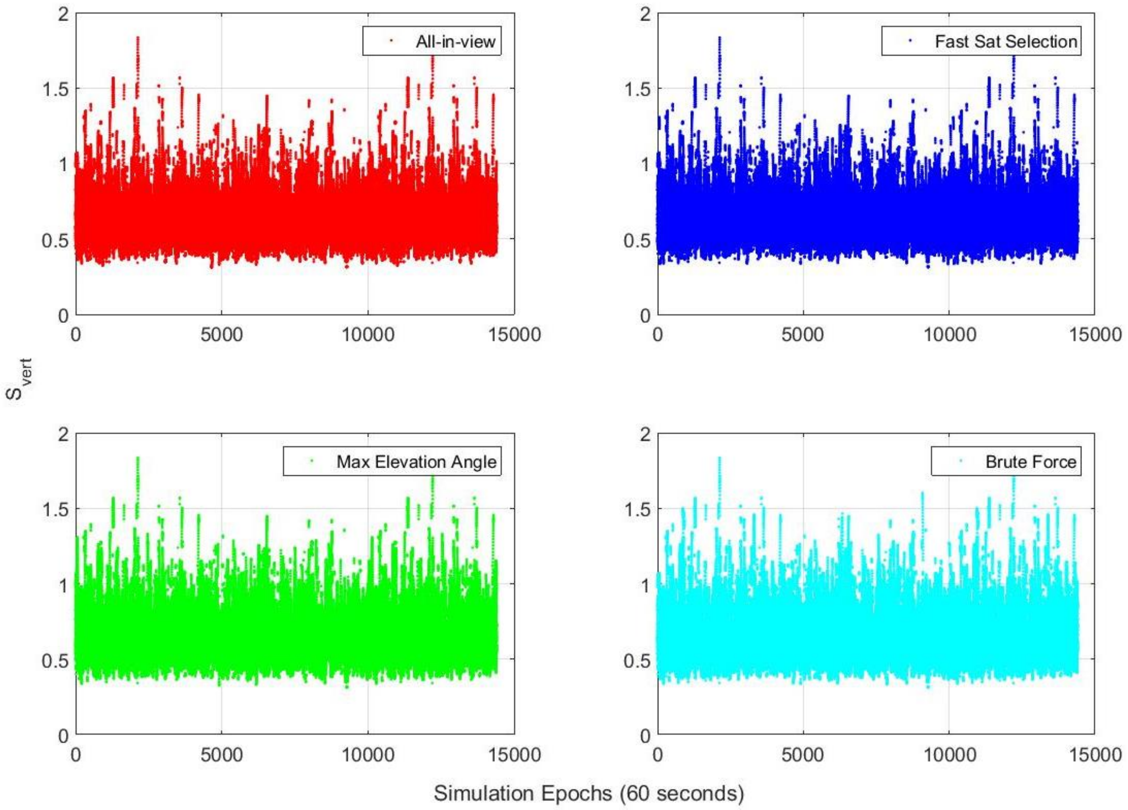

Figure 70 – GAST D S_{vert} computed for all the epochs and airports for all the analyzed methods and all-in-view satellite

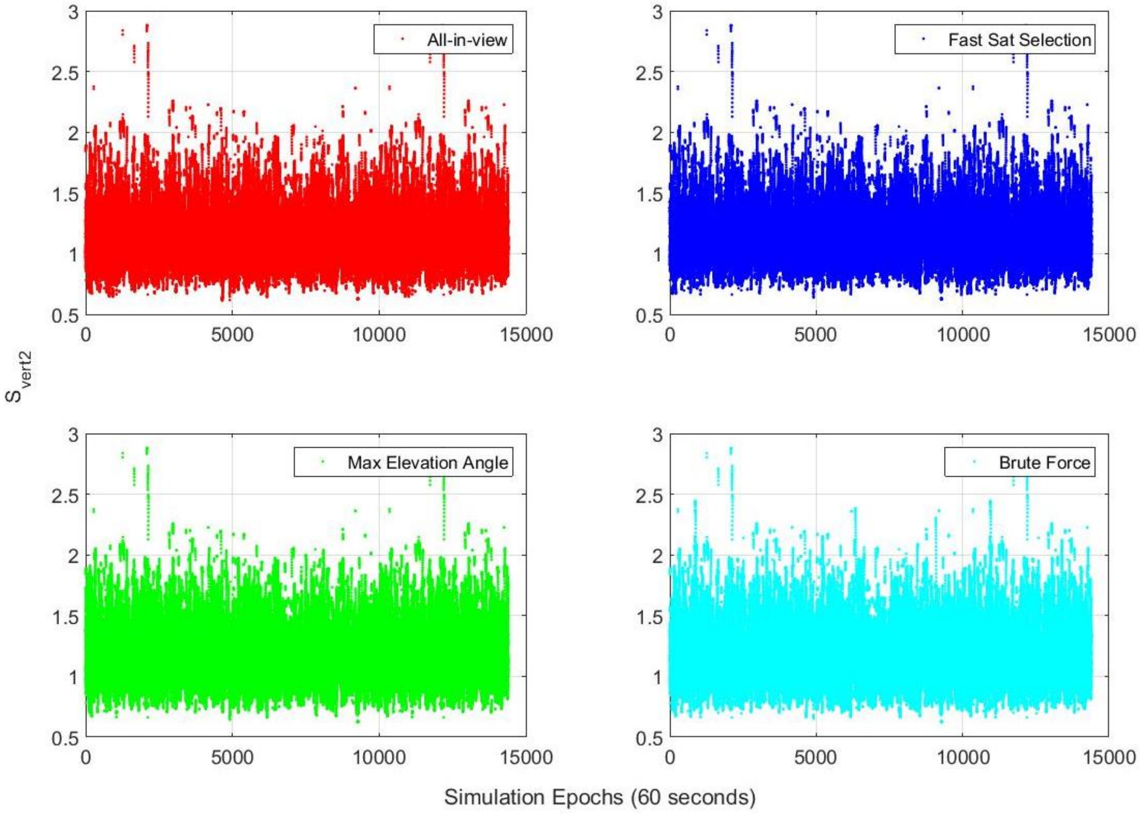

Figure 71 – GAST D S_{vert2} computed for all the epochs and airports for all the analyzed methods and all-in-view satellites

As expected, in more than the half of the epochs, the results between the all-in-view case and the ones computed using a subset are the same. There are no cases of system unavailability due to bad geometry condition. It is possible to note, for the VPL analysis in Figure 68, that the maximum elevation angle algorithm provides values of VPL slightly bigger than the other two selection methods.

4.5.2.3 I-Free Protection Level

In this simulation the parameters used are the same as in 4.5.2.3, the only difference is the dimension of the subset. The next two figures shows the VPL and the LPL for computed for this processing mode.

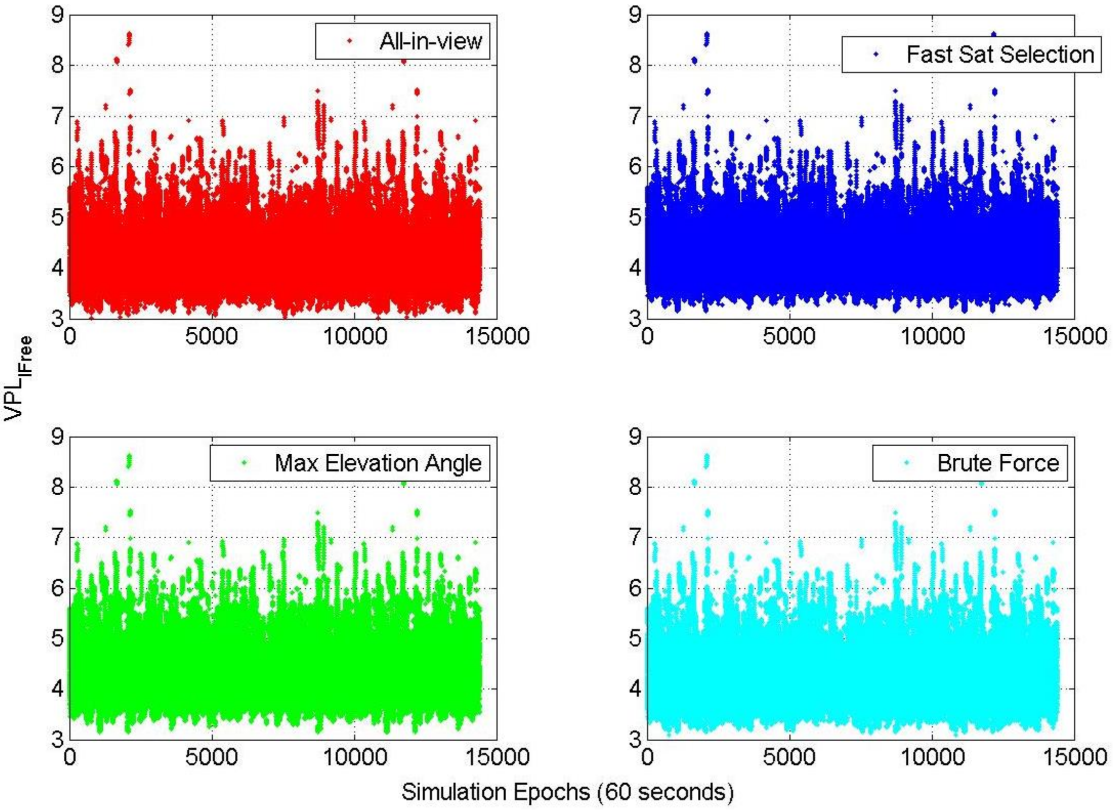

Figure 72 – I-Free VPL for all the epochs and airports for all the analyzed methods and all-in-view satellite

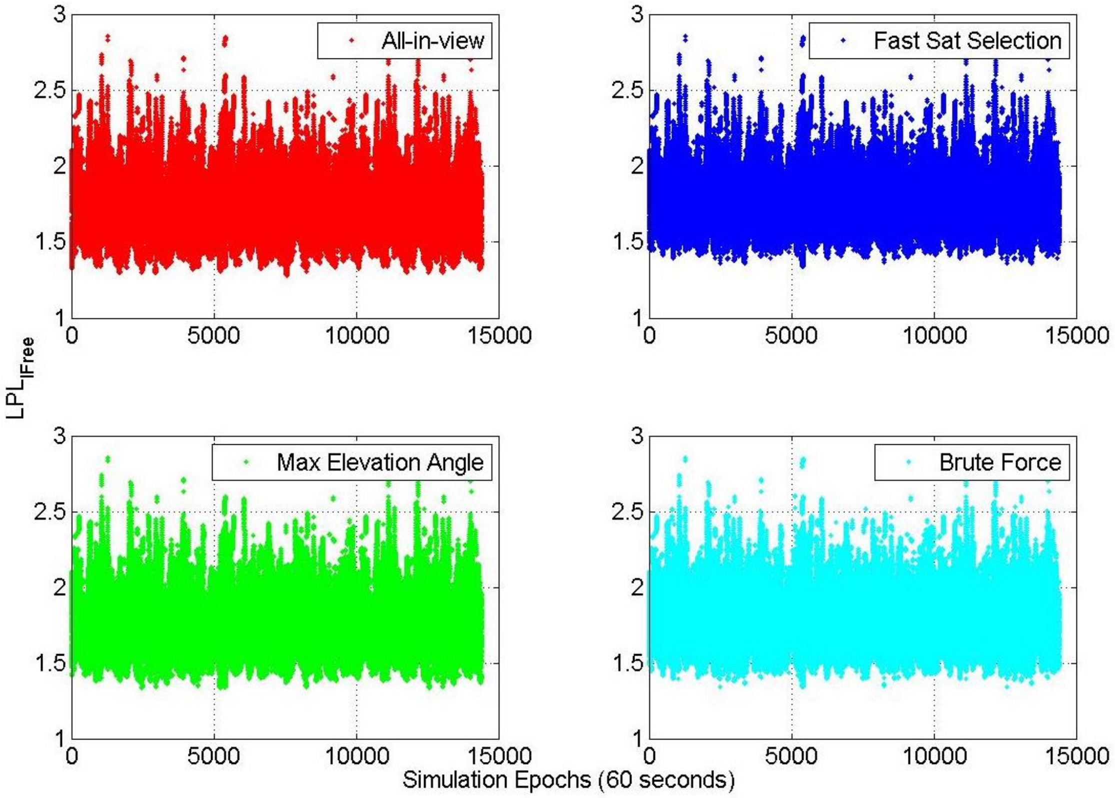

Figure 73 – I-Free LPL for all the epochs and airports for all the analyzed methods and all-in-view satellites

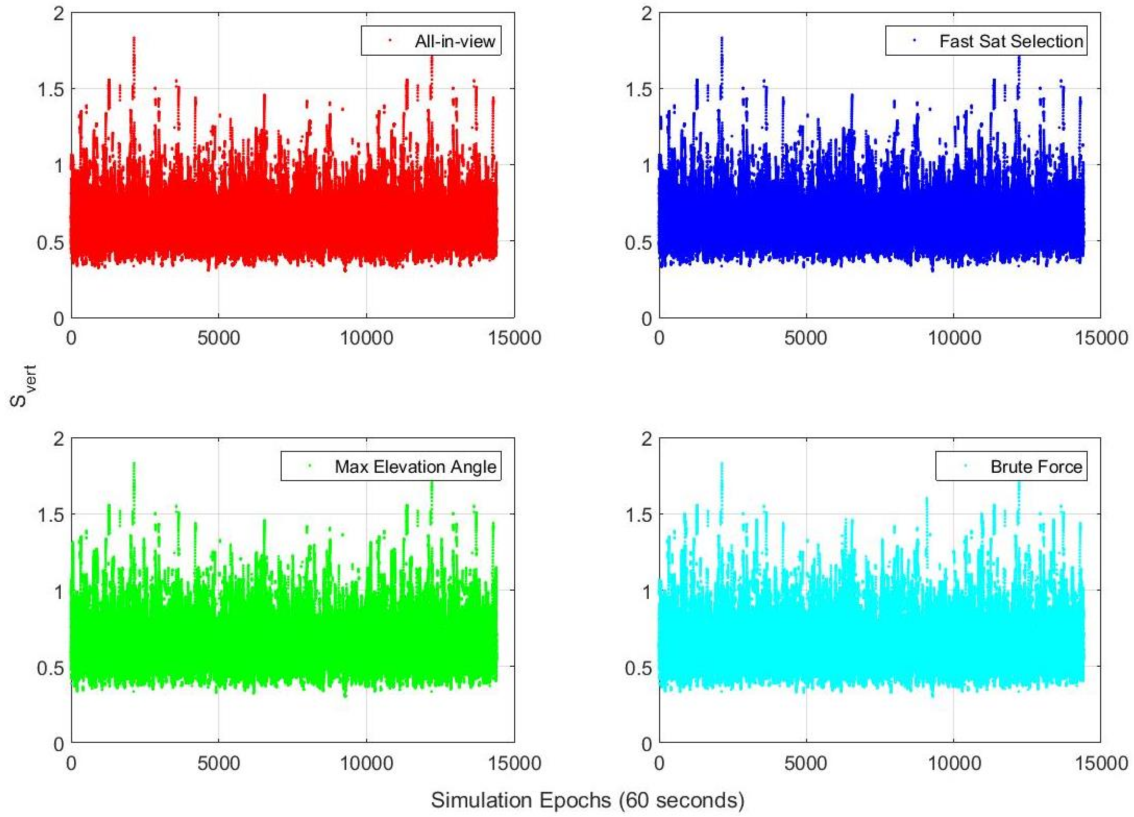

Figure 74 – I-Free S_{vert} computed for all the epochs and airports for all the analyzed methods and all-in-view satellites

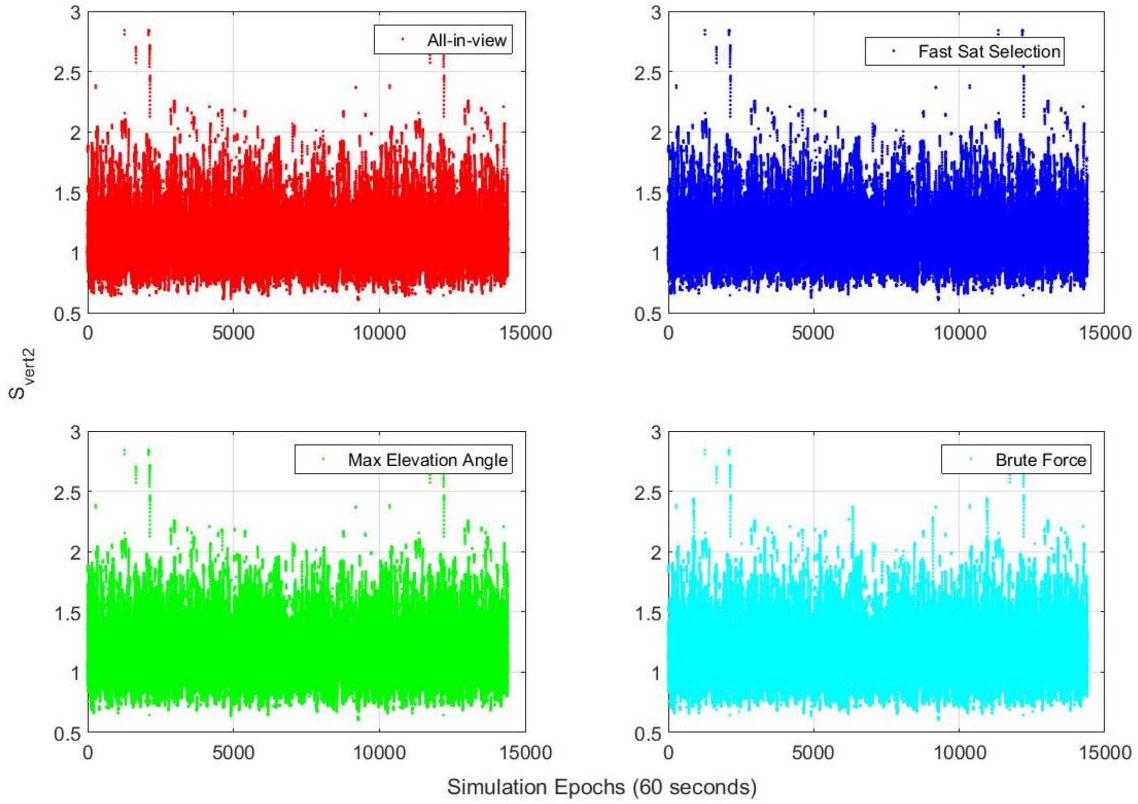

Figure 75 – I-Free S_{vert2} computed for all the epochs and airports for all the analyzed methods and all-in-view satellites

In this I-Free case, due to the increased number of satellites for the subset dimension, there are no epochs flagged as unavailable for exceeding the 10 meters limit or overcoming the S_{vert} limit. As for the GAST D case the maximum elevation angle seems to provide values of the protection level slightly bigger than the other selection criteria.

4.6 Conclusions

In this chapter, the possibility of using a satellite subset instead of using all the satellites in view has been investigated. The reason for this analysis stemmed from:

- The high number of signals coming from visible satellites to track with two constellations and two frequencies.
- The limitation of the number of corrections that is possible to broadcast in the current GBAS messages structure. The current limit for GAST D is 18 satellites, but with the development of GAST F, and the requirement to maintain interoperability between services, the limit could drop to lower values.

Considering these conditions, together with the number of visible satellites, has been chosen to analyse subsets composed of 12 and 15 satellites.

The first conclusion regards the minimum number of satellites to use as subset. For the dual constellation case, two subset sizes have been tested. The use of 12 satellites, as it is possible to see from the results in section 4.5, seems to not be sufficient from a geometrical point of view. The loss of accuracy analyzed by plotting the DOPs indicates that the vertical domain experiences an important degradation of the accuracy (VDOP increased by 2 in the worst cases). The only methods that seems able to work under this condition is the brute force solution, able to find subsets providing values of DOP similar to the all-in-view solution. The analysis of the computational load, however, clearly show that this method is not adapted to be used for a real time application due to the high number of combinations to be analyzed in some epochs. Analysing the protection level for the two processing modes, it is possible to see that the VPL, being the most critical protection level, overcomes in some epochs the limit of 10 meters in the I-Free case making these epochs unavailable. The analysis of the S_{vert} and S_{vert2} values confirms what has been seen in the VPL analysis. The use of a subset with 15 satellites provides better results, the values of the DOP are similar and the accuracy degradation is less important than the previous case. Analysing also the different processing modes, the it is possible to find out that no epochs can be flagged as unavailable due to a bad geometry, the VPL, the S_{vert} and the S_{vert2} do not overcome the alarm limit in any epoch.

The second conclusion regards the comparison between the three selected methods. The optimal solution is the best methods to find the lowest VPL in all the simulations done. If, on one side, this method works better than the other, on the other hand, its computational burden results to be much higher than any other. Therefore, this methodology could be inappropriate for a real time application.

The maximum elevation angle provides the opposite result than the optimal solution: it has almost no computational load but it does not take into account the geometrical aspect of the accuracy derivation. It can be observed, especially in the vertical domain, that the loss of accuracy is very important, because the selection of the highest elevation satellites reduces the spread in the elevation angle. Considering the analysis of the protection level and the S values, this method provides the highest values and in several epochs the GBAS service may result as unavailable if a subset is used.

The fast satellite selection seems to be a compromise methodology between the two other methods, it has almost the same computational load as the maximum elevation angle criteria but it is able to find subset with good geometry. This method, in fact, takes into account the geometry as an important factor but is more efficient than the optimal solution in term of computational load. It takes into account also the elevation angle because in the slice of sky with more than one satellite, the one with the highest elevation angle can be selected.

Considering the joint analysis, the use of a subset with 15 satellites seems to be a better choice in order to guarantee the availability of the GBAS service, the fast satellite selection method is the one providing the best joint results: accuracy and low computational burden. Moreover with this subset size is possible to rely on the use of the I-free combination. Considering that GAST-D is still under validation due to a lack of integrity performance in detecting ionosphere anomalies and knowing that the I-free combination is the only one able to totally remove the ionospheric delay from the code measurement this condition has a relevant importance in the choice of the optimal subset size.

This analysis does not take into account other kinds of problems that may rise in GBAS, such as the impact of satellite selection on the smoothing process or monitors. It is well known that the smoothing steady state performances are reached when the time elapsed from the start of the filter is at least equivalent the smoothing constant used. This condition can represent a problem if the used selection methodology has a rate of change of subset that is too high. To be suitable for GBAS, the rate of change of subset for any methods has to be checked and the results must be taken into account with the previous analysis. A useful algorithm to avoid losing a setting satellite during the approach phase is the "Constellation Freezing" proposed in (Neri, 2011). It may help not to take into account in the subset search satellites that are present at the beginning of the approach and are going to set before the landing. Thanks to the use of this algorithm, the rate of change of subsets could be further reduced.

Another problem not considered in this study may be represented by the difference of satellites in view between the ground and the airborne subsystem, if the ground station selects a certain subset but for any reason one of them is not tracked by the aircraft, this would lead to an extra-degradation. A possible solution to this kind of problem is the application of the satellite selection only at airborne level, in this way the probability to have a difference between the satellites in view is reduced.

5 GBAS Integrity

Integrity has been for all GBAS services one of the most critical parameter to meet. According to the level of service that each GAST service is expected to provide, the integrity concepts have been developed following different methodologies which are now summarised.

In GAST-C, the ground station is responsible for monitoring the entire system. In order to bound errors present at the aircraft side, where no monitors are present, the ground station computes a series of protection levels based on conservative assumptions such as accounting for a number of measurement outages. This complements the fault-free protection level determined within the aircraft whose role is to protect against positioning failures due to nominal errors. The ground based bounding is designed to ensure that undetected faults cannot cause a positioning failure for a 'worst' aircraft geometry under certain conditions. This service has been validated to provide CAT I precision approach operations. In case of anomalous ionospheric conditions the availability of the service is strongly impacted due to the absence of monitors at aircraft level and due to the conservative assumption done to cope with this absence.

The demonstrations of GAST-D airworthiness relying on the same concept used in GAST-C, linearization of the ILS performances, is not possible due to the higher level of performances expected for this kind of operations Figure 110. In order to better reproduce GBAS properties another concept has been used for GAST-D, the auto-land model. This consider the ability of the aircraft to land in a defined "box" (figure in appendix A) based on two main error sources.

- The Navigation System Error (NSE).
- The Flight Technical Error (FTE)

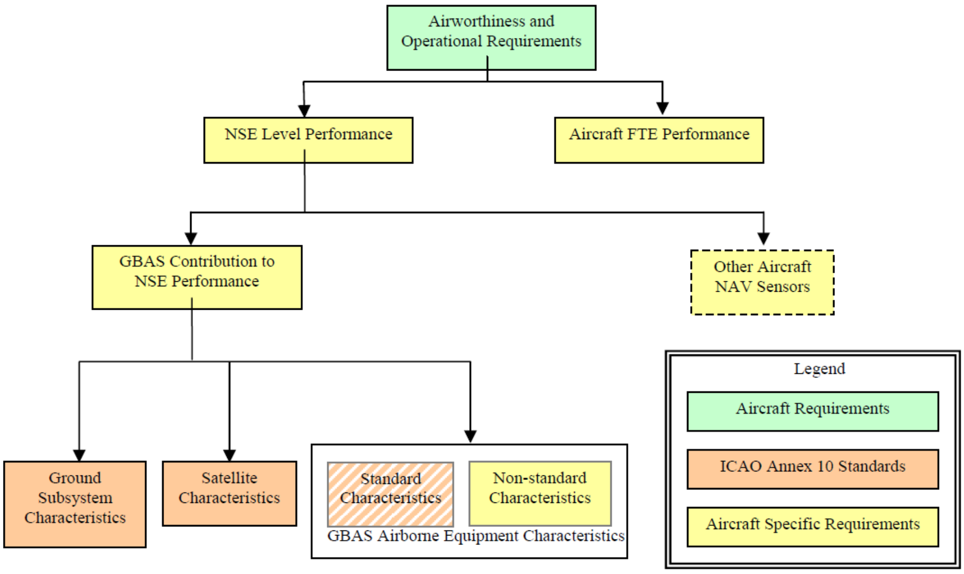

Figure 76 GBAS standards to support CAT III operations (ICAO NSP, 2010)

GBAS, under GAST-D, contributes only for the NSE. Considering the touchdown performances as dependent from the Total System Error (TSE), and this last being the sum of NSE and FTE. The derivation of the “expected GBAS contribution to NSE” may be derived. The challenge has been to derive GBAS performances that permit to demonstrate airworthiness to a large number of aircraft.

So in this service the aircraft is now responsible for determining its own airworthiness which partly relies on additional responsibilities regarding the monitoring of ionosphere anomalies. The ground station, on the other side, is only responsible for monitoring all ranging sources failures. In spite of the development of a new concept, and new monitors, this service remains to be fully validated and standardised since the proof of integrity relating to ionosphere monitoring has yet to be achieved.

Initial developments into a GAST F service, also with the goal of supporting Cat II/III operations, have begun within SESAR 15.3.7. A common requirements framework to GAST D has been assumed which will require the aircraft to assess its total system performance assuming a standardised ground monitoring capability for ranging source faults. New integrity challenges have been identified which are related to the use of new signals, DF combinations and possible new processing modes (different update rate for the PRC and RRC). Moreover the impact of the threats on new signals (frequency, constellation) must be assessed, for example the ionospheric delay differs according to the frequency used. For this new service, fallback modes has to be defined in case of loss of a frequency or loss of a constellation. In Figure 77 an example of fallback modes for GAST-F is shown.

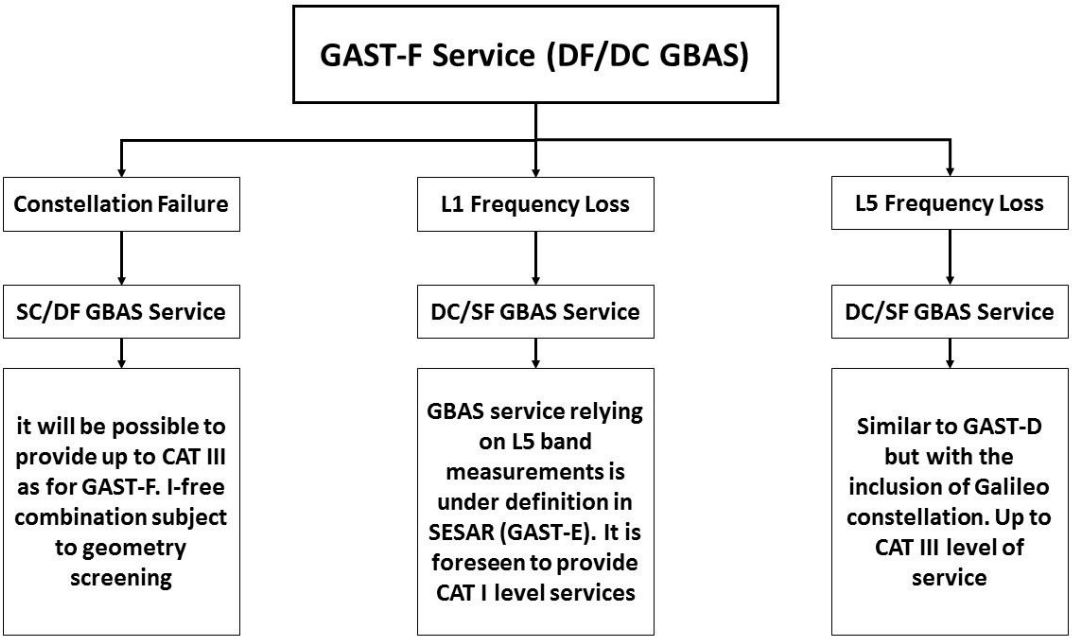

Figure 77 – GAST-F fallback modes example

5.1 The GAST D Concept

For GAST-C, international standardization bodies (ICAO, RTCA and EUROCAE) have worked jointly to define a standard that reuses the known performance of ILS Category I, which is defined angularly, to derive GBAS Landing System (GLS) Cat I performance. For GAST C, responsibility of the performance is ensured by the ground subsystem in the position domain for all aircraft operating in the GBAS Service volume and for all associated constellation geometries.

When the concept for GAST-D has been developed the fact that associated requirements, TSE and consequentially the FTE and NSE, are much more challenging to achieve for CAT II/III operation level has led to important new considerations. To derive GAST-D airworthiness a different approach was chosen, touchdown performance-based, instead of using the ILS-like method. Furthermore, performance allocation was split between air and ground taking advantage of the fact that the airborne subsystem knows best, which navigation data (e.g. which satellite set) it actually uses. This allows to not use conservative values of the FTE and NSE to derive the TSE and to use less conservative integrity requirements.

According to the GAST-D concept, the ground station protects the aircraft in the range domain instead of protecting it in the position domain (as GAST-C) by monitoring each GPS (or GLONASS) measurement against an acceptable error limit. Then, it is the airborne receiver which has now the responsibility to select satellite geometry because considering that the aircraft knows its own geometry is less conservative than assuming a degraded geometry at the ground as it was made in GAST C.

Finally, the mitigation of errors induced by anomalous ionospheric condition has been allocated to both the airborne system (RTCA Inc.; DO253-C, 2008) by adding a Dual Solution Ionospheric Monitoring Architecture (DSIGMA) monitor algorithm and the ground subsystem by implementing the Ionospheric Gradient Monitoring (IGM).

GAST-F is expected to follow the same concept adopted for GAST-D as outlined above yet with potentially different range error requirements.

5.1.1 Low Level Performance Requirements for Ground Monitors

Under GAST-D the ground station is responsible for the monitoring only of the ranging errors. At this scope a new requirement, considering the probability of an unsafe landing for a varying vertical error, has been developed in the range domain. It considers that under GAST-D the FTE is no longer estimated by the GS, using conservative values, the requirement is considered to have a low level of performances thanks to the possibility to relax the NSE.

The process followed in (ICAO NSP, 2010) is based at first on the probability to have an unsafe landing (P_{UL}), this means to land outside of a pre-defined box, computed considering standard NSE and FTE values and varying the vertical error. Then the values of P_{md},knowing that any unsafe landing condition has to be monitored with a $P_{md} < 10^{-5}$, is determined as:

$$P_{md}(E_v) = \frac{P_{UL}(E_v)}{10^{-5}}$$

Where:

- $P_{md}(E_v)$ is the probability of missed detection of a vertical error E_v
- $P_{UL}(E_v)$ is the probability of an unsafe landing for a given vertical error

Then the P_{md} curve is converted in the range domain dividing the vertical error by a worst-case S_{vert} value of 4. This process establishes the P_{md} requirement for the limit case (Figure 78)

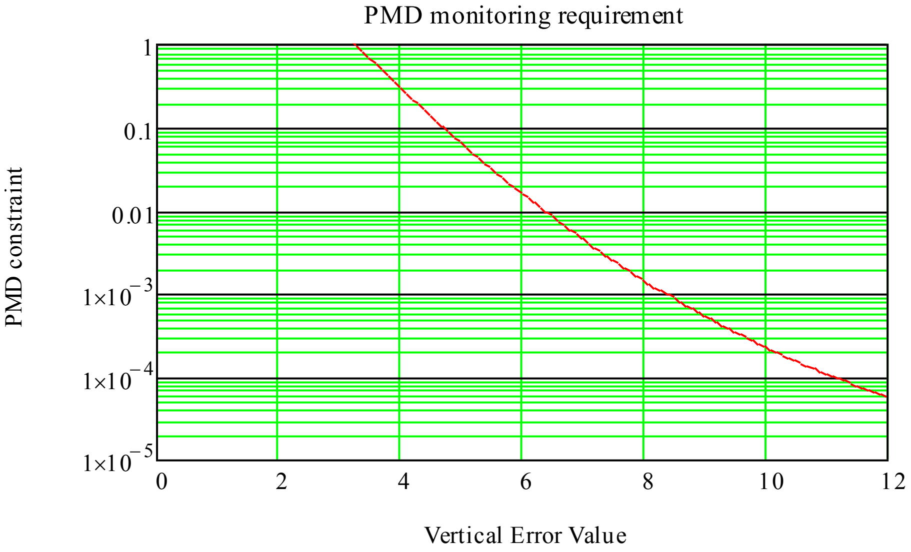

Figure 78 – Derived limit case P_{md} requirement for ranging source monitor (ICAO NSP, 2010)

The same analysis has been done for the malfunction case where an undetected error affects one range measurement. In this case the maximum vertical error that leads to a safe landing, always considering fixed values of NSE and FTE, has been computed. Once that the value, 6.44 meters, has been found, it has been converted in the range domain dividing it by 4, the worst S_{vert} possible, obtaining a value of 1.61 meters. This error must be monitored with a probability of missed detection of $1.3 \cdot 10^{-4}$, considering an a priori probability of fault $P_{fault} = 7.5 \cdot 10^{-6}$, in order to have a safe landing.

From the union of the two requirement, for limit and malfunction case, has been derived the general P_{md} requirement curve shown in Figure 79 for the range domain.

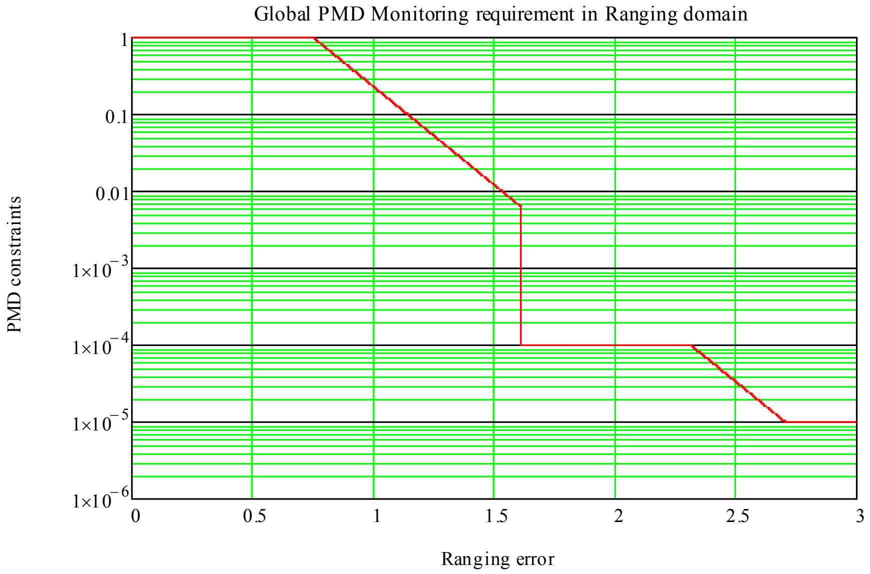

Figure 79 – General P_{md} requirement for ranging source monitors in range domain

For each monitor the performances have to be computed considering the test metric used, its distribution, its standard deviation and the P_{fa}. In Figure 80 an example of a compliant and a non- compliant monitor is shown.

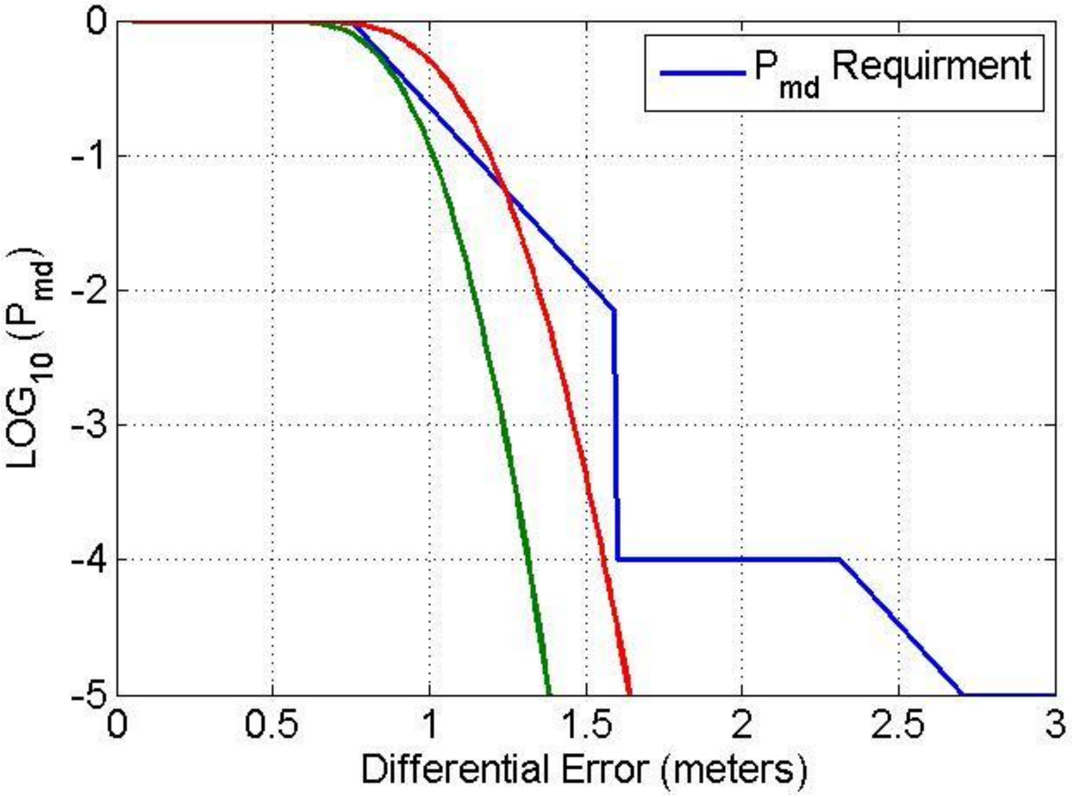

Figure 80 – Example of monitor performances Vs. P_{md} *requirements*

The red curve is related to the performances of a monitor with a test metric following a Gaussian distribution with $\sigma_{test} = 0.15$ meters and threshold set at 1 meter. This kind of monitor is compliant with the “malfunction case” requirement but it exceeds the “limit case” one in some case. The green curve is instead relative to a similar monitor where the $\sigma_{tets} = 0.123$ meters and the threshold is set to 0.85 meters. In this case the monitor is able to meet the requirement for all differential errors.

5.1.2 Geometry Screening

In GAST-D the aircraft is responsible for the selection of a satellite geometry, the subset that is adapted to its performance (CAT III for GAST-D). This process is done at aircraft level by geometry screening. Considering that relationship between errors on measurements and errors on the estimated position coordinates and receiver clock offset:

$$E_{sol} = E_{range}\, S \qquad \text{Eq. 5.1}$$

Where:

- E_{sol} is a vector of four terms expressing the estimation errors on X, Y, Z axis and the receiver clock bias
- E_{range} is the vector, with a length equal to the number of satellites used to compute the solution, indicating the differential errors on each corrected measurement
- S is the projection matrix presented in 2.3.3.2

Eq. 5.1 can be rewritten considering only the vertical and lateral components of the position error as

$$E_{vert,i} = E_i \, S_{vert,i} \qquad \text{Eq. 5.2}$$

$$E_{lat,i} = E_i \, S_{lat,i} \qquad \text{Eq. 5.3}$$

Where:

- $E_{vert,i}$ is the vertical position error caused by satellite i
- $E_{lat,i}$ is the lateral position error caused by satellite i
- E_i is the range error on the i^{th} satellite, is a vector with a length equal to the number of satellites, with zero values everywhere except at the i^{th} line, where the value is E_i
- $S_{vert,i}$ is defined in 2.3.3.2
- $S_{lat,i}$ is defined in 2.3.3.2

Knowing that the magnitude of the differential error is limited thanks to the presence of monitors, both at the grounds and aircraft side, by limiting the magnitude of S_{vert} and S_{lat}, it is possible to limit the error in the position domain.

For GAST-D considering the requirement in (ICAO NSP, 2010), any range error bigger than 1.6 meters must be detected with a P_{md} of 10^{-9}, the following limits are adopted: $S_{vert,i}$ and $S_{lat,i} < 4$ for any satellite. In order to protect the user, especially in the vertical position domain, against the presence of a fault on a second satellite at the same epoch, another value has to be monitored as well: $S_{vert2,i}$. This last value represents the sum of all possible pairs of satellites (ICAO NSP, 2010) and it shall not exceed 6.

5.1.3 SiS TTA

An important parameter to derive the integrity performances of the monitors is the SiS TTA. Although it has been already presented in 2.3.3, it is helpful to clarify the time-to-alert scheme as proposed in Figure 15. In (ICAO, 2006) the value, in seconds, of the TTA is set at 2.5 seconds. This time is the maximum interval that has to pass from the first faulty measurement received by the ground segment, to the reception at the airborne side of a message containing integrity information about the fault. This time takes into account for 1.5 seconds as the maximum time to process and broadcast the information and two missed messages for the airborne equipment.

In Figure 81 a detailed scheme of the SiS TTA and the TTDAB (Time-To-Detect And Broadcast) is shown.

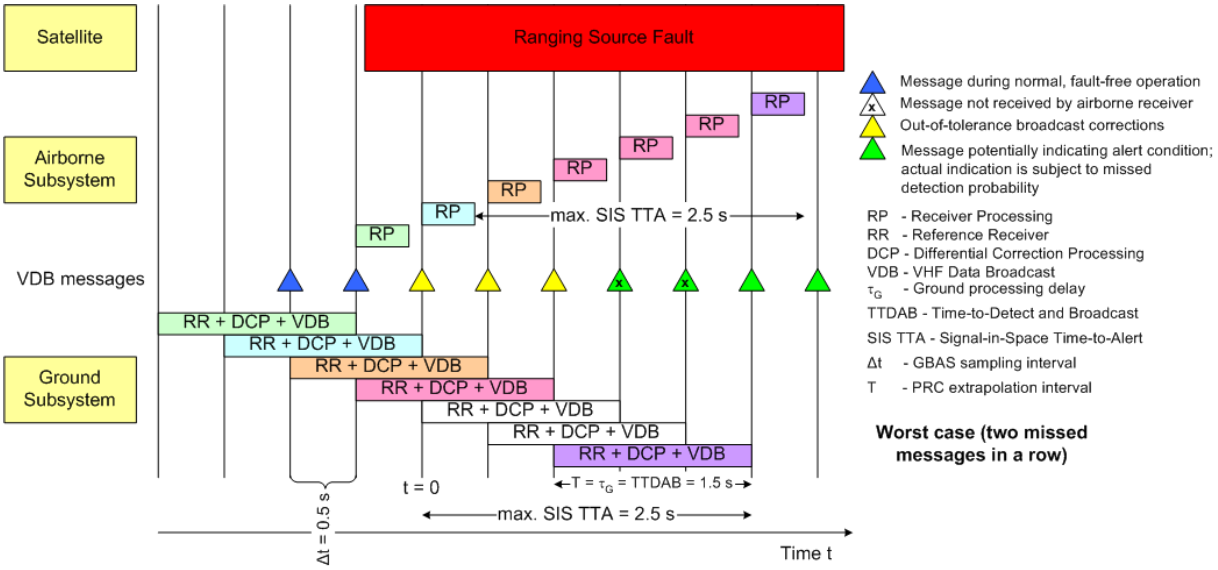

Figure 81 – Timing diagram derivation for below 200 ft. processing derived from (SESAR JU, 2011)

Figure 81 also helps to understand how an error impacts a differential system like GBAS. Considering an error onset just after $t = -0.5\ s$, it could be detected in measurement done at time $t = 0$ s by the ground station for which the measurement rate is 2 Hz. Corrections are received with a time delay of 1.5 seconds due to the time needed to process and broadcast the PRC and RRC. Considering the possibility to have two missed messages, the maximum time that can pass before receiving an integrity message after detection by the ground segment of the first faulty measurement is 2.5 seconds. Knowing that the SiS TTA is 2.5 seconds, and according to Figure 81, the biggest differential error is reached at $t = 2$ generated by an undetected fault lasting 2.5 seconds. It has to be considered that the aircraft measurements sampling rate can be different from the one adopted at ground station, with values bigger than 2 Hz. Moreover, the two subsystem's sampling times could be unsynchronized. According to this condition, it is more realistic to compute the maximum differential error at $t = 2.5$ generated by a fault lasting 3 seconds.

In (ICAO NSP, 2010) it is stated to not consider the airborne processing time (RP box in Figure 81) to derive the monitor performances

5.2 GAST D Integrity Monitoring

This section introduces the monitors present at ground and airborne levels for GAST-D service. Some of them have been already introduced in 2.3.3.3 since they were developed to work also for GAST-C. Monitors developed for GAST-D, or for which a relevant role is expected in the ionosphere anomalies detection, will be described more in details for sake of clarity of the following sections.

5.2.1 GAST D Monitors State-of-Art

5.2.1.1 SQM (Signal Quality monitor)

The Signal Deformation threat has been already introduced in 2.3.3.3.1. In this section a more detailed description of the threat and the monitor will be given.

In (ICAO, 2006) three fault types A, B, C are identified.

- Dead zones; if the correlation function loses its peak, the receiver's discriminator function will include a flat spot or dead zone. If the reference receiver and aircraft receiver settle in different portions of this dead zone, Misleading Information (MI) can result.
- False peaks: If the reference receiver and aircraft receiver lock to different peaks, MI could exist.
- Distortions: If the correlation peak is misshapen, an aircraft that uses a correlator spacing different than the one used by the reference receivers may experience MI.

Signal Quality Monitor (SQM) are designed to protect the users from deformations defined by a threat model, which has three parts that can reproduce the three faults listed above. It is valid for GPS L1 C/A signal:

A. Threat Model A (TMA) consists of the normal C/A code signal except that all the positive chips have a falling edge that leads or lags relative to the correct end-time for that chip. This threat model is associated with a failure in the navigation data unit (NDU), the digital partition of a GPS or GLONASS satellite (ICAO, 2006).

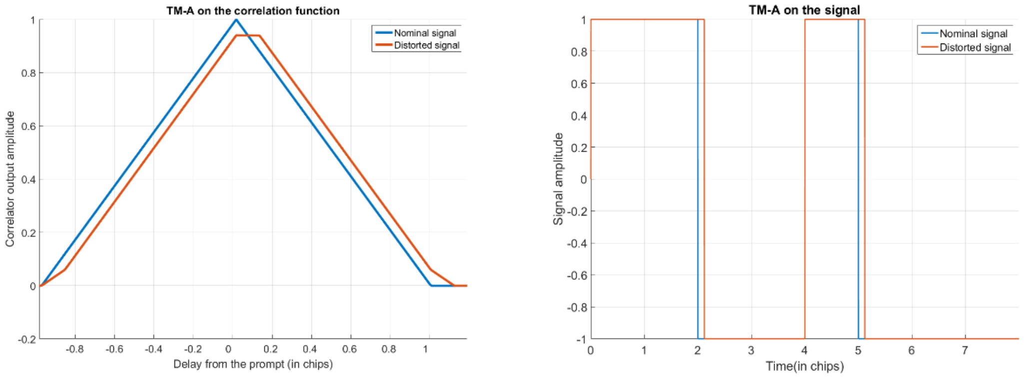

Figure 82 – Threat Model A: Digital failure

Details about the parameters of this threat are shown in (ICAO, 2006)

B. Threat Model B (TMB) introduces amplitude modulation and models degradations in the analog section of the GPS or GLONASS satellite. More specifically, it consists of the output from a second order system when the nominal C/A code baseband signal is the input. Threat Model B assumes that the degraded satellite subsystem can be described as a linear system dominated by a pair of complex conjugate poles. These poles are located at $\sigma \pm j2\pi fd$, where σ is the damping factor in nepers/second and fd is the resonant frequency with units of cycles/second.

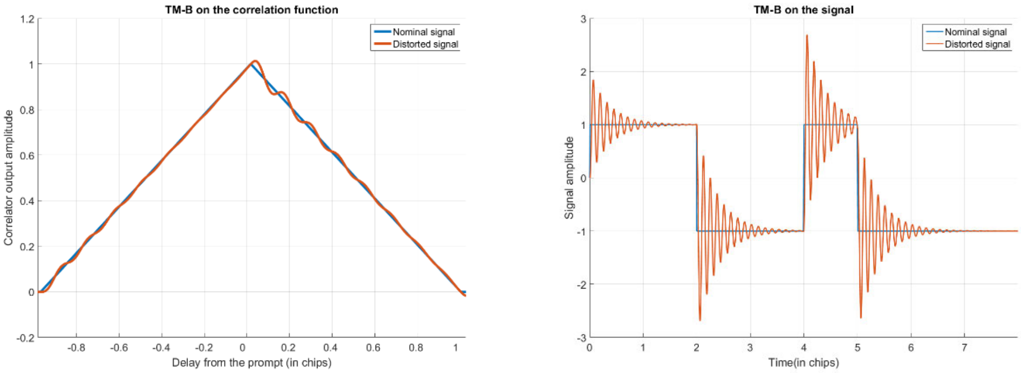

Figure 83 – Threat Model B: Analog failure mode

Details about the parameters of this threat are shown in (ICAO, 2006)

C. Threat Model C introduces both lead/lag and amplitude modulation. Specifically, it consists of outputs from a second order system when the C/A code signal at the input suffers from lead or lag. This waveform is a combination of the two effects described above.

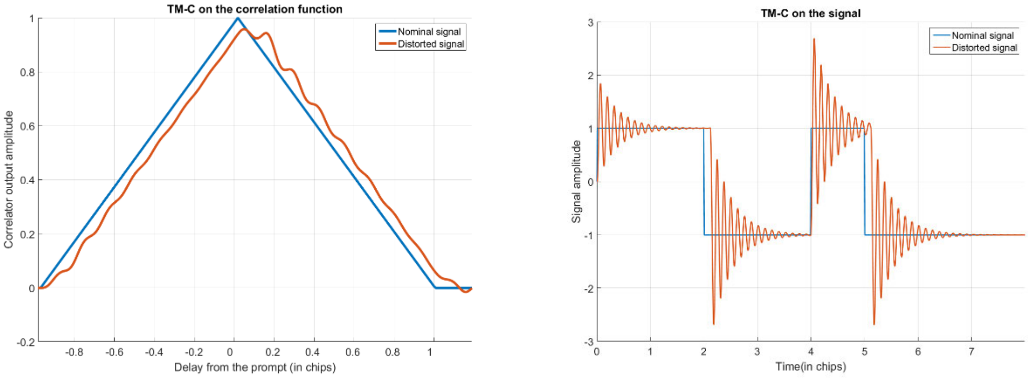

Figure 84 – Threat Model C: Analog and digital failure mode.

Two types of test metrics are formed: early-minus-late metrics (D) that are indicative of tracking errors caused by peak distortion and amplitude ratio metrics (R) that measure slope and are indicative of peak flatness or close-in, multiple peaks. More details about the metrics are given in (Enge, et al., 2000) and (Mitelman, 2004).

The last step is the definition of the thresholds for the two metrics. They are defined as the Minimum Detectable Error (MDE) or Minimum Detectable Ratio (MDR).

$$MDE = (K_{ffd} + K_{md})\sigma_{D,test}$$

$$MDR = (K_{ffd} + K_{md})\sigma_{R,test}$$

Where:

- $K_{ffd} =$ 5.26 is a typical fault-free detection multiplier representing a false detection probability of 1.5×10^{-7} per test;
- $K_{md} =$ 3.09 is a typical missed detection multiplier representing a missed detection probability of10^{-3}per test;
- $\sigma_{D,test}$ is the standard deviation of measured values of difference test metric D;
- $\sigma_{R,test}$ is the standard deviation of measured values of ratio test metric R.

As for the metrics, further details are given in (Enge, et al., 2000) and (Mitelman, 2004).

A failure is declared when the metrics is bigger than the threshold

$$|D,test - \mu_{D,test}| \geq MDE \quad or \quad |R,test - \mu_{R,test}| \geq MDR$$

Where μ, for both the test metric, is the median value across all visible satellites considered as the nominal value of the metric for an undistorted satellite.

5.2.1.2 Low Signal Level Monitor

As said in 2.3.3.3.2 this kind of threat is covered by the SQM.

5.2.1.3 Code-Carrier Divergence (CCD) Monitor

The code-carrier divergence threat is a fault condition that causes the excessive divergence between the measured carrier phase and the code phase. Possible causes of this divergence could be a payload failure or an ionospheric front. However since payload failure has never been observed, it is mainly attributed to the detection of ionosphere anomalous conditions.

Even if this monitor is present also for GAST-C service, for GAST-D service it has to be present at aircraft level as well.

The threat space, in this case, is 2-dimensional and corresponds to the time of the fault onset relative to initialization of the airborne smoothing filter and the divergence rate. The timing of the fault onset relative to the initialization of the airborne filter defines one axis of the threat space since the filter at the ground is supposed to be already in the steady state. If both the filters, at airborne and ground side, are in steady state the differential error introduced by any divergence is minimal (Jiang, et al., 2015).

As mentioned in 2.3.3.3.3 the monitor analyzes the rate of change of two consecutive CMC.

$$CMC(t) = \rho(t) - \phi(t) \qquad \text{Eq. 5.4}$$

Noting ΔT as the sample interval, it is possible to compute the CMC rate as

$$dCMC(t) = \frac{CMC(t) - CMC(t - \Delta T)}{\Delta T} \qquad \text{Eq. 5.5}$$

Thus errors common to code and carrier measurements, such as satellite and receiver clock offsets, troposphere delay error and etc. are eliminated. Constant errors are removed, e.g. the integer ambiguity. The difference between two epochs removes largely the slowly varying biases. The leftover errors appear in the form of rate of change of the ionosphere delay, multipath and noise (Simili, et al., 2006). The errors are then smoothed via two cascaded first order low pass filters f are defined as,

$$F_1(k) = \left(\frac{\tau_{F1} - \Delta T}{\tau_{F1}}\right) F_1(k-1) + \alpha \cdot dCMC(k) \qquad \text{Eq. 5.6}$$

$$F_2(k) = \left(\frac{\tau_{F2} - \Delta T}{\tau_{F2}}\right) F_2(k-1) + \alpha \cdot F_1(k) \qquad \text{Eq. 5.7}$$

Where:

- τ is the filter constant for the first and the second low pass filter
- F_1 is the first order filter output; F_2 corresponds to the second order filter output
- $\alpha = \frac{\Delta T}{\tau}$ is the filter weight

Shorter time constant results in faster detection of CCD failure, and therefore less susceptible to the build-up of divergence induced filter lag errors, but also in noisier test metric.

The test metric can be expressed in the Laplace domain as in (Hwang, et al., 1999):

$$F_2(s) = \frac{1}{(\tau s + 1)^2}\, dCMC(s) = \frac{s}{(\tau s + 1)^2} CMC(s) \qquad \text{Eq. 5.8}$$

The non-centrality parameter of the test metric is the divergence rate d, and the steady state is the same which is independent of the time constant τ,

$$\lim_{s \to 0} sF_2(s) = \frac{s^2}{(\tau s + 1)^2} \frac{d}{s^2} = d \qquad \text{Eq. 5.9}$$

Where:

- d is the divergence rate

In the steady state, assuming the input noise follows a first-order Gauss-Markov distribution, the resulting noise attenuation is derived below when the filter weight is small,

$$\sigma_{F2}^2 \cong \frac{\alpha}{4}\sigma_{dCMC}^2 \qquad \text{Eq. 5.10}$$

The next step is to compute the threshold value for the metric,

$$Th_{CCD} = K_{ffd,mon}\,\sigma_{F2} \qquad \text{Eq. 5.11}$$

The value of sigma is related to the smoothing constants employed in the two low pass filters. The value of $K_{ffd,mon}$ is selected in order to meet the probability of fault-free alarm (Simili, et al., 2006). The value of the monitor standard deviation has been derived in (Simili, et al., 2006) and (Jiang, et al., 2015) for the ground monitor using 30 seconds smoothing constant and airborne one using 100 seconds smoothing constant. For the ground station, the monitor standard deviation is 0.00399 m/s and, considering a probability of false alarm at 10^{-9} ($K_{ffd,mon} = 5.83$), the threshold is set at 0.0233 m/s. The airborne monitor standard deviation is 0.0022 m/s, smaller than for the ground station monitor due to the use of 100 seconds as smoothing constant, and the threshold is set at 0.0125 m/s

The metric F_2 is finally compared to the threshold Th_{CCD} to perform a decision test and detect possible faults on the measurements. The performance of the monitor is related to the magnitude of the divergence rate (Simili, et al., 2006).

The detection capabilities of the monitor are, however, not only related to the divergence rate. The time elapsed from the fault onset is at same time important to correctly derive them (Jiang, et al., 2015). In this context only the case where both filters have similar properties (same smoothing constant and in steady state) and they have converged to a new steady state after the divergence fault onset is considered. Under this hypothesis the divergence rate that can be detected with a $P_{md} = 10^{-9}$ can be estimated. This value can be considered as a sort of limit since all values bigger than this will be detected with a $P_{md} < 10^{-9}$.

$$F_{2,limit} = \sigma_{F2}(K_{ffd,mon} + K_{md}) \qquad \text{Eq. 5.12}$$

The value of $K_{ffd,mon} = 5.83$ and $K_{md} = 5.81$ as for the VPL and LPL computation (Simili, et al., 2006).

The limit divergence rates for the ground and airborne monitor are 0.0464 and 0.256 m/s.

5.2.1.4 Excessive Acceleration (EA) Monitor

The Excessive Acceleration (EA) threat is a fault condition in a GNSS satellite that causes the carrier (and code in unison) of the broadcast signal to accelerate excessively. The most probable causes would be a fault of the operational satellite clock or an undesired acceleration in the satellite position due to an unscheduled manoeuvre. Even if this monitor is already present for GAST-C service, the analysis of the test statistic is useful to introduce the innovations or the analysis done for GAST-F. Moreover an alternative test statistic based on the estimated acceleration and the velocity has been proposed (Stakkeland, et al., 2014).

The range acceleration error is estimated for any satellite measured over any 3-epochs interval, the formula is given in (Brenner, et al., 2010).

$$\ddot{\phi}(k-1) = \frac{\left(\phi(k) - 2\phi(k-1) + \phi(k-2)\right)}{\Delta T^2} \qquad \text{Eq. 5.13}$$

Where:

- $\phi(k)$ is the phase measurement for epoch k
- ΔT is the sampling interval in s, for GBAS ground station this value is 0.5 seconds.

Considering the SiS TTA requirement (5.1.3), the differential error after 2.5 seconds from the first faulty measurement, and caused by 3 seconds acceleration, is given as:

$$E_r\left(t_{fault}\right) = \frac{1}{2}\,a\left(t_{fault}\right)^2 - \frac{1}{2}\,a\left(t_{fault} - t_{gs}\right)^2 - \left(\frac{0.5\,a\left(\left(t_{fault} - t_{gs}\right)^2 - \left(t_{prc} - \Delta T\right)^2\right)}{\Delta T}\right)\cdot t_{az} \qquad \text{Eq. 5.14}$$

Where:

- E_r is the differential error caused by any acceleration, the term in bracket refers to time elapsed from the fault onset
- a represents an acceleration with no limitation in magnitude
- t_{fault} is the time elapsed from the fault onset
- t_{az} is the time between PRC and RRC computation and their application at aircraft side
- $t_{gs} = t_{PRC\,rate} + t_{gnd\,proc}$; $t_{PRC\,rate}$ is the PRC, and RRC, update period in seconds. $t_{gnd\,proc}$ is the time needed at ground station to process measurement, it is assumed to be 1 second.

The first term in Eq. 5.14 is the error induced in the measurement at the aircraft side. The second one, represents the part of acceleration error present in the PRC and compensated when PRCs are applied. The last term is the computation of the RRC based on the difference between two consecutive epochs. RRC are then multiplied by the time elapsed from their computation to the moment when they are used at aircraft side. Developing Eq. 5.14 with a $t_{fault} = 3$; $t_{gs} = 1.5$, $t_{az} = 1.5$ and a $\Delta T = 0.5$ it is possible to derive the impact of an acceleration a on the differential error.

$$E_r\ (3) = 4.5\ a - 1.125\ a - 1.875\ a = 1.5\ a \qquad \text{Eq. 5.15}$$

Eq. 5.15 can be generalized as:

$$E_r\ (3) = a\ \left(t_{gs}\left(t_{gs} + 0.5\right)\right)/2 \qquad \text{Eq. 5.16}$$

In Figure 85, it is possible to see the differential error, computed as in Eq. 5.16, at $t = 3.0$ seconds. The fault onset, for this case, is at $t = 0$ just after the measurement done at the same epoch. The first faulty measurement is so recorded at $t = 0.5$ seconds. The maximum differential error, always considering a SiS TTA of 2.5 seconds, is at $t = 3$ s. From this epoch, the PRC and RRC, containing information about the acceleration, permit to decrease the total differential error. It has to be considered that the aircraft may have a different measurement interval than the one used at ground. In this case the differential error after $t = 3$ grows and each 0.5 seconds is reduced by the received PRC and RRC.

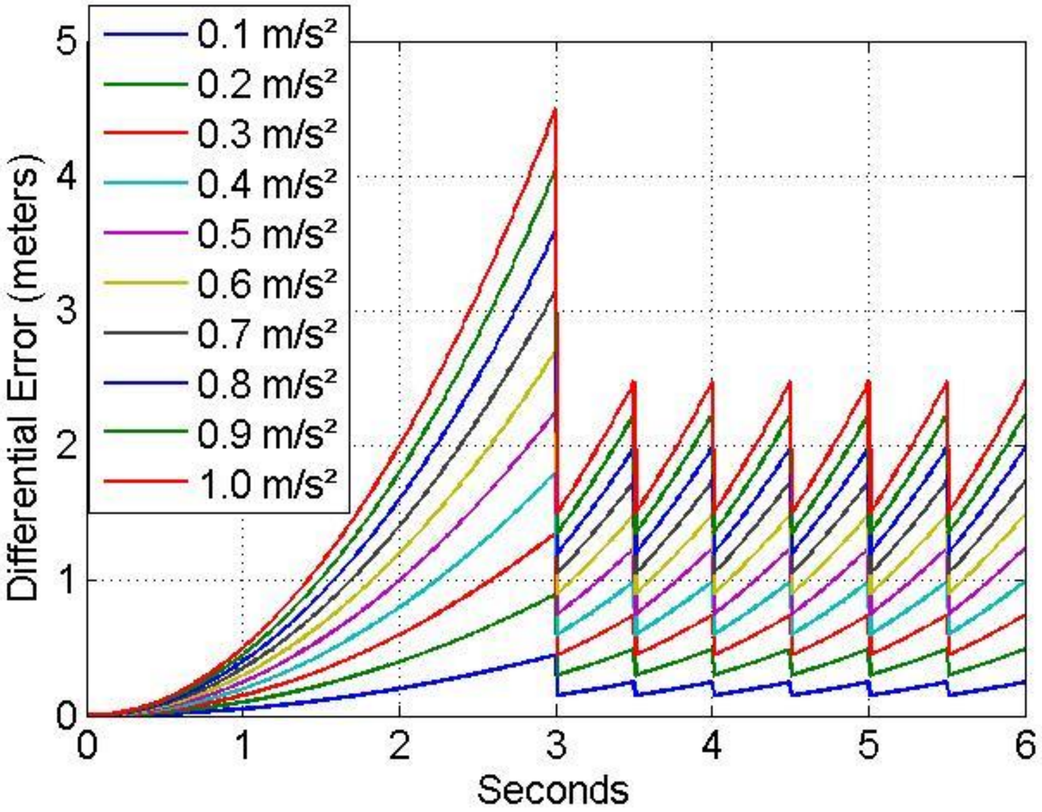

Figure 85 – Acceleration induced differential range error

The shape of the curves, in Figure 85, is caused by the non-synchronization of the measurements between the GS and the aircraft and the possible difference in the measurements interval between the two. Each 0.5 seconds the differential error decreases thank to the reception of a new set of PRC and RRC.

Considering the requirement for the ground monitor presented in 5.1.1, and also taking into account the performances of monitors with respect to the P_{md} curve requirement a maximum differential error of 1.4 meter to detect with a $P_{md} < 1 \cdot 10^{-4}$ is considered (Brenner, et al., 2010).

Knowing that the maximum error after 2.5 seconds from the first faulty measurement is 1.5 a, it is possible to derive the maximum acceleration which must be detected by the monitor with the required probability in order to meet the constraint of $E_r < 1.4$ meters.

$$1.5 * a = 1.4 \ \rightarrow a = \frac{1.4}{1.5} \rightarrow a = 0.933\, m/s^2 \qquad \text{Eq. 5.17}$$

It has to be considered however that the detected acceleration, at first epoch after the fault onset, is the half of the real value (considering the case of a fault onset just after the measurement) or less (considering the case of fault onset in between two ground measurements). Simulating a constant value of the errors on phase measurements ϕ, after the compensation for satellite motion, clock drifts and receiver clock compensation and including an acceleration a lasting 0.5 seconds only on measurement at epoch t, equation Eq. 5.13 becomes:

$$\ddot{\phi}(t - \Delta\mathrm{T}) = \frac{\left(\phi(t) + 0.5a\Delta T^2 - 2\phi(t - \Delta T) + \phi(t - 2\Delta T)\right)}{\Delta T^2} = \frac{0.5a\Delta T^2}{\Delta T^2} = 0.5a \qquad \text{Eq. 5.18}$$

Considering that the detected acceleration in the first epoch is the half of its real value the threshold must be lower than the half of the values computed in Eq. 5.17, so lower than0.4665 m/s^2, to be sure that all undetected values will not cause a differential error bigger than 1.4 meters.

The last step is to analyze the feasibility of the monitor including the noise contribution to the acceleration. According to (Brenner, et al., 2010), the phase noise sigma with only 2 RR and the lowest carrier-to-noise ratio at 32 dB-Hz and PLL tracking loop bandwidth of 10 Hz is $0.25/\sqrt{2}\, cm$. Considering the model of the test as in equation Eq. 5.13, the variance of the test is

$$Var[\ddot{\phi}] = \left(\sigma_\phi^2 + 4\sigma_\phi^2 + \sigma_\phi^2\right)/0.5^4 \qquad \text{Eq. 5.19}$$

Replacing the value of the standard deviation stated before, the standard deviation of the test becomes

$$\sigma_{\ddot{\phi}} = \sqrt{6}\,\left(\frac{0.25}{\sqrt{2}}\right) /\, 0.25 \ = 1.73\, cm/s^2 \qquad \text{Eq. 5.20}$$

Assuming that the threshold is set at 6 sigma in order to take into account the probability of false alarm and another margin of 4 is considered for the probability of missed detection (Brenner, et al., 2010), the value of 10 times sigma represent the limit case and it is $0.173\ m/s^2$ that is well below the acceleration limit of $0.4665\, m/s^2$ (Brenner, et al., 2010). This shows that the monitor is feasible for GAST-D processing scheme with 0.5 seconds update period for PRC and RRC.

5.2.1.5 Ephemeris Error/Failure Monitor

Ephemeris fault has been described in 2.3.3.3.5. According to (ICAO NSP, 2010) several kinds of monitors can be used to monitor ephemeris

- **Long Baseline**. This requires the ground subsystem to use receivers separated by large distances to detect ephemeris errors that are not observable by a single receiver.
- **SBAS**. Using the information provided by the SBAS satellites is possible to monitor the ephemeris data, this technique provides optimum performance improving the detection of small errors.
- **Ephemeris Data Monitoring**. This approaches compare the broadcast ephemeris over consecutive satellite orbits. This monitor assumes that the only possible threat is due to an upload failure from the ground control center.
- **Delta-V**. This monitor covers the cases of uncommented satellite manoeuvres or manoeuvres out of view under unchanged ephemeris.

A last way to monitor the ephemeris state is the computation of the ephemeris error bound. This method is similar to the protection level seen in section 2.3.3.2. The vertical and lateral position bound is computed as:

$$VEB = \max_{j} \{VEB_j\} \qquad \text{Eq. 5.21}$$

$$LEB = \max_{j} \{LEB_j\} \qquad \text{Eq. 5.22}$$

The value is computed for each ranging source, j, used in the position solution computation. For each source the error position bound is:

$$VEB_j = |S_{vert,j}|\, x_{air}\, P_{e,j} + K_{md\,e,j}\sqrt{\sum_{i=1}^{N} S_{vert,i}^2 \times \sigma_i^2} \qquad \text{Eq. 5.23}$$

$$LEB_j = |S_{lat,j}|\, x_{air}\, P_{e,j} + K_{md\,e,j}\sqrt{\sum_{i=1}^{N} S_{lat,i}^2 \times \sigma_i^2} \qquad \text{Eq. 5.24}$$

Where:

- x_{air} is the slant distance between the LGF and the aircraft
- N is the number of used ranging sources

- $P_{e,j}$ is the ephemeris decorrelation parameter for the j^{th} ranging source in message type 1
- $K_{md\ e,j}$ is the broadcast ephemeris missed detection multiplier from message type 2

As for the protection level, the VEB and LEB do not have to overcome the VAL and LAL limit.

5.2.1.6 Ground Receiver Fault Monitor

In order to detect possible failures of one of the reference receivers used at ground station B values are computed (Shively, 2009). The monitor compares the B-values, computed for each satellite and excluding one station per time to a detection threshold (Shively, 2009). The equation to compute B values is given in Eq. 2.62.

$$B_j^i = PRC^i - \frac{1}{M-1}\sum_{\substack{j=1 \\ j\neq m}}^{M} PRC_j^i$$

Where

- i is related to the i^{th} satellites
- j is related to the j^{th} reference receiver
- PRC^i is the correction computed for satellite i using all RRs

In case of threshold exceeding the related PRC and RRC for a precise satellite-receiver couple are removed from the averaging process shown in 2.3.2.

5.2.1.7 Dual Solution Ionosphere Gradient Monitor Algorithm (DSIGMA)

One of the main threats in GNSS is the ionosphere, and in particular for GBAS, the detection of the ionospheric gradients. This condition generates a different delay between the ground and the airborne that is not fully corrected via the differential process.

In order to mitigate errors induced by ionospheric anomalies, the position solutions is computed relying on two different carrier smoothing time constants (RTCA Inc.; DO253-C, 2008) is used. This dual solution computation has two purposes.

1. The first one is the detection of large ionospheric gradients between ground measurement and airborne measurement observables through both filter outputs. Hence a threshold can be applied to this detection statistic in order to detect a large portion of the ionospheric anomalies.
2. The second application of the dual solutions is to compute a bound for the 30 seconds smoothed position (excluding the impact of ionospheric anomalies). By adding the direct observation of the magnitude of the difference between the 30 seconds smoothed position and the 100 seconds smoothed position to the protection level computation, a new protection level, which is

guaranteed to bound the 30-second position solution with the required 1x10-7/approach is obtained.

At ICAO NSP level, a DSIGMA algorithm has been proposed also in the corrected range domain (ICAO NSP, 2016). The scope of this algorithm is mostly the detection of anomalous ionospheric gradients since information about the position accuracy are not available. The test is performed by analyzing the difference between the corrected pseudoranges smoothed by 2 different time constant, 100 s and 30 s.

$$test = \rho^c_{100} - \rho^c_{30} \qquad \text{Eq. 5.25}$$

Where ρ^c_x are the corrected pseudoranges smoothed with a filter having a time constant x.

Eq. 5.25 can be rewritten considering how the corrected pseudoranges are derived.

$$test = \tilde{\rho}_{air\,100} - PRC_{100} - \tilde{\rho}_{air\,30} + PRC_{30} \qquad \text{Eq. 5.26}$$

Where:

- $\tilde{\rho}_{air\,100}$ is the smoothed pseudorange at airborne side according to the used smoothing constant, 100 seconds for this case
- PRC_{100} are the pseudorange correction for the used smoothing constant.

The test relies on the different response of the filter for 100 and 30 seconds smoothing case in presence of a time-varying ionospheric delay.

In Figure 86, it is possible to see the filter response for the two smoothing constants in presence of a varying ionospheric delay. The delay induced by an ionosphere gradient, impacting an aircraft, is simulated. In this scenario, the aircraft moves faster than the front and the raw delay is decreasing at airborne level (red line on left side figure). The ground station is, instead, impacted at epoch 420 and the delay is growing. In the right side of Figure 86 the filter response for both, aircraft and ground station, is represented for 30 and 100 seconds smoothing constants. It is possible to see that the filter response differs for the two constants.

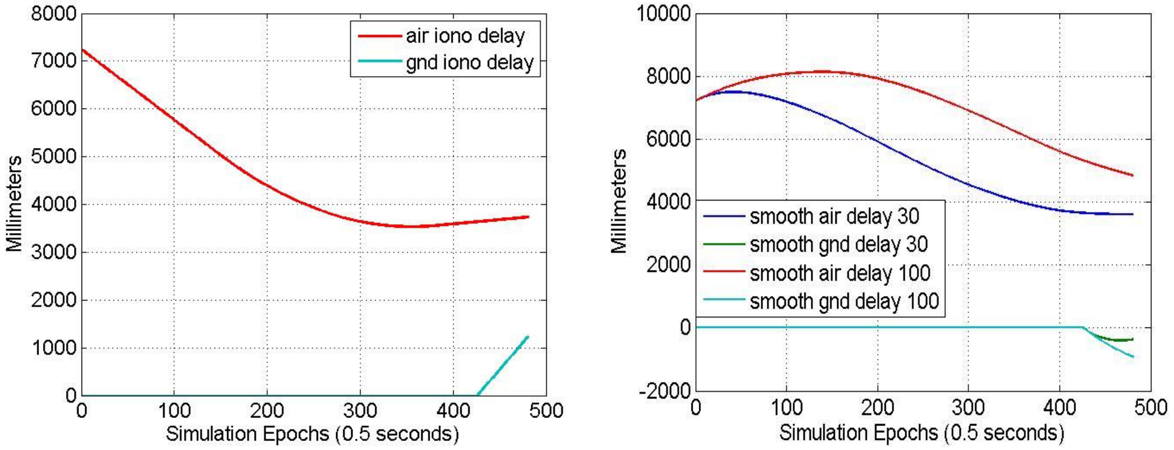

Figure 86 – simulated ionospheric delay (left) and related smoothing time variant filter response

In the case of fault free measurements, the test statistic is assumed to follow a central normal distribution. Results in (ICAO NSP, 2016) show that the standard deviation obtained must be bounded to cover the CDF of the obtained errors. In (ICAO NSP, 2016) the value of the standard deviation of the monitor is determined for all elevations, below 30° elevation angle and above 30° elevation angle.

Table 24 – DISGMA test metric standard deviation (ICAO NSP, 2016)

All Elevations	< 30°	>30°
0.1740791 m	0.2075552 m	0.1309688 m

Assuming a $P_{fa} = 10^{-8}$ it is possible to compute the P_{md} for each of the test metrics standard deviation.

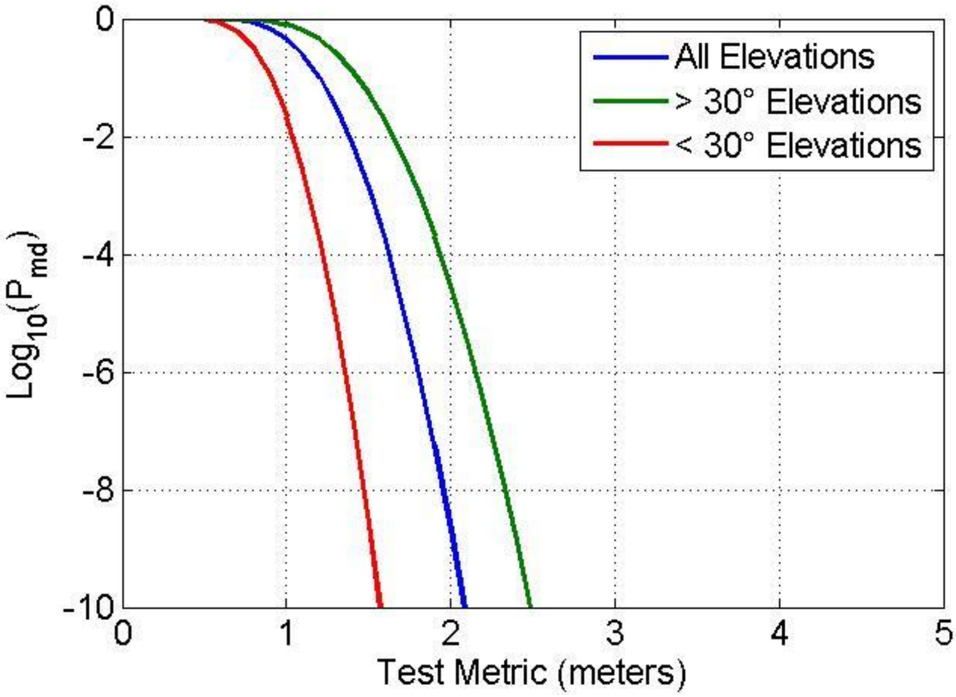

Figure 87 - P_{md} performances for DSIGMA

Figure 87 shows the results for the three test metrics defined in Table 24, it is possible to see that using the all elevations standard deviation, any error bigger than 2 meters can be detected with a $P_{md} < 10^{-9}$.

5.2.1.8 Ionosphere Gradient Monitor (IGM)

In (ICAO NSP, 2010), it is stated that any ground system providing a GAST-D service must monitor "if the probability that there is an undetected spatial ionospheric delay gradient with a magnitude greater than 1.5m/D in the direction of any approach supporting GAST-D is greater than 1×10^{-9}". Where D is the distance between the reference point of the ground subsystem and the threshold typically set at 5 km. The direction of the approach is defined by the runway heading.

To meet previous requirement, an ionosphere gradient monitor algorithm is installed in any ground station providing GAST-D service. The way it works is presented in (Khanafseh, et al., 2010). It uses the phase measurements from different RRs. The principle is based on the phase measurements difference, between at least two RRs, that could exist in presence of an ionospheric gradient. In Figure 88 an example of phase difference due to an ionospheric gradient is shown.

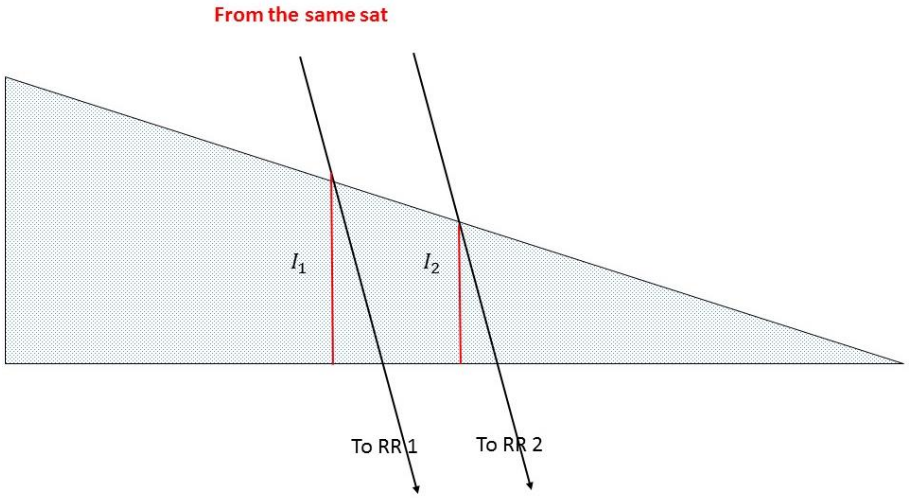

Figure 88 – Ionospheric delay on two different RRs

Under nominal ionospheric conditions, if the baseline length between the 2 RRs is relatively short (less than a kilometre), $I_2 - I_1$ (Figure 88) will be on the order of millimeters and usually can be neglected (Khanafseh, et al., 2010). If an ionospheric front exists, the difference can be detected using the phase measurement from two RRs.

Considering the phase measurement as in Eq. 2.11, the difference between phase measurements from two RRs at the same epoch is (Khanafseh, et al., 2010):

$$\Delta\phi_{RR1/RR2} = e^t\, x_b + \Delta t_{u_{RR1-RR2}} + \lambda\, \Delta \mathrm{N}_{\mathrm{RR1-RR2}} + \Delta \mathrm{I}_{\mathrm{RR1-RR2}} + \eta_{\mathrm{RR1-RR2}} \qquad \text{Eq. 5.27}$$

Where:

- $e^t\, x_b$ is the geometrical term including e, the user-satellite unit line of sight vector, and x_b the baseline vector between the two RR antennas
- $\Delta t_{u_{RR1-RR2}}$ is the receiver clock difference
- λ is the wavelength of the used frequency
- $\Delta \mathrm{N}_{\mathrm{RR1-RR2}}$ is the phase ambiguity difference (only integer values are allowed)
- $\Delta \mathrm{I}_{\mathrm{RR1-RR2}}$ is the ionospheric delay difference
- $\eta_{\mathrm{RR1-RR2}}$ is the phase noise and multipath difference term

Looking at Figure 88, it is possible to rewrite the ionospheric delay difference term as

$$\Delta \mathrm{I}_{\mathrm{RR1-RR2}} = \alpha\, |x_b| \qquad \text{Eq. 5.28}$$

α is the ionospheric gradient given in mm/km. typical values of α are from two to six Table 2.

A problem to solve in Eq. 5.27 is the removal of the receiver clock difference. Assuming that the satellite under analysis is affected by an ionospheric gradient, it is possible to find another one that is assumed to be fault-free (Khanafseh, et al., 2010). To verify this assumption, the other satellite should be spatially separated from the monitored satellite, so that it is not affected by the same ionospheric anomaly. The computation of the double measurement difference with this fault-free satellite removes the receiver clock from Eq. 5.27. The double measurement difference can be written as:

$$\Delta\nabla\phi = \Delta\nabla e^t\, x_b + \lambda\, \Delta\nabla N_{RR1-RR2} + \alpha|x_b| + \Delta\nabla\eta_{RR1-RR2} \qquad \text{Eq. 5.29}$$

All terms now take into account the difference from the two satellites and two receivers (Δ^{∇}), except the ionospheric delay term $\alpha|x_b|$ that is supposed to impacts only the first satellite.

The geometrical term can be removed from Eq. 5.29 knowing the user-satellite vector for any of the two satellites and knowing the baseline vector as well. Eq. 5.29 becomes

$$\Delta\nabla\phi - \Delta\nabla e^t\, x_b = \lambda\, \Delta\nabla N_{RR1-RR2} + \alpha|x_b| + \Delta\nabla\eta_{RR1-RR2} \qquad \text{Eq. 5.30}$$

The test statistic as in Eq. 5.30 is still affected by the phase ambiguity difference term $\Delta\nabla N_{RR1-RR2}$, and so it cannot be used to estimate ionospheric gradients. Knowing that the phase ambiguity is an integer, it is possible to remove it by removing the integer part from Eq. 5.30 (Khanafseh, et al., 2010).

$$s_{IGM} = \Delta\nabla\phi - \Delta\nabla e^t\, x_b - round\left(\Delta\nabla\phi - \Delta\nabla e^t\, x_b\right)\lambda_{L1} = \alpha|x_b| + \Delta\nabla\eta_{RR1-RR2} \qquad \text{Eq. 5.31}$$

The necessary condition for a front detection is that its value is not an integer number of wavelength.

In absence of ionospheric gradients, the test statistic follows a normal distribution with zero mean and standard deviation equal to $\sigma_{test} = 2\sigma_{\phi}$ (Khanafseh, et al., 2010). The threshold for the test statistic is defined as:

$$Th = K_{ffd}\, \sigma_{test} \qquad \text{Eq. 5.32}$$

Considering that an ionospheric front can have all possible direction, at least two non-collinear baselines are needed to have detection for all possible fronts. The advantage of this monitor for the detection of ionosphere fronts, with respect to the CCD monitor, is the non-dependency from the ionospheric delay rate of change.

Details about the monitor performance are given in (Khanafseh, et al., 2010).

5.2.2 GAST D Monitoring Challenges

Despite the implementation of monitors at the airborne side and the development of requirements in the range domain, GAST-D has still some problems related to the integrity that does not allow this service to be validated.

In this section the conditions under which the integrity is not reached will be presented. Finally, after the identification of the threat area to monitor the proposed solution will be presented as well.

5.2.2.1 CCD Inefficiency for Slow-Moving Fronts

As seen in 5.2.1.2, the CCD monitor efficiency is strictly related to the rate of change of the code-carrier divergence. For an ionospheric front, this rate depends on the projection of the speed difference between the satellite-user Ionospheric Pierce Point (IPP) and the front gradient called $slope$ in the following equation.

$$d\left(\frac{m}{s}\right) = \Delta v\left(\frac{km}{s}\right) * slope\left(\frac{m}{Km}\right) \qquad \text{Eq. 5.33}$$

In equation Eq. 5.33 the value of Δv is the difference between the IPP speed and the ionospheric front speed as:

$$\Delta v = \left|v_{sat,proj} - v_{front}\right|$$

Where $v_{sat,proj}$ is the projection of the satellite-user IPP speed in the same direction of the ionospheric front speed.

In case of small values of Δv, a front is undetected by the CCD. In Figure 89, it possible to see a case of stationary front with two satellites impacted by the front. It has to be considered that it is quite unlikely that both satellites have the same value of $v_{sat,proj}$, so just one of them is considered to be totally undetected.

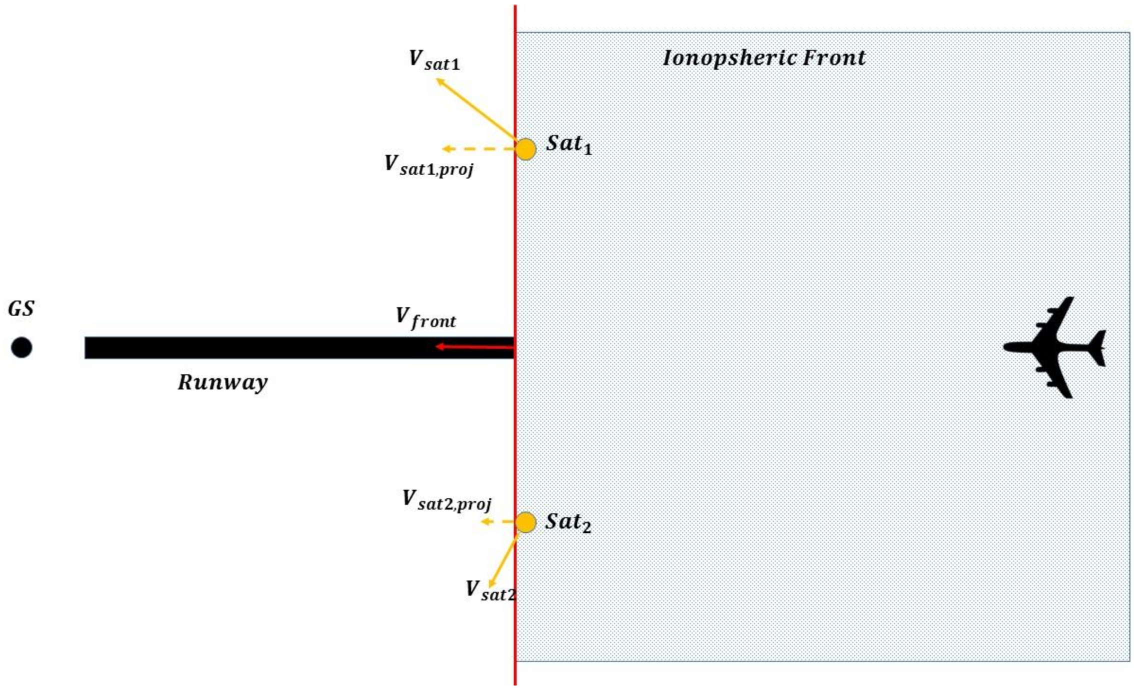

Figure 89 – example of stationary front for possible worst case geometry (Lee, et al., 2011)

Knowing that the detection limit value of d are 0.0464 m/s and 0.0256 m/s, it is possible for defined values of the ionospheric front gradient to compute the limit of Δv according to Eq. 5.33.

Table 25 – Difference speed limit for CCD detection

$\boldsymbol{Iono\ Front\ Gradient\ \left(\frac{m}{Km}\right)}$	$\boldsymbol{\Delta v\ limit\ \left(\frac{km}{s}\right)}$	
	Ground CCD	Airborne CCD
0.1	0.464	0.256
0.2	0.232	0.128
0.3	0.155	0.0853
0.4	0.116	0.0640
0.5	0.0928	0.0512

It is useful to say that the detection performance of the CCD is not related only to the divergence rate. The filter time constant used impacts the time-to-detect (Simili, et al., 2006)as well. The time of the fault onset with respect to the airborne and ground filter initialization impacts the differential error that may occur due to a divergence fault. The analysis has only the scope to derive a series of Δv limits to simulate an undetected ionospheric front.

5.2.2.2 Anomalous Atmospheric Behaviour on IGM

The IGM monitor, as seen in 5.2.1.8, is not dependent from the ionospheric gradient divergence rate, and consequentially from the front/IPP speed. This monitor is supposed to cover all the zones of the ionospheric gradient threat space not covered by the CCD. Unfortunately, Honeywell has observed some malfunctions for an IGM installed at Houston airport (ICAO NSP WGW/WP 16, 2014). In particular, in certain day and more precisely in certain hours, the noise level of the test statistic was increased. In Figure 90, it is possible to see the test statistic for an entire day.

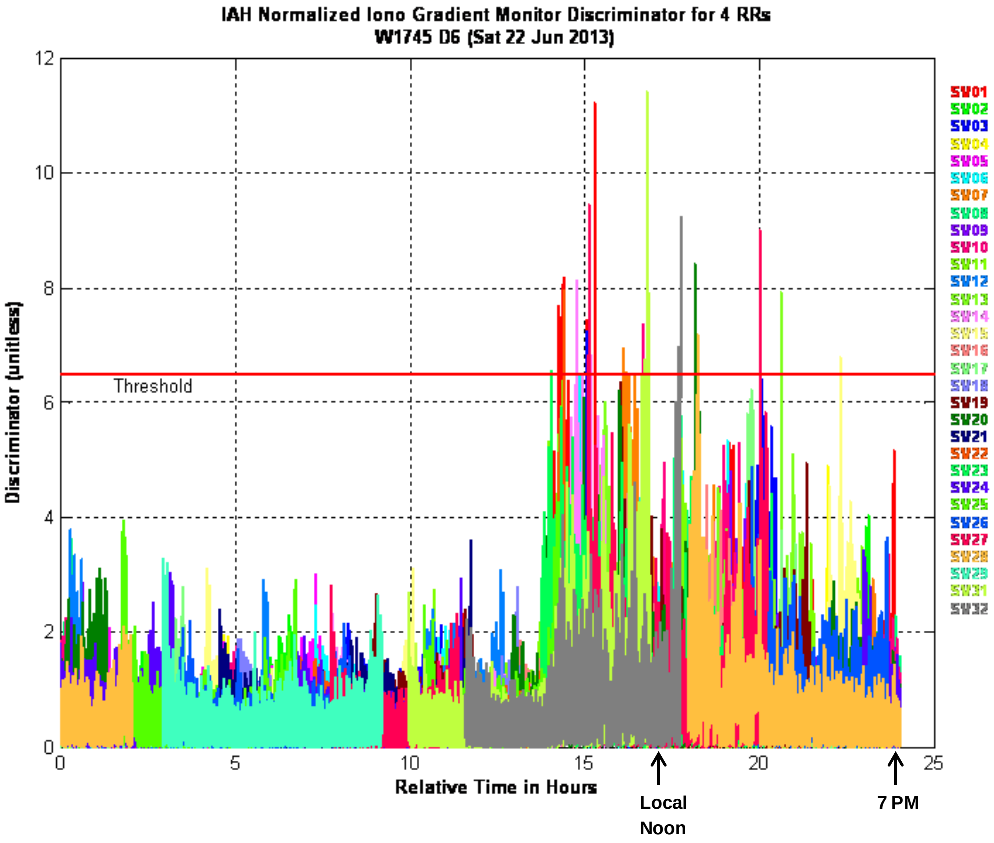

Figure 90 – IGM test statistic for Houston airport (ICAO NSP WGW/WP 16, 2014)

As visible from Figure 90, starting from the local 10:00 and until 19:00, the test statistic is frequently exceeding the detection threshold.

Further investigation of additional days and additional sites revealed these phenomena were present at other locations. General statements about these gradients which could be made based on the observed data include:

1. Observed from approximately 10 AM to 8 PM local time
2. Not observed at night
3. Observed mostly during hotter, mostly clear days
4. Not observed during cold, overcast, or rainy days
5. Observed at all azimuths
6. Observed mostly at lower elevations

This analysis done by Honeywell has led to exclude the ionosphere as a cause of these alarms, since no effects were seen on the other monitors installed in the GS like the CCD or the EA monitor. After further analysis, the possible cause of this anomaly has been identified to be a gradient of the troposphere (or at least the lower region of the troposphere) (ICAO NSP WGW/WP 16, 2014).

This effect can impact the GBAS in two different ways:

- Continuity; A double-difference-based IGM similar to Honeywell's implementation will be impacted by this "tropospheric" activity, which will likely result in false monitor alarms and loss of GAST-D functionality. Based on observed troposphere gradients, the frequency of false monitor trips could lead to unacceptable continuity performance for GAST-D operations.
- Although the range error impact from these hypothesized "tropospheric" gradients is small in comparison to anomalous ionospheric gradients, they could be hazardous when combined with the presence of an anomalous ionosphere gradient. It is possible that these troposphere gradients, although short lived, may blind the Ground Subsystem Monitor used for detection of anomalous ionosphere gradients.

In order to guarantee the integrity level requirement for GAST-D, another monitor has to be found in order to validate it for CAT II/III operations.

5.2.2.3 Residual Ionosphere Threat Model to Monitor

Sections 5.2.2.1 and 5.2.2.2 have shown some particular atmospheric conditions that do not permit to reach the required integrity level for GAST-D service. Before proposing a solution to the presented problems, it is good to identify the area of the ionosphere threat space that is responsible for this issue. It is also important to estimate the maximum ionosphere delay that may impact all the undetected satellites.

Resuming what has been presented in the previous chapter, the critical conditions are assumed to occur under the following circumstances:

- IGM provides insufficient integrity since it is impacted by a tropospheric gradient event. This condition appears in some hours of the day and not all days.
- The front moves with a relatively low speed in order to be undetected by airborne CCD for one or more satellites.
- The ionospheric delay d, given in m/s, has to be limited since it impact the test metric of the DSIGMA. The bigger the induced delay is, the bigger the test metric, and the lower the P_{md} of the test.
- The ionospheric front does not impact the GS since the PRC and RRC may compensate the induced error delay. Moreover the CCD at the ground has different performances than the one at the airborne side, if a front impacts both ground and airborne receivers, the detection performance is improved.

Considering that the critical point for GAST-D is at CAT I decision height (200 ft.), a critical case for an ionospheric front respecting the previous condition is represented in Figure 91.

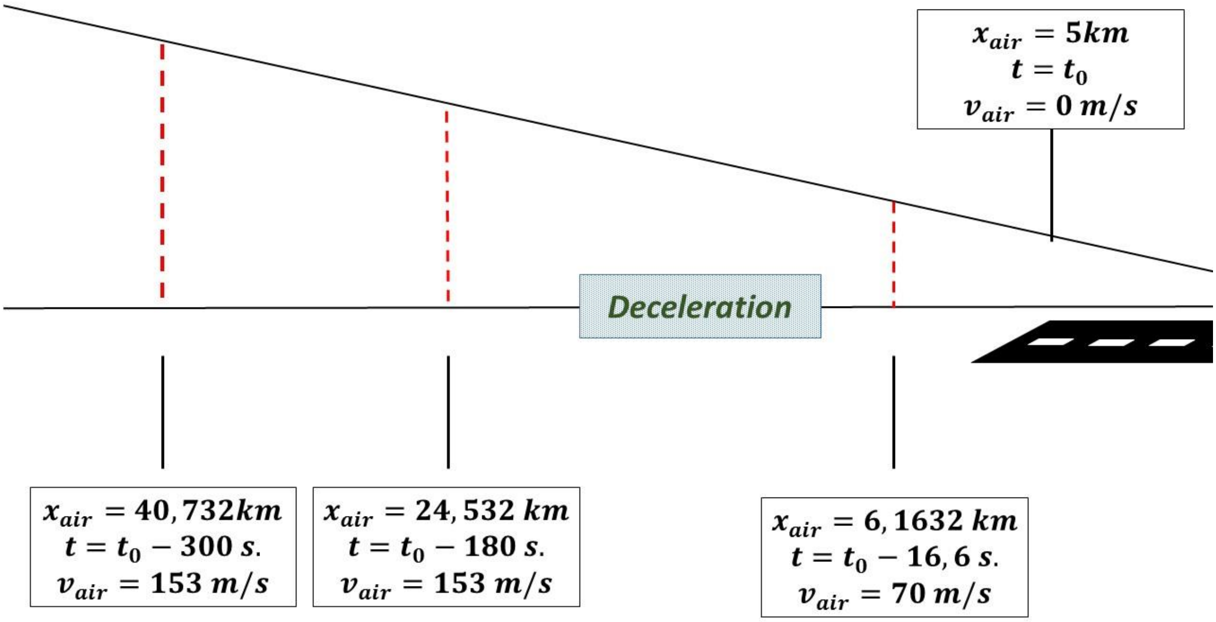

Figure 91 – Simulation of maximum induced delay for an ionospheric front impacting the aircraft but no the GS

The induced range delay for the case depicted in Figure 91 can be computed, taking into account the impact of the smoothing filter and the relative speed between the user IPP and the ionospheric front as:

$$D = slope * \min\left\{(x_{air} + 5) + \left(2 * \tau * \left(v_{IPP} - v_{front}\right)\right); W\right\} \qquad \text{Eq. 5.34}$$

Where:

- x_{air} is the horizontal distance between the aircraft and the LTP
- $2 * \tau * \left(v_{IPP} - v_{front}\right)$ is the contribution of the smoothing filter to the range error.
- W is the width of the ionospheric front as depicted in Figure 3

In Eq. 5.34, the smoothing filter contribution term refers to the steady state condition for both 30 and 100 seconds filters. This condition represents the maximum value induced by the smoothing filter. For a 100 seconds smoothing filter, this condition is verified after 360 seconds, during this time the induced range error is smaller than the one in Eq. 5.34.

Considering the biggest slope provided in the threat model, a smoothing time constant of 30 seconds and a relative speed of 0.11 km/s, the value of the delay in equation Eq. 5.34 is 6.38 meters. The value of 6.1632 km is valid only if the front speed is aligned with the aircraft speed. In other cases, the distance can be even lower. Figure 92 shows an example of an aligned front and one of a misaligned front where the induced range error is lower than the one induced by an aligned front.

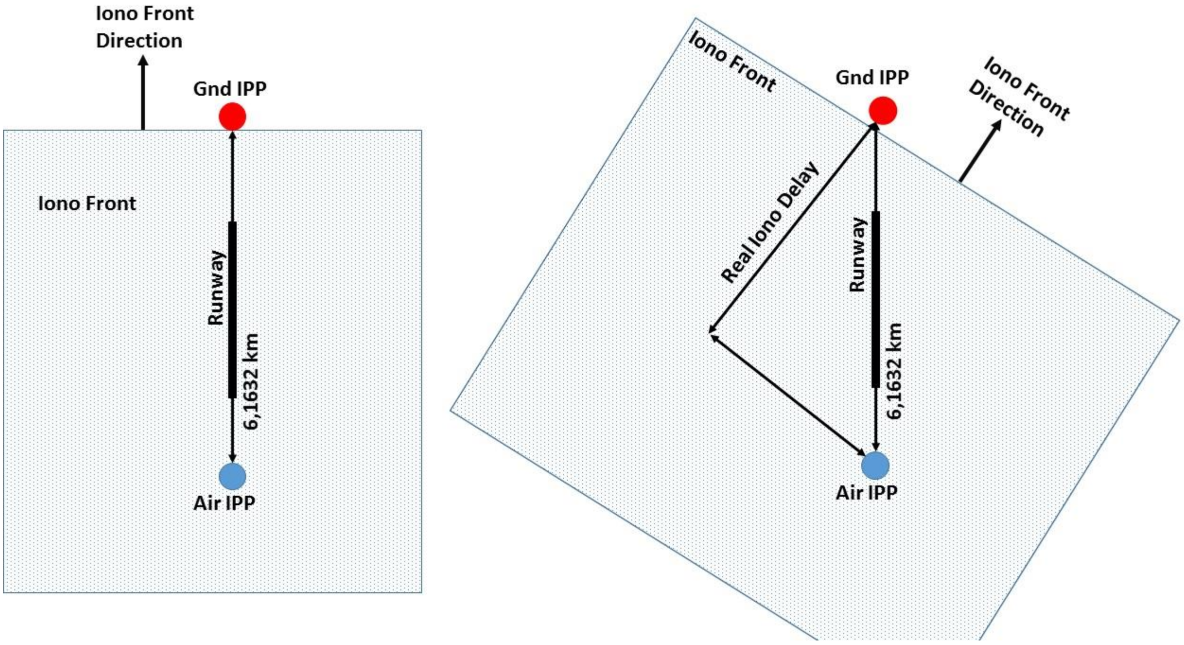

Figure 92 – Ionospheric induced range error for different ionospheric angle

The condition depicted in Figure 91 and Figure 92 describes a possible case on which a faulty satellite may impact the aircraft but not the GS providing the maximum induced range error. When this scenario is considered for all satellites in view, due to their different position in the sky, different interactions with the front are possible. For some of them, both air and ground IPP will be impacted by the front. For other satellites, the differential speed will be different causing either a CCD detection or a lower range error. Satellites present at the opposite azimuth may be not impacted by the front at all.

The scenario presented before can be considered as the worst-case for one satellite, considering an ionospheric front moving in the same direction of the aircraft and impacting only the aircraft IPP but not the ground one.

5.2.2.4 Proposed Solution for GAST-D Ionosphere Monitoring

A possible solution to the integrity issue for this GBAS service is the use of Receiver Autonomous Integrity Monitoring (RAIM) for the monitoring of ionospheric front.

The RAIM technique uses the redundant information to detect possible blunders affecting measurements used to compute the position solution (Brown, et al., 1997) . Considering the need of four measurements to compute the single constellation solution, a minimum of five satellites is necessary to perform a test assuming only one faulty measurement per epoch. In case of dual constellations, the measurement must be at minimum six as, since a fifth unknown term has to be computed in the solution. In the literature, two main tests have been proposed to detect faults in the snapshot mode: residual-based test and solution separation test. In the following, only the solution separation test will be analyzed and used since it provides marginally better detection performance than the residual test. Details about RAIM residual test can be found in (Liu, et al., 2005).

The solution separation test relies on the comparison between the all-in-view position solution and the one computed using a subset of tracked satellites, where one satellite has been removed (Blanch, et al., 2012). Considering a bias affecting one measurement, this creates a difference between the all-in-view and the subset position solution. Removing the biased satellite, or another critical satellite, in the position computation for subset i, it is possible to obtain the following test statistic.

$$\Delta\hat{x}^{(i)} = \left(\delta\hat{x}^{(i)} - \delta\hat{x}^{(0)}\right) = \left(S^{(i)} - S^{(0)}\right)\Delta y \qquad \text{Eq. 5.35}$$

Where:

- x_0 is the position used to linearize the least square solution.
- $\delta\hat{x}^{(0)}$ is the estimated correction to add to x_0 to obtain the estimate positon computed using all satellites in view
- $\delta\hat{x}^{(i)}$ is the estimated correction to add to x_0 to obtain the estimate positon computed using all satellites except the satellite numerated by i
- $S^{(0)}$ is the S matrix computed as $(G^tWG)^{-1}G^tW$
- $S^{(i)}$ is computed as $\left(G^tW^{(i)}G\right)^{-1}G^tW^{(i)}$ and $W^{(i)}$ is the weight matrix with the i^{th} value on the diagonal is zero.
- G is the observation matrix presented in 2.3.3.2
- Δy is the vector containing the difference between the pseudorange measurements and the range distances computed relying on a point used for the linearization of the position solution

Knowing the relationship between measurements, geometry matrix, user position and error on pseudorange it is possible to write the following equation (Kaplan, et al., 2006):

$$\Delta y = G\,\delta x + \varepsilon \qquad \text{Eq. 5.36}$$

Where:

- δx is the solution vector composed by the x, y, and z corrections to apply to the point coordinates used to linearize the position solution and the receiver clock offset

- ε is a vector containing the measurements error.

It is possible to replace the measurement vector in Eq. 5.35 with the relation provided in Eq. 5.36

$$\Delta\hat{x}^{(\mathrm{i})} = \left(S^{(i)} - S^{(0)}\right)(G\ \delta x + \varepsilon) \qquad \text{Eq. 5.37}$$

The development of this product make the following term appear: $\left(S^{(i)} - S^{(0)}\right)G\ \delta x = S^{(i)}\ G\ \delta x - S^{(0)}\ G\ \delta x$.

$$S^{(0)}\ G\ \delta x = (G^t W G)^{-1} G^t W G\ \delta x = \delta x \qquad \text{Eq. 5.38}$$

$$S^{(i)}\ G\ \delta x = \left(G^t W^{(i)} G\right)^{-1} G^t W^{(i)} G\ \delta x = \delta x \qquad \text{Eq. 5.39}$$

Therefore, $\left(S^{(i)} - S^{(0)}\right)G\ \delta x = 0$ and Eq. 5.37 is simplified to:

$$\Delta\hat{x}^{(\mathrm{i})} = \left(S^{(i)} - S^{(0)}\right)\varepsilon \qquad \text{Eq. 5.40}$$

In case of no bias on measurements, the elements of ε are given by a centered normal distribution with a different variance for each satellite according to the used model. Under this condition, the value of $\Delta\hat{x}^{(i)}$ is expected to be under a normal distribution with zero mean and sigma of the test as (Blanch, et al., 2012):

$$\sigma_{ss}^{2\,(i)} = \left(S^{(i)} - S^{(0)}\right)C\left(S^{(i)} - S^{(0)}\right)^T \qquad \text{Eq. 5.41}$$

Where:

- C is the covariance matrix of the measurement errors, $C = W^{-1}$

In case of one faulty measurement the vector ε can be seen as:

$$\varepsilon = \begin{vmatrix} \eta_1 \\ \eta_2 \\ \vdots \\ \eta_i \end{vmatrix} + \begin{vmatrix} 0 \\ b \\ \vdots \\ 0 \end{vmatrix} = H + B \qquad \text{Eq. 5.42}$$

Where:

- η_i is the noise term of the i^{th} satellite and it follows a centered normal distribution
- b is a bias affecting one or more satellites at the same epoch.
- H and B are the vectors containing respectively η and b

In this case, the value of $\Delta\hat{x}^{(i)}$ follows a normal distribution with standard deviation as in Eq. 5.41 and mean value given by:

$$\mu^{(i)} = \left(S^{(i)} - S^{(0)}\right)B \qquad \text{Eq. 5.43}$$

Where $\mu^{(i)}$ contains the mean value for the three axis, x, y, z and the receiver clock offset.

If the test has to be executed on one of the three axis, x, y or z, or on two of them, for example x and y for the horizontal plane the values of the test standard deviation is

$$\sigma_{ss,q}^{2\,(i)} = \sigma_{ss}^{2\,(i)}(q)$$

Where q could be 1, 2, 3 and it considers the first, the second or the third term on the diagonal of $\sigma_{ss}^{2\,(i)}$

In case of test on two axis, for example x and y the first and the second values have to be used:

$$\sigma_{ss,1-2}^{2\,(i)} = \sigma_{ss}^{2\,(i)}(1) + \sigma_{ss}^{2\,(i)}(2)$$

The same has to be done with the values of μ.

A fault is detected when the solution separation test metric exceeds the threshold which is determined as a multiple of the test statistic noise according to (Blanch, et al., 2012).

$$Th_q = K_{fa}\sigma_{ss,q}^{(\mathrm{i})} \qquad \text{Eq. 5.44}$$

Where:

- $K_{fa}$is the multiplier for the fault-free detection, it is equal to $Q^{-1}\left(\frac{P_{fa}}{2N_{fault\ modes}}\right)$, Q is the quantile of a Gaussian distribution. In case of test of more than one axis, for example the horizontal plane is composed by the x and y axis, the multiplier is computed considering $Q^{-1}\left(\frac{P_{fa}}{4N_{fault\ modes}}\right)$
- P_{fa} is the probability of false alarm
- $N_{fault\ modes}$ is the number of combinations to monitor according to the selected fault mode. One or more faulty satellites can be considered

Therefore for each satellite, it is possible to compute the Minimum Detectable Bias (MDB) according to the required P_{fa} and P_{md}.

$$MDB^{(i)} = (K_{fa} + K_{md}) \cdot \sigma_{ss}^{(i)} \qquad \text{Eq. 5.45}$$

The value of MDB is multiplied by the related S_{vert} and S_{lat} will represent Minimum Detectable Error (MDE) in the vertical and lateral domain.

$$MDE_{vert} = \max_i\left(MDB^{(i)} \cdot S_{vert}^{(i)}\right) \qquad \text{Eq. 5.46}$$

$$MDE_{lat} = \max_i\left(MDB^{(i)} \cdot S_{lat}^{(i)}\right) \qquad \text{Eq. 5.47}$$

The biggest MDE, in vertical and latera domain, is representative of the worst case for the related epoch.

Using RAIM algorithm in GBAS, the value of C in Eq. 5.41 is smaller than using RAIM in stand-alone GNSS thanks to the better accuracy of the corrections. The small values of C directly reflect into σ_{ss} improving the test capability for errors detection. In this context it can be defined as Differential RAIM (DRAIM)

5.2.3 GAST-D RAIM Baseline and Results

5.2.3.1 GAST-D RAIM Simulation Baseline

DRAIM has been tested in 18 airports Table 26 gives the coordinates and the heading of one of the runways for all of them.

Table 26 – Airport latitude, longitude and runway heading for DRAIM simulation

Airports	Latitude (°)	Longitude (°)	Main RWY Heading (°)
Memphis	35.0424	-89.9767	360
Denver	39.8584	-104.667	80
Dallas	32.8964	-97.0376	360
Newark	40.6925	-74.1687	40
Washington	38.9445	-77.4558	10
Los Angeles	33.9425	-118.4081	70
Orlando	28.4289	-81.3160	180
Minneapolis	44.8805	-93.2169	300
Chicago	41.9796	-87.9045	100
Tacoma	47.1377	-122.4765	340
Anchorage	61.2167	-149.90	70
Bremen	53.0429	8.7808	90
Malaga	36.68	4.5124	310
Sydney	-33.9636	151.1859	340
Amsterdam	52.30907	4.763385	360
Rio	-22.8088	-43.2436	100
Peking	40.080109	116.584503	180
Johannesburg	-26.139099	28.246000	30

The heading of the runway will be used to derive a coordinate system with the x-axis aligned with the aircraft longitudinal axis and positive direction in the direction of aircraft speed. The y-axis aligned with the lateral axis and positive direction pointing toward the left side. The z-axis aligned with the vertical and positive direction on the up direction.

Being a threat affecting GAST-D, the constellation used is GPS. The satellites position and the errors are computed for an entire day with a time resolution of one minute. Two configurations of the GPS constellation has been used:

- GPS Optimal 24 (DoD, Department of Defence USA, 2008)
- GPS 31 satellites constellation as in YUMA almanac (week 862; $T_{oe} = 589824$)

The measurement error model has been defined using the model proposed in 2.3.3.2, with the following parameters:

- Airborne Accuracy Designator (AAD) B
- Airborne Multipath Designator (AMD) B
- Ground Accuracy Designator as derived for L1 band measurement in 2.3.4.1
- $\sigma_{vig} = 6.4$ mm/km as in (Seo, et al., 2012)
- Residual tropospheric and ionospheric errors standard deviation as in (RTCA Inc.; DO253-C, 2008)

The main point analyzed is the CAT I decision height. Because an ionospheric front may be present also before that the airplane reaches this point, and the ionospheric delay being different, performances are computed also for other two points: 3 and 5 minutes before the landing.

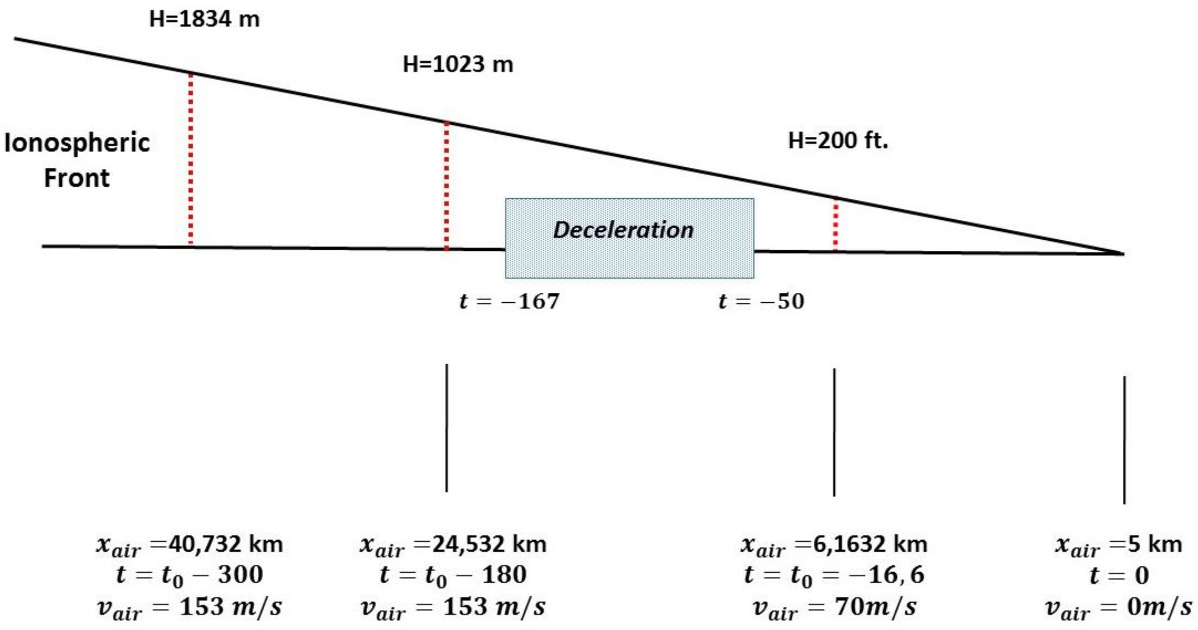

Figure 93 – Point along the approach used to derive DRAIM performances

In Figure 93, jointly with the horizontal distance and the altitude of the points, are shown the aircraft speeds at the different points derived from (ICAO NSP, 2015). The last parameter to define is the maximum range error that may be caused by the ionospheric front. Knowing that the range error caused by a front is given in Eq. 5.34, the parameters of this equation must be defined.

- The value of x_{air} has been already defined according to the three points in along a straight-in trajectory.
- The ionospheric front gradient is assumed to be at his maximum value; 0.5 m/km
- the smoothing time constant $\tau = 30$ seconds
- Δv, considering also the values in Table 25, has been set to 0.07, 0.035 and 0 km/s. Negative values, simulating a front faster than the aircraft will not be considered. The induced range error for this cases, in fact, is smaller than the real one due to the smoothing filter response.

Computing the range error induced by the front for each value of Δv, the following results may be obtained for the three points along the approach. In Table 27, the maximum range error according to the three analyzed velocity are shown. The range error is, however, dependent on the vertical error. In the following of the section the process to compute it is explained.

Table 27 – ionospheric front induced range error (m)

$\Delta v \left(\frac{km}{s}\right)$	x_{air} (km)		
	$\mathbf{6.1632}$	$\mathbf{24.532}$	$\mathbf{40.732}$
$\mathbf{0.07}$	5.5	16.9	25
$\mathbf{0.035}$	4.2	12.66	19
$\mathbf{0}$	3.1	8.5	12.4

The values of the range error computed for the two points along the approach takes into account the following assumptions:

- The speed of the IPP is considered to be driven by the one of the aircraft at CAT I point. This permits to derive that the front is not moving in the case $\Delta v = 0.07\ km/s$, is moving at almost $0.035\ km/s$ in the second one and $0\ km/s$ for the last one.
- The satellite dynamics is not considered for the derivation IPP speed since it is at an approximated height of 350 km and at this height the aircraft speed is the one having a relevant

impact on it. Moreover considering that an approach and landing procedure last no longer than 5 minutes the satellite may appear as stationary for a ground, or aircraft, user.

The matrix G, the observation matrix, is computed in the same coordinate frame proposed in 2.3.3.2, where the x-axis is aligned with the runway with positive direction in the same direction of the landing. The z-axis is pointing to the up direction and the y-axis is oriented to be orthogonal to the previous two.

The values of S_{vert} and S_{lat} are given in 2.3.3.2

The test standard deviation is computed as in Eq. 5.41, the values of the vector e_q are different for the vertical and lateral cases. In the vertical case it is assumed to be:

$$e_{vert} = \begin{bmatrix} tan(GPA) \\ 0 \\ 1 \\ 0 \end{bmatrix}$$

This because also the longitudinal error, in the runway direction, impact the vertical error.

For the lateral case

$$e_{lat} = \begin{bmatrix} 0 \\ 1 \\ 0 \\ 0 \end{bmatrix}$$

The values in the two cases reflect how the range errors impact the four values of the S matrix to compute the vertical and lateral error.

The test threshold is computed as in Eq. 5.44. The $P_{fa} = 10^{-7}$; the $N_{fault\,modes}$ in this case is equal to the number of satellites used to compute the all-in-view position solution. For the vertical case $K_{fa,vert} = Q^{-1}\left(\frac{P_{fa,vert}}{(2+2\cdot\tan(\mathrm{GPA}))\,N_{fault\,modes}}\right)$, instead for the lateral one $K_{fa,lat} = Q^{-1}\left(\frac{P_{fa,vert}}{2N_{fault\,modes}}\right)$. GPA has been already defined, in this test it is assumed to be 3°.

The scope of simulations is to verify the capability of DRAIM to detect the range error due to ionospheric gradient with a required P_{md}. It is useful to say that in (ICAO NSP, 2010), it is assessed that all errors, in the vertical domain, smaller than 6.4 meters can be undetected. Errors with a bigger magnitude have to be detected with a $P_{md} < 10^{-9}$.

The P_{md} will be computed for all satellites according to the proposed scheme:

- Computation of the range error of each satellite providing a vertical error bigger than $\pm$ 6.44 meter as ${\varepsilon_r}^{(i)} = 6.44/\left|S_{vert}^{(i)}\right|$

- Removal of all satellites having an $|\varepsilon_r|$bigger than the maximum induced error computed in Table 27 because it is out of the residual ionospheric threat model.
- Computation of the P_{md} for all remaining ε_r and selection of the one providing the highest P_{md} as worst case
- Analysis of P_{md} for the points along the trajectory for the same satellites in order to analyze if detection is improved in previous points.
- The induced ionospheric range error for the points along the approach is computed as a linear extrapolation knowing the relationships in Table 27. For example considering the first case, $\Delta v = 0.07\ km/s$ the relation between errors is 5.5 : 16.9. the induced range error for this point can be computed as:
    - $x = \frac{16.9 \cdot \varepsilon_r}{5.5}$
- The satellites geometry is computed for 3 and 5 minutes offset with respect to the analyzed epoch. If the satellite is not present in one of the two points the P_{md} for the related case is set to 1 because the system cannot be protected by a detection done in one or both the point along the approach analyzed.
- The same process is used for all other velocities adapting the used maximum range delay.

5.2.3.2 GAST-D RAIM Results

A critical parameter to derive RAIM performances is the number of faulty measurements at the same time. Analysing the condition under which an ionospheric front is undetected by all monitors, for GAST-D service, a single “faulty and not detected” satellite seems to be the most probable case. This condition is not, however, the only one possible. A two “faulty and not detected” satellites scenario is therefore possible.

The results of simulations done considering the baseline presented in 5.2.3.1 are shown here. In Figure 94 the results for a stationary front ($\Delta v = 70\ m/s$) are shown for the optimal 24 GPS constellation.

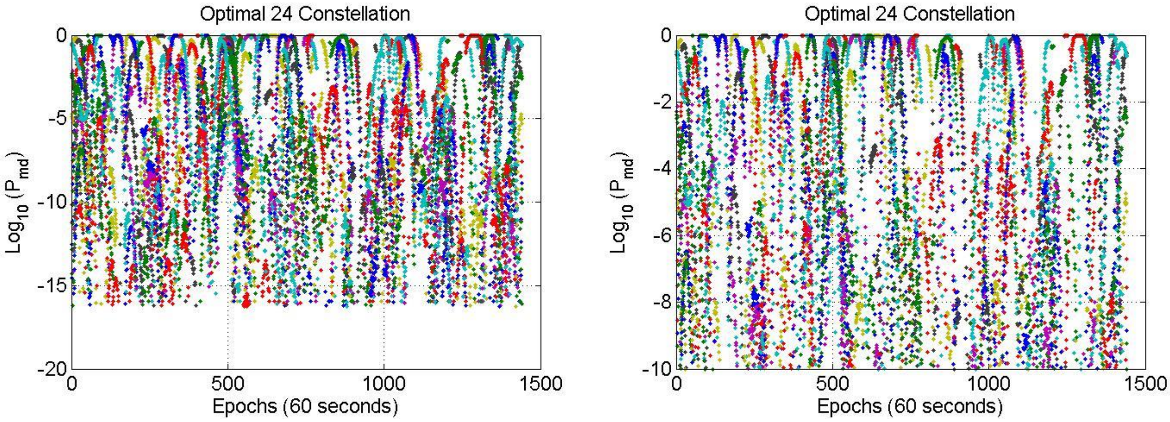

(CAT I DH point) **(CAT I DH zoom)**

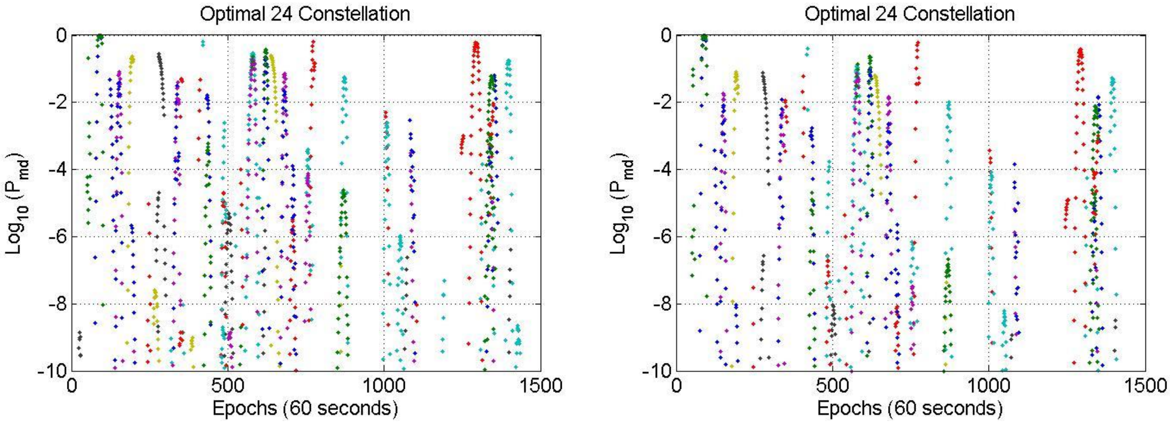

(3 minutes before landing) **(5 minutes before landing)**

Figure 94 – DRAIM P_{md} of ionospheric front induced error for GPS Optimal 24 and $\Delta v = 70\ m/s$ for all airports

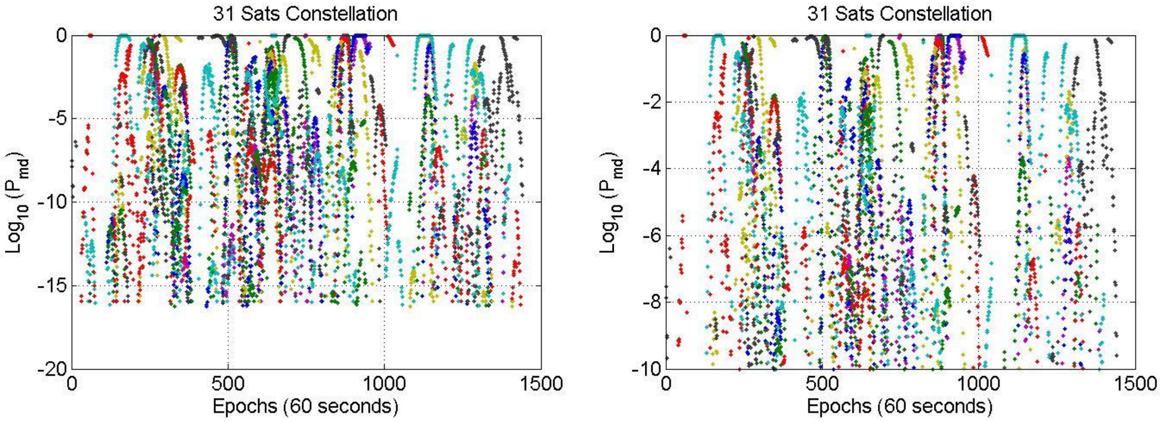

(CAT I DH point) **(CAT I DH zoom)**

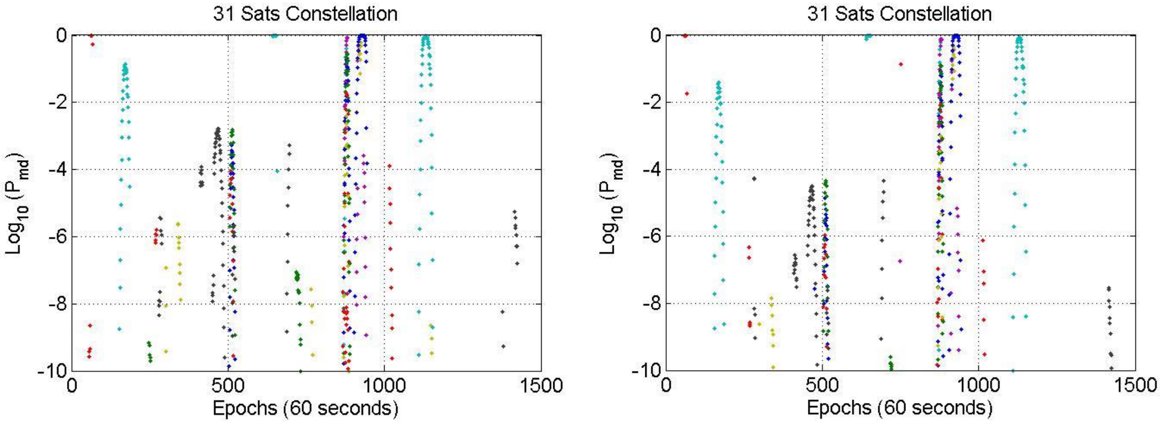

(3 minutes before landing) **(5 minutes before landing)**

Figure 95 – DRAIM P_{md} for ionospheric front induced error for GPS 31 Satellites and $\Delta v = 70\ m/s$ for all airports

Figure 94 and Figure 95 show the P_{md} for the vertical error bigger than ± 6.44 meters and for which the range error, on one single satellite, does not exceed the 5.5 meters at CAT I DH point.

Knowing that any error bigger than 6.4 meters has to be monitored with a $P_{md} < 10^{-9}$ it is possible to see that DRAIM alone is not able to guarantee the required P_{md} at CAT I decision point. In a lot of cases, the P_{md} is bigger than this limit. If the front is present at the time of the beginning of the approach, the monitor provides better results thanks to the increased magnitude of the induced range error. In some cases also the satellites geometry changes between the points along the approach providing better performances. It has to be considered however that under these conditions the IPP is moving faster than the front, the CCD and the DSIGMA monitor can provide low level of P_{md} once integrated with the one from RAIM leading to the required level. The use of 31 satellites constellation provides better results than the optimal 24, as expected, because the bigger number of visible satellites improves the DRAIM detection capability.

In Figure 96 and Figure 97 the results for the case $\Delta v = 35\ m/s$ are shown. The range error for this case are respectively: 4.2, 12.66 and 19 meters.

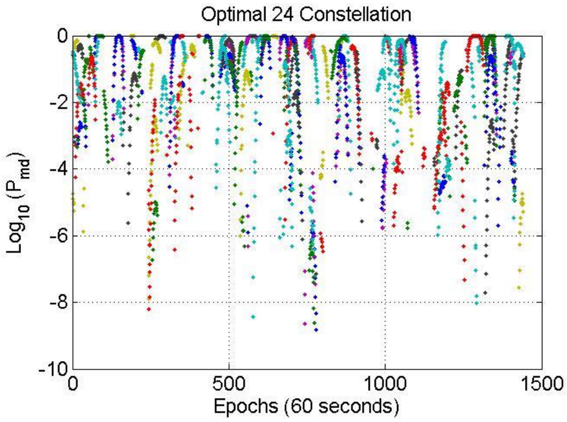

(CAT I DH point)

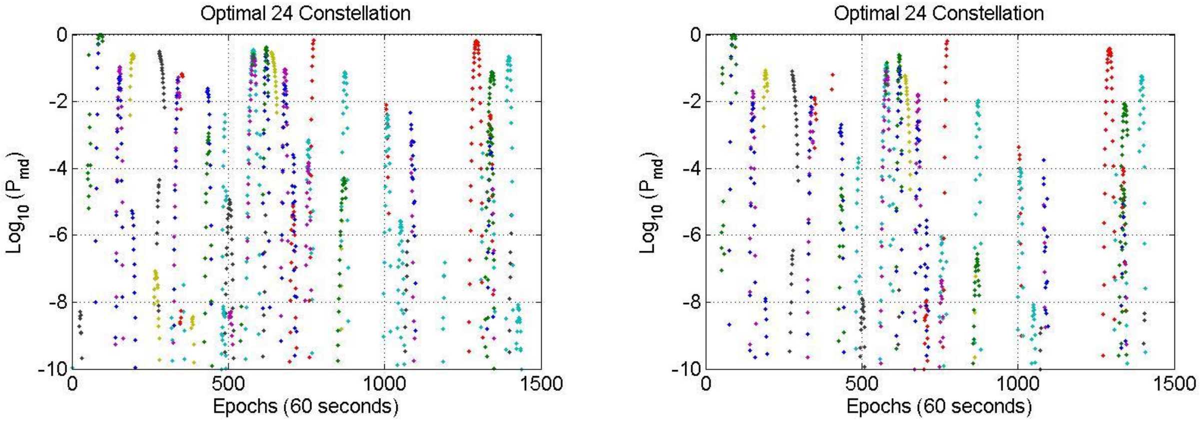

(3 minutes before landing) **(5 minutes before landing)**

Figure 96 – DRAIM P_{md} *for ionospheric front induced error for GPS optimal 24 and* $\Delta v = 35\ m/s$ *for all airports*

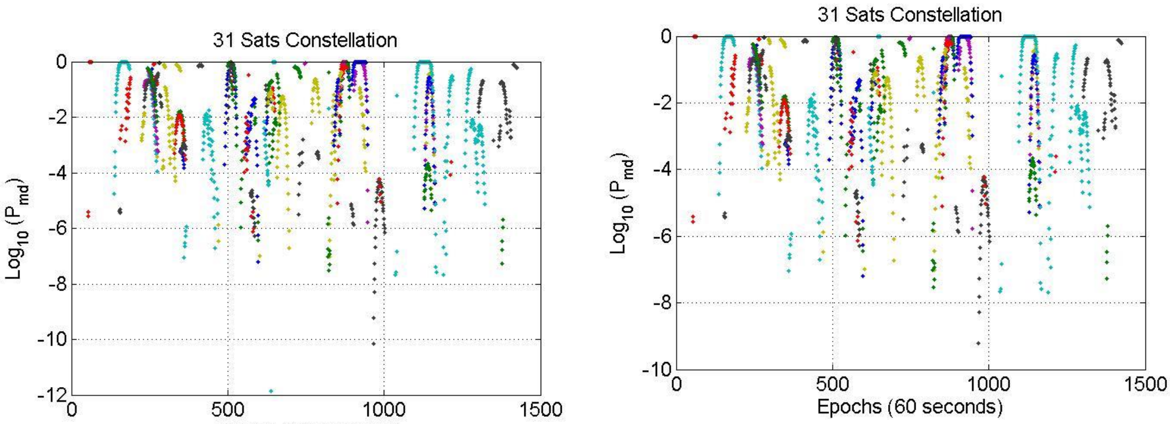

(CAT I DH point)

(CAT I DH zoom)

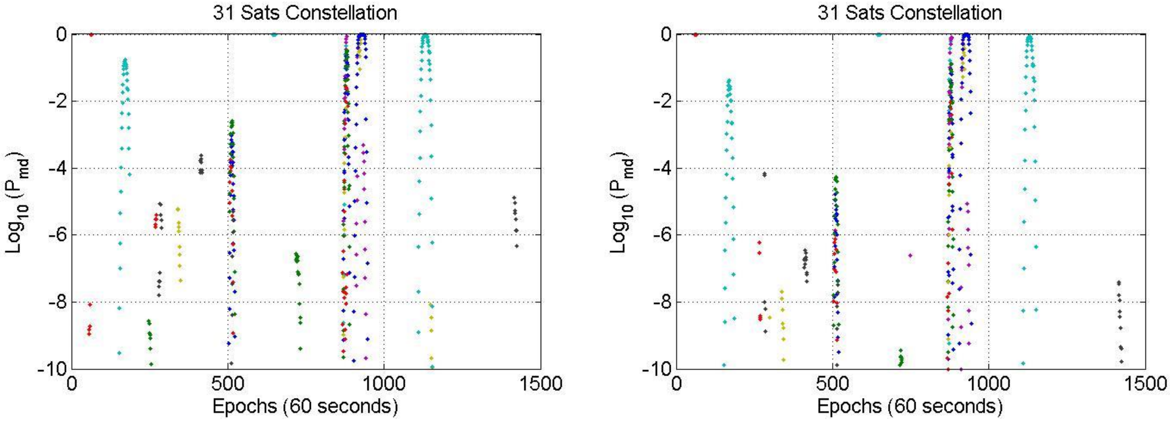

(3 minutes before landing)

(5 minutes before landing)

Figure 97 – DRAIM P_{md} for ionospheric front induced error for GPS 31 Satellites and $\Delta v = 35\ m/s$ *for all airports*

Comparing Figure 96 and Figure 97 with Figure 94 and Figure 95, it is possible to see that the number of undetected faults ($P_{md} > 10^{-9}$) is lower because, thanks to the lower range error, the number of epochs where the vertical error overcomes 6.4 meters is reduced thanks also to the presence of the geometry screening monitor that limits the cases of bad geometry. In Figure 96 and Figure 97, it is possible to see that relying on detections done along the approach the performance of DRAIM can improve thanks to the increased range error. In this condition, considering that the Δv is reduced, the detection capabilities of the CCD and DSIGMA are reduced if compared to the previous case where Δv was 70 m/s.

Figure 98 and Figure 99, show the results for the last case analyzed: $\Delta v = 0\ m/s$. In this case thanks to the non-contribution of the smoothing filter to the induced range error the values are: 3.1,8.5 and 12.4 meters respectively.

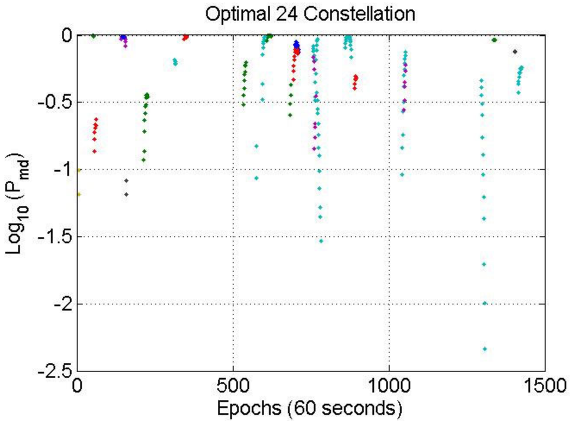

(CAT I DH point)

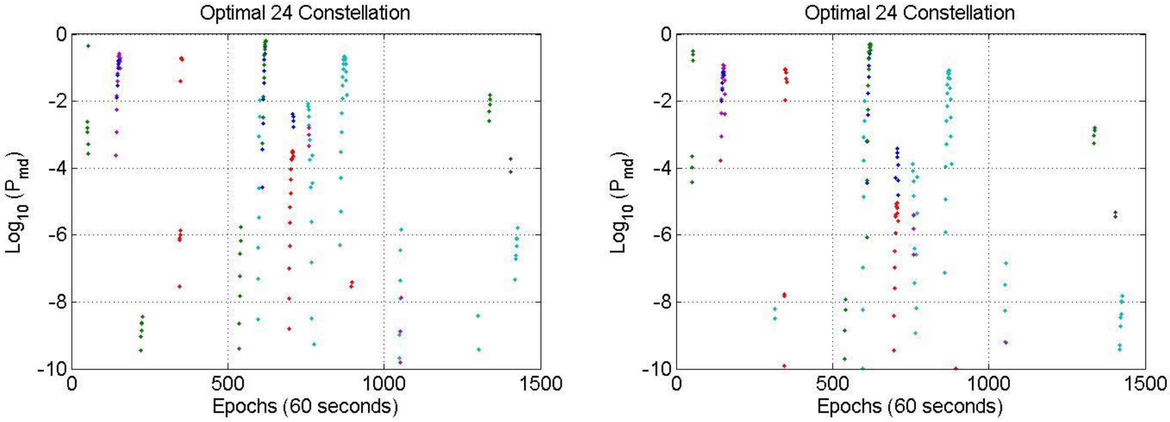

(3 minutes before landing) **(5 minutes before landing)**

Figure 98 – DRAIM P_{md} *for ionospheric front induced error for GPS optimal 24 and* $\Delta v = 0\ m/s$ *for all airports*

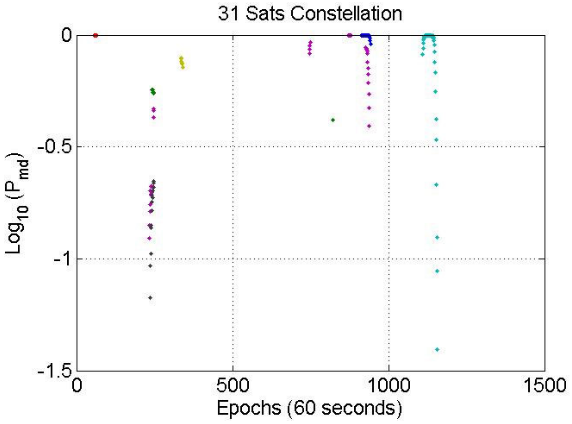

(CAT I DH point)

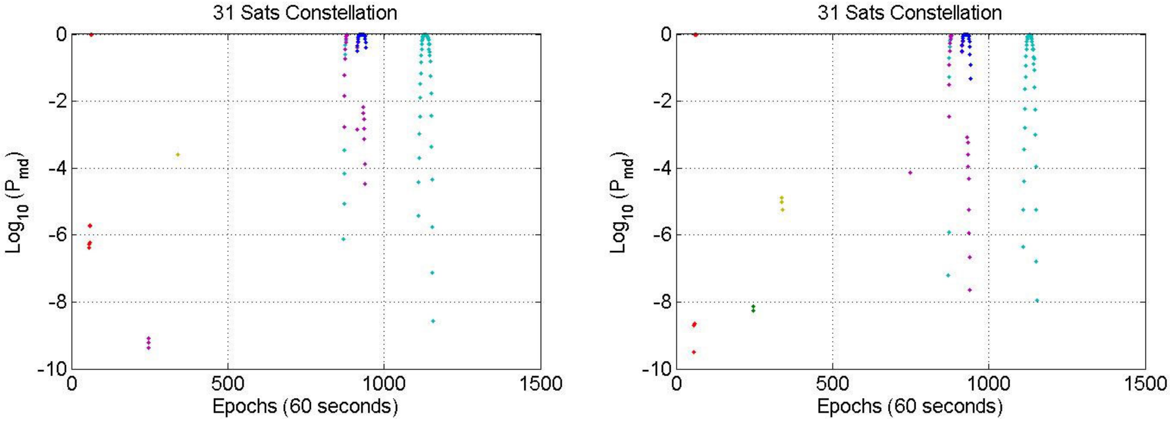

(3 minutes before landing) **(5 minutes before landing)**

Figure 99 – DRAIM P_{md} *for ionospheric front induced error for GPS 31 satellites and* $\Delta v = 0\ m/s$ *for all airports*

The analysis of the last case, Figure 98 and Figure 99, provides the best results among the three analyzed cases. A few cases provide a vertical error bigger than 6.4 and are not detected ($P_{md} > 10^{-9}$) by DRAIM. Under this condition in fact, the range error is only determined by the ionospheric gradient because the smoothing filter does not see any changes of the ionospheric delay. In this condition, however, the detection relying on points along the approach provides the worst results since the front is moving with the plane and the delay is not changing too much. Moreover, it has to be said that the airborne monitors are assumed to have high P_{md} level due to the low differential speed between IPP and ionospheric front. The monitors at ground station can help whenever the ionospheric front impacts the ground station IPP, in this case the differential speed is quite significant.

In order to summarize the results obtained so far, it is useful to evaluate the system availability inside the simulation. This means to see how many epochs have a vertical error that is lower than 6.4 meters (also considering the limitation of the errors in the range domain) and that is not detected with a $P_{md} < 10^{-9}$. In Table 28 the percentage of epochs where the P_{md} is not meeting the 10^{-9} requirement is computed for each analyzed case.

Table 28 – Percentage of epoch with a not sufficient P_{md} for GAST-D

Δv	**GPS Constellation used**	**Unavailability for CAT I DH point ($\lvert E_V\rvert > 6.4$ and $P_{md} > 10^{-9}$)**	**Unavailability for point along the approach (3, 5 min before)**	
$70\ m/s$	Optimal 24	29.4 %	3.78 %	2.92 %
	31 Satellites	15.23 %	1.96 %	1.61 %
$35\ m/s$	Optimal 24	11.86 %	3.48 %	2.58 %
	31 Satellites	6.72 %	1.68 %	1.39 %
$0\ m/s$	Optimal 24	1.0 %	0.61 %;	0.56 %
	31 Satellites	0.67 %	0.51 %;	0.52 %

Analyzing the values in Table 28, it is good to remind that the simulation considers already particular atmospheric conditions with a limited occurrence probability. These values are not indicative of the total system availability since the probability that an ionosphere front occur, denoted as P_{priori}, is not considered. To derive the total system availability the P_{md} computed before has to be mulitpalied by the P_{priori} and then the availability can be computed. The value of the P_{priori} for an ionospheric front has not been determined however.

Examining the results for all the cases, it is possible to assess, under the assumption of “one faulty and not detected” satellite that the use of DRAIM with the other monitors may help to reach the required integrity level. DRAIM is, in fact, not dependent on the front speed or the other atmospheric activities.

5.3 GAST-F Integrity Monitoring

The concept to derive the airworthiness for GAST-F is foreseen to be similar to the one adopted for GAST-D. Advantages of the new service will be provided by lower values of the NSE and FTE that will permit to further relax some integrity requirements. Moreover with the use of DF measurements the monitoring of the ionosphere activity will be improved in term of better detection performances or reduction of the induced differential error.

Despite the advantages some challenges rises due to the use of new signals, DF combination, and possible new processing modes.

5.3.1 GAST-F Monitoring Challenges

With the development of a DC/DF GBAS system, a lot of challenges have arisen. Concerning the integrity monitoring these challenges may be divided into three major groups:

- Threats on new signals or DF combinations. Up to now all threats presented in 2.2.3.1 have been defined for GPS L1 C/A signal. It is necessary to analyze the impact of threats on GPS L5, Galileo E1 and E5a and as well on D-free and I-free combinations. In case of significant differences, new threat models have to be derived.
- Integrity issues for new update rate. A possible processing solution to broadcast all corrections and information in case of DF/DC GBAS, is to change the PRC and RRC update interval. Currently, the used value is 0.5 s and integrity performances are derived, for GPS L1 C/A, according to this rate. The integrity considering new values must be re-assessed to verify the feasibility of the monitors.
- Re-assessment of the monitors according to the characteristics of any new signal or DF combination.
- Definition of the monitors to use in case of loss of one constellation or loss of one frequency.

In this thesis the following issues have been analyzed:

- ➢ Impact of an extended PRC and RRC update interval on the excessive acceleration monitor
- ➢ Use of DRAIM to improve monitoring performances in case of frequency loss

5.3.2 GAST-F Monitors Evaluation

In (Milner, et al., 2015) the impact of using an update interval bigger than the current one, 0.5 seconds, has been analyzed. Results show that a value of 2.5 seconds is feasible in term of system accuracy degradation. In the integrity context, the impact of this proposed update rate on the excessive acceleration monitor has been investigated

5.3.2.1 EA for Extended Latency

With the use of DF combinations new information has to be broadcast in the VDB message to provide a GAST-F service maintaining the inter-operability with the GAST-C/D services. This condition leads to an issue considering the GAST-D message structure, which has a limited free capacity. One possible solution is to decrease the update rate for the PRC and RRC, as proposed in (Milner, et al., 2015) to send corrections for all satellite and all signals or combinations. It has to be clarified that this change does not concern the integrity message for which the structure remains the same as in Figure 81

To cope with this modification, the differential error must be computed at the time when the PRC and RRC are received to also check that a non-detected acceleration does not cause a differential error bigger than 1.4 meters. Figure 100 helps to understand the processing scheme for the new timing diagram. First of all, it can be noted that the two bars representing the time to process and broadcast corrections are now 3.5 seconds long instead of 1.5 s for GAST-D. This is because the time to process measurement at ground does not change, 1 second, and only the VDB part changes from 0.5 to 2.5 seconds. The yellow triangles represent RRC and PRC which do not contain information about the acceleration threat. The green triangle is the first message where the PRC and RRC take into account for the acceleration. An integrity message is generated each 0.5 seconds and received at airborne side 1.5 seconds later.

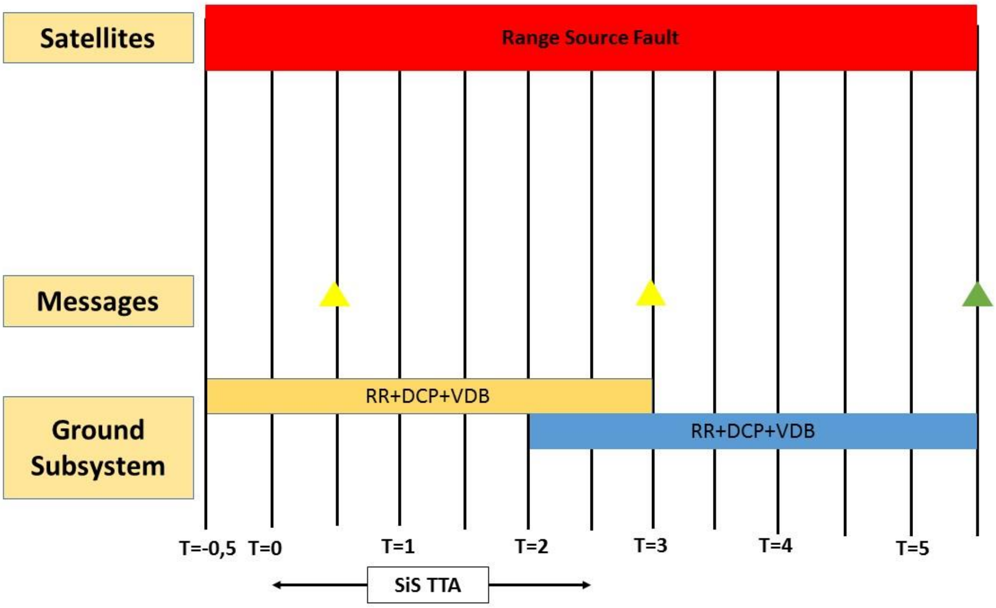

Figure 100 – Timing diagram derivation for below 200 ft. processing with PRC update rate at 2.5 seconds

Knowing that the SiS TTA does not change, it is possible to see that the maximum error, caused by a non-detected acceleration, is obtained at $t = 5.5$. After $t = 5.5$ the PRC and RRC containing information about the acceleration are received and the magnitude of the differential error decreases. Considering that the maximum differential error is caused by an acceleration of 6 seconds the differential error can be computed as:

$$\frac{1}{2}\,a\,(6^2) = 18\,a$$

The acceleration threshold is

$$18\,a = 1.4 \quad a = 0.078\,\frac{m}{s^2}$$

Considering the performances of the linear metric for the EA monitor shown in 5.2.1.4 this acceleration cannot be detected with a sufficient P_{md}.

A new monitor to detect accelerations has been presented in (Stakkeland, et al., 2014). The test metric is formed using the rate of the phase measurement across two consecutive epochs and the phase acceleration estimated as in Eq. 5.13.

$$x(k) = \begin{bmatrix} \dot{\phi} \\ \ddot{\phi} \end{bmatrix}$$

The detection metric is the chi-squared distributed quadratic norm:

$$d(k) = x^T \Sigma^{-1} x \qquad \text{Eq. 5.48}$$

Knowing that the variance of the acceleration detector is 6 σ_{ϕ}^2/T^4 and the one for the velocity estimation is 2 σ_{ϕ}^2/T^2 ($v = \frac{\phi(k)-\phi(k-1)}{T}$). Considering the correlation between the two as 3 σ_{phi}^2/T^3 it is possible to compute the covariance matrix for the test as (Brenner, et al., 2010) and (Stakkeland, et al., 2014):

$$\Sigma_x = \frac{\sigma_{\phi}^2}{T^2} \frac{N}{M(N-1)} \begin{bmatrix} 2 & 3/T \\ 3/T & 6/T^2 \end{bmatrix} = {\sigma_{\phi}}^2 \frac{N}{M(N-1)} \begin{bmatrix} 8 & 24 \\ 24 & 96 \end{bmatrix}$$

- N is the number of satellites tracked at all ground receivers
- M is the number of ground receivers in operation

When a fault occurs, the detection statistic contains a bias term. The non-centrality parameter is (Stakkeland, et al., 2014):

$$\lambda(k_{fault}) = m(k_{fault})^T \Sigma^{-1} m(k_{fault}) \qquad \text{Eq. 5.49}$$

The value of m is impacted by the value of k_{fault} that represents the epochs elapsed from the acceleration onset

$$m(1) = a \begin{bmatrix} \frac{1}{4} & \frac{1}{2} \end{bmatrix}^T$$

$$m(k > 1) = a \begin{bmatrix} \frac{1}{4}(2k-1) & 1 \end{bmatrix}^T$$

Replacing the values of $m(k)$ in Eq. 5.49, it is possible to compute the non-centrality parameter for the detection test.

$$\lambda(1) = \frac{1}{96} \frac{a^2 M(N-1)}{N\,{\sigma_{\phi}}^2} \qquad \text{Eq. 5.50}$$

$$\lambda(k > 1) = \frac{1}{96} \frac{a^2 M(N-1)}{N\,{\sigma_{\phi}}^2} (12k^2 - 24k + 13) \qquad \text{Eq. 5.51}$$

Setting:

- $P_{fa} = 10^{-9}$
- $\sigma_{\phi} = 0.0025$
- $M = 3$
- $N = 4$

It is possible to compute the P_{md} performance for each acceleration value. The value of k can be at maximum three in order to have time to process and broadcast an integrity message.

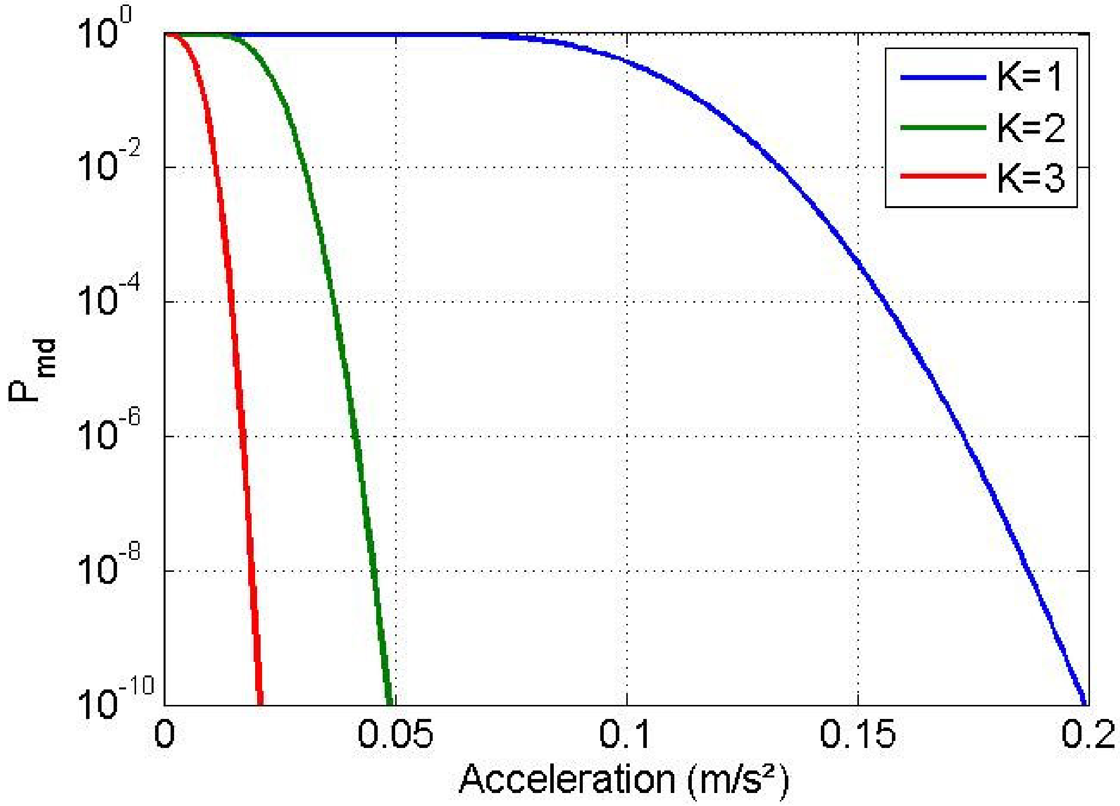

Figure 101 – P_{md} values for different accelerations and K-values for new metric

In Table 29, the values of the acceleration detected with a $P_{md} = 10^{-9}$ are shown.

Table 29 – Acceleration detected with $P_{md} = 10^{-9}$ for different K-values

$\boldsymbol{k_{fault}}$	$\boldsymbol{P_{md} = 10^{-9}}$
1	$a = 0.193\ m/s^2$
2	$a = 0.047\ m/s^2$
3	$a = 0.020\ m/s^2$

As it is possible to see in Figure 101, the performance of this new metrics improves with the growing of k. However, using $k = 1$ it is not possible to have a differential range error after 6 seconds of acceleration lower than 1.4 meters:

$$E_r(6) = 18 * 0.193 > 1.4\, meters$$

Relying on the detection at $k = 2$ it is possible to have a differential error at $t = 5.5$ lower than 1.4.

$$E_r(6) = 18 * 0.047 < 1.4\, meters$$

This condition will allow only one missed integrity message in the 2.5 seconds of the SiS TTA.

In Figure 102 a possible worst case is considered. The first integrity message (yellow triangle) generated at $t = 0$ and received at $t = 1.5$ could not detect an acceleration lower than 0.193 m/s² with the required P_{md}. The other two integrity messages (red) may be missed at airborne before receiving a new one (green) at $t = 3$. At this time, relying on detection with k_{fault} bigger than 2, any undetected acceleration has a magnitude lower than 0.02 m/s^2. It is possible to see that the worst differential error in this case is at $t = 3$ generated by a 3.5 seconds acceleration.

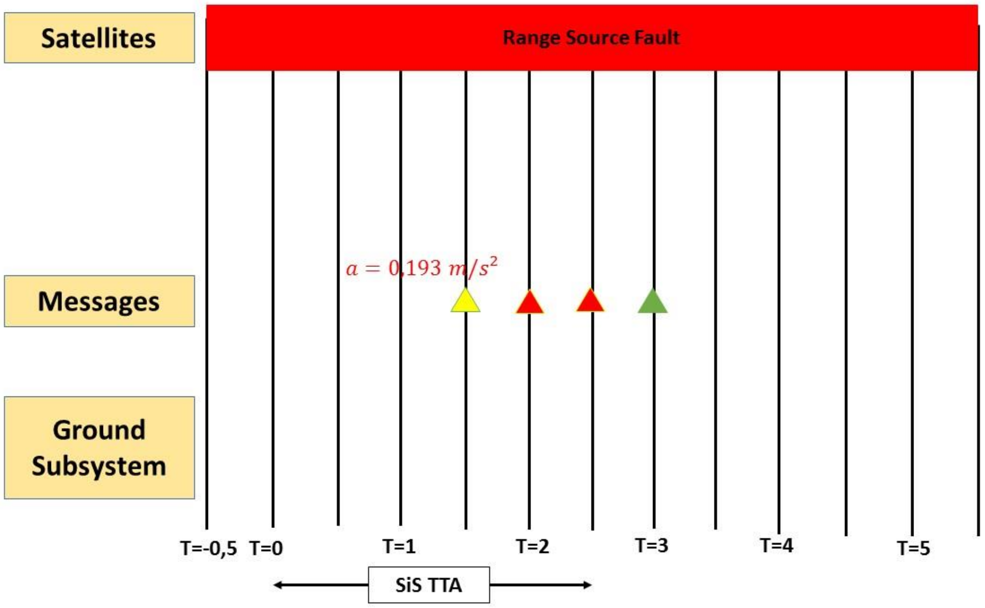

Figure 102 – integrity messages scheme

The differential error at this epoch, $t = 3$, can be generated only by a non-detected acceleration that according to the new metric is not bigger than 0.193 m/s^2. The differential error at this epoch can be computed as:

$$diff\ err\ (3.5) = 6.125\ * 0.193 < 1.4\, meters$$

If the acceleration is not detected, its value is lower than $0.02\ m/s^2$ and the induced range error does not overcome the limit of 1.4 meters until PRC and RRC are received. After the reception of the corrections the error is further reduced.

Using this new metric to monitor the acceleration threats makes possible to extend the PRC and RRC update time up to 2.5 seconds. The maximum undetected differential error does not exceed the 1.4 meters limit in any epoch. It is important to remind that the performances for this metric have been computed considering a more stringent value of the P_{md} than for what done for the linear metric in 5.2.1.4.

5.3.2.2 DRAIM Fallback Mode

As said in 5.3 thanks to the use of DF measurements the monitoring of the ionosphere anomalous activities may be improved or, using I-free combination, ionosphere anomalies no longer present a DF GBAS threat.

Although this condition seems to suggest that integrity could no longer represent a problem for ionospheric anomalies, the case of “fallback” to a SF GBAS service must be taken into account.

In GNSS “history”, the Newark airport jamming episode (Grabowski, 2012) is quite famous. The use of personal GPS jammers led to a GBAS unavailability due to the interference. Under this condition, the signals in the jammed band cannot be used, and this require a fall-back situation from DF/DC GBAS to SF/DC GBAS. This condition, due to the presence of measurements on one single frequency, is from a monitor point of view similar to a GAST-D service with a bigger number of satellites. In this case, the integrity level must be provided relying on the same monitors developed so far for GAST-D.

In 5.2.3, the detection capabilities of DRAIM to monitor ionospheric fronts that could not be detected with the required P_{md} by the airborne or the ground monitors have been investigated. Relying on a bigger number of satellites available, this technique can be used also as fall-back monitor for GAST-F service. The following section will study the performances of DRAIM in a SF/DC GBAS case.

5.3.3 GAST-F RAIM Baseline and Results

5.3.3.1 GAST-F RAIM Simulation Baseline

Simulations for GAST-F has been done using some of the parameters presented in 5.2.3.1 for GAST-D. The list of analyzed airports is the same as in of the runways for all of them.

Table 26. Constellations used are GPS and Galileo. In particular for GPS the used almanacs are the same described in 5.2.3.1. For the Galileo case the optimal constellation almanac of 24 satellites has been used (EU-U.S Cooperation on Satellite Navigation, 2016).

The error model used to derive the covariance matrix is the same used for GAST-D and developed for GPS L1 C/A. Simulations considering L5 band measurements error model have not been done because a model similar to the one developed for GPS L1 does not exists and although in 3.4.7 values of $\sigma_{pr\ gnd}$ have been derived for GPS L5 and GALIELO E5a it has been chosen to not use these values because the issues seen in using the BAE ARL-1900 antenna for L5 ban measurements. Another consideration that justify the analysis using the L1 model is the ionospheric delay on the two frequencies. Relying on the relationship state in Eq. 2.13, in fact, it is possible to see that the ionospheric induced delay on L5 band measurement is bigger than the one on L1 band measurements. Considering that in theory L5 band measurements, both on GPS and Galileo, are expected to have better performance than on L1 band, RAIM results are expected to be better than on L1 band measurements. For this reason analysing RAIM performances on L1 band measurements can be seen as the worst case for the detection of an ionospheric front.

The analysed points along the approach are the same as in 5.2.3.1.

For this simulation, considering the results obtained in 5.2.3.2 for single fault measurement with single constellations, the dual "faulty and undetected" cases will be analyzed. For a dual constellation case the analysis of single fault case provides better performances thanks to the presence of more satellites and an improved geometry. For this reason in this analysis the dual fault case is analyzed without any constraints on the selection of the worst satellite pair. It means that 2 satellites can be faulty, no matter their geometric configuration is. No particular model for the spatial extension of the ionospheric front is assumed, which is a conservative assumption.

The procedure to determine the worst pair of faulty satellites to monitor and the magnitude of the range error on each one is the following for any couple:

- Computation of the vertical error setting the maximum induced range, according to the ionosphere front speed, on both satellites. If the vertical error is not bigger than 6.44 meters the current couple of satellites is not analyzed. For example in the first ionospheric case the maximum range error at CAT I point is 5.5 meters, so the vertical error is:

  $$E_v = 5.5 \cdot (S_{vert}^1 + S_{vert}^2)$$

  Where E_v is the vertical error, S_{vert}^i is the S_{vert} value for the i-the assumed faulty satellites under analysis; S_{vert} has been presented in 2.3.3.2
- In case of vertical error bigger than 6.44 meters the relationship between the range errors on the two satellites providing the worst case to monitor is computed using the methodology described in (ANGUS, 2006) using the eigenvalues and eigenvectors. The range error on each satellite is (ANGUS, 2006):

$$E_r^1 = b \cdot \varepsilon^1$$
$$E_r^2 = b \cdot \varepsilon^2 \qquad \text{Eq. 5.52}$$

Where E_r^i is the range error on the i-thsatellite under analysis, b is the bias to apply to both range sources and is computed at next step, ε^1 and ε^2 are the first and second eigenvalues

- The value of b is computed starting from:

$$E_v = E_r^2 \cdot S_{vert}^1 + E_r^2 \cdot S_{vert}^2 \qquad \text{Eq. 5.53}$$

Replacing Eq. 5.52 in Eq. 5.53 it is possible to obtain

$$E_v = b \cdot \varepsilon_1 \cdot S_{vert}^1 + b \cdot \varepsilon_2 \cdot S_{vert}^2 \qquad \text{Eq. 5.54}$$

Setting E_v to 6.44 meters, it is possible to compute b and then to derive the range error for both satellites. If one of the two range errors is bigger than the maximum error than can be induced by an ionospheric front given in Table 27, it is set to the maximum values and the other one is increased to reach a vertical error of 6.44 meters. For example setting the first range error to 5.5 the second one is computed as:

$$E_r^2 = E_v - (5.5 \cdot S_{vert}^1)/S_{vert}^2 \qquad \text{Eq. 5.55}$$

- The P_{md} is then computed for the couple under analysis.
- If the value of the P_{md} is bigger than the required level of 10^{-9}, the same analysis, if both satellites are visible, is done for the two selected points along the approach. The satellites geometry is computed relying on the constellation status 3 and 5 minutes before the epoch under analysis. If one of the two satellites is not visible the P_{md} for these two points is set to 1 because the system cannot be protected using detections at the analyzed points. The range error for both is computed as done for GAST-D for both satellites.

5.3.3.2 GAST-F RAIM Results

As done for the results of GAST-D RAIM the P_{md} for the analyzed cases will be shown here. Figure 103 and figure YY show the results for the two 24 satellites constellations with a relative front-aircraft speed of 0.07 km/s.

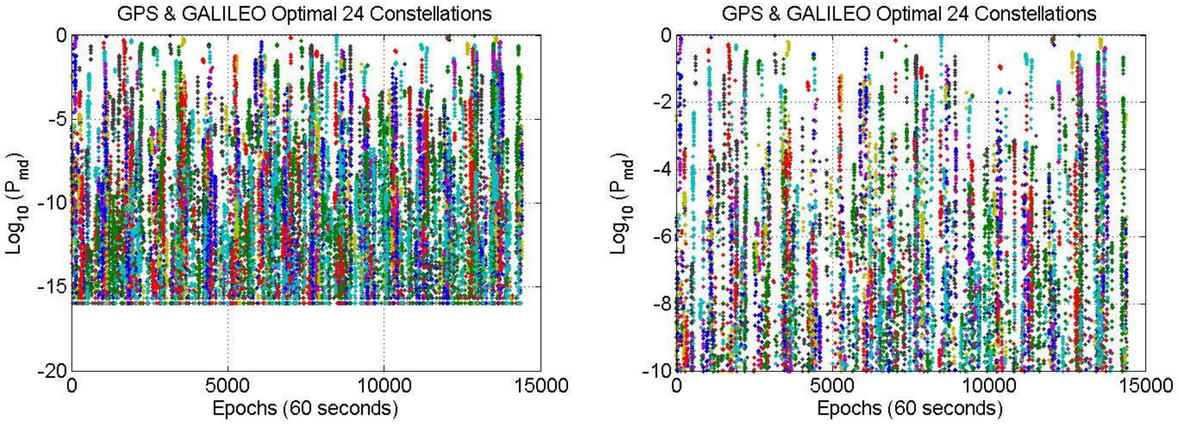

(CAT I DH point) **(CAT I zoom)**

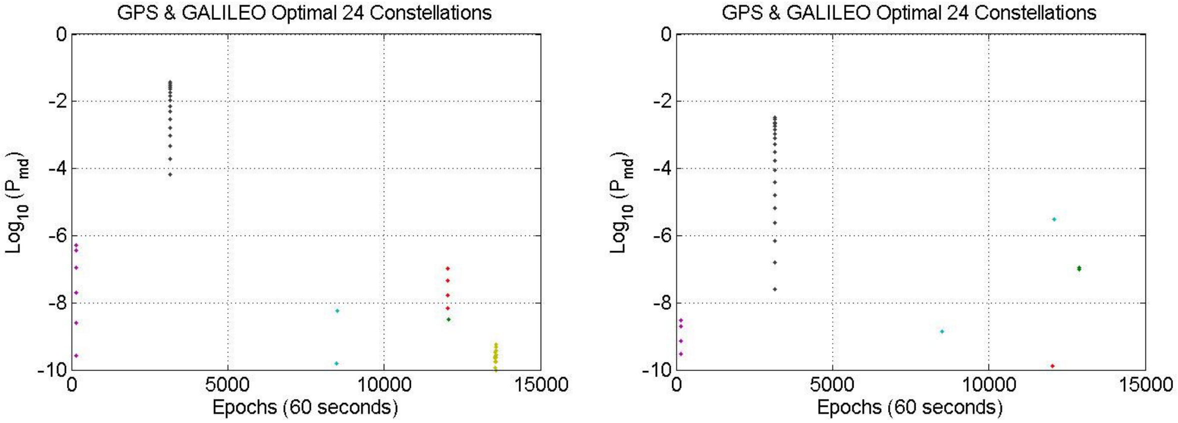

(3 minutes before landing) **(5 minutes before landing)**

Figure 103 – DRAIM P_{md} for an ionospheric front induced error for GPS & Galileo Optimal 24 and $\Delta v = 70\ m/s$ for all airports

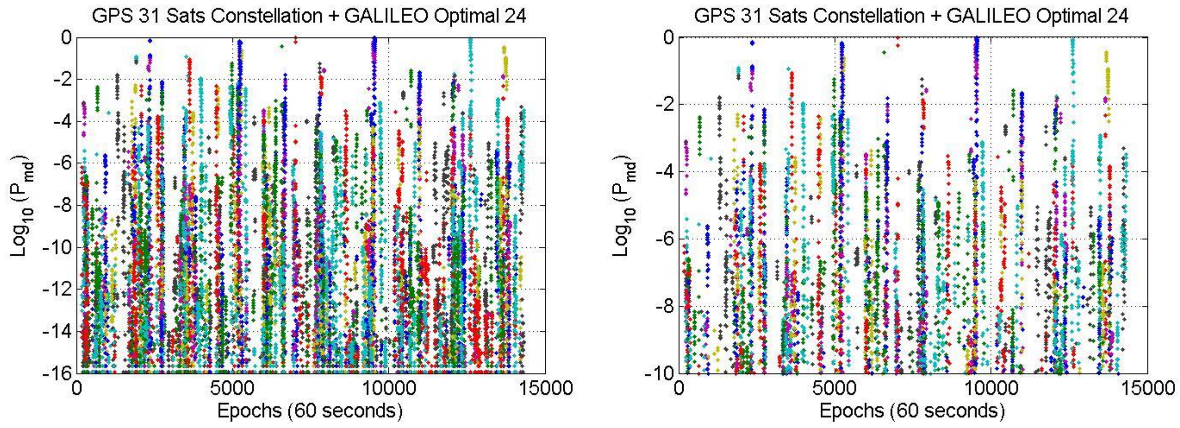

(CAT I DH point) **(CAT I zoom)**

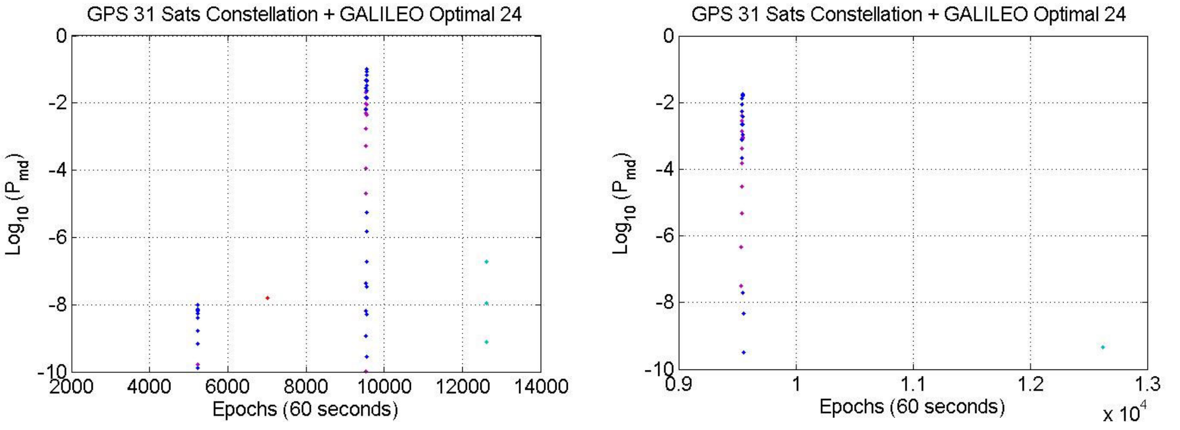

(3 minutes before landing) **(5 minutes before landing)**

Figure 104 – DRAIM P_{md} for an ionospheric front induced error for GPS 31 satellites and Galileo Optimal 24 and $\Delta v = 70\ m/s$ for all airports

As for the GAST-D case, in Figure 103 and Figure 104, the P_{md} for the CAT I points are shown. In the same figure the results for the two points along the approach, 3 and 5 minutes before landing. It is possible to see that thanks to detection in points along the approach the system, relying only on RAIM detection, is protected for almost all epochs.

Figure 105 and Figure 106 show the results for a front moving with a relative speed of 35 m/s.

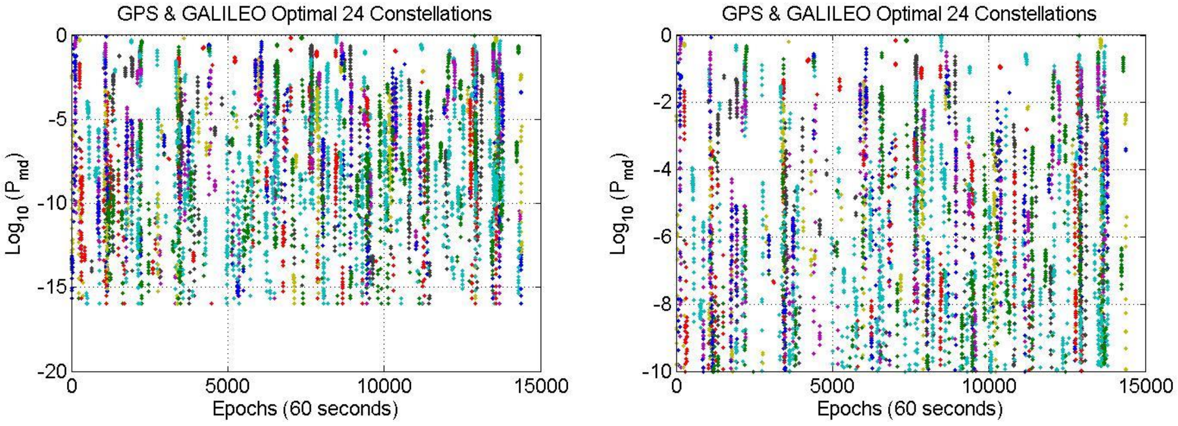

(CAT I DH point) **(CAT I DH zoom)**

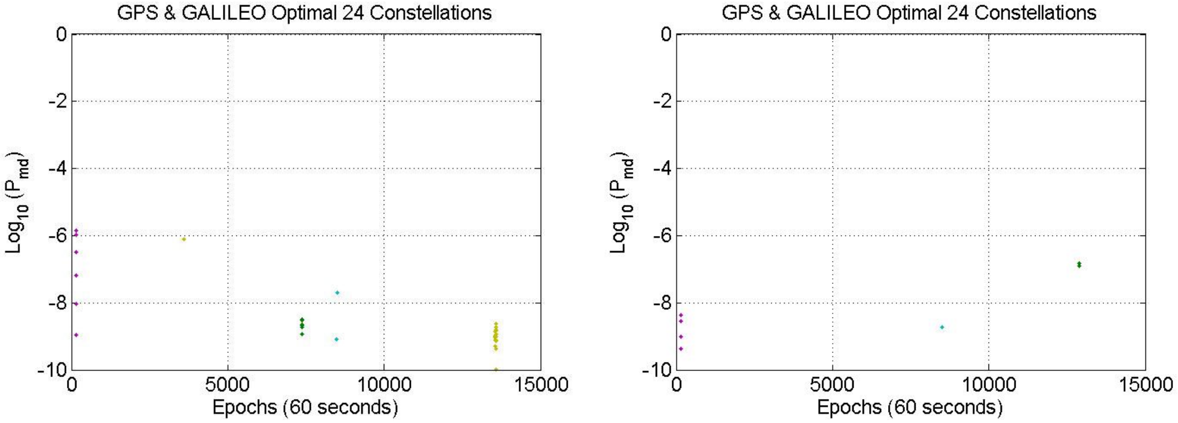

(3 minutes before landing) **(5 minutes before landing)**

Figure 105 – DRAIM P_{md} for an ionospheric front induced error for GPS & Galileo Optimal 24 and $\Delta v = 35\ m/s$ for all airports

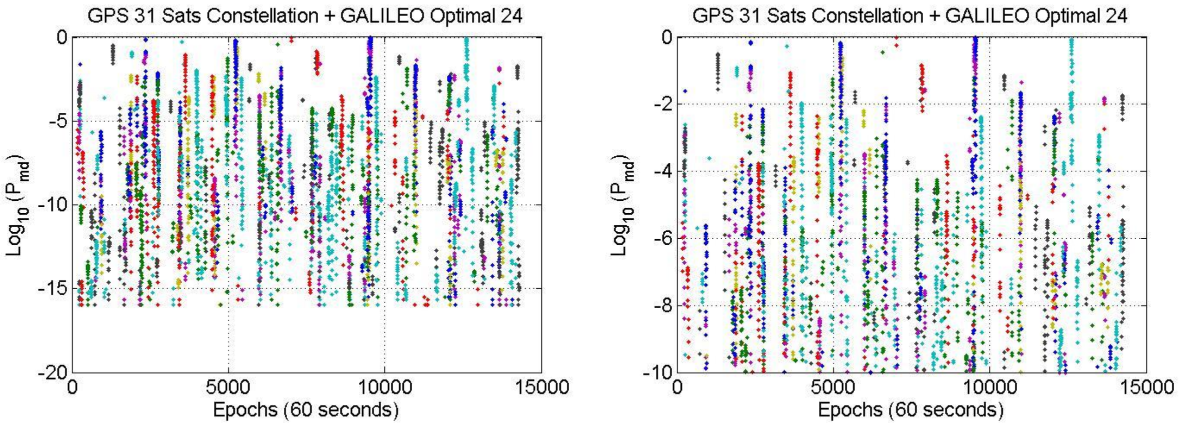

(CAT I DH point) **(CAT I DH zoom)**

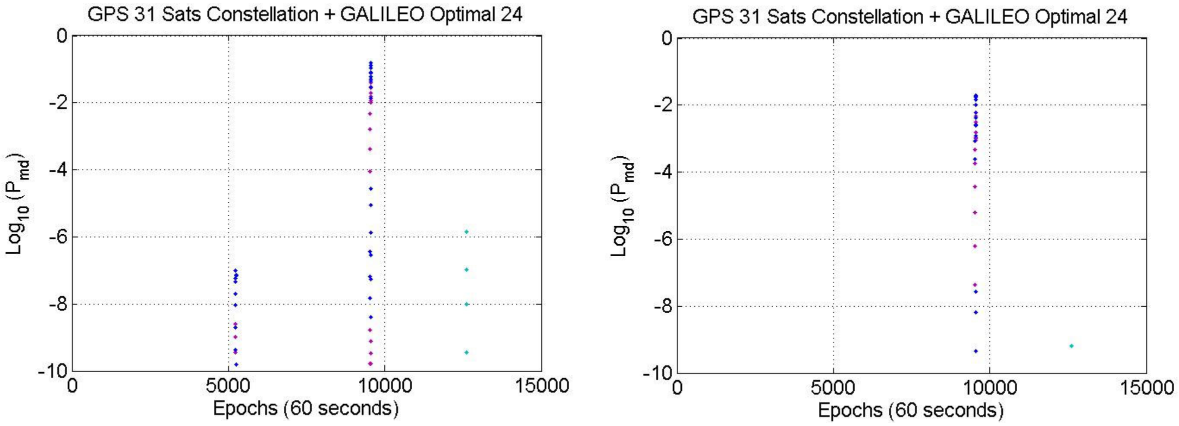

(3 minutes before landing) **(5 minutes before landing)**

Figure 106 – DRAIM P_{md} for an ionospheric front induced error for GPS 31 satellites and Galileo Optimal 24 and $\Delta v = 35\ m/s$ *for all airports*

As for the previous case the two figures show the results for the two analyzed cases, GPS optimal 24 and 31 satellites. In both cases thanks to the detection of errors in points along the approach the RAIM detection probability can be strongly improved.

The results for front and IPP front moving at same speed are not shown due to the low number of satellites couples, for all epochs, providing a vertical error bigger than 6.44 meters for a range error of 3.1 meters.

In Table 30 the percentage of epochs where the P_{md} is higher than 10^{-9} is computed.

Table 30– Percentage of epoch with a not sufficient P_{md} for GAST-F

Δv	**GPS Constellation used** + Galileo **Optimal 24**	**Unavailability for CAT I DH point ($\lvert E_V\rvert > 6.4$ and $P_{md} > 10^{-9}$)**	**Unavailability for point along the approach (3, 5 min before)**	
$70\ m/s$	Optimal 24	3.41 %	<0.1 %	<0.1 %
	31 Satellites	1.65 %	<0.1 %	<0.1 %
$35\ m/s$	Optimal 24	1.76 %	<0.1 %	<0.1 %
	31 Satellites	0.94 %	<0.1 %	<0.1 %
$0\ m/s$	Optimal 24	<0.1 %	<0.1 %	<0.1 %
	31 Satellites	<0.1 %	<0.1 %	<0.1 %

5.4 Conclusions

In this chapter the main challenges concerning the integrity of GBAS GAST-D and GAST-F have been analyzed.

The GAST-D service remains under validation due to the difficulties experienced in monitoring the ionosphere with the current monitor scheme. A first analysis has investigated the use of the RAIM algorithm to improve the monitoring of the ionospheric fronts for GAST-D service. After the analysis of the cases for which the monitors are not able to provide the required P_{md} levels the "residual threat model" has been identified. The analysis of the RAIM performances, according to the derived ionospheric front threat model, has provided the following results. DRAIM alone is not able to provide the integrity monitoring for only one satellite to monitor according to the requirement. Performances can be improved relying on, when possible, detection in different points along the trajectory where the error is expected to be bigger than the ones at CAT I DH point. It has to be considered that P_{md} values are computed only for DRAIM, considering the presence of the DSIGMA and CCD monitors, at airborne level, the joint analysis may improve the performances by decreasing the P_{md} down to 10^{-9} meeting the requirement. The same analysis for a dual "fault and undetected" case has not been done due to the lack of information about the shape of an ionosphere front in the horizontal domain. Despite the good results obtained the integrity issue for GAST-D service cannot be considered as solved. Analysis about the possible presence of more than one satellite "faulty and not detected" have to be done as well as the joint analysis including other monitors performances.

In the following of the chapter, two of the integrity challenges identified for GAST-F service have been analyzed.

The first challenge concerns the possibility to adopt a new PRC and RRC update rate to increase the VDB capacity in order to transmit the additional differential corrections present in a DF/DC GBAS. The impact of this possible new processing modes has been investigated on the EA monitor. Results show that using the test metric as proposed for GAST-D does not permit to have an undetected error lower than 1.4 meters, with a P_{md} lower than 10^{-4}, after the 2.5 seconds imposed by the SiS TTA. Relying on a new metric proposed in (Stakkeland, et al., 2014) it is possible to adopt the proposed PRC and RRC update thanks to the improved detection performances. Adopting the new metrics, the monitoring of the acceleration threat is feasible.

The last analysis has analyzed the case of "frequency loss" for GAST-F. Despite all advantages, especially in the ionosphere monitoring, brought by the use of DF measurements combinations, in case of frequency loss the ionosphere has to be monitored as done for GAST-C or D. Relying on the analysis of RAIM performances done for GAST-D, the same algorithm has been used for a dual-constellation case. In this case, knowing that monitoring one satellite with a DC RAIM provides good results, a dual "faulty and not detected" satellites case has been analyzed. Due to the absence of an ionosphere front model in the horizontal plane, no limits to the selection of the worst satellites couple to monitor have been imposed. This condition has a conservative impact in some cases because, even if it is not possible to derive a unique model for an ionosphere front in the horizontal domain, it is almost impossible that a unique front impacts two satellites at the opposite of the user skyplot. Results for this analysis are better than the one derived for GAST-D thanks to the presence of a second constellation. The worst case remains the one where the IPP is faster than the front with some cases where the P_{md} is not meeting the requirement. Relying on detection along different points on the approach trajectory improve performances consequently thanks to the increased magnitude of the range error on one side and the change in the satellites geometry on the other. Also, in this case P_{md} values are computed considering only RAIM detection, the analysis of joint performances between RAIIM, CCD and DSIGMA may provide even better results. RAIM can help the detection of ionosphere front also in this case, furthermore, if the worst couple of satellites to monitor could be limited by any ionosphere front model results are expected to be better in some cases. As for the GAST-D case at this stage RAIM cannot be considered as a definitive solution for the monitoring of ionospheric fronts in SF cases.

6 Conclusions and Future Works

This section presents the conclusions from the results obtained from the analysis of the results obtained in the previous chapters. Perspectives for future works are also presented.

6.1 Conclusions

The development of a DC/DF GBAS service, known as GAST-F, brings a series of benefits with respect to GAST-D that is intended to provide the same level of service: up to CAT III precision approach and landing guidance. The system, in fact, relying on two constellations is more robust against a constellation failure. Moreover, with the use of new signals, GPS L5, Galileo E1 and E5a better level of accuracy may be reached. The availability of two frequencies permits also to improve the monitoring of the ionosphere anomalies, and it has to be reminded that GAST-D is still under validation cause of lack of integrity. Dual frequency combinations permit also to further mitigate the residual errors increasing consequentially the total system availability. If on one side this new concept brings a lot of benefits it has to be said that the use of a new constellation, Galileo, and new signals rise a series of challenges that have to be solved to have a full benefit of the advantages of this new concept

In this thesis some of the issues related to the development of a DC/DF GBAS system have been investigated. The aim of the work was to provide analysis and results for some of the challenges that have risen in the initial development of the GAST-F concept

To select the optimal processing mode for GAST-F, especially considering the possibility to adopt DF combinations, the accuracy of the new signals and combinations has to be derived. On this topic, the impact of errors at ground level has been derived analysing the impact of noise and multipath on the PRC. Data used to perform the analysis were recorded at Pattonville airport and at Toulouse Blagnac airport. The antenna used was, for both data collection, the BAE ARL-1900 (Lopez, 2008) which was designed to have good multipath rejection properties for GPA L1 C/A signals and to be used particularly in a GBAS ground station.

The first outcome of the analysis is the need to calibrate the antenna for GPS L5 and Galileo E5a measurements because they are affected by an elevation dependent bias similar for all satellites, constellations, and for both locations. After that calibration is applied, results show that GPS L1 and Galileo E1, for smoothed case, have a lower noise and multipath error standard deviation than GPS L5 and Galileo E5a. This results, considering the used modulation (BPSK(10)) on both GPS L5 and Galileo E5a, is surprising because the opposite of was expected from theory or another analysis done, e.g. (Circiu, et al., 2015). A possible cause of this results is the antenna characteristics that were optimized for GPS L1 C/A signal. The computation of $\sigma_{pr\ gnd}$ values, for Toulouse data, and comparison with GAD curves shows that the antenna is not able to provide the required accuracy for GPS L5 and Galileo E5a signal. Their values of $\sigma_{pr\ gnd}$ are, in fact, bigger than the lowest GAD curves denoted as C. Values are provided also for I-free combination even if they are affected by the L5 band performances and no accuracy model is provided for this combination. the $\sigma_{pr\ gnd}$ computed for GPS L1 C/A and Galileo E1 signals show that the values are lower than the most accurate GAD curve. If results, at least on L1 band, are confirmed analysing data from other airports a new class of GAD curves may be defined for this kind of antenna.

The implementation of a MC/MF GBAS directly leads to a problem related to the increased number of satellites and the use of a second frequency. The big number of satellites, in particular, raises the problem of broadcasting a big number of PRCs and RRCs on the VDB link, which has a limited capacity. This problem is also related to the limitation, especially at the airborne side, of the number of tracking channels of the MC/MF receivers.

To cope with this issue a possible solution is to implement a satellite selection algorithm. Results show that relying on a 15-satellites subset, values of VDOP < 2 and HDOP < 1.15, indicator of a good geometry, are provided in more than 99.9% of the simulated cases. The protection level is lower than 10 meters for 100% of cases, and the parameters S_{vert} and S_{vert2} do not exceed the related limits. The same analysis for a 12 satellites subset, despite providing similar results for DOP values, leads to some availability problems. Protection levels, S_{vert} or S_{vert2} values exceed the related limits, in 0.2% of cases, when the all-in-view solution has the 100% of the availability across all simulations. The results do not consider the impact of smoothing and integrity process on the performances. The fast satellite selection (Zhang, et al., 2008) method is the one providing the best combination of good availability, low DOP values and low computational burden.

The last analysis has concerned the integrity monitoring. Because GAST-D service, due to a lack of integrity performances in monitoring ionosphere anomalous conditions, is still under the validation process, a first analysis has regarded the state-of-art of the monitors for this service. The aim was to understand under which circumstances the integrity requirement is not met. The analysis has permitted to derive a "residual" ionospheric threat model under which not all satellites are monitored with the required P_{md}. In particular ionosphere fronts moving with a relative low speed, and considering all possible slope values, are representative of this residual threat.

To improve monitoring performances, the use of RAIM algorithm has been proposed. Results show that for one "faulty and not detected" satellite, considering that the maximum range error is limited by the ionospheric front, RAIM provides good results. Moreover relying on detection on several points along the approach, 3 and 5 minutes before the landing, P_{md} values are further reduced, this because the value of the induced range error, according to the simulated scenarios, is bigger than in the first analysed case; the CAT I Decision Height (DH) point. It has also to be considered that the performances of the other monitors are not taken into account. This lead to the consideration that in some epochs where the P_{md} is below the requirement ($P_{md} < 10^{-5}$), including the performances of CCD and DSIGMA a global value lower than 10^{-9} may be obtained.

The analysis of a "dual faulty and not detected" case is also needed since this case cannot be excluded a priori. However it has to be considered that the choice of the worst couple of satellites to monitor has to be done considering an ionosphere front horizontal shape. This information is necessary to exclude cases where the two satellites are separated by a distance that exceeds the ionosphere front dimensions. Unfortunately a model for the ionosphere front, in the horizontal domain, does not exist. For this reason, and to avoid to compute performances under a quite pessimistic case, the simulation for the dual fault case has not been done. For the moment, due to the absence of simulations considering more than one faulty satellite, RAIM cannot be considered as a solution to the monitoring issue for GAST-D.

In the following of the integrity monitoring study, the challenges that have risen with the implication of a new constellation and new signals or new processing mode in GAST-F are presented.

Considering analysis done in (Milner, et al., 2015), where the impact of a lower PRC and RRC update rate is analyzed in term of accuracy loss, the impact of a lower update rate (2.5 s update interval instead of 0.5 s) is analyzed on the excessive acceleration monitor. Results show that the current monitor test metric, as used for GAST-D, is not able to meet the requirements (to monitor all faults that cause a differential error bigger than 1.6 meters) when an update period of 2.5 seconds is used. Relying on a new test metric proposed in (Stakkeland, et al., 2014), the requirement can be met thanks to the improved detection performances.

Another integrity issue regarding GAST-F is the possibility to lose a frequency, for example due to the presence of interferences in one of the frequency bands, as experienced at the Newark airport in 2009 (Grabowski, 2012). In this case, the expected integrity monitoring conditions are similar to the ones of GAST-D, except that a second constellation is present. To guarantee the integrity under this condition, the GAST-D monitor scheme is not sufficient to meet the integrity requirement. Relying on the proposal done for GAST-D, the performance analysis of adding RAIM to other monitors has been done for a SF/DC GBAS system. For this simulation, a "dual faulty and not detected" case has been analysed. No constraints have been imposed to the selection of the worst satellites couple, i.e. no geometric constraint on the spatial extent of the ionospheric front, so that a pessimistic scenario is taken into account. Results are better than the ones obtained for GAST-D, and relying on detection on several points along the approach, the integrity can be provided by RAIM in almost 100% of the analyzed epochs. The impact of 3 "faulty and not detected" satellites has not been analysed due to the lack of information about ionospheric front in the horizontal domain. As for GAST-D, due to the lack of information about all possible fault monitors, RAIM cannot be considered as the definitive solution based only on this study.

6.2 Perspectives for Future Works

The $\sigma_{pr\ gnd}$ computed for GPS L1 C/A signals using Toulouse Blagnac data is well below the most accurate GAD curve. The same analysis has not been done for Pattonville data due to the absence of several RRs. However the comparison between the standard deviation shows that the accuracy is similar to the one obtained in Toulouse. Analysing data collected in more airports will permit to define a new GAD curve for GPS L1 C/A. Curves for L5/E5a signals and I-free combination may be established as well by applying the presented methodology, but require solving the calibration issue (elevation-dependent pseudorange bias) of the antenna. Some of the analysis done in this context may be applied to aircraft data to derive performances of ne signals and combinations.

Satellite selection is one of the proposals done to overcome the problem of the increased number of available signals to track and the number of corrections to broadcast. If this solution is selected, more analysis have to be done to determine the rate of change of the best subset. Due to the smoothing process and the presence of monitors in the range domain, too frequent changes in the satellites subset are not possible. Considering that a convergence time (360 seconds for 100 seconds smoothing filter) is needed from the first tracking of a satellite, such frequent changes in the satellites subset may impact the system availability and in some case the integrity performances. A new solution taking into account this parameter should be derived.

On the integrity aspect, more simulations have to be done when more information about ionosphere fronts will be available. The dual fault case must be analyzed for GAST-D case and for GAST-F considerations about three faulty and not detected satellites have to be derived. The aim is to determine if RAIM can solve the integrity issue present for SF GBAS to provide CAT II/III services. Simulations with considerations about the time of onset of the ionospheric fault, jointly with the other information about aircraft position and impacted satellites and the transient state of the carrier-smoothed tracking, have to be done in order to derive also performances for the airborne CCD and the DSIMGA monitor in the range domain, thus obtaining a global analysis of the integrity monitoring performances for GAST-D and GAST-F in presence of the identified residual ionospheric threats.

7 References

A. R. Lopez "LAAS/GBAS Ground Reference Antenna with Enhanced Mitigation of Ground Multipath"; ION ITM. - San Diego, CA; 2008.

J. E. ANGUS "RAIM with Multiple Faults. Navigation". Navigation the Journal of the ION, 2006. - Vol. 53.

B. Arbesser-Ratsburg "The Galileo Single Frequency Ionospheric Corection Algorithm". Third European Space Weather Week. - Nov. 2006.

ARINC Engineering Services "Navstar GPS Space Segment/Navigation User Interfaces", IS-GPS-200 Revision D. 2004.

F. Beck, O. Glaser and B. Vauvy "Standards – Draft Standards for Retained Galileo GBAS Configurations".

J. W. Betz and K. R. Kolodziejski "EXTENDED THEORY OF EARLY-LATE CODE TRACKING FOR A BANDLIMITED GPS RECEIVER" NAVIGATION, Journal of The Institute of Navigation, Vol. 47, No. 3, Fall 2000. - 2000. - pp. 211-226.

J. Blanch, T. Walter, P. Enge, Y. Lee, B. Pervan, M. Rippl and A. Spletter "Advanced RAIM user Algorithm Description: Integrity Support Message Processing, Fault Detection, Exclusion, and Protection Level Calculation". Proceedings of the 25th International Technical Meeting of The Satellite Division of the Institute of Navigation (ION GNSS 2012). - Nashville, TN; 2012. - pp. 2828-2849.

M. Brenner and F. Liu "Ranging Source Fault Detection Performance for Cat III GBAS". ION GNSS. - Oregon Convtion Center; Portland, OR, 2010.

R. G. Brown and G. Y. Chin "GPS RAIM: Calculation of Threshold and Protection Radius Using Chi Square Methods - a Geometric Approach". ION GPS - 1997

H. Cabler and B. DeCleene "LPV: New Improved WASS Instrulment Approach". Proceeding of ION GPS 2002, International Technical Meeting of the Satellite Division of the Institute of Naviagtion. - Portland, Oregon, U.S., 2002. - pp. 1012-1021.

R. Cassel and S. Smith "Development of Required Navigation Performance (RNP) Requirement for Airport Surface Movement Guidance and Control". Digital Avionics Conference. 1995.

M. S. Circiu, M. Felux and S. Pullen " Galileo E1, E5a Performance for Multi-Frequency, Multi-Constellation GBAS" GPS WORLD. - 2015.

S. Cryan, P. Montez and N. Moises "A Survey of GPS Satellite Selection Algorithms for Space Shuttle Autolanding" ION GPS. - Albuquerque, 1992. - pp. 1165-1171.

DO-246D RTCA Inc. “GNSS based precision approach LAAS Signal-in-Space ICD”. 2008.

DoD, Department of Defence USA Global Positioning System Standard Positioning Serivce Performance Standard; 4th edition. 2008.

EASA CS AWO 1, “Joint Aviation Requirements – All Weather Operations”, Subpart 1, “Automatic Landing Systems”. 2003.

Egis avia "EUROCONTROL’S FUNDED STUDY,STUDY ON THE IMPACT OF SOLAR ACTIVITIES ON AVIATION APPLICATIONS BASED ON GNSS OVER ECAC", D2.2 final work plan. 2010.

P. Enge, E. R. Phelts, D. Akos and A. J.Van Dierendonck "SQM Validation" RTCA SC159-WG 2/4 Meeting, 2000

Escher A. C. and Milner C. "GNSS for Civil Aviation – part 3 SBAS"; Dispenses for courses. ENAC - Toulouse

A. C. Escher and C. Milner "GNSS for Civil Aviation – part 2 ABAS, RAIM"; Dispenses for the course. ENAC, Toulouse

EUROCAE http://www.eurocae.net - 2010.

EUROCAE WG-62 “Interim Minimum Operational Performance Specification for Airborne Galileo Satellite Receiving Equipment”, version 0.26, 2007.

EU-U.S Cooperation on Satellite Navigation Working Group C, ARAIM Technical Subgroup. 2012.

EU-U.S Cooperation on Satellite Navigation Working Group C, ARAIM Technical Subgroup, Milestone 3 Report. - 2016.

FAA Advisory Circular 120-28D, “Criteria for Approval of Category III Weather Minima for Takeoff, Landing and Rollout". 1999.

M. Felux, T. Dautermann and H. Becker "GBAS Approach Guidance Performance - A Comparison to ILS," Proceedings of the 2013 International Technical Meeting of The Institute of Navigation. San Diego, California, 2013. pp. 409-414.

GJU- Galileo **Joint Undertaking** “European GNSS (Galileo) Open Service, Signal In Space Interface Control Document (OS SIS ICD)”, Issue 1.1. 2010.

GPS SPS “Global Positioning System Standard Positioning Service Performance Standard”,Department of Defense. 2008.

J. C. Grabowski "Personal Privacy Jammers: Locating Jersey PPDs Jamming GBAS Safety-of-Life Signal". GPS WORLD. 2012.

P. Groves and M. Petovello"Multipath Vs. NLOS Signals" GNSS Solutions. 2013.

R. Hatch "The synergism of GPS code and carrier measurements". International Geodetic Symposium on Satellite Doppler Positioning. Las Crucs, 1982.

L. Heng "Safe Satellite Naviagation With Multiple Constellations: Global monitoring of GPS and GLONASS Signal-in-Space Anomalies". - Stanford L. J. University : Ph.D. Thesis, 2012.

K. Hiroyuki"Dual-Frequency Smoothing for CAT III LAAS: Performance Assessment Considering Ionosphere Anomalies". Proceedings of the 20th International Technical Meeting of the Satellite Division of The Institute of Navigation (ION GNSS). - Forth Worth, TX, 2007. - pp. 424-437.

D. Holaschutz, R. H. Bishop, B. R. Harris and B.Tolman "Inter-frequency Bias Estimation for the GPS Monitor Station Network,". Proceedings of the 21st International Technical Meeting of the Satellite Division of The Institute of Navigation (ION GNSS 2008). Savannah, GA, Sep. 2008. - pp. pp. 2405-2415..

P. Y. Hwang, G. McGraw and J. R. Bader "Enhanced Differential GPS Carrier-Smoothed Code Processing Using Dual-Frequency Measurements". NAVIGATION the Journal of the Institute of NAvigation. - 1999. - pp. 127-137.

ICAO "International Standards and Recommended Practices, Annex 6 to Convention on International Civil aviation, Operation of aircraft". Eight Edition, 2001.

ICAO "Manual on Required Navigation Perfomance (RNP)". DOC 9613, Second Edition, 1999.

ICAO "Performance-based Navigation (PBN) Manual". Third Edition . - 2008.

ICAO "International Standards and Recommended Practices, Annex 10 to Convention on International Civil aviation". Volume I, Radio Navigation Aids, Sixth Edition. 2006.

ICAO NSP "Airborne DSIGMA Monitor Performance Validation". Montreal, Canada, 2016.

ICAO NSP "Airborne DSIGMA Range Monitor Performace Validation Update". Seattle, United States, 2016.

ICAO NSP "GBAS CAT II/III Development Baseline SARPs". 2010.

ICAO NSP "SARPs for GNSS elemets and signals (GBAS)". Proposed amendement to Annex 10, GBAS provision. Montreal, Canada, 2015.

ICAO NSP WGW/Flimsy29 “Development Baseline SARPs Proposal”, presented by Tim Murphy, Montreal, May 2010.

ICAO NSP WGW/WP 16 "Observed Nominale Atmospheric Behavior Using Honeywell's GAST-D Ionosphere Gradient Monitor". Montreal, Canada, 2014.

ICAO PANS ATM

Y.Jiang, C. Milner and C. Macabiau “Code-Carrier Divergence Monitoring for GAST-F GBAS”. European Navigation Conference 2015. Bordeaux, France, 2015.

O. Julien "Advanced Concepts of GNSS-IENAC 3rd year". ENAC, Toulouse, 2011/2012.

H. Kannemans"Cycle slip detection for static and moving receivers". NLR-TR-2003-019, 2003.

E. D. Kaplan and C. Jr. Hegarty "Understanding GPS: principles and applications", (Second Edition). Boston, London; Artech House, Inc., 2006.

S. Khanafseh, F. Yang, B. Pervan, S. Pullen and J. Warburton "Carrier Phase Ionospheric Gradient Ground Monitor for GBAS with Experimental Validation". ION GNSS; Portland; OR, 2010.

P. Ladoux "Task T008, System Verification. GBAS Toulouse Airport Testing Activities". SESAR 15.3.7 Meeting, Barcelona; 2016.

J. Lee, J. Seo Shin, P. Young, S. Pullen and P.Enge "Ionospheric Threat Mitigation by Geometry Screening in Ground-Based Augmentation Systems". Journal of Aircraft: 2011. - pp. 1422-1433.

A. Leick “GPS Satellite Surveying”. Wiley-Interscience, 2nd edition, 1995.

J. Liu, M. Lu, Z.Feng and J. Wang "GPS RAIM: Statistics Based Improvement on the Calculation of the Threshold and Horizontal Protection Radius". 2005.

M. Liu, M. A. Fortin and R. Jr.Landry “A Recursive Quasi-Optimal Fast Satellite Selection Method for GNSS Receivers”. ION GPS GNSS; 2009. - pp. 3022-3032.

M. Luo, S. Pullen, S. Datta-Barua, G. Zhang, T. Walter and P. Enge"Ionosphere Spatial Gradient Threat for LAAS:Mitigation and Tolerable Threat Space". ION NTM; 2004

C. Macabiau “Analysis of the Feasibility of Using GPS Carrier Phase Ambiguity Resolution Techniques for Precision Approaches”, PhD thesis. Institute Nationale Politecnique, Toulouse, 1997

A. Martineau "Performance of Receiver Autonomous Integrity Monitoring (RAIM) for Vertically Guided Approach", PhD Thesis. Institute Nationale Politecnique, Toulouse, 2008

G. A McGraw, T.Murphy, M. Brenner, S. Pullen and A.J.Van Dierendonck "Development of the LAAS Accuracy Models". Proceedings of the 13th International Technical Meeting of the Satellite Division of The Institute of Navigation; ION GPS. Salt Laken UT, 2000. - pp. 1212-1223.

C. Milner "GBAS Evolutions". International Technical Symposium on Navigation and Timing (ITSNT). ENAC, Toulouse, France, 18th November 2014.

C. Milner, A. Guilbert and C. Macabiau "Evolution of Corrections Processing for MC/MF Ground Based Augmentation System (GBAS)". ION ITM. Dana Point, CA, United States, 2015.

A. M. Mitelman "SQM for GPS augmentation systems". 2004.

L. Montloin “Review of State of the Art of A/C navigation”. ENAC, Toulouse, France, 2011.

L. Montloin "GNSS Integrity Monitoring in the Presence of Singular Events", Ph. D. Thesis. ENAC, Toulouse, France, July 2014.

T. Murphy and J. Booth "GBAS SARPs Review and Validation of Airborne Multipath Requirements" GNSSP WG B Toulouse 10/99 WP43.

T. Murphy, M. Harris and S. Beauchamp "Implications of 30-Second Smoothing for GBAS Approach Service Type D". Proceedings of the 2010 International Technical Meeting of The Institute of Navigation,. San Diego, CA, 2010. - pp. 376-385.

P. Neri "Use of GNSS signals and their augmentations for Civil Aviation navigation during Approaches with Vertical Guidance and Precision Approaches” Ph.D. Thesis. Ecole Nationale de l’Aviation Civile, Toulouse-, 2011.

M. S. Nolan "Fundamentals of Air Traffic Control". Wadsworth Publishing Company, 2nd, 1994.

B. Pervan, I. Sayim and S. Khanafseh "Synthesis of Empirical and Theoretical Approaches Toward the Establishment of GBAS sigma_pr_gnd". The Journal of Navigation. 2005. - pp. 297-313.

S. Pullen and P. Enge "An Overview of GBAS Integrity Monitoring with a Focus on Ionosheric Spatial Anomalies". Indian Journal of Radio & Space Physics, VOL. 36. August 2007.

M. Rees "EUROCONTROL Policy for GNSS in Europe". ENRI International Workshop on ATM/CNS. 2009

M. Roelandt "PBN fleet equipage according to FPL content". RAiSG/PBN TF meeting. 2014.

G. Rotondo, P. Thevenon, C. Milner, C. Macabiau, A. Hornbostel, M. Felux and M. S. Circiu "Methodology for Determining Pseudorange Noise and Multipath Models for a Multi-Constellation, Multi-frequency GBAS System". Proceedings of the 2015 International Technical Meeting of The Institute of Navigation. Dana Point, California, 2015. - pp. 383-392.

RTCA Inc. DO245-A Minimum Aviation System Performance Standards for Local Area Augmentation System [Book]. - 2004 : [s.n.].

RTCA Inc.; DO253-C Minimum operational performance standards for GPS local area augmentation system airborne equipment [Book]. - 2008.

RTCA, Inc. "Minimum Operational Performance Standards for Global Positioning System/Wide Area Augmentation System Airborne Equipment", DO229-D,RTCA SC-159 [Book]. - 2006.

W. Schuster and W. Ochieng "Harmonisation of Category-III Precision Approach Navigation System Performance Requirements". THE JOURNAL OF NAVIGATION. 2010.

J. Seo, J. Lee, S. Pullen, P. Enge, S. Close. "Targeted Parameter Inflation Within Ground-Based Augmentation System to Minimize Anomalous Ionospheric Impact". Journal of Aircraft; Vol. 49, No 2; March-April 2012

SESAR 15.3.7; WP3 "VDB Assumption and Requirements" 2015.

SESAR JU 15.3.6.D03 "High Level Performance Allocation and Split of Responsibilities between Air and Ground". 2011.

SESAR www.sesarju.eu. 2009.

A. Shively Curtis "GBAS GAST-D (CAT IIIB) Aircraft Monitor Performance Requirements for Single Referene Receiver Faults". Proceedings of the 2009 International Technical Meeting of The Institute of Navigation. Anaheim, CA, 2009. - pp. 903-916.

V. Simili Dwarakanath and B. Pervan "Code-Carrier Divergence Monitoring for the GPS Local Area Augmentation System". Proceedings of IEEE/ION PLANS 2006. San Diego, CA, 2006. - pp. 483-493.

M. Stakkeland, L. Andalsvik Yngvild and S. Jacobsen Knut "Estimating Satellite Excessive Acceleration in the Presence of Phase Scintillations". Proceedings of the 27th International Technical Meeting of The Satellite Division of the Institute of Navigation ION GNSS+ 2014. Tampa, Florida, 2014. - pp. 3532-3541..

Thales "GBAS CAT II/III L1 Approach", CAT II-III L1 as a step to multiconstellation GBAS,D05. 2006.

K. Van Dyke, K. Kovach, J. Kraemer, J. Lavrakas, J. P. Fernow, J. Reese, N. Attallah and B. Baevitz "GPS Integrity Failure Modes and Effects Analysis". Proceedings of the National Technical Meeting of The Institute of Navigation. Anaheim, CA, 2003. pp. 689-703.

Z. Wang, C. Macabiau, J. Zhang and A. C. Escher "Prediction and analysis of GBAS integrity monitoring availability at LinZhi airport", Springer Verlag. 2014. - pp. 27-40.

M. Zhang, J. Zhang and Y. Qin “Satellite Selection for Multi-constellation”. Position, Location and Navigation Symposium, IEEE/ION. 2008.

A. Civil Aviation Authorities and Requirements

A.1 Civil Aviation Authorities

The navigation equipment has to meet a number of requirement, to be authorized for use aboard aircraft, so as to ensure their capability to perform their function. The aim of this section is to briefly present and describe the main organisations which issue these requirements in the World.

A.1.1 International Civil Aviation Organization (ICAO)

ICAO is the agency of the United Nations created in 1944 to promote the safe and orderly development of international civil aviation throughout the world, which codifies the principles and techniques of international air navigation and fosters the planning and development of international air transport to ensure safe and orderly growth and the environmental protection. The ICAO Council adopts standards and recommended practices (SARPs) concerning air navigation, prevention of unlawful interference, and facilitation of border-crossing procedures for international civil aviation. In addition, the ICAO defines the protocols for air accident investigation followed by transport safety authorities in countries signatory to the Convention on International Civil Aviation, commonly known as the Chicago Convention (ICAO, 2008).

In particular, The International Civil Aviation Organization (ICAO) is responsible for establishing the standards for radio navigation aids, including the ones concerning GNSS. They are mainly defined in Annex 10 to the Convention on International Civil Aviation.

A.1.2 Radio Technical Commission for Aeronautics (RTCA, Inc.)

Founded as the Radio Technical Commission for Aeronautics in 1935, RTCA, Inc. is a private, not-for-profit corporation that develops consensus-based recommendations regarding communications, navigation, surveillance, and air traffic management (CNS/ATM) system issues. RTCA works in response to requests from the Federal Aviation Administration (FAA) to develop comprehensive, industry-vetted and endorsed recommendations for the government on issues ranging from technical performance standards to operational concepts for air transportation.

In particular, the working group SC-159 of RTCA focuses on GNSS systems. His task is to develop minimum standards that form the basis for FAA approval of equipment using GPS as primary means of civil aircraft navigation.

Different RTCA publications cover an important role in satellite navigation and will be cited in this work:

- DO-229D – *Minimum Operational Performance Standards for Global Positioning System/Wide Area Augmentation System Airborne Equipment.*
- DO-245A – *Minimum Aviation System Performance Standards for Local Area Augmentation System*
- DO-246D – *GNSS Based Precision Approach Local Area Augmentation System (LAAS) Signal-in-Space Control Document (ICD)*
- DO-253C – *Minimum Operational Performance Standards for GPS Local Area Augmentation System Airborne Equipment*

A.1.3 European Organization for Civil Aviation Equipment (EUROCAE)

The European Organization for Civil Aviation Equipment (EUROCAE) is a non-profit making organization which was formed to provide a European forum for resolving technical problems with electronic equipment for air transport. EUROCAE deals exclusively with aviation standardization (Airborne and Ground Systems and Equipment) and related documents as required for use in the regulation of aviation equipment and systems (EUROCAE, 2010).

EUROCAE is composed of manufacturers, service providers, national and international aviation authorities as well as users (airlines, airports). EUROCAE can be considered as the equivalent of RTCA for Europe.

To develop EUROCAE documents, it organizes Working Groups (WG). In particular, the WG-62 is responsible for the preparation of aviation use of Galileo and the development of initial Minimum Operation Performance Specifications (MOPS) for the first generation of Galileo airborne receivers.

A.1.4 Federal Aviation Authority (FAA) and European Aviation Safety Agency (EASA)

The official authorities which publish mandatory requirements to be respected by aircraft manufacturers and airliners to fly an aircraft are the FAA and EASA. The FAA is an agency of the United States Department of Transportation. The EASA can be considered as the equivalent structure for the European Commission. Their main goal is to ensure the safety of the civil aviation air traffic. Many of their publications are based on or refer to the standardization publications emitted by the previous organisations.

It can be mentioned here publications which are directly related to this study and which are the airworthiness criteria for landing operations. These can be found in FAA Advisory Circular AC 120-28D (FAA, 1999) and EASA CS AWO (EASA, 2003).

A.2 Phases of Flight

Before introducing the all the civil aviation requirements is necessary to introduce the different phases of flight for a typical commercial aircraft. Due to the varying physical requirements during these phases as well as the alterations in airspace properties, the technologies and performance requirements vary greatly between operations within each phase.

Next figure shows a scheme of a classical commercial aircraft operation starting from the taxing operation until the landing; for each operation is included the accident percentage.

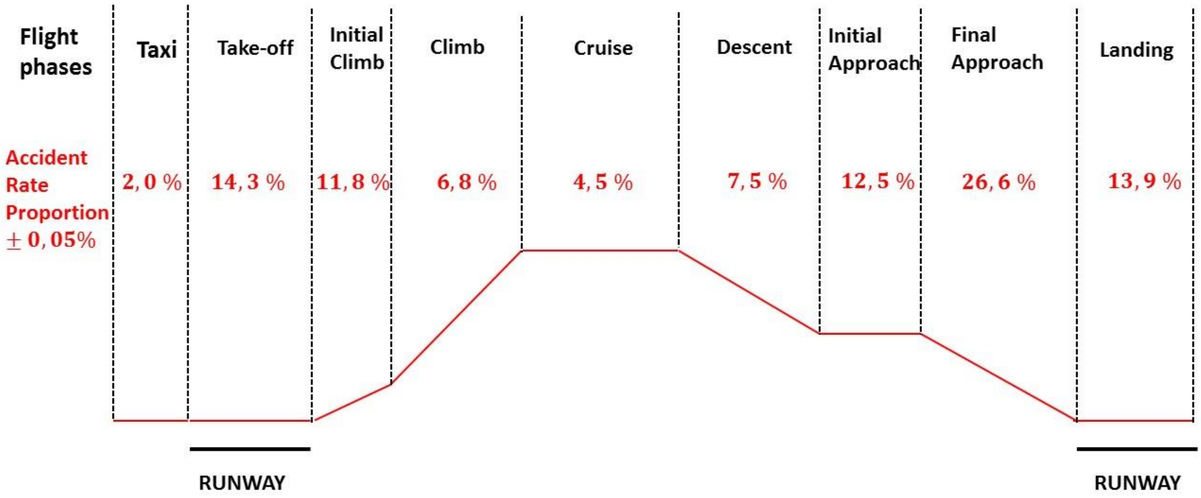

Figure 107 – Typical phases of flight (Cassel, et al., 1995)

As it is possible to see from Figure 107 typical flight is divided into different phases:

- **Taxing**; this operation involves all the movements from the gate to the departure runway.
- **Take-off**; this is the process of applying take-off power to the engines followed by reaching sufficient speed to generate lift before climb 35 ft. above the runway elevation. This operation accounts for the 14.3% of fatal accidents.
- **Initial Climb**; this phase follows the take-off, generally for a commercial flight the pilot switch to an auto-pilot system. Initial claim accounts for 11.8% of accidents.
- **Climb**; this phase is characterized by the entrance in the high-density air traffic zone and may require a series of complex manoeuvres. It’s potentially more dangerous than the en-route phase due to the closeness to the ground.
- **Cruise**; after the aircraft has climbed to cruising altitude, it performs en-route operations via waypoints. Waypoints may be defined either by the position of NavAids over ground, longitude and latitude fixes over water or when using GPS or combined GPS/INS by custom waypoints entered in the integrated GPS receiver.
- **Descent**; occurs between the en-route flight at cruise altitude and terminal arrival at the Initial Approach Fix (IAF) required for initiating an approach. An increase from the en-route phase to 7.5% of accidents is noted due to increased traffic and critical aircraft functions.

- **Initial Approach**; phase after the IAF point where the pilot starts the navigation towards the FAF (Final Approach Fix), a position aligned with the runway from where a safe controlled descent towards the runway can be achieved. The accident rate for this operation accounts for the 12.5 %.
- **Final Approach**; it begins at the FAF and continues beyond the Minimum Decision Height (MDH) until the pilot performs the landing manoeuvre. The MDH is the height above the runway at which the pilot must abort if the required visual reference to the runway is not obtained. It is usual that the better the landing aids, the lower the MDH. Final approach is the most dangerous flight phase of flight (26.6% of accidents) due to high traffic densities, obstacles and frequency and complexity of mechanical operations.
- **Landing**; this is the final part of a flight, after this phase other taxiing operations are performed to reach the arrival gate. Alignment of the aircraft to the runway is determined just prior to the touchdown during the de-crab manoeuvre. In high winds, the aircraft will approach at a ‘crabbed’ angle. These processes may be performed by the pilot visually or by the autopilot coupled to the navigation and landing aids. The landing phase is completed at the end of the main runway before the aircraft returns to the taxi area. Landing accounts for 13.9% of fatal accidents.

Due to particular conditions like high-density traffic, extreme weather condition or poor visibility a pilot or an air traffic control can perform a **Missed approach** procedure. This procedure usually consists of a climb and then a holding procedure formed of two straight segments and two 180 degree turns. Terminal navigation aids are usually used for navigation such as the ILS or terminal VOR (Nolan, 1994).

A.2.1 Approach

From the analysis of the flight phases is possible to note how the two approach phases account for over 39% of the accident rate in a commercial flight; whit no doubt we can say that this phase is the most important and the most critical during the flight. To better analyze the approaches phase we need to describe this operation in deep.

The categories of approach are defined according to the level of confidence that can be placed by the pilot into the system he is using to help him land the plane safely. Approaches are divided in two main segments: the aircraft first follows the indication provided by the landing system, and then the pilot takes over in the final part and controls the aircraft using visual outside information. As the reliability of the aircraft, the crew and the landing system increases, the height of the aircraft above the ground at the end of the interval of use of the information provided by the system can be decreased (Macabiau, 1997).

The next figure shows a focus of the last part of a commercial flight, in particular the approach phase is divided according with the ICAO approach and landing classification. The type of GNSS augmentations which allow conducting navigation operations for civil aviation during the corresponding phase of flight are shown at the bottom of the figure.

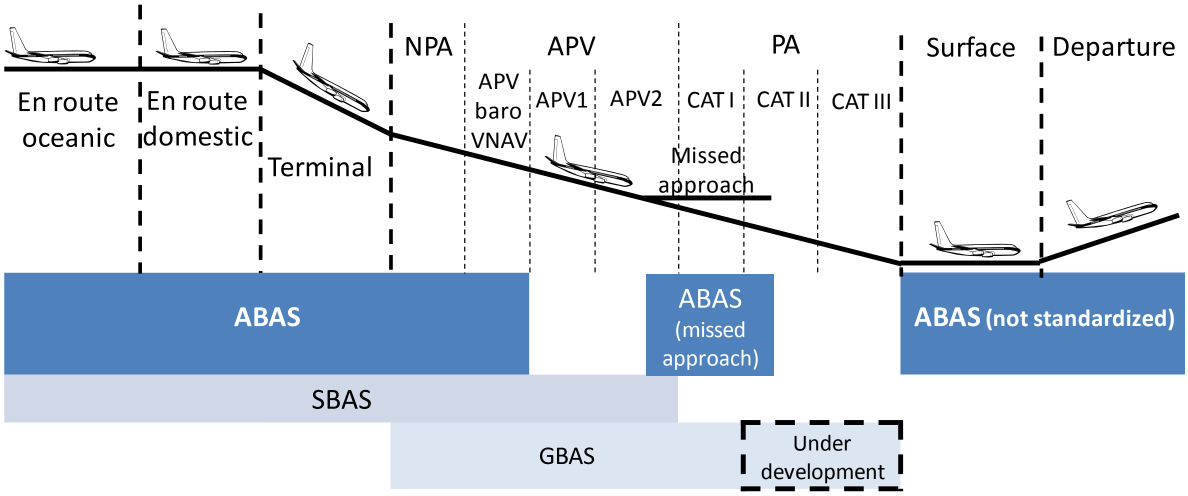

Figure 108 – Phases of flight and GNSS augmentation (Montloin, 2011)

The ICAO defines, in Annex 6, three main approaches and landing categories (ICAO, 2001) and they are classified as follows:

- **Non-Precision Approaches and landing operations (NPA)**: an instrument approach and landing which utilizes lateral guidance but does not utilize vertical guidance.
- **Approaches and landing operations with vertical guidance (APV)**: an instrument approach and landing which utilizes lateral and vertical but does not meet the requirements established for precision approach and landing operation.
- **Precision approaches and landing operation (PA)**: an instrument approach and landing using precision lateral and vertical guidance with minima as determined by the category of operation.

Three different operational parameters which are the Decision Height (DH), the Distance of Visibility and the Runway Visual Range (RVR) can be used to describe better the previous category for approach and landing. These parameters are defined as follows (Cabler, et al., 2002):

- Decision Height (DH) is the minimal height above the runway threshold at which as missed approach procedure must be executed if the minimal visual reference required in order continuing the approach has not been established.
- Distance of Visibility is the greatest distance, determined by atmospheric conditions and expressed in units of length, at which it is possible with unaided eye to see and identify, in daylight a prominent dark object, and at night a remarkable light source.

- Runway Visual Range (RVR) is the maximum distance in the landing direction at which the pilot on the centre line can see the runway surface markings, runway lights, as measured at different points along the runway and in particular in the touchdown area.

In the next table the requirements, as function of the previous parameters, are listed.

Table 31 – Decision height and visual requirements (ICAO, 2001)

Category			**Minimum Descent Altitude (MDA)** **Minimum Descent Height (MDH)** **Decision Altitude (DA)** **Decision Height (DH)**	**Visual Requirement**
NPA			MDA ≥ 350 ft.	Depending on the airport equipment
APV			DA ≥ 250 ft.	
LPV 200			DH ≥ 60 m (200 ft.)	
Precision Approaches	**CAT-I**		DH ≥ 60 m (200 ft.)	Visibility ≥ 800 m
				RVR ≥ 550 m
	CAT-II		30 m (100 ft.) ≥ DH ≤ 60 m (200 ft.)	RVR ≥ 300 m
	CAT-III	**A**	0 m ≥ DH ≤ 30 m (100 ft.)	RVR ≥ 175 m
		B	0 m ≥ DH ≤ 15 m (50 ft.)	50 m ≤ RVR ≥ 175 m
		C	DH = 0 m	RVR = 0 m

A.3 Performance Based Navigation (PBN)

The Performance Based Navigation (PBN) concept specifies aircraft RNAV (Area Navigation) system performance requirements defined in terms of the accuracy, integrity, availability, continuity and functionality, which are needed for the proposed operations in the context of a particular airspace concept. The PBN concept represents a shift from sensor-based to performance-based navigation. Performance requirements are identified in navigation specifications, which also identify the choice of navigation sensors that may be used to meet the performance requirements. These navigation specifications are defined at a sufficient level of detail to facilitate global harmonization by providing specific implementation guidance for States and operators (ICAO, 2008).

The PNB criteria offers a certain number of advantages over the sensor-based developing of the airspace and obstacle clearance criteria:

- Reduces the need to maintain sensor-specific routes and procedures, and their associated costs.
- Avoids the need for developing sensor-specific operations with each new evolution of navigation systems, which would be cost-prohibitive.
- Allows for more efficient use of airspace (route placement, fuel efficiency and noise abatement)
- Clarifies how RNAV systems are used.

Facilitates the operational approval process for operators by providing a limited set of navigation specifications intended for global use.

The RNB concept relies on RNAV system and Required Navigation Performance (RNP) procedures, the ICAO definitions for these two key terms and other key terms are listed below (ICAO, 2001):

- Area Navigation (RNAV): A method of navigation which permits aircraft operation on any desired flight path within the coverage of station-referenced navigation aids or with the limits of the capability of self-contained aids, or a combination of these.
- Area Navigation Equipment: Any combination of equipment used to provide RNAV guidance.
- Required Navigation Performance (RNP) Systems: An area navigation system which supports on-board performance monitoring and alerting.
- Required Navigation Performance (RNP): A statement of the navigation performance necessary for operation within a defined airspace.

The RNP settled by ICAO in (ICAO, 2006) can by defined by the Total System Error (TSE); the next figure illustrates how the TSE is composed.

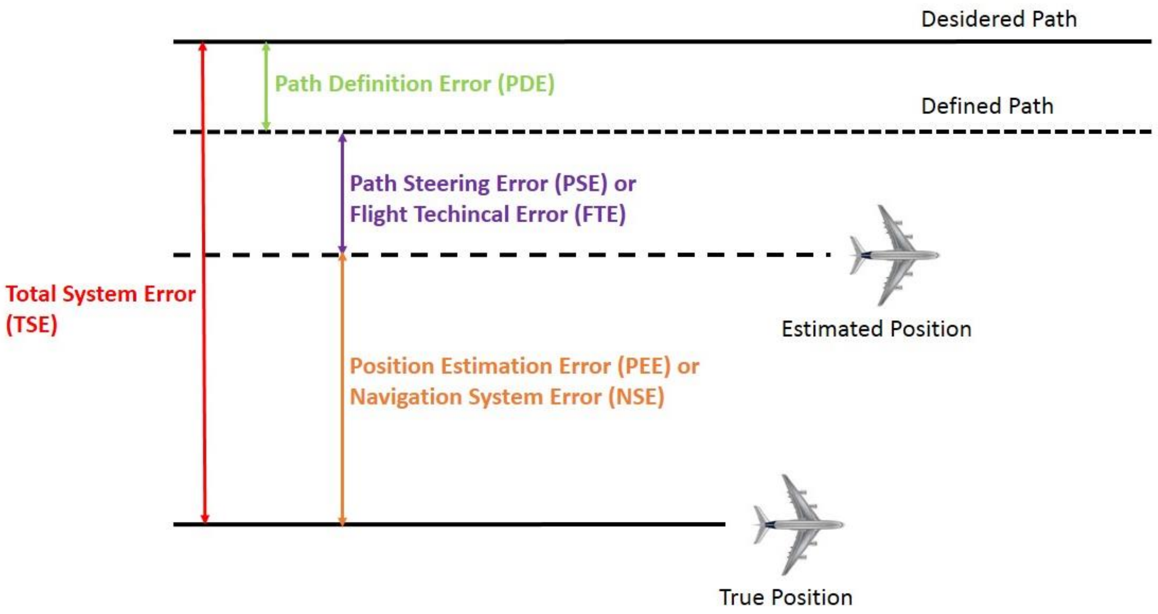

Figure 109 – Total system error components (Martineau, 2008)

The terms presented in Figure 109 are:

- Desired Path is the path that the flight crew and the air traffic control can expect by the aircraft for a given route or leg.
- Defined Path is the output of the definition function.
- PDE (Path Definition Error) is the difference the desired path (the path that the crew and air traffic control can expect the aircraft to fly) and the path defined by the Flight Management System (FMS).
- PSE (Path Steering Error) or FTE (Flight Technical Error) is the difference between the estimated position of the aircraft and the path defined by the FMS (Flight Management System). This error is due to the way the aircraft is controlled, and it is also called XTK (Cross Track Error).
- NSE (Navigation System Error) is the difference between the estimated position and the true position of the aircraft.

A.4 Performance Navigation Criteria

Navigation system performance requirements are defined in the Manual on Required Navigation Performance (ICAO, 1999) for a single aircraft and for the total system which includes the signal-in-space, the airborne equipment and the ability of the aircraft to fly the desired trajectory. These total system requirements were used as a starting point to derive GNSS signal-in-space performance requirements which criteria definitions are given in this section (ICAO, 2006).

A.4.1 Accuracy

"GNSS position error is the difference between the estimated position and the actual position. For an estimated position at a specific location, the probability should be at least 95 per cent that the position error is within the accuracy requirement." (ICAO, 2006).

The accuracy is the measure of the quality of the positioning element of the navigation function; it describes a relationship between the real position and the estimated position displayed to the pilot. In order to characterize the accuracy on the estimated quantity, ICAO has defined a 95% confidence level. It means that for any estimated position at a specific location, the probability that the position error is within the former requirement should be at least 95%.

A.4.2 Availability

"The availability of GNSS is characterized by the proportion of time the system is to be used for navigation during which reliable navigation information is presented to the crew, autopilot or other system managing the flight of the aircraft." (ICAO, 2006).

The availability of a navigation system is the ability of the system to provide the required function and performance at the initiation of the intended operation.

A.4.3 Integrity

"Integrity is a measure of the trust that can be placed in the correctness of the information supplied to the total system. Integrity includes the ability of a system to provide timely and valid warnings to the user (alerts) when the system must not be used for the intended operation." (ICAO, 2006)

Integrity requirements are defined thanks to three parameters:

- The integrity risk
- The time to alert
- The alert limit

The **Integrity risk** is the probability of providing a signal that is out of tolerance without warning the user in a given period of time.

Time-to-Alert is the maximum allowable elapsed time from the onset of a positioning failure until the equipment annunciates the alert.

Alert limits, for each phase of flight, ensures that the position error is acceptable, alert limits are defined and represent the largest position error which results in a safe operation.

- The Horizontal Alert Limit (HAL) is the radius of a circle in the horizontal plane (the local plane tangent to the WGS-84 ellipsoid), with its centre being at the true position, that describes the region that is required to contain the indicated horizontal position with the required probability for a particular navigation mode.
- The Vertical Alert Limit (VAL) is half the length of a segment on the vertical axis (perpendicular to the horizontal plane of WGS-84 ellipsoid), with its centre being at the true position, that describes the region that is required to contain the indicated vertical position with the required probability for a particular navigation mode.

The probability of non-integrity detection quantifies the integrity risk. It represents the probability that an error exceeds the alert limit without the user being informed within the time to alert. The values assigned to these three parameters depend on the specific application and intended operation. They are determined by the International Civil Aviation Organization.

A.4.4 Continuity

"Continuity of Service of a system is the capability of the system to perform its function without unscheduled interruptions during the intended operation." (ICAO, 2006).

Continuity relates to the capability of the navigation system to provide a navigation output with the specified accuracy and integrity throughout the intended operation, assuming that it was available at the start of the operation. The occurrence of navigation system alerts, either due to rare fault-free performance or to failures, constitute continuity failures. For en-route, since the durations of these operations are variable, the continuity requirement is specified as a probability on a per-hour basis. For approach and landing operations, the continuity requirement is stated as a probability for a short exposure time. More specifically, continuity is the probability that the specified system performance will be maintained for the duration of a phase operation, presuming that the system was available at the beginning of that phase operation and was predicted to operate throughout the operation.

A.5 Annex 10 Signal in Space Requirements

According to (ICAO, 2006) the combination of GNSS elements and a fault-free GNSS user receiver shall meet the signal-in-space (SiS) requirements.

Table 32 – SiS performance requirements (ICAO, 2006)

Typical Operation	**Accuracy Horizontal 95% (Note 1 and 3)**	**Accuracy Vertical 95% (Note 1 and 3)**	**Integrity (Note 2)**	**Time-to-Alert (Note 3)**	**Continuity (Note 4)**	**Availability (Note 5)**
En-Route	$3.7\ km$	N/A	$1-10^{-7}/h$	$5\ min$	$1-10^{-4}/h$ to $1-10^{-8}/h$	0.99 to 0.99999
En-Route Terminal	$0.74\ km$	N/A	$1-10^{-7}/h$	$15\ s$	$1-10^{-4}/h$ to $1-10^{-8}/h$	0.99 to 0.99999
Initial Approach, Intermediate Approach, Non-Precision Approach, Departure	$220\ m$	N/A	$1-10^{-7}/h$	$10\ s$	$1-10^{-4}/h$ to $1-10^{-8}/h$	0.99 to 0.99999
Approach Operations with Vertical Guidance (APV-I)	$16\ m$	$20\ m$	$1-2\cdot 10^{-7}/app$	$10\ s$	$1-8\cdot 10^{-6}/15\ s$	0.99 to 0.99999
Approach Operations with Vertical Guidance (APV-II)	$16\ m$	$8\ m$	$1-2\cdot 10^{-7}/app$	$6\ s$	$1-8\cdot 10^{-6}/15\ s$	0.99 to 0.99999
Category I Precision Approach	$16\ m$	$4\ m \sim 6\ m$	$1-2\cdot 10^{-7}/app$	$6\ s$	$1-8\cdot 10^{-6}/15\ s$	0.99 to 0.99999

Note for Table 32 as defined by (ICAO, 2006)

1. The 95th percentile values for GNSS position errors are those required for the intended operation at the lowest height above threshold (HAT), if applicable.
2. The definition of the integrity requirement includes an alert limit against which the requirement can be assessed. For Category I precision approach, a vertical alert limit (VAL) greater than 10 m for a specific system design may only be used if a system-specific safety analysis has been completed. Further guidance on the alert limits is provided in (ICAO, 2006) Attachment D. These alert limits are:

Table 33 – Alert limit associated to the typical operations (ICAO, 2006)

Typical Operation	**Horizontal Alert Limit**	**Vertical Alert Limit**
En-Route (Oceanic/Continental Low Density)	*7.4 Km (4 NM)*	*N/A*
En-Route (Continental)	*3.7 Km (2 NM)*	*N/A*
En-Route, Terminal	*1.85 Km (1 NM)*	*N/A*
NPA	*556 m (0.3 NM)*	*N/A*
APV-I	*40 m (130 ft.)*	*50 m (164 ft.)*
APV-II	*40 m (130 ft.)*	*20 m (66 ft.)*
CAT-I Precision Approach	*40 m (130 ft.)*	*35 to 10 m (115 to 33 ft.)*

3. The accuracy and time-to-alert requirements include the nominal performance of a fault-free receiver.
4. Ranges of values are given for the continuity requirement for en-route, terminal, initial approach, NPA and departure operations, as this requirement is dependent upon several factors including the intended operation, traffic density, and complexity of airspace and availability of alternative navigation aids. The lower value given is the minimum requirements for areas with low traffic density and airspace complexity. The higher value given is appropriate for areas with high traffic density and airspace complexity. Continuity requirements for APV and Category I operations apply to the average risk (over time) of loss of service, normalized to a 15-second exposure time.
5. A range of values is given for the availability requirements as these requirements are dependent upon the operational need which is based upon several factors including the frequency of operations, weather environments, the size and duration of the outages, availability of alternate navigation aids, radar coverage, traffic density and reversionary operation procedures. The lower values given are the minimum availabilities for which a system is considered to be practical but are not adequate to replace non-GNSS navigation aids. For en-route navigation, the higher values given are adequate for GNSS to be the only navigation aid provided in an area. For approach and departure, the higher values given are based upon the availability requirements at airports with a large amount of traffic assuming that operations to or from multiple runways are affected but reversionary operational procedures ensure the safety of the operation.
6. A range of values is specified for Category I precision approach. The 4.0 m (13 feet) requirement is based upon ILS specifications and represents a conservative derivation from these specifications.
7. GNSS performance requirements for Category II and III precision approach operations are under review and will be included at a later date.
8. The terms APV-I and APV-II refer to two levels of GNSS approach and landing operations with vertical guidance (APV) and these terms are not necessarily intended to be used operationally

The concept of a fault-free user receiver is applied only as a means of defining the performance of combinations of different GNSS elements. The fault-free receiver is assumed to be a receiver with nominal accuracy and time-to-alert performance. Such a receiver is assumed to have no failures that affect the integrity, availability and continuity performance.

8.1 CAT II/III Requirements

While the Signal-In-Space (SIS) performance requirements for Category-I approaches are well established, those for Category-II and III approaches have been under debate by the two main regulatory agencies – the EUROCAE – EU and the RTCA – USA- for several years. Two separate methods were used in the derivation of these requirements, the first one is named "ILS Look-Alike Method" is based on the concept of matching the performance of the ILS at the Navigation System Error (NSE) level through linearization of current specifications at a given height. The second method is called "Autoland Method" is based on the need to protect the safety of a landing operation using the current specification for the probability to land in a given landing box (Schuster, et al., 2010).

The first method named "ILS Look-Alike Method" is based on the concept of matching the performance of the ILS at the Navigation System Error (NSE) level through linearization of current specifications at a given height. The figure below explains this method

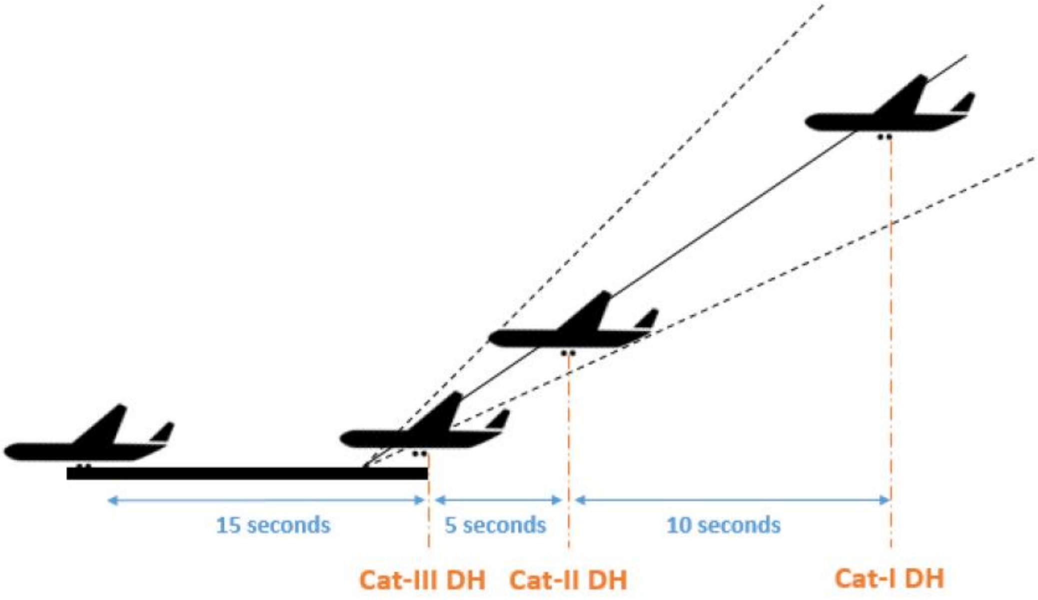

Figure 110 – "ILS look-alike method"

The second one called "Autoland Method" is based on the need to protect the safety of a landing operation using the current specification for the probability to land in a given landing box. The following figure describes this method.

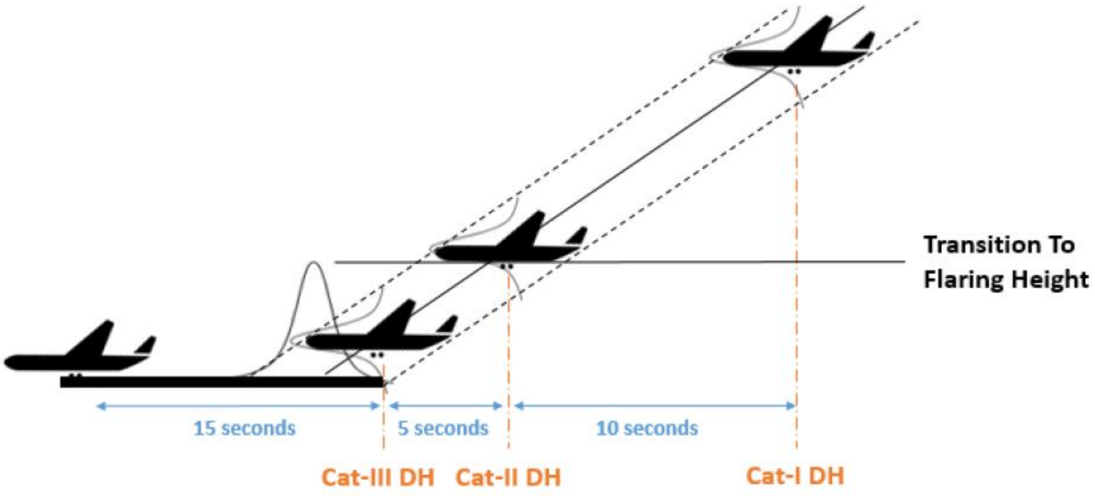

Figure 111 – Autoland method

The use of this two method has given results quite different.

Table 34 – SiS performance requirements for various phases of aircraft operation

Category III		**ILS look-alike (EUROCAE)**	**Autoland (RTCA)**
Accuracy	***SIS Accuracy***	3.6 m (L) 1.0 m (V)	6.2 m (L) 2.0 m (V)
	Alert Limit	10.4 m (L) 2.6 m (V)	15.5 m (L) 10.0 m (V)
Integrity	***Integrity Risk***	$1e^{-9}$ per 30 s (L) $1e^{-9}$ per 15 s (V)	$1e^{-9}$ per 30 s (L) $1e^{-9}$ per 15 s (V)
	Time to Alert	2 s	2 s
Continuity	***Continuity Risk***	$2e^{-6}$ per 30 s (L) $2e^{-6}$ per 15 s (V)	$2e^{-6}$ per 30 s (L) $2e^{-6}$ per 15 s (V)
Availability	***Probability of Availability***	0.99 – 0.99999	0.99 – 0.99999

B. GBAS Messages

To send the corrections, and others parameters, from the ground station to the aircraft, a series of messages is used. Table 35 lists the content of each message (DO-246D, 2008).

Table 35 – LAAS VHF Data Broadcast (VDB) messages and broadcast rate (DO-246D, 2008)

Message Type	**Message Name**	**Minimum Broadcast Rate**	**Maximum Broadcast Rate**
1	Differential Correction for 100 s Smoothed Pseudorange	For Each Measurement Type: All Measurement Blocks, once per Frame (Note 1)	For Each Measurement Type: All Measurement Blocks, once per Frame (Note 1)
2	GBAS Related Data	Once per 20 Consecutive Frames	Once per Frame
3	Null Message	N/A	N/A
4	Final Approach Segment (FAS) Construction Data	All FAS Blocks Once per 20 Consecutive Frames (Note 2)	All FAS Blocks Once per Frames (Note 2)
	Terminal Area Path (TAP) Construction Data	(notes 2 and 3)	notes 2 and 3)
5	Ranging Source Availability (Optional)	All Impacted Source once per 20 Consecutive Frames	All Impacted Source once per 5 Consecutive Frames
6	Reserved for Carriers Corrections	-	-
7	Reserved for Military	-	-
8	Reserved for Test	-	-
11	Differential corrections 30 s Smoothed Pseudoranges	For Each Measurement Type: All Measurement Blocks, once per Frame (Note 5)	For Each Measurement Type: All Measurement Blocks, once per Frame (Note 5)
101	GRAS Pseudorange Correction (as defined in (ICAO, 2006))	-	-

Note 1: each type 1 message or linked type 1 message pair broadcast in a given frame includes a set of 100 second smoothed corrections with the common modified z-count for its measurement type.

Note 2: if no FAS or TAP are currently being supported, than is not necessary to transmit type 4 message.

Note 3: the minimum and maximum broadcast rate for TAP data will be the standardized commensurate with the procedure supported as in the operational concept is matured.

Note 4: message type 3 was previously reserved to support an airport pseudolite (APL) or Ground Based Ranging Source (GBRS). APLs are not included in LAAS ICD (DO-246D, 2008).

Note 5: each type 11 message (or a linked set to type 11 message) include a set of a 30 s smoothed corrections with the common modified z-count for its measurement type.

According to the active service each message can be optional or required, in the next table the requirement are listed (DO-246D, 2008).

Table 36 – GBAS message type required for each service level

Message type	**GAST A**	**GAST B**	**GAST C**	**GAST D**
MT1	Optional (note1)	Required	Required	Required
MT2	Required	Required	Required	Required
MT2-ADB1	Optional	Optional	Optional	Required
MT2-ADB2	Optional	Optional	Optional	Optional
MT2-ADB3	Optional	Optional	Optional	Required
MT2-ADB4	Optional	Optional	Optional	Required
MT3	Optional	Optional	Optional	Required
MT4	Optional	Required	Required	Required
MT5	Optional	Optional	Optional	Optional
MT11	Not applicable	Not Applicable	Not Applicable	Required
MT101	Optional (note1)	Not Allowed	Not Allowed	Not Allowed

Note 1; for GAST A either message type 1 or message type 101 are broadcast not both.

In the next part some of the most important messages will be shown in detail. All the details about the other messages are described in (DO-246D, 2008).

B.1 Type 1 Message – Pseudorange Correction

Message type 1 provides the differential corrections data for individual GNSS ranging sources applicable to pseudorange that are carrier smoothed with a time constant of 100 s. The message contains three sections: message information (time of validity, additional message flag, number of measurement and message flag), low frequency correction information (ephemeris decorrelation parameters, ranging source ephemeris CRC and ranging source availability duration information) and the ranging source data measurements blocks.

In (DO-246D, 2008), the message type 1 format is defined thanks to this following table:

Table 37 – Message type 1 format

Data Content	**Bit Used**	**Range of Values**	**Resolution**
Modified z-count	14	0-1199.9 sec	0.1 sec
Additional Message Flag	2	0-3	1
Number of Measurement	5	0-18	1
Measurement Type	3	0-7	1
Ephemeris Decorrelation Parameters (note 2,5)	8	$0\text{-}1.275 \times 10^{-3}\ m/m$	$5 \times 10^{-6}\ m/m$
Ephemeris CRC (note 2,5)	8 (Most significant byte) (note 6)	-	-
	8 (least significant byte) (note 7)		
Source Availability Duration (note 4,5)	8	0-2450 sec	10 sec
For N Measurement Blocks:			
Ranging Source ID	8	1-255	1
Issue of Data (IOD)	8	0-255	1
Pseudorange Corrections(PRC)	16	$\pm 327.67\ m$	0.01 m
Range Rate Correction (RRC)	16	$\pm 32.767\ m/s$	0.001 m/s
$\sigma_{pr\ gnd}$	8	0-5.08 m	0.02 m
B_1 (note 1)	8	$\pm 6.35\ m$	0.05 m
B_2 (note 1)	8	$\pm 6.35\ m$	0.05 m
B_3 (note 1)	8	$\pm 6.35\ m$	0.05 m
B_4 (note 1)	8	$\pm 6.35\ m$	0.05 m

Notes

1. *1000 0000 indicates the measurement is not available*
2. *For SBAS satellite the parameter is set to zero*
3. *1111 1111 indicates the source is invalid*
4. *1111 1111 indicates that value is not completed and should not be used*
5. *Parameter is associated with the first transmitted measurement block*
6. *Ephemeris CRC most significant byte – this byte contain the remainder coefficients,* r_9 *to* r_{16} *of the 16 bit ephemeris CRC*
7. *Ephemeris CRC least significant byte – this byte contains the remainder coefficients,* r_1 *to* r_8 *of the 16 bit ephemeris CRC.*

Details on the parameters will be provided in the following of the work.

B.2 Type 2 Message – GBAS Related Data

It identifies the exact location for which the differential corrections provided by the ground augmentation system are referenced. The message also contains configuration data and data to compute a tropospheric correction.

Additional data blocks may be appended to the end of this type of message. In the following section the Additional data block 3 could be useful to defined GAST-D pseudorange measurement error models. It contains missed detection "K" values for ephemeris error and ionospheric parameters for GPS and GLONASS.

In (DO-246D, 2008) the message type 2 format is defined thanks to this following table:

Table 38 – Message Type 2 format

Data Content	Bit Used	Range of Values	Resolution
Ground Station Reference Receivers	2	2-4	-
Ground Stations Accuracy Designator	2	-	-
Spare	1	-	-
Ground Station Continuity/integrity Designator	3	-	-
Local Magnetic Variation	11	$\pm 180°$	$0.25°$
Spare	5	-	-
$\sigma_{iono\ vert\ gradient}$	8	$0 - 25.5 \times 10^{-6}\ m/m$	$0.1 \times 10^{-6}\ m/m$
Refractivity Index	8	16-781	3
Scale Height	8	0-25500 m	100 m
Refractivity Uncertainty	8	0-255	1
Latitude	32	$\pm 90°$	0.0005 arcsec
Longitude	32	$\pm 180°$	0.0005 arcsec
Reference Point Height	24	$\pm 83886.07\ m$	0.01 m
Additional Data block 1 (if provided)			
Reference Station Data Selector	8	0-48	1
Maximum use Distance D_{max}	8	$2 - 510\ Km$	2 km
$K_{md\ e\ POS,GPS}$	8	0-12.75	0.05
$K_{md\ e\ C,GPS}$	8	0-12.75	0.05

$K_{md\ e\ POS,GLONASS}$	8	0-12.75	0.05
$K_{md\ e\ C,GLONASS}$	8	0-12.75	0.05
Additional data block(s) (if provided may be included only if Additional block 1 is also provided			
Repeat for Additional Data Blocks			
Additional Data Block Length	8	2-198	1 byte
Additional data Block Number	8	2-255	1
Data Content	Variable		

And for the Additional data block 3:

Table 39 – Additional data block 3

Data Content	Bits Used	Range of Values	Resolution
Additional Data Block Length	8	6	1 byte
Additional Data Block Number	8	3	1
$K_{md\ e\ D,GPS}$	8	0-12.75	0.05
$K_{md\ e\ D,GLONASS}$	8	0-12.75	0.05
$\sigma_{vert\ iono\ gradient,D}$	8	$0 - 25.5 \times 10^{-6}\ m/m$	$0.1 \times 10^{-6}\ m/m$
Spare	8	-	-

B.3 Type 11 Message – Pseudorange Corrections for 30 Seconds Smoothed Pseudorange

It provides the differential correction data for individual GNSS ranging sources applicable to pseudorange that are carrier smoothed with a time constant of 30 seconds. The message also includes parameters that describe the distribution of errors in the 30 second smoothed corrections as well as parameters that describe the error in the corresponding 100 seconds smoothed corrections (in type 1 message) as applicable for GAST-D.

In (DO-246D, 2008) the message type 11 format is defined thanks to this following table:

Table 40 – Message Type 11 format

Data Content	**Bits Used**	**Range of Values**	**Resolution**
Modified Z-count	14	0-1199.9 sec	0.1 sec
Additional Message Flag	2	0-3	1
Number of Measurement	5	0-18	1
Measurement Type	3	0-7	1
Ephemeris Decorrelation Parameters (note 1 and 3)	8	$0 - 1.275 \times 10^{-3}\ m/m$	$5 \times 10^{-6}\ m/m$
For N Measurement			
Ranging source ID	8	1-255	1
Pseudorange Correction ($PRC_{\tau\ 30}$)	16	$\pm 327.67\ m$	0.01 m
Range Rate Correction ($RRC_{\tau\ 30}$	16	$\pm 32.767\ m$	0.001 m/s
$\sigma_{pr\ gnd\ 100}$ (note 2)	8	0-5.08 m	0.02 m
$\sigma_{pr\ gnd\ 30}$ (note 2)	8	0-5.08 m	0.02 m

Notes

1. *For SBAS satellites the parameter is set to all 0's.*
2. *1111 1111 indicate the source is invalid*
3. *Parameter is associated with the firs transmitted measurement block*

C. MC/MF GBAS Ground Multipath and Noise Model

In this appendix the results obtained from some of other days of data collection done at Toulouse Blagnac airport. One day analysis will be shown also for Pattonville data collection of the 50 meters and 100 meters case.

C.1 Pattonville 50 Meters Case

Figure 112 shows the raw and smoothed CMC for GPS L1, L5 and I-free combination for data collected at Pattonville with a building 50 meters far.

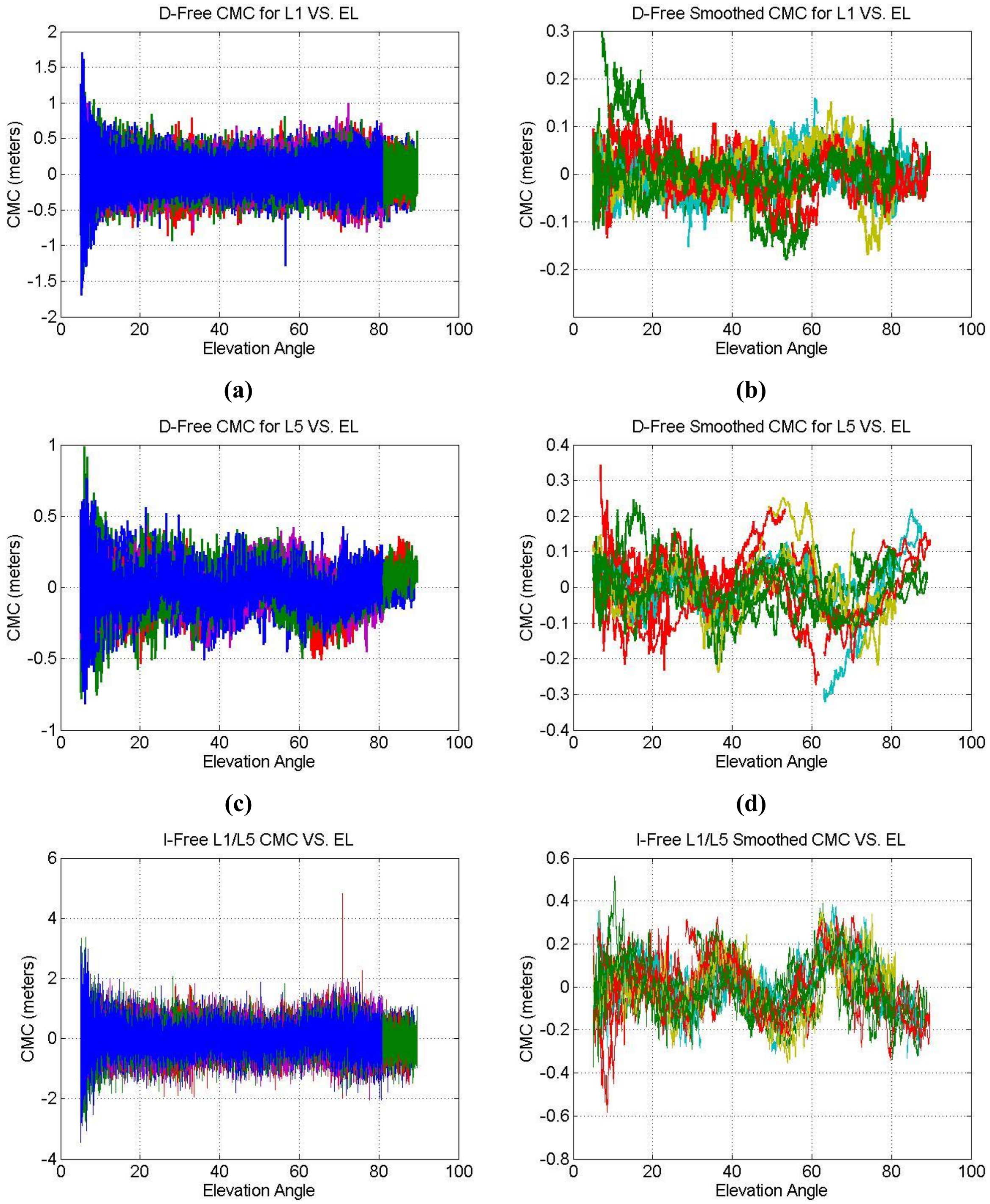

(a) **(b)**

(c) **(d)**

(e) **(f)**

Figure 112 – GPS L1 C/A, GPS L5 and I-Free raw and smoothed CMC for all satellites Pattonville 50 m. case

The CMCs for this scenario are similar to the one obtained in 3.3.2 for Toulouse Blagnac. It is possible to note in (d and f) the same oscillations affecting the CMC derived from Toulouse data, this results confirms the hypothesis of an antenna calibration issue.

The standard deviation of the raw and smoothed CMCs for all signals and for I-free combination across all days are shown in Figure 113. The elevation angle binning has been done selecting all the CMCs in the interval $\pm$ 0.5°.

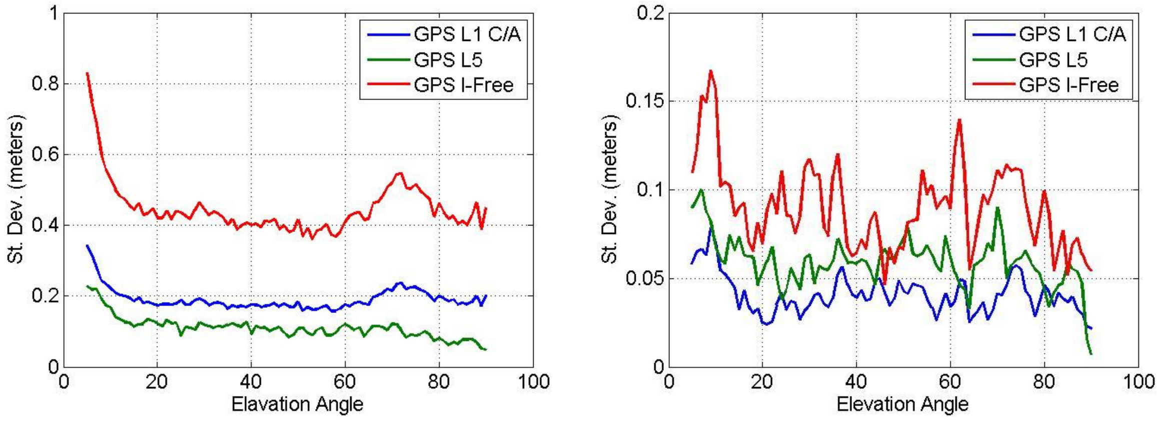

Figure 113 – Raw (left) and 100 s. smoothed (right) CMC standard deviation for GPS L1, L5 and I-Free combinations Pattonville 50 m. case

The values of the standard deviation for this analysis provides results similar to the ones obtained in 3.3.2.

C.2 Pattonville 100 Meters Case

As for the previous section, the next three plots show the raw CMCs, L1 and L5 D-Free and I-Free, for one day out of the three analysed.

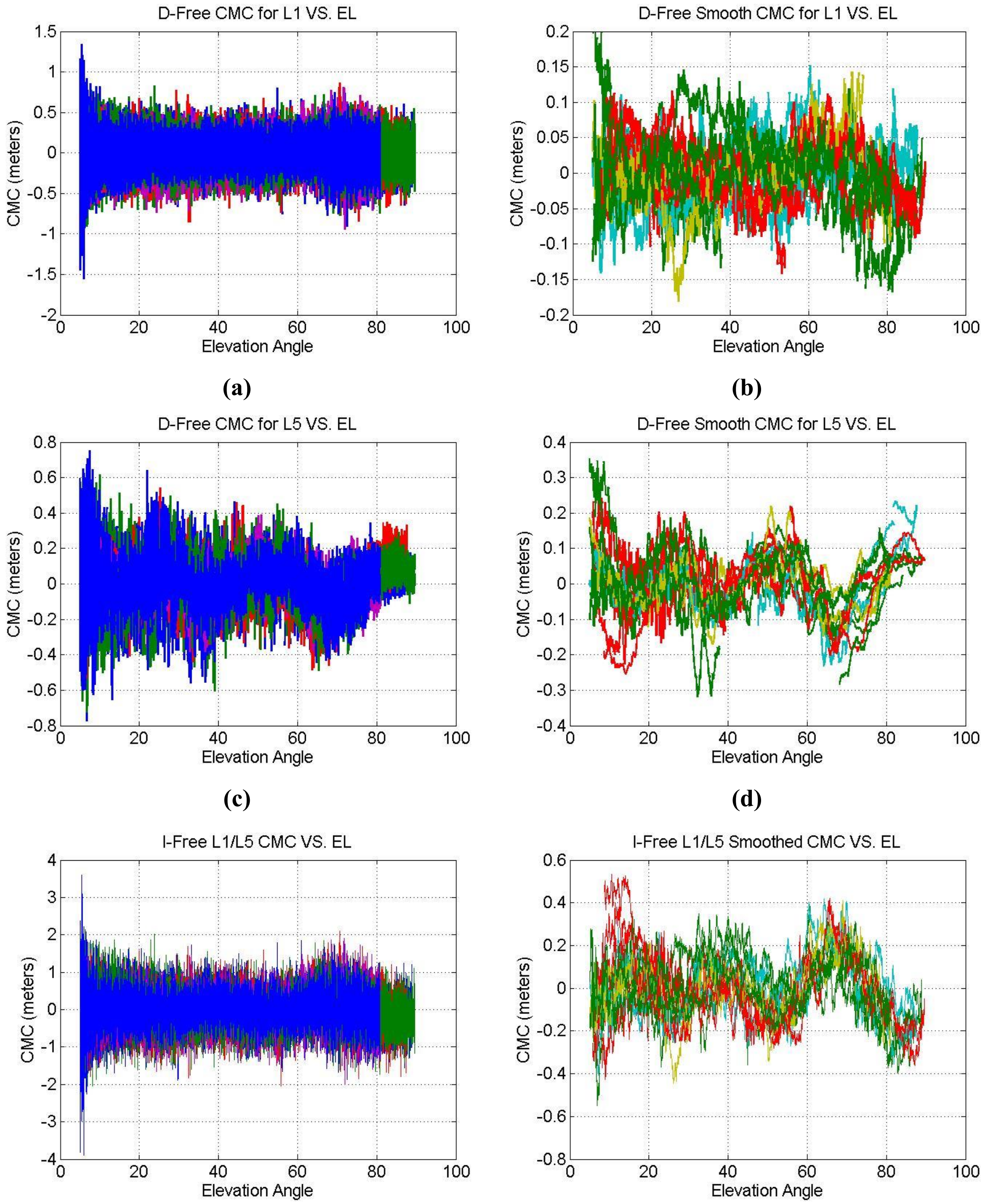

(a) **(b)**

(c) **(d)**

(e) **(f)**

Figure 114 – GPS L1 C/A, GPS L5 and I-Free for raw and smoothed CMCs for all satellites Pattonville 100 m. case

Results in Figure 114, for all the cases, are similar to one obtained for the previous case, building 50 meters far, showing the multipath rejection properties of the used antenna. Also for this scenario the oscillations impacting GPS L5 (d) and I-free (f) are visible and they are similar to the ones seen in the other cases.

The last analysis regards the standard deviation of the raw and smoothed CMCs analyzed before. Figure 115 shows the obtained values.

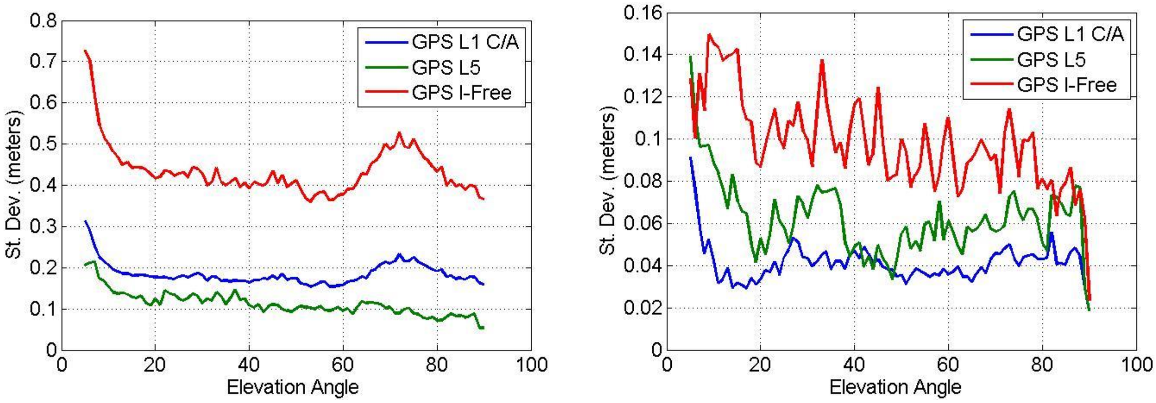

Figure 115 – Raw (left) and 100 s. Smoothed (right) CMCs Standard Deviation for GPS L1, L5 and I-Free Combinations Pattonville 100 m. case

Results are similar to the ones obtained for the 50 meters case.

C.3 Toulouse Blagnac Airport

In 3.3 results from the analysis of data collected the 02/04/2016 are shown. In this section results for other three days will be shown. Results for the RR 2 will be shown as well. The scope is to check if the results are similar to the ones obtained. The three days analyzed are:

1. 03/04/2016
2. 06/04/2016
3. 09/04/2016

C.3.1 03/04/2016

Figure 116 shows the results for the RR1 on 03/04/2016.

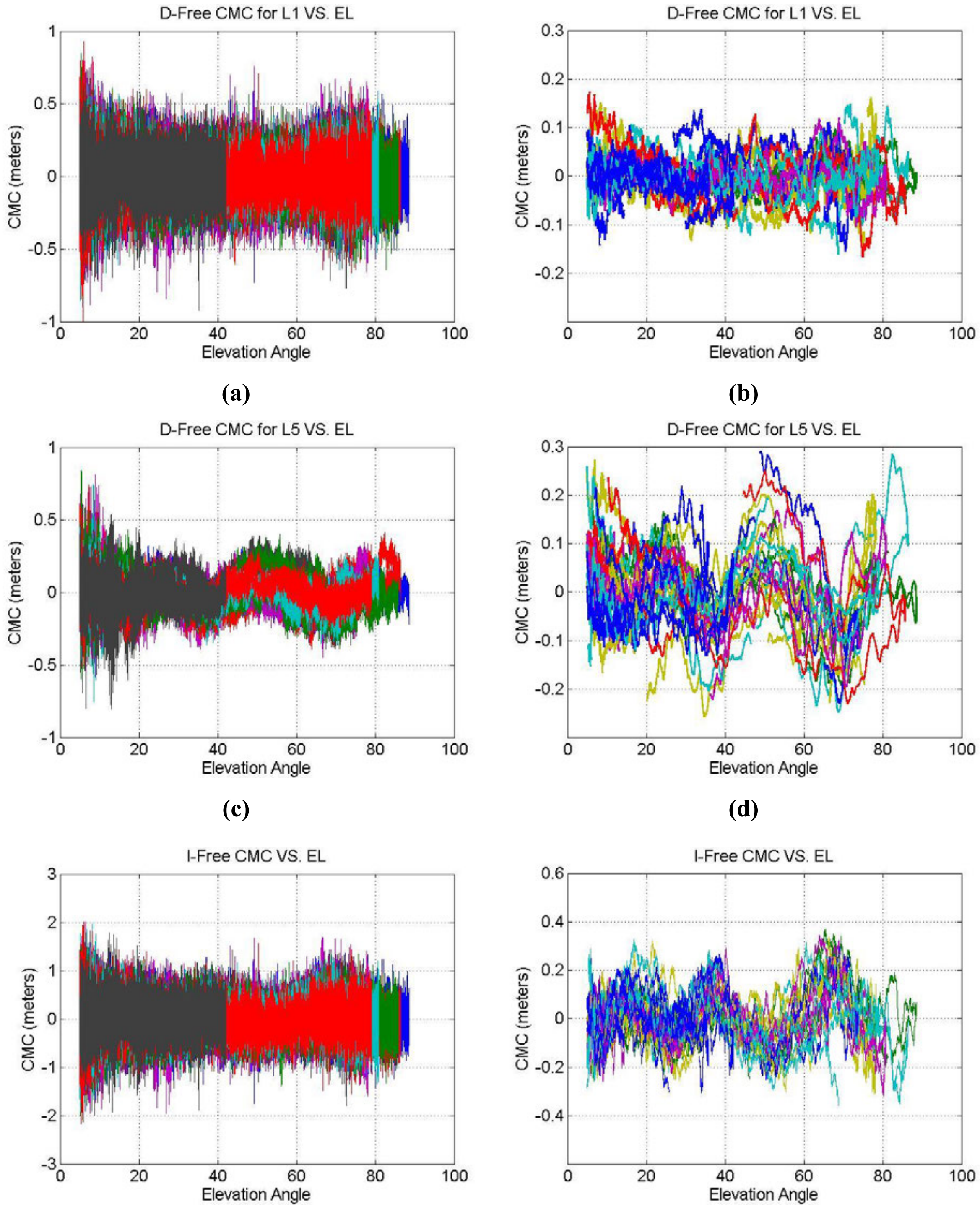

(a) (b)

(c) (d)

(e) (f)

Figure 116 – GPS L1 C/A, GPS L5 and I-Free raw and 100 seconds smoothed CMCs for all satellites Toulouse Blagnac RR1 03/04/2016

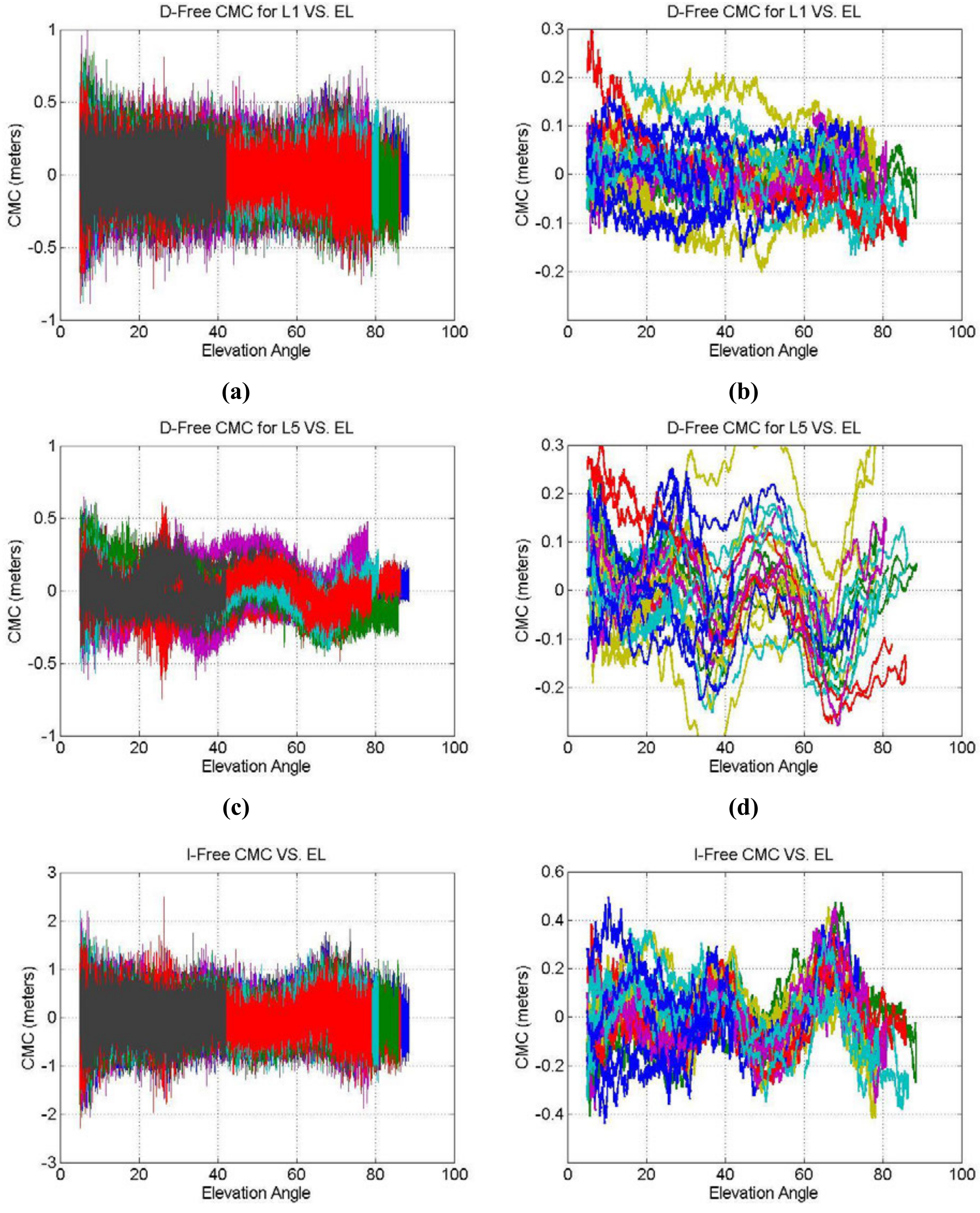

(a) **(b)**

(c) **(d)**

(e) **(f)**

Figure 117 – GPS L1 C/A, GPS L5 and I-Free raw and 100 seconds smoothed CMCs for all satellites Toulouse Blagnac RR2 03/04/2016

Figure 116 and Figure 117 show results similat to the ones obtained in Figure 26, it is possible to see that the CMCs from RR2 are affected by a bigger level of noise and multipath than the one on L1.

The same analysis has been done for Galileo CMCs and it will be shown in Figure 118.

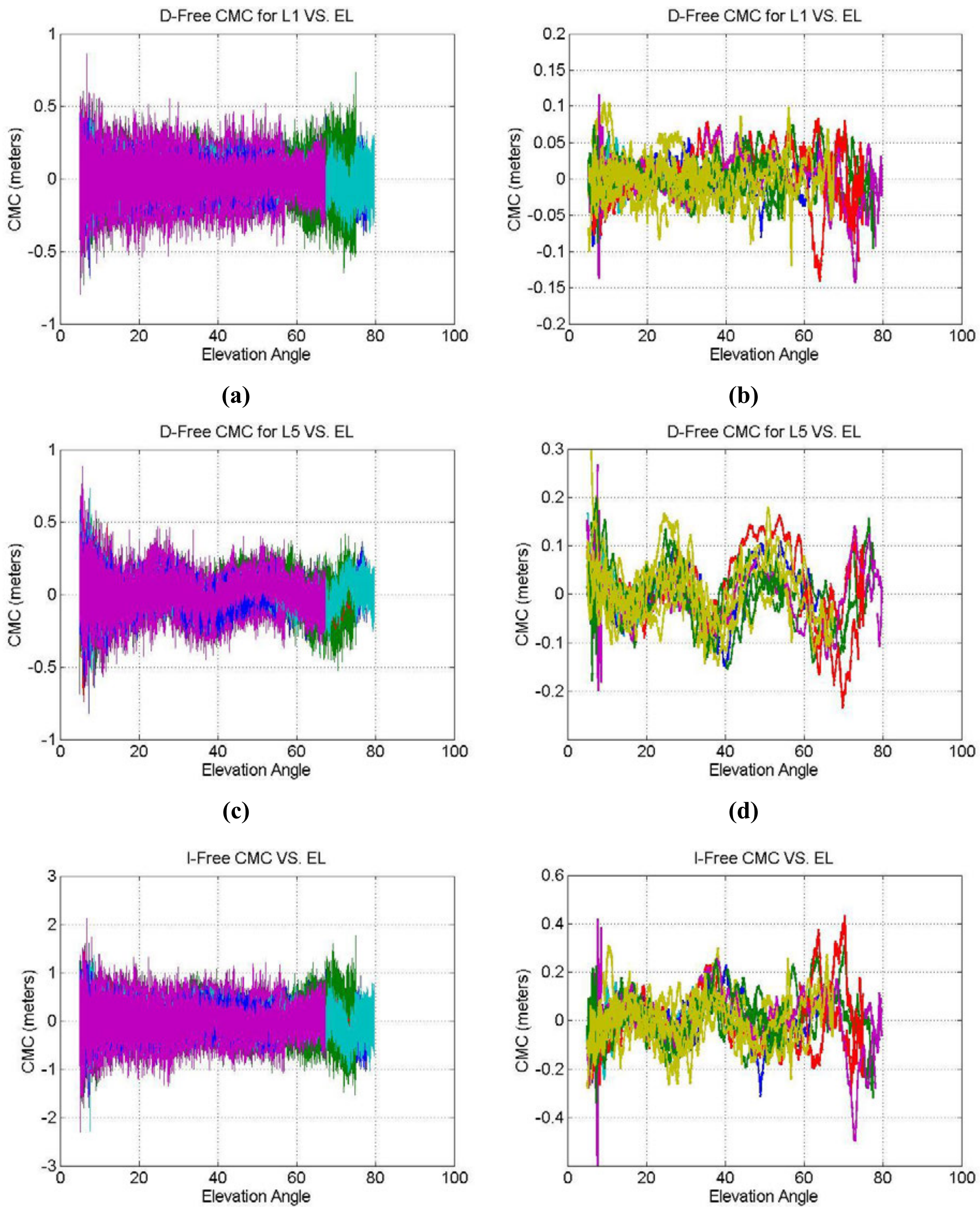

(a) **(b)**

(c) **(d)**

(e) **(f)**

Figure 118 – Galileo E1, Galileo E5a and I-Free raw and 100 seconds smoothed CMCs for all satellites Toulouse Blagnac RR1 03/04/2016

The results for RR2 are shown in Figure 119

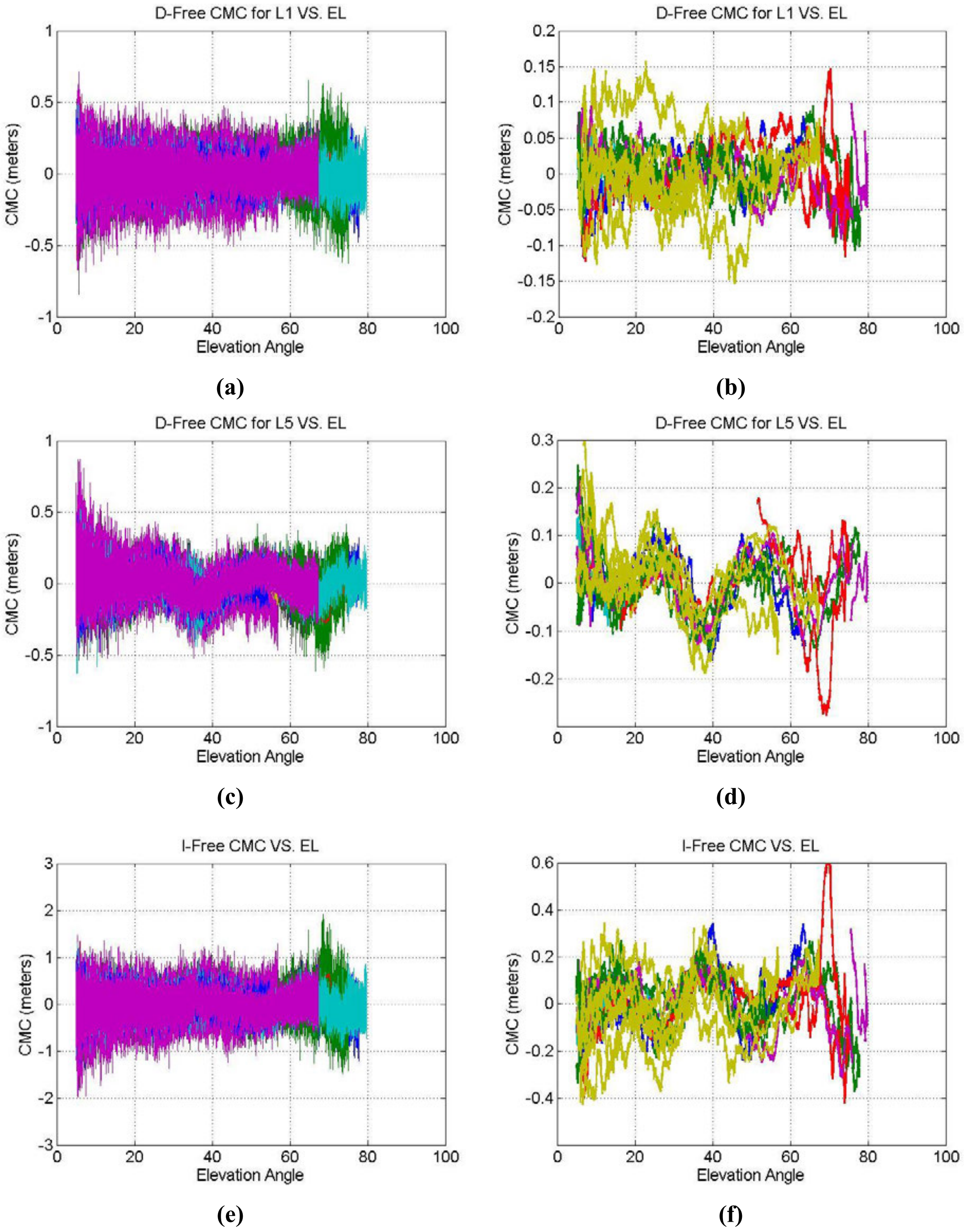

(a) **(b)**

(c) **(d)**

(e) **(f)**

Figure 119 – Galileo E1, Galileo E5a and I-Free raw and 100 seconds smoothed CMCs for all satellites Toulouse Blagnac RR2 03/04/2016

As for the GPS case, Figure 118 and Figure 119 provide results similar to the one obtained in 3.3.2. Also for Galileo constellation the RR2 has CMCs noisier than the RR1. Possible cause of differences between the two RRs, already keeping into account that the two antennas are not positioned at the same place, is the height with respect to the soil. The two antennas have a difference of about one meter, all other parameters related to the Low Noise Amplifier (LNA) or to the receiver are similar.

C.3.2 06/04/2016

Figure 120 shown the results for the RR1 on 06/04/2016.

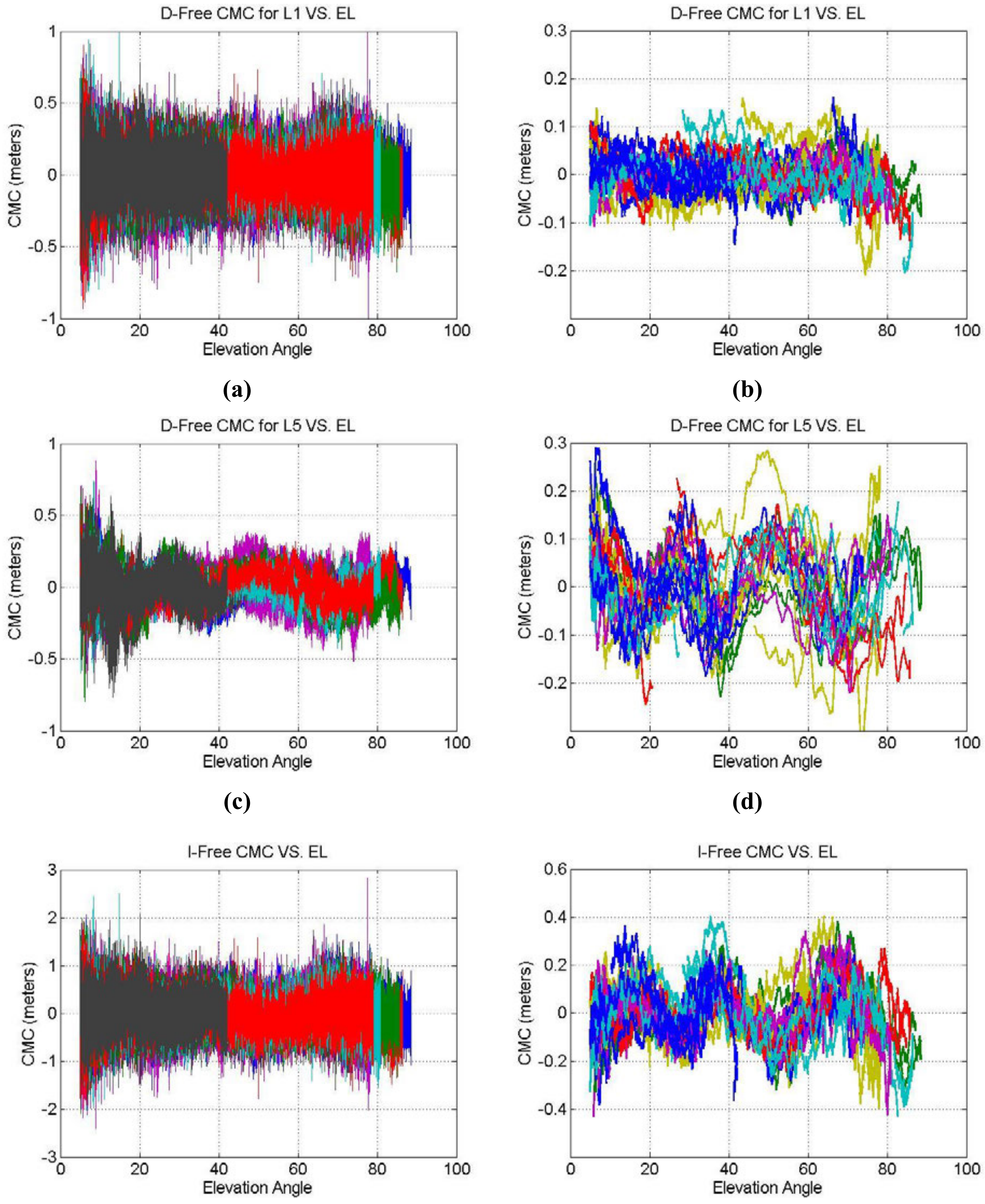

(a) **(b)**

(c) **(d)**

(e) **(f)**

Figure 120 – GPS L1 C/A, GPS L5 and I-Free raw and 100 seconds smoothed CMCs for all satellites Toulouse Blagnac RR1 06/04/2016

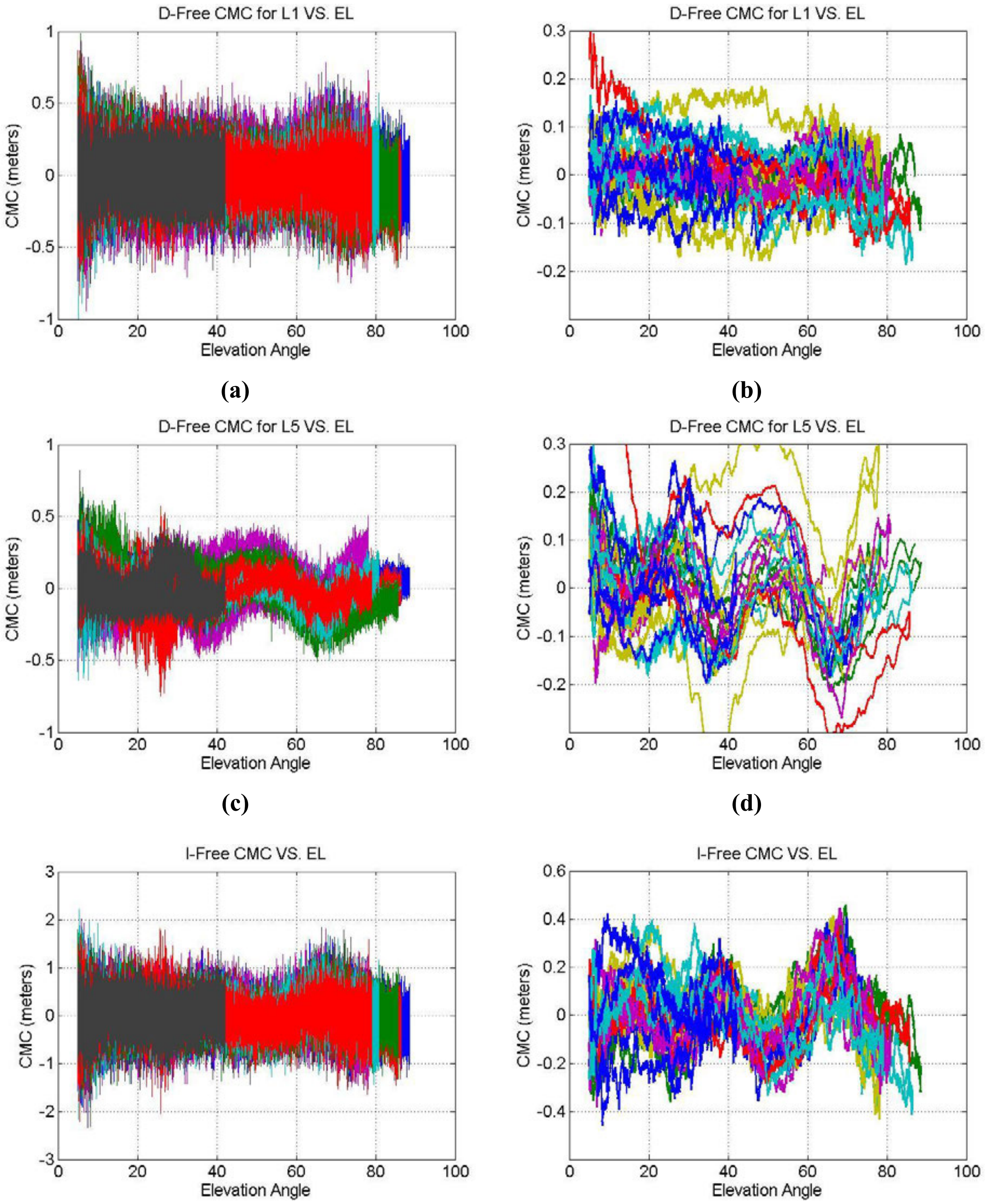

(a) (b)

(c) (d)

(e) (f)

Figure 121 – GPS L1 C/A, GPS L5 and I-Free raw and 100 seconds smoothed CMCs for all satellites Toulouse Blagnac RR2 06/04/2016

Results obtained in Figure 120 and Figure 121 are consistent with the ones obtained in the other analyzed days. Oscillations affecting L5 and I-free measurement are visible also for this day. Data form RR2 seem to be noisier than RR1 ones.

The results for Galileo constellation are given in Figure 122

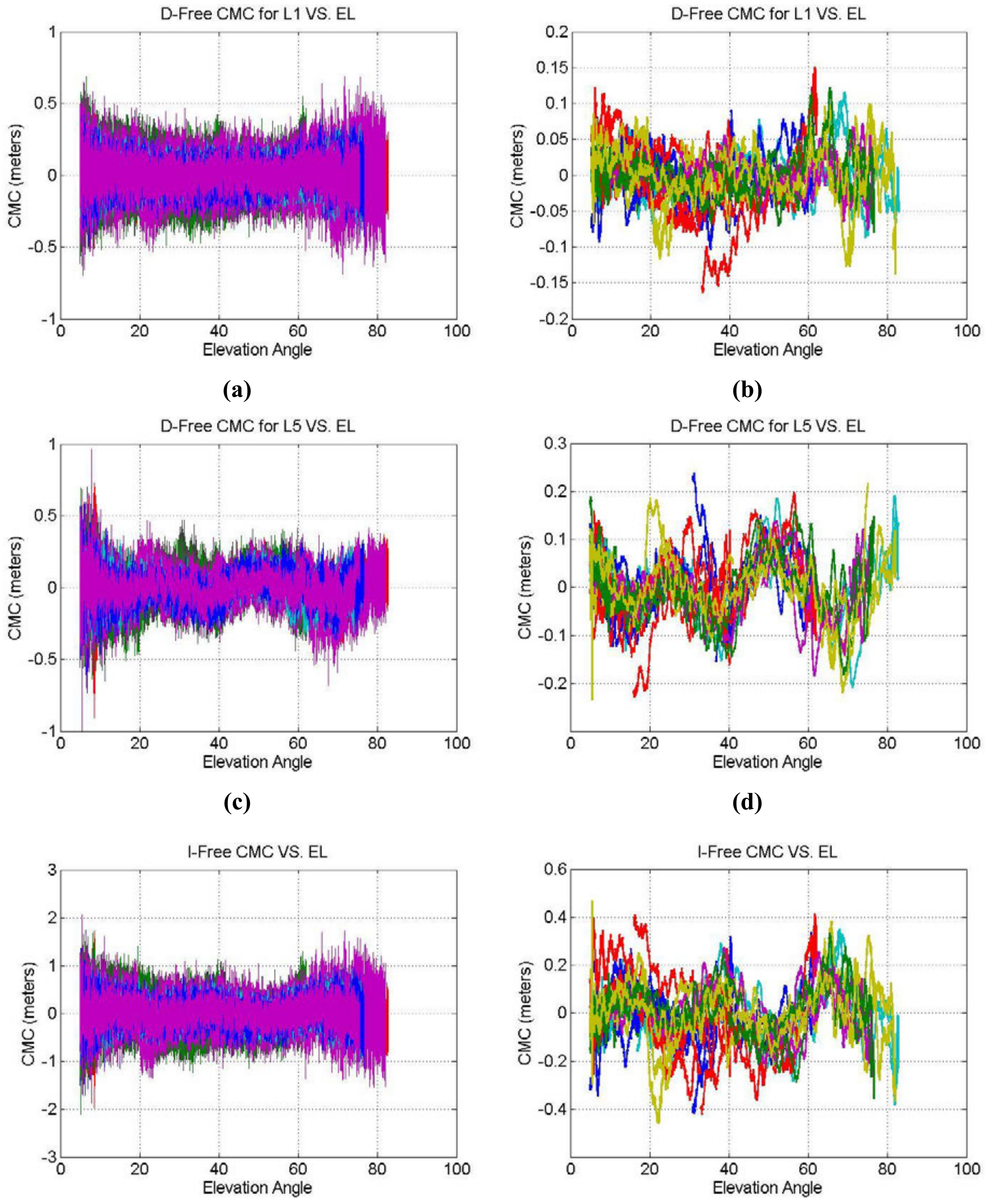

(a) **(b)**

(c) **(d)**

(e) **(f)**

Figure 122 – Galileo E, Galileo E5a and I-Free raw and 100 seconds smoothed CMCs for all satellites Toulouse Blagnac RR1 06/04/2016

Results for RR2 are instead provided in Figure 123

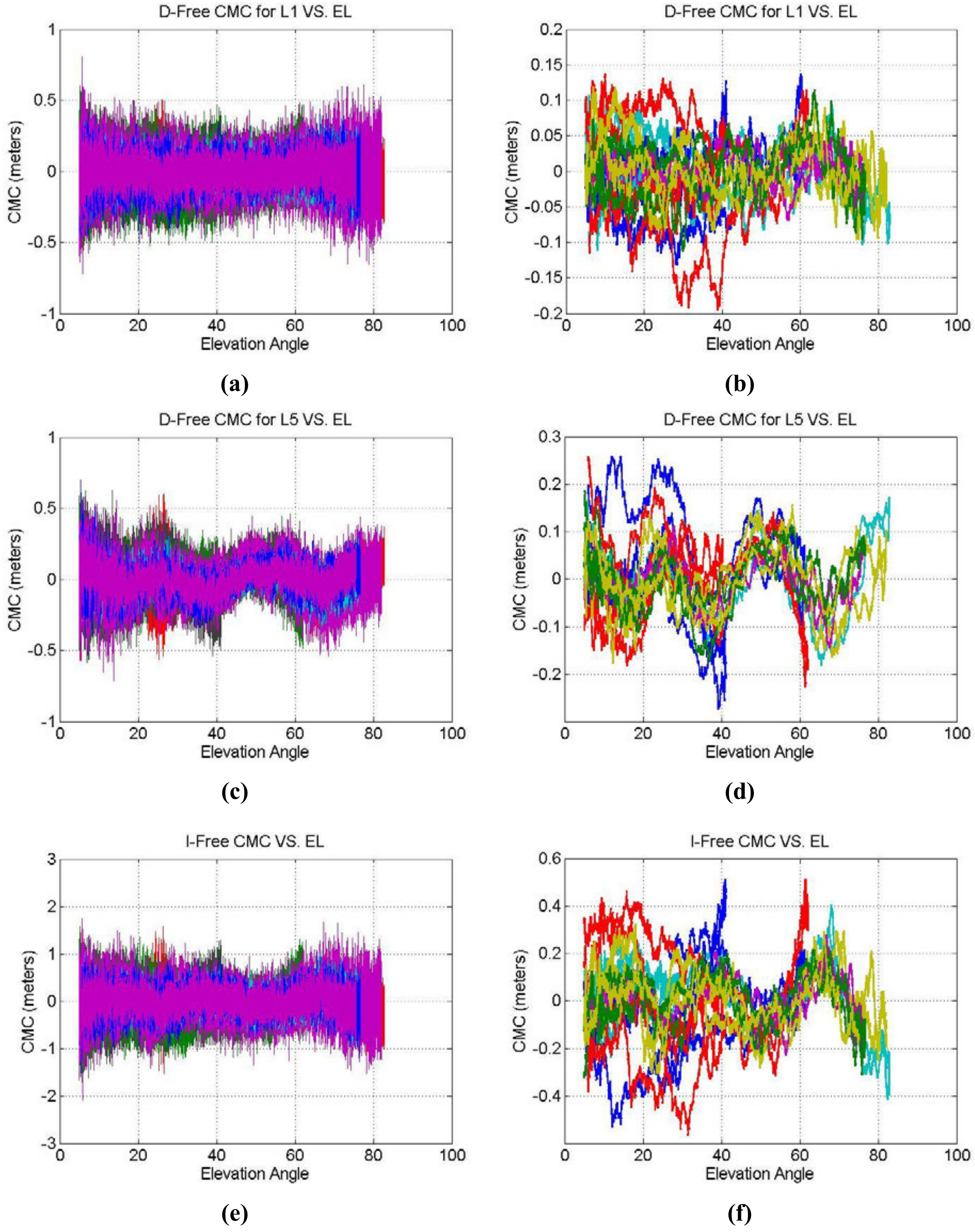

(a) (b)

(c) (d)

(e) (f)

Figure 123 – Galileo E1, Galileo E5a and I-Free raw and 100 seconds smoothed CMCs for all satellites Toulouse Blagnac RR2 06/04/2016

Results for Galileo constellation, Figure 122 and Figure 123, reflects the results obtained for GPS case. Oscillations on E5 and I-free combination are visible also for this case.

C.3.3 09/04/2016

Results for the last analyzed day are given, for RR1, in Figure 124

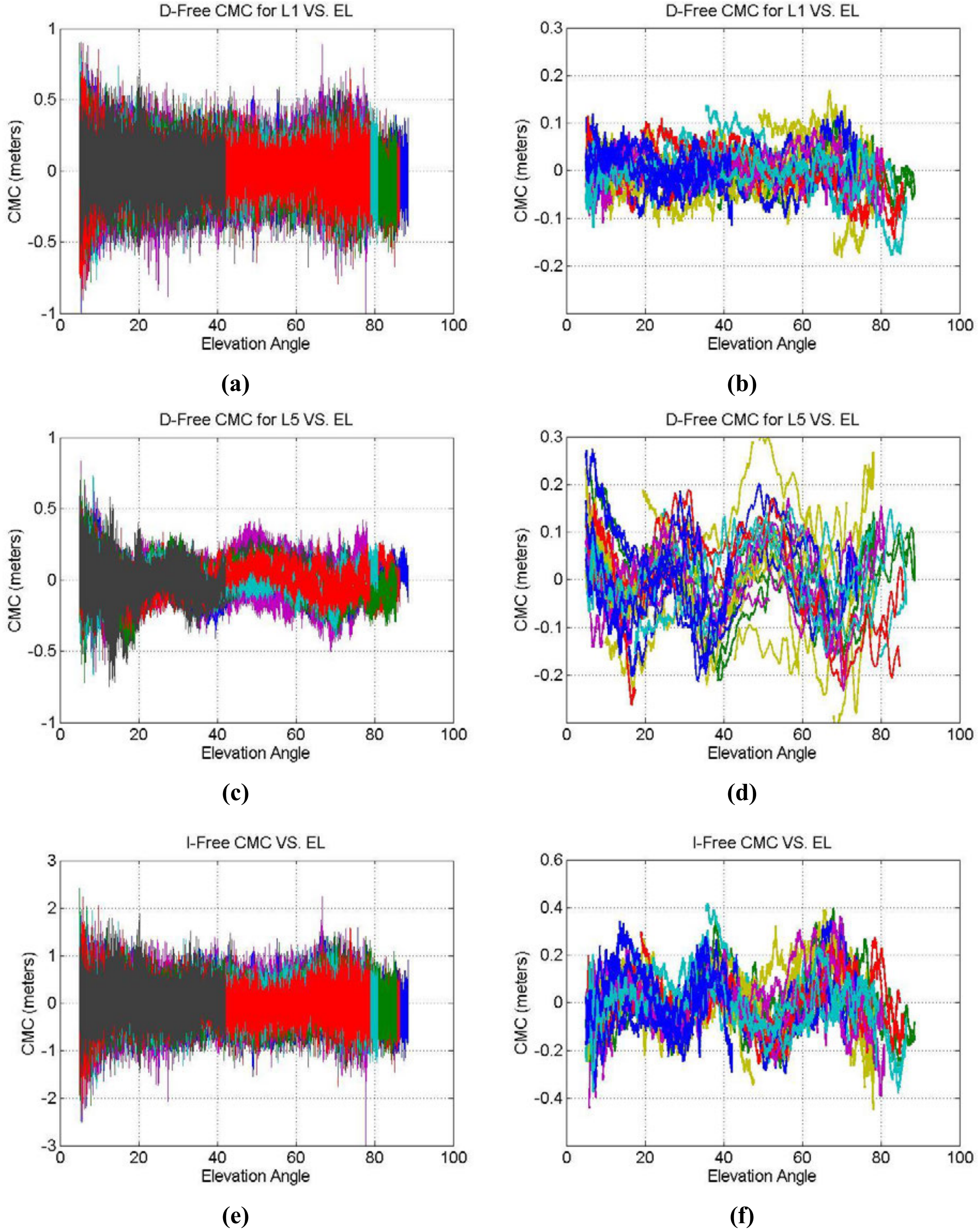

(a) **(b)** **(c)** **(d)** **(e)** **(f)**

Figure 124 – GPS L1 C/A, GPS L5 and I-Free raw and 100 seconds smoothed CMCs for all satellites Toulouse Blagnac RR1 09/04/2016

In Figure 125 results from RR2 are shown.

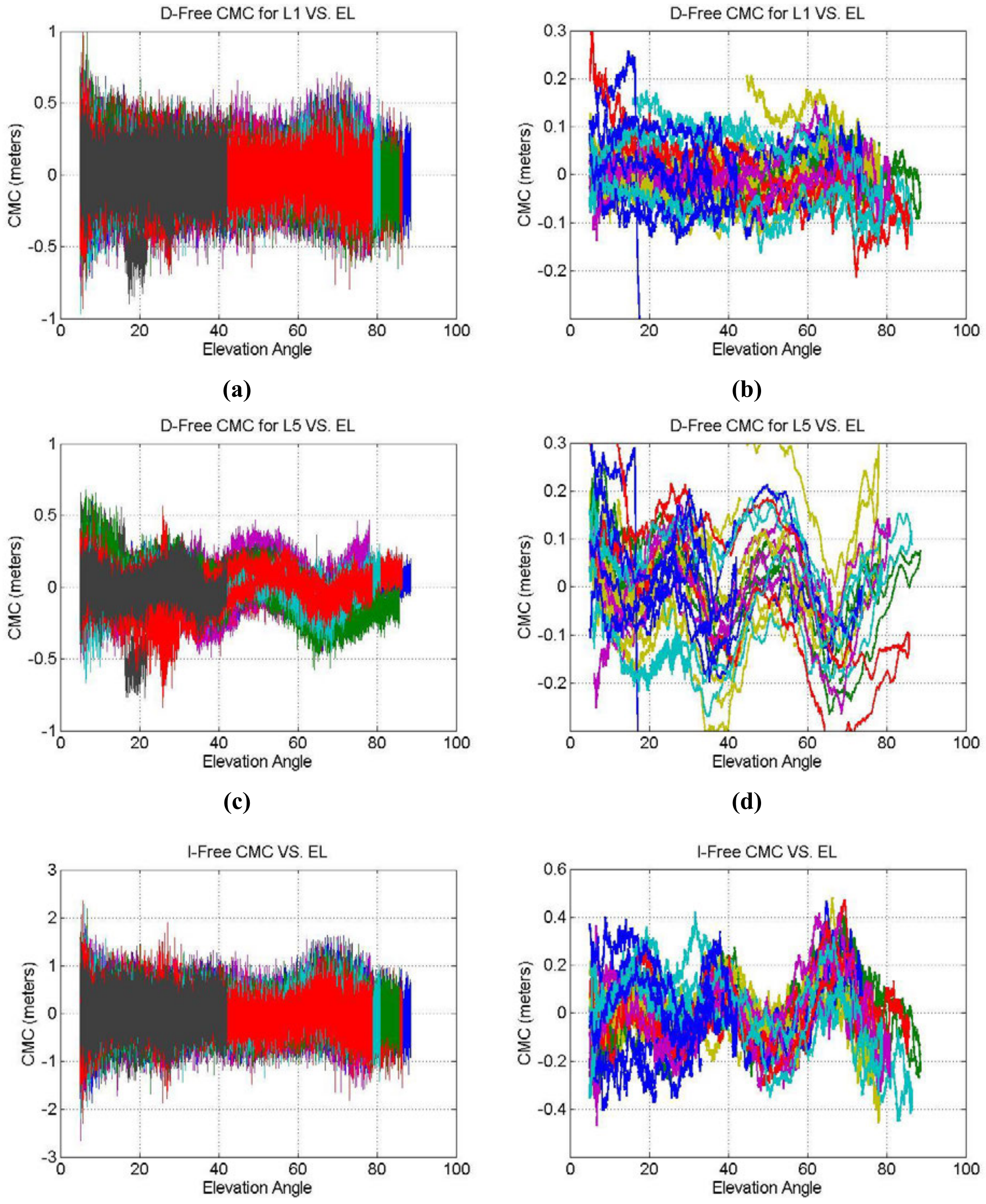

(a) **(b)**

(c) **(d)**

(e) **(f)**

Figure 125 – GPS L1 C/A, GPS L5 and I-Free raw and 100 seconds smoothed CMCs for all satellites Toulouse Blagnac RR2 09/04/2016

Results for GPS signals for 09/04/2016, given in Figure 124 and Figure 125, are similar to the ones obtained in the other days.

Figure 126shows the results for Galileo constellation.

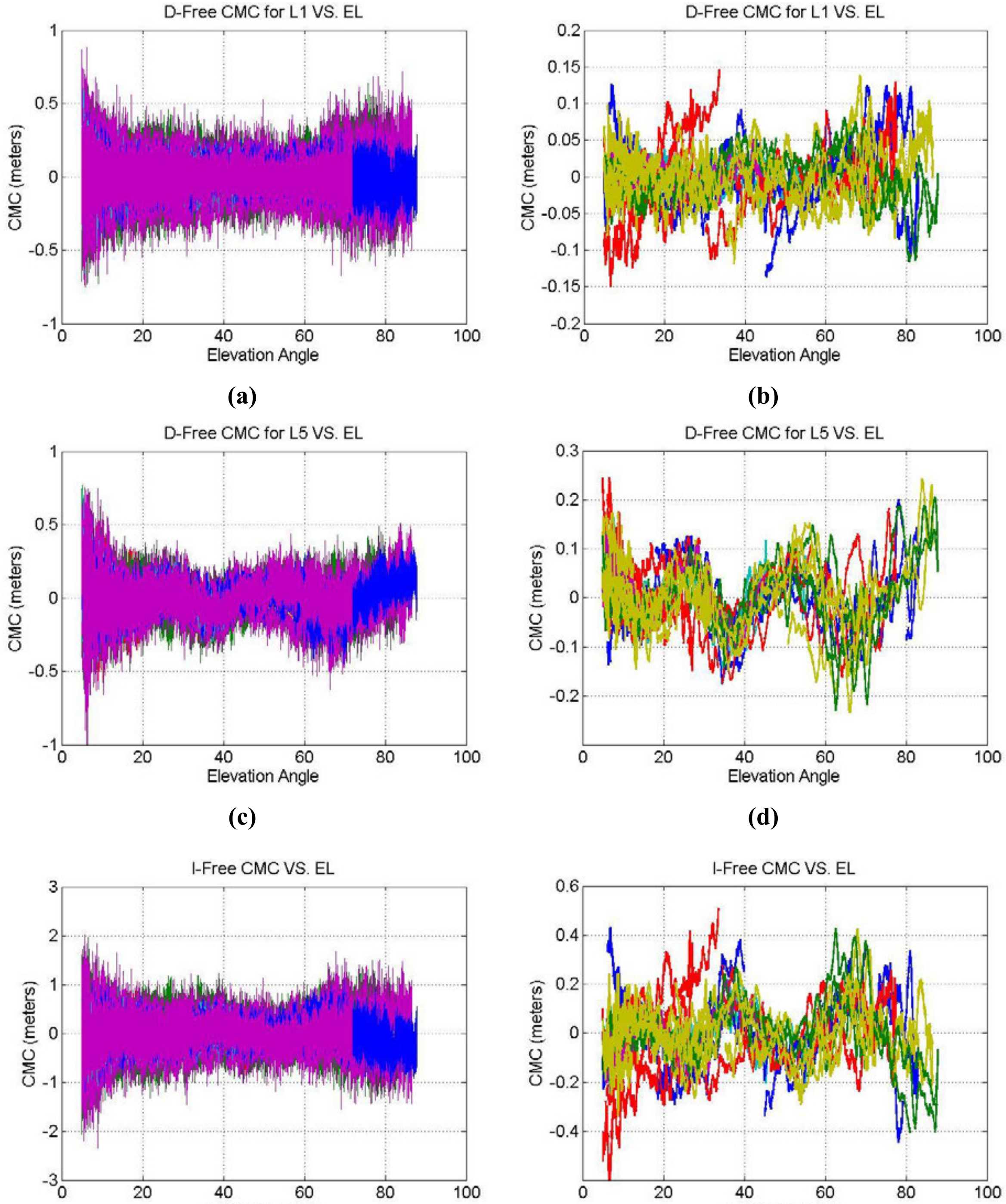

(a) **(b)**

(c) **(d)**

(e) **(f)**

Figure 126 – Galileo E1, Galileo E5a and I-Free raw and 100 seconds smoothed CMCs for all satellites Toulouse Blagnac RR1 09/04/2016

Figure 127 provides results for RR2

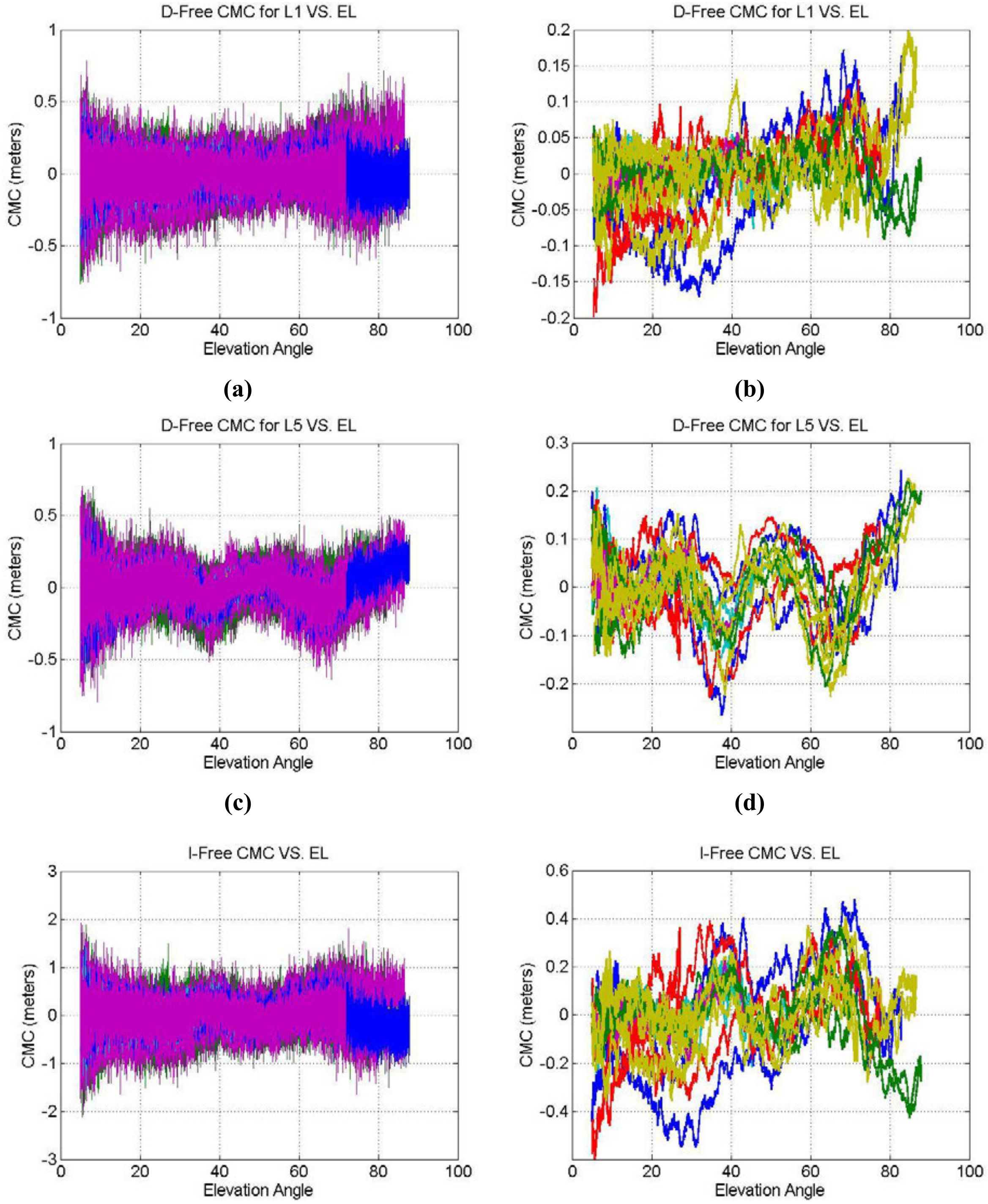

(a) **(b)**

(c) **(d)**

(e) **(f)**

Figure 127 – Galileo E1, Galileo E5a and I-Free raw and 100 seconds smoothed CMCs for all satellites Toulouse Blagnac RR1 09/04/2016

Figure 126 and Figure 127 show the result for Galileo signals for the last analyzed day. The result are coherent with the ones obtained on previous days.

C.4 MLA Calibration on L5

In section 0 the comparison between RMS and standard deviation has been done to find possible residual biases on the CMCs. In this section the same analysis will be done on all other days in order to see if the same oscillations are present.

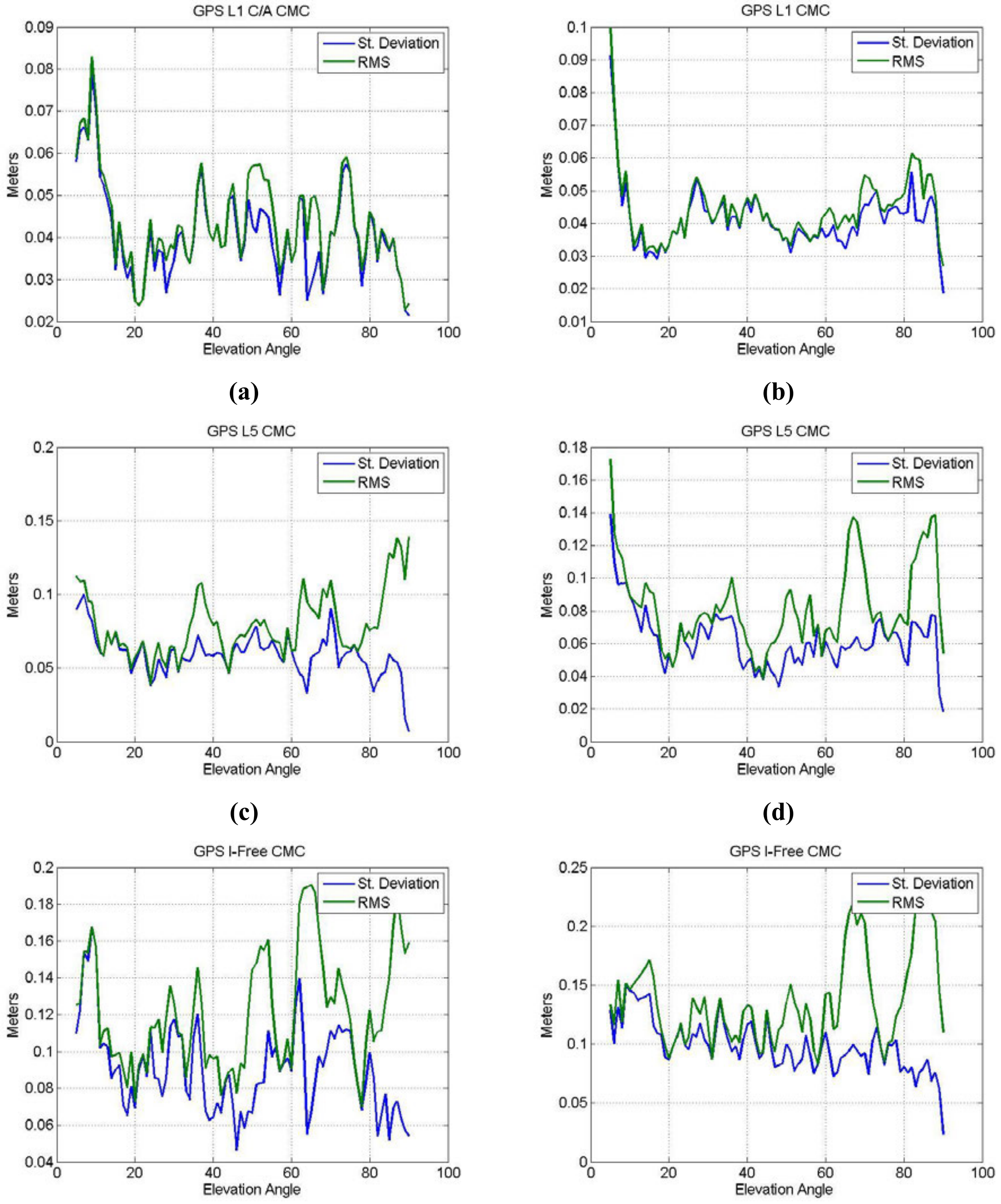

(a) **(b)**

(c) **(d)**

(e) **(f)**

Figure 128 – Comparison between RMS and standard deviation for Pattonville 50 m (left side) and 100 m (right case).

Figure 128 shows that oscillations similar to the one observed for Toulouse Blagnac data collection are visible also on data from Pattonville. This result exclude the possibility of a bias related to the surrounding environment.

In Figure 129 and Figure 130 the CMCs obtained applying the calibration coefficient, computed in 0, are shown.

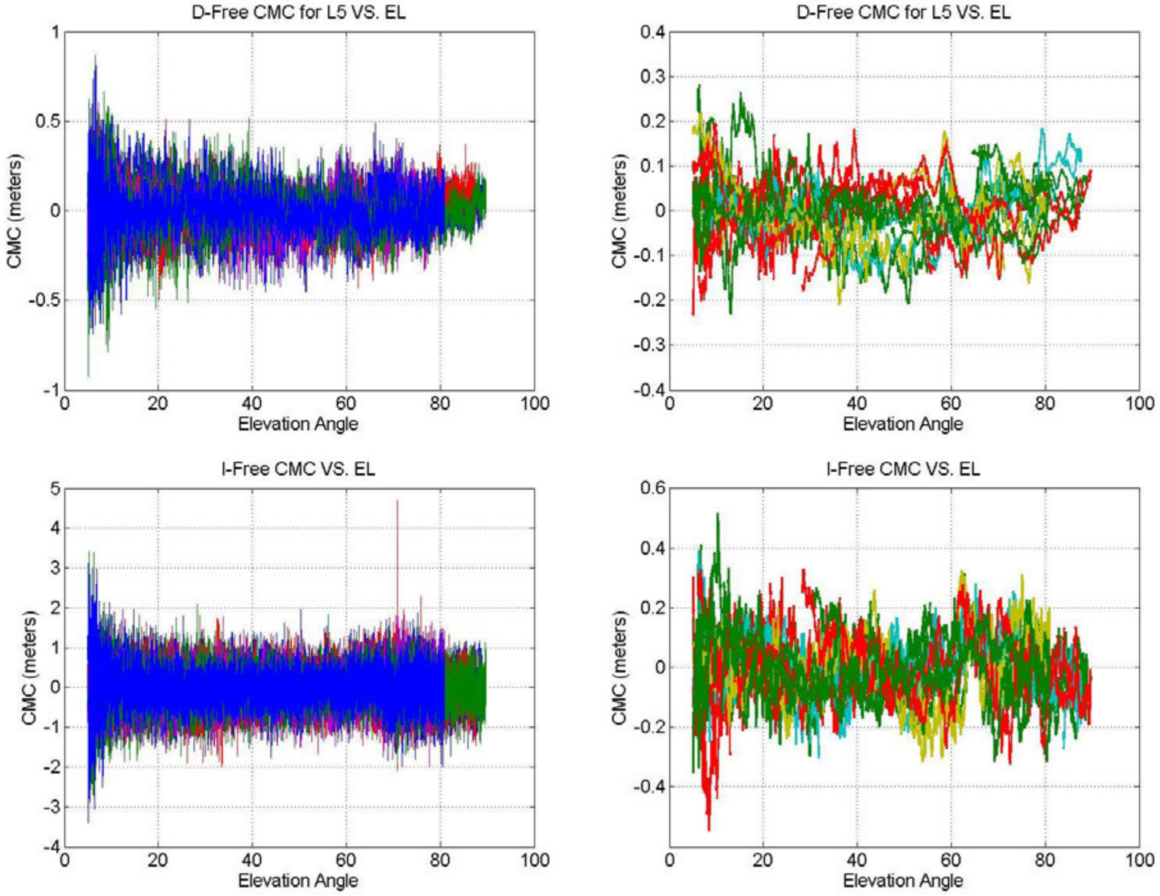

Figure 129 – Calibrated raw and 100 s smoothed CMCs for GPS L5 and I-Free for Pattonville 50 m. case

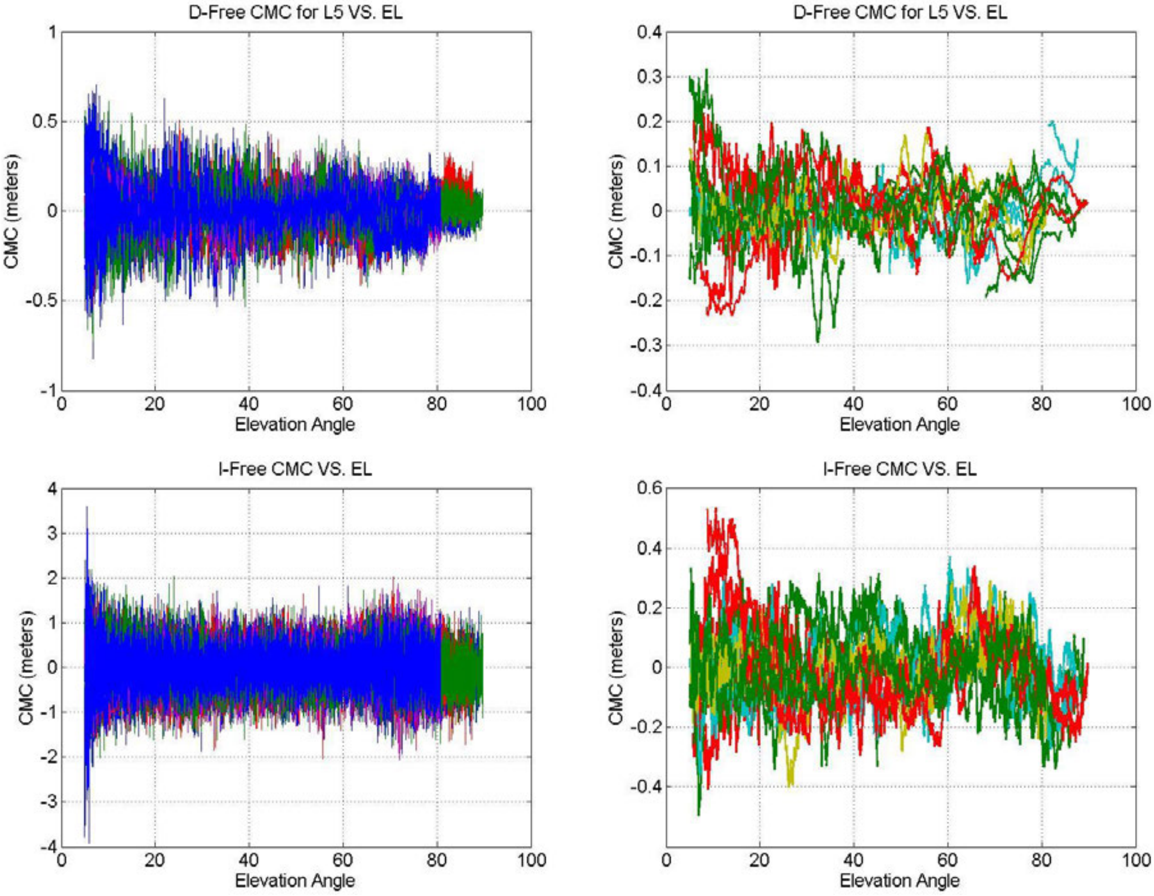

Figure 130 – Calibrated raw and 100 s smoothed CMCs for GPS L5 and I-Free for Pattonville 100 m. case

As for Toulouse CMCs (Figure 26 and Figure 27) the application of the calibration values on the CMCs obtained at Pattonville removes the oscillations seen before.

C.5 Smoothing Efficiency

C.5.1 Pattonville Results

Results about smoothing efficiency have been shown on section 3.3.4 for Toulouse data. In this section the results for Pattonville will be shown.

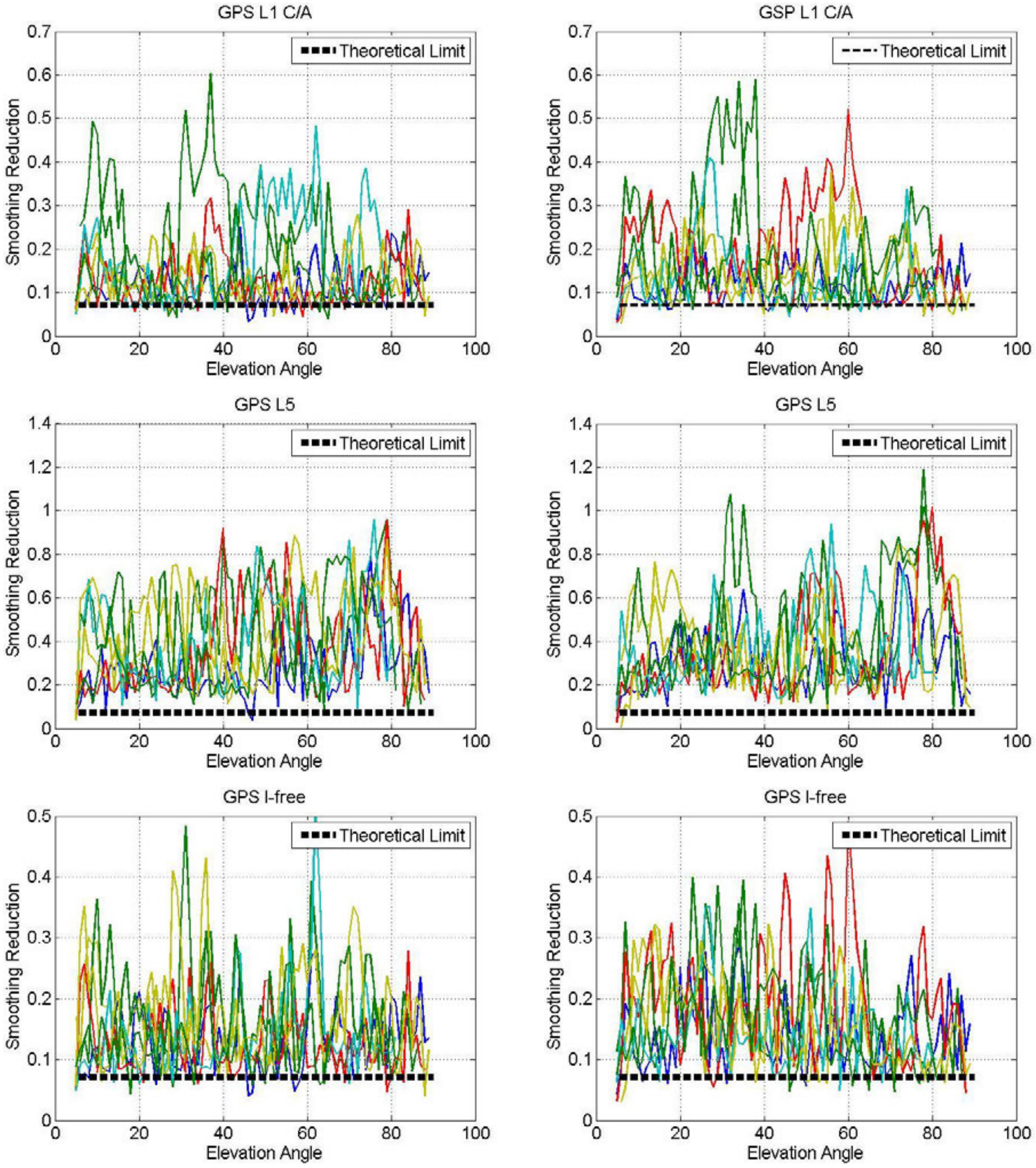

Figure 131 – Real Vs. theoretical smoothing gain for GPS L1 C/A, GPS L5 and GPS I-Free for Pattonville 50 m (left side) and 100 m (right side)

Analyzing Figure 131 it is possible to see that results are consistent with the ones obtained from the analysis of Toulouse data.

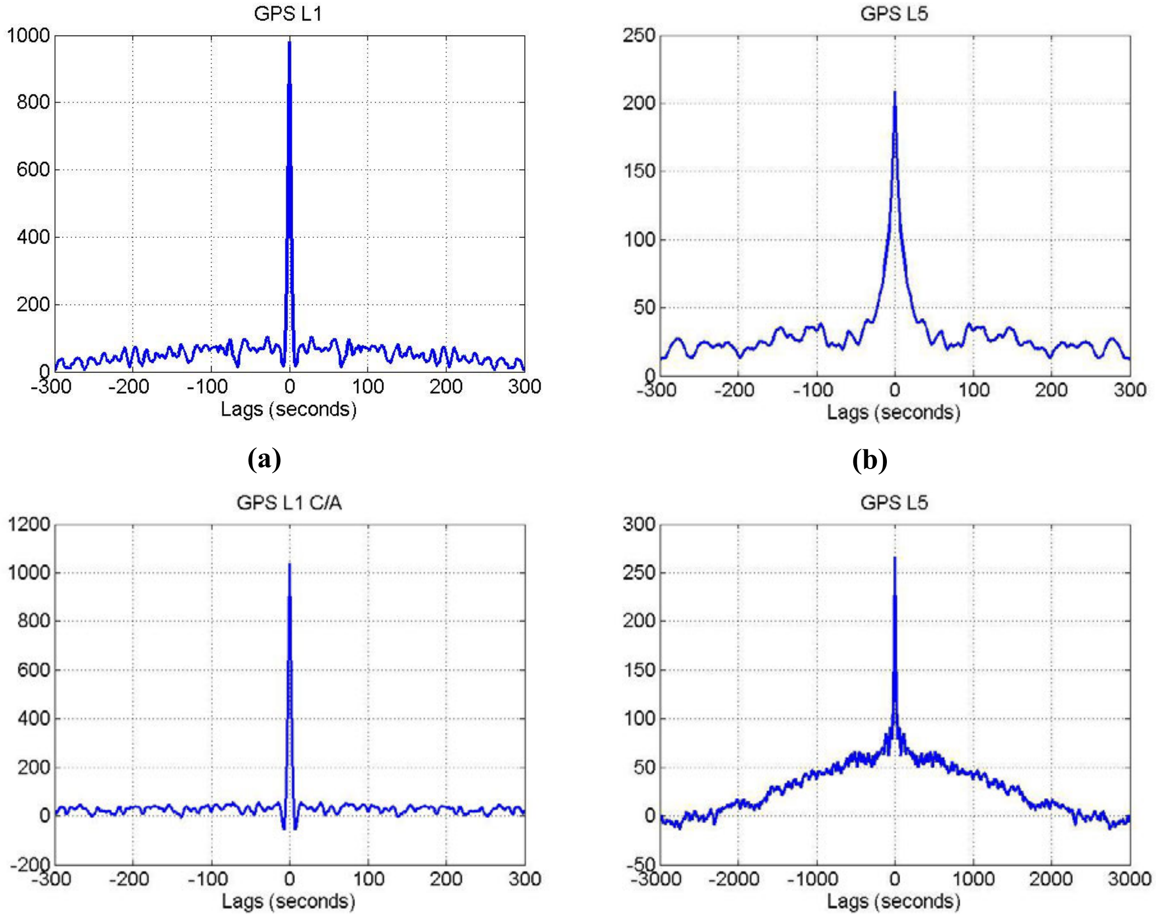

(a) **(b)**

(c) **(d)**

Figure 132 – Autocorrelation function for GPS L1 C/A and L5 for satellite PRN 1 (a, b) and 24 (c, d) on Pattonville 50 m

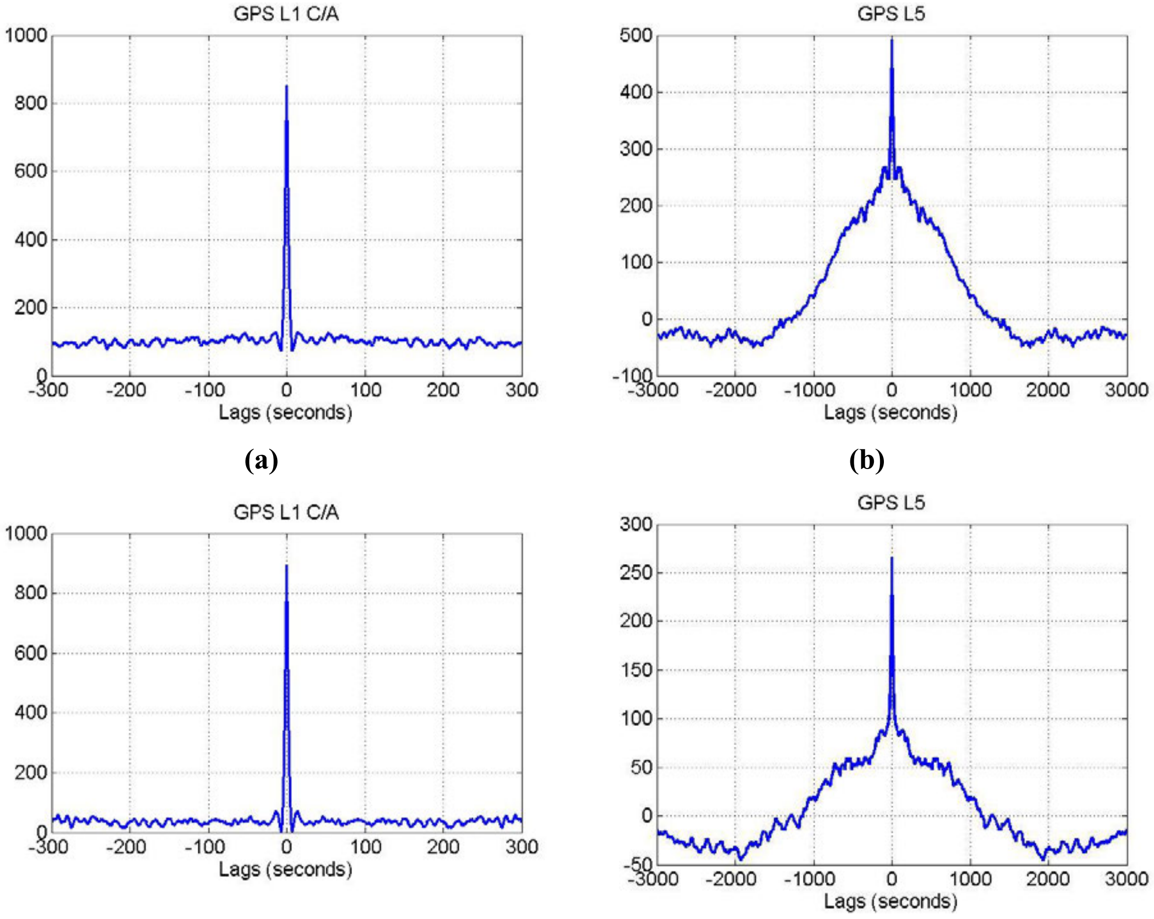

(a) **(b)**

(c) **(d)**

Figure 133 – Autocorrelation function for GPS L1 C/A and L5 for satellite PRN 9 (a, b) and 25 (c, d) on Pattonville 100 m

Results from Figure 132 and Figure 133 confirm what assesses in 3.3.4. The time correlation for L1 measurements is comprised between 3 and 5 seconds, on the contrary it is not possible to define unique value for GPS L5.

C.5.2 Toulouse Blagnac 03/04/2016 Results

Figure 134 will show the results obtained for Toulouse Blagnac data of the 03/04/2016 on the two RRs

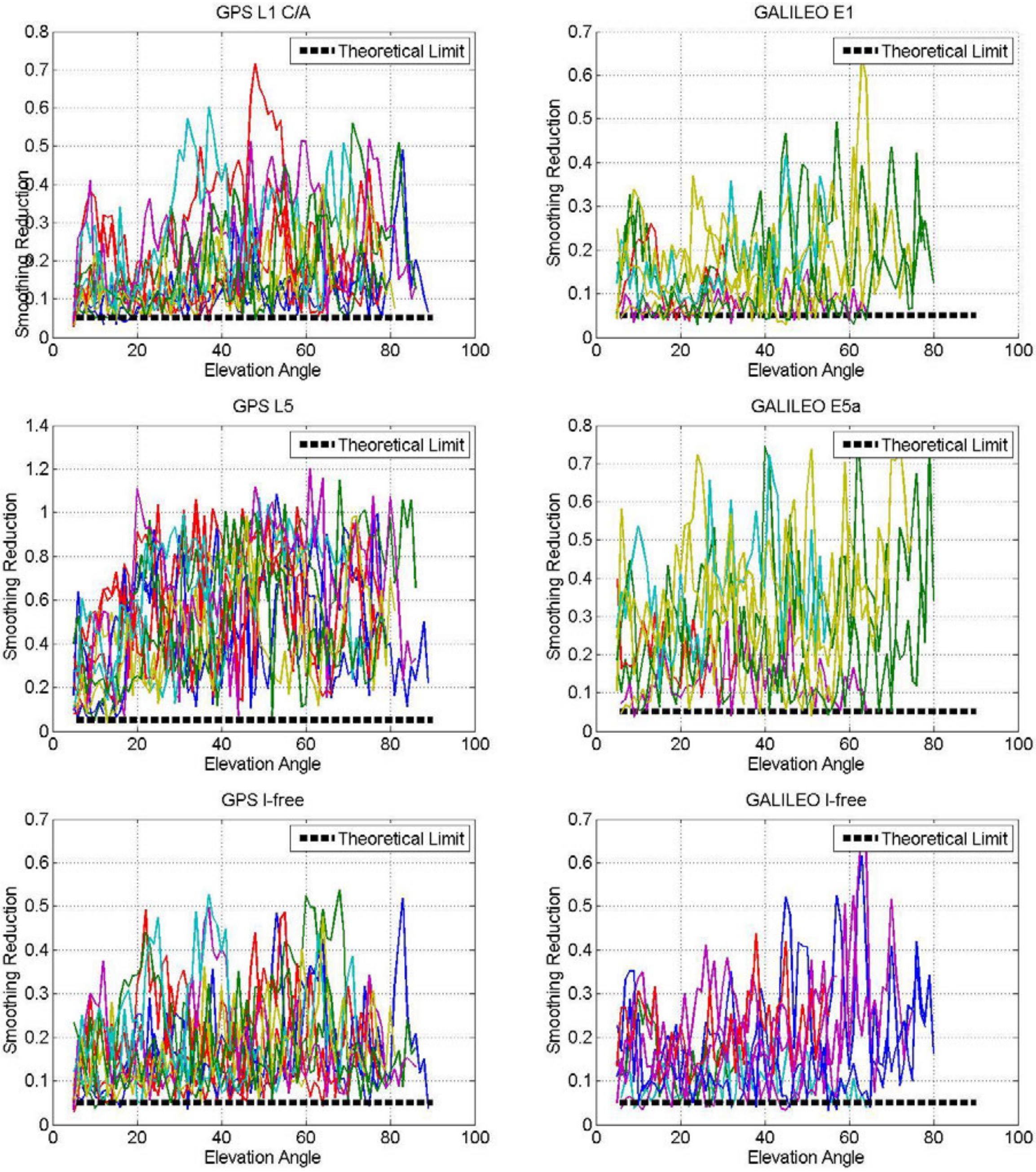

Figure 134 – Real Vs. theoretical smoothing gain for GPS (left side) and Galileo (right side) signals for Toulouse Blagnac 03/04/2016 on RR1

Figure 135 shows the same analysis for the second RR at ground

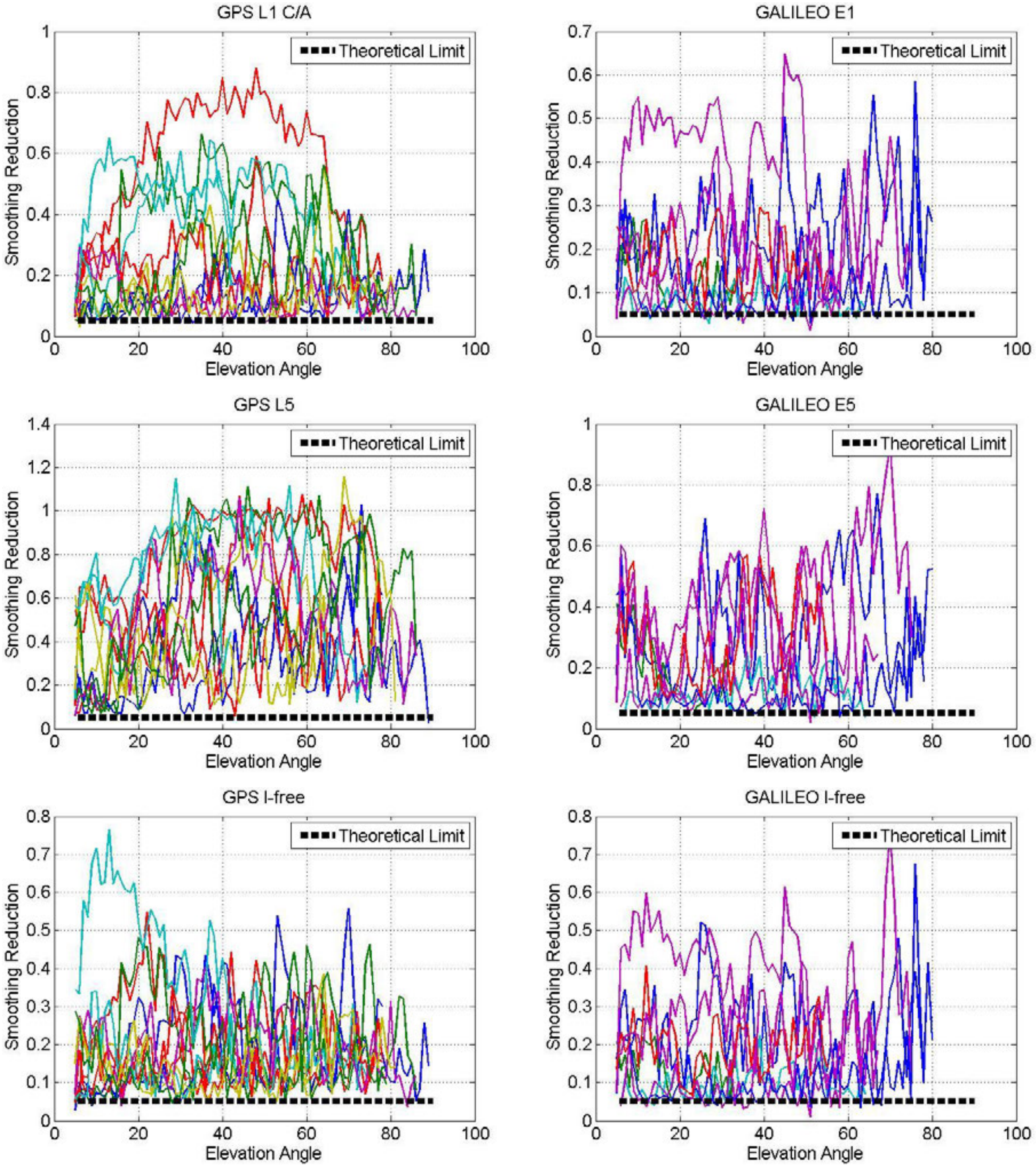

Figure 135 – Real Vs. theoretical smoothing gain for GPS (left side) and Galileo (right side) signals for Toulouse Blagnac 03/04/2016 on RR2

Results from Figure 134 and Figure 135 are consistent with the ones obtained in 3.3.2

C.5.3 Toulouse Blagnac 06/04/2016 Results

Results for the 06/04/2016 on the RR1 at Blagnac airport are shown in Figure 136

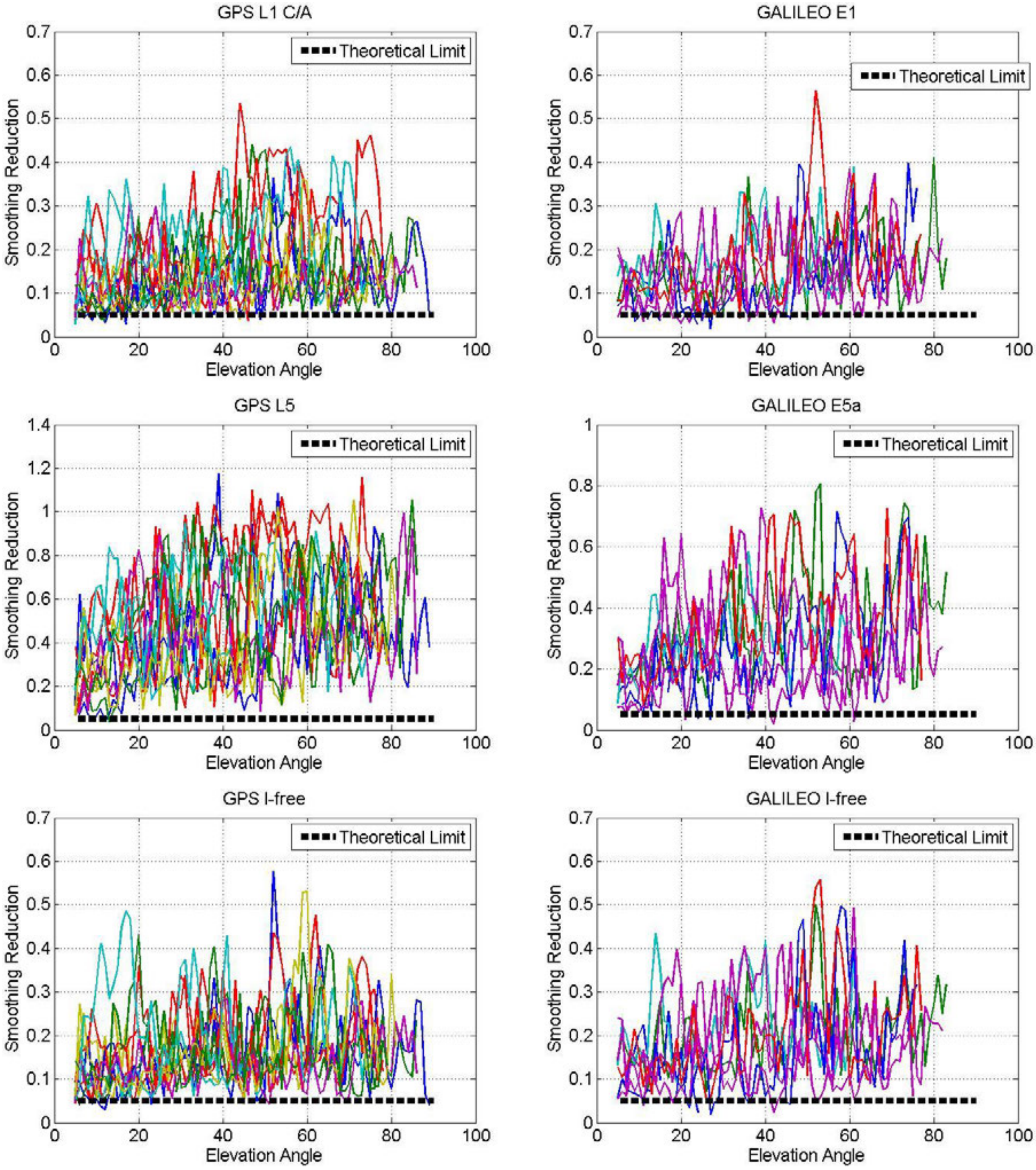

Figure 136 – Real Vs. theoretical smoothing gain for GPS (left side) and Galileo (right side) signals for Toulouse Blagnac 06/04/2016 on RR1

Figure 137 provides the results for the second RR.

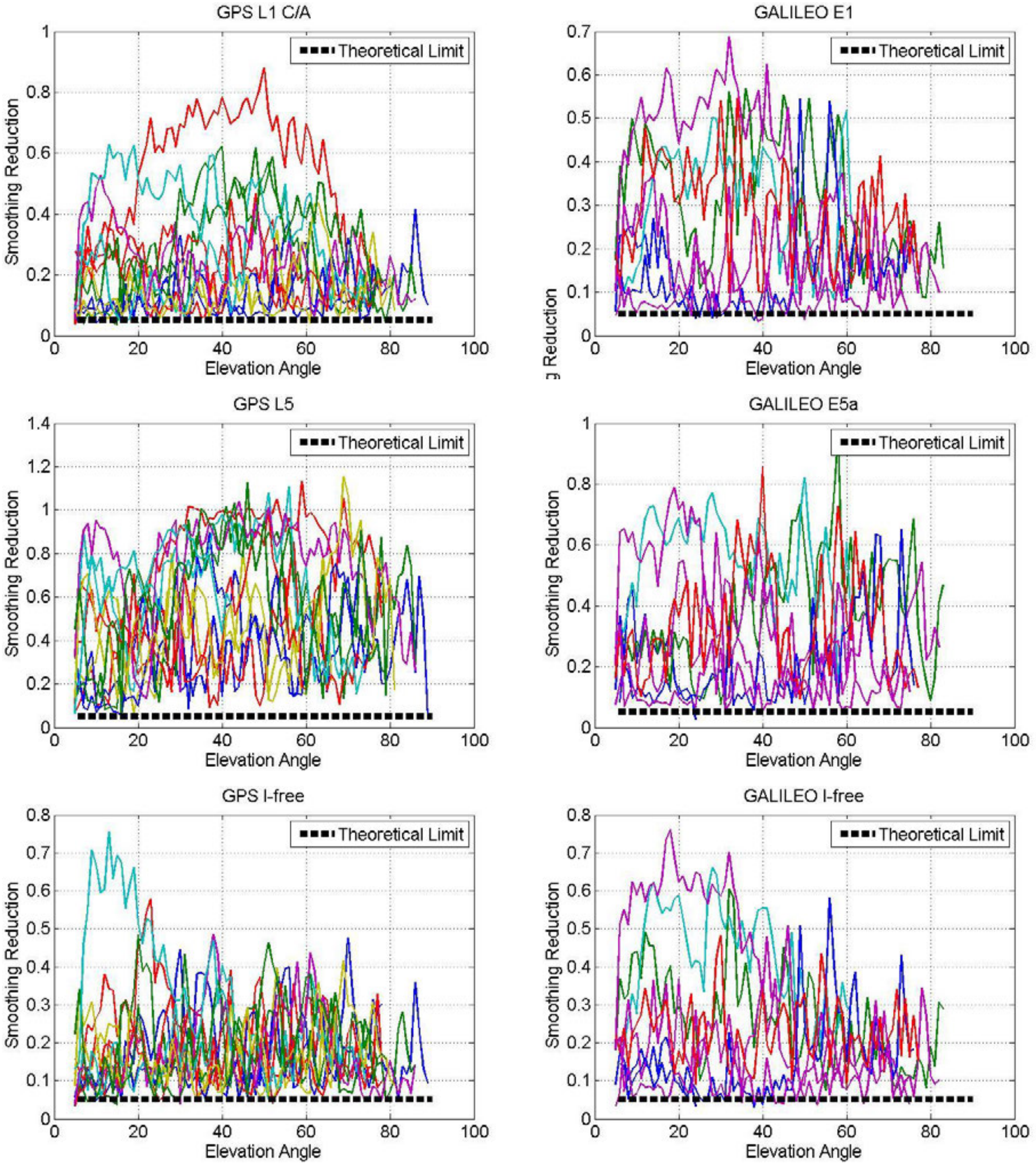

Figure 137 – Real Vs. theoretical smoothing gain for GPS (left side) and Galileo (right side) signals for Toulouse Blagnac 06/04/2016 on RR2

Also for this day results are similar to the ones analyzed so far.

C.5.4 Toulouse Blagnac 09/04/2016 Results

Results for the last analyzed day for Toulouse Blagnac are given in Figure 138

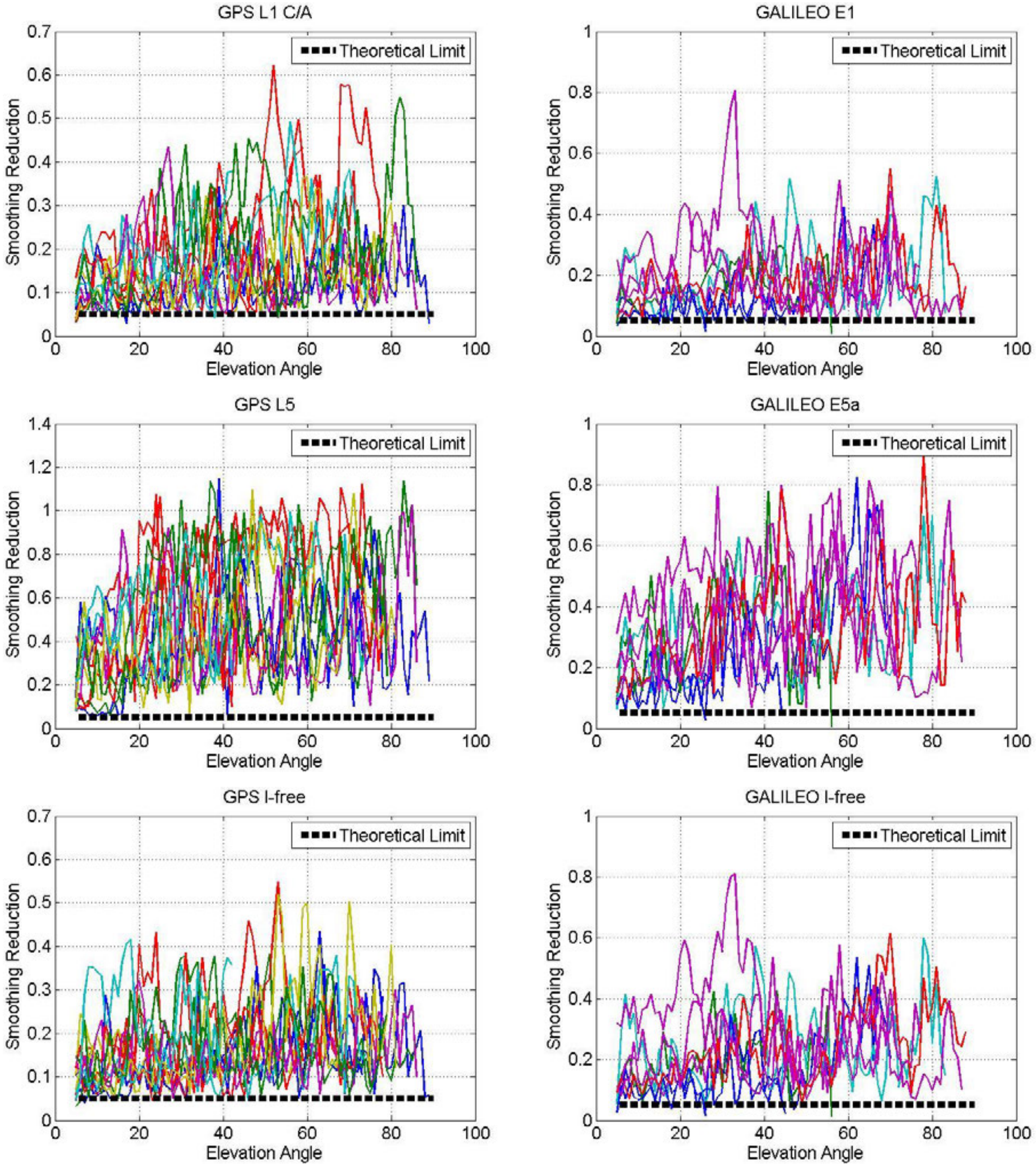

Figure 138 – Real Vs. theoretical smoothing gain for GPS (left side) and Galileo (right side) signals for Toulouse Blagnac 09/04/2016 on RR1

Figure 139 shows the results for the RR2

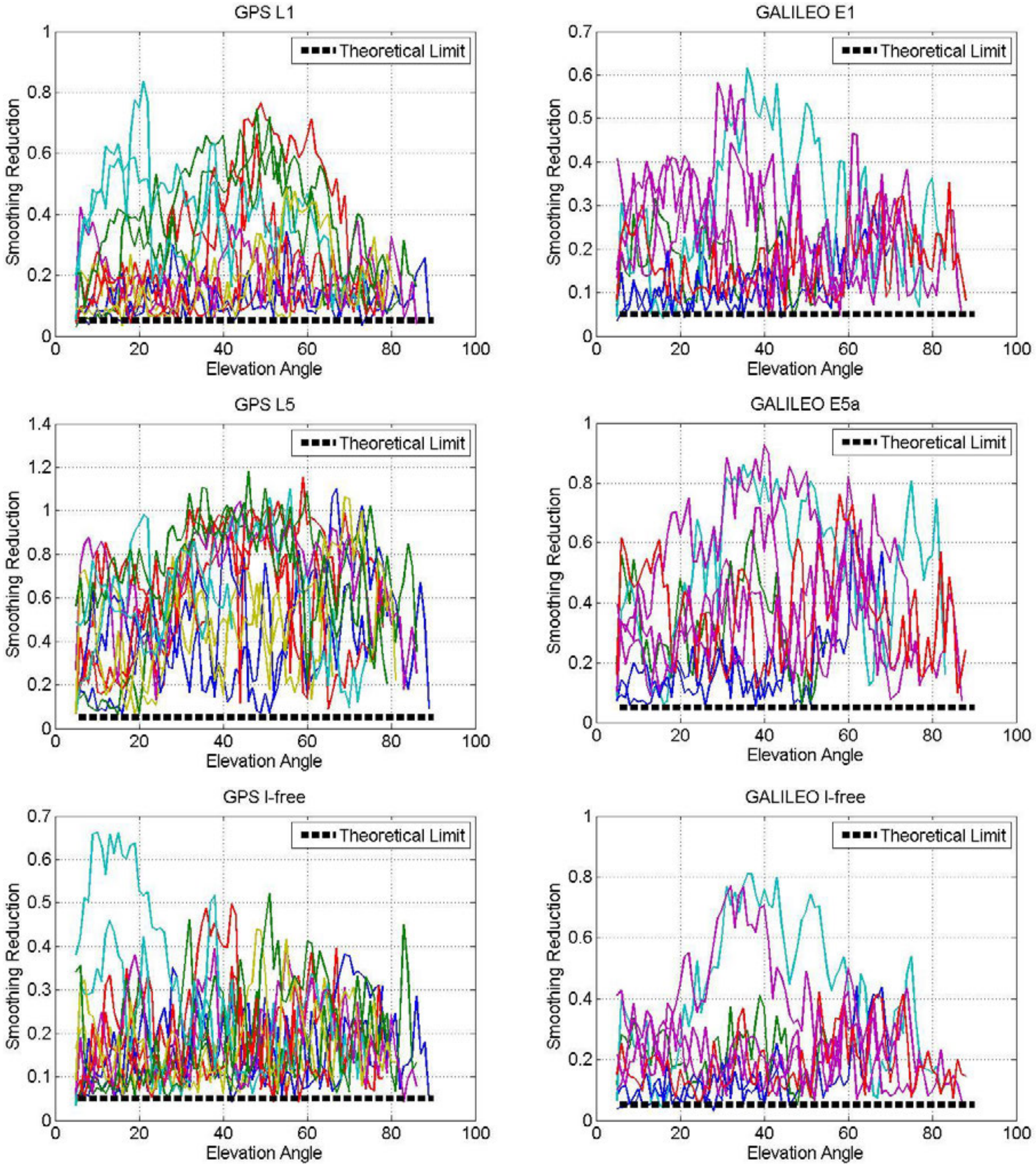

Figure 139 – Real Vs. theoretical smoothing gain for GPS (left side) and Galileo (right side) signals for Toulouse Blagnac 09/04/2016 on RR2

As for the previous days, also in this case results are similar to the ones obtained in the previous cases.

C.6 Optimal Smoothing Constant

The same analysis done in 3.3.4 will be presented here for Pattonville data

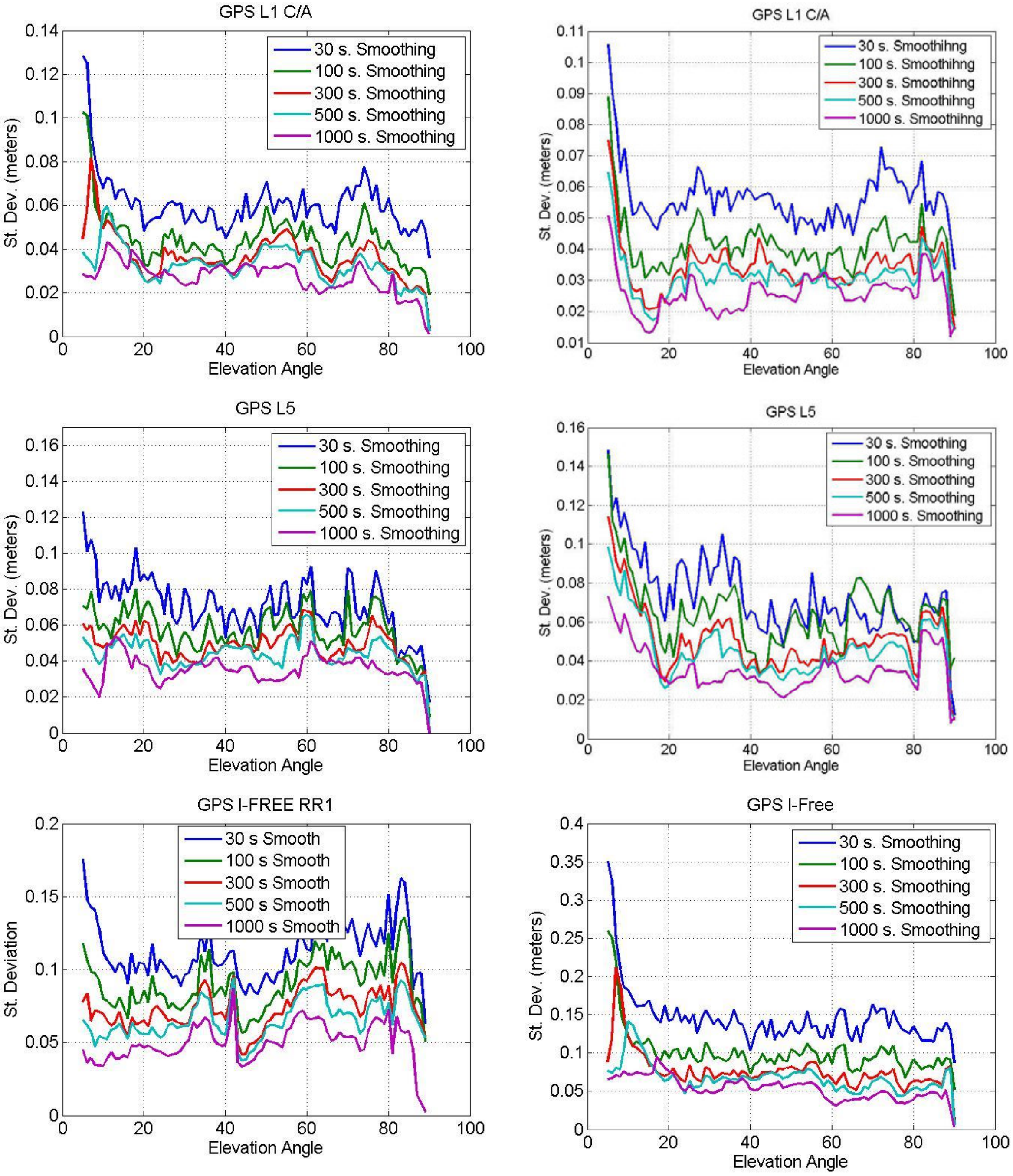

Figure 140 – Standard Deviation Comparison for Different Smoothing Constants for GPS L1, GPS L5 and I-free on Pattonville 50 m (left side) and Pattonville 100 m (right side)

Results shown in Figure 140 are similar to the one obtained for Toulouse analysis. Also in this case for GPS L1 the choice of 100 seconds as smoothing constant can represent the optimal choice, considering the time needed before reaching the steady state. For GPS L5 and I-free combination the use of a bigger smoothing constant seems more logic in order to further reduce the noise and multipath contribution. As fir Toulouse case 300 seconds seems to be the optimal choice.

C.7 Assessment of I-Free RMS

Results obtained analysing Pattonville data will be shown here.

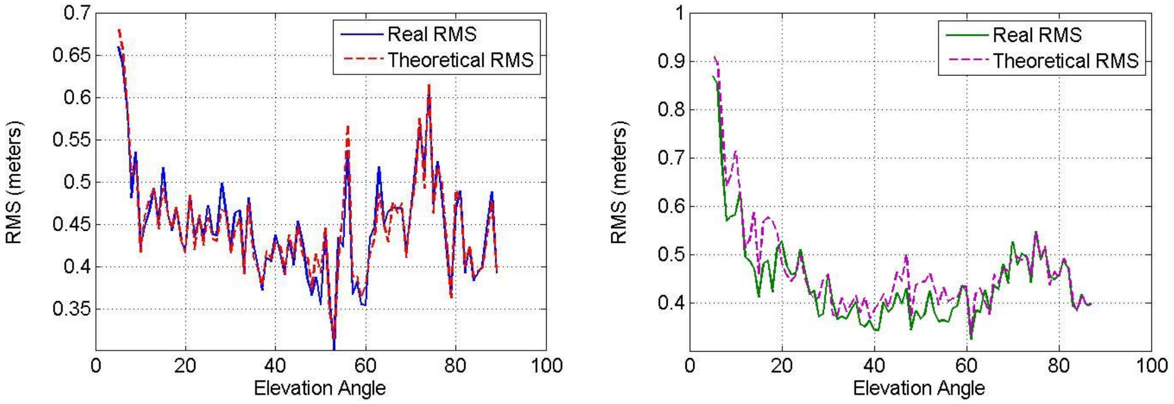

Figure 141 – Real and theoretical I-free CMCs RMS comparison for satellite PRN 1 (left) and PRN 8 (right) Pattonville 50m

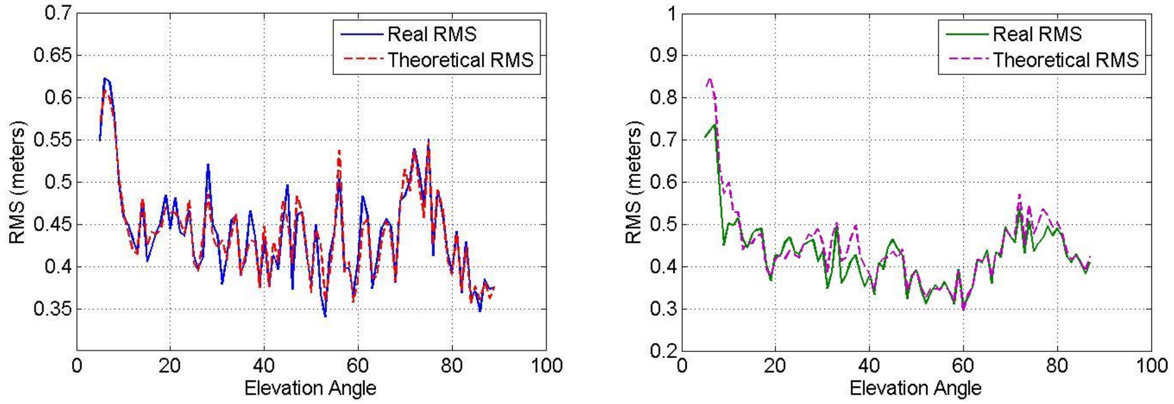

Figure 142 – Real and theoretical I-free CMCs RMS comparison for satellite PRN 1 (left) and PRN 8 (right) Pattonville 100m

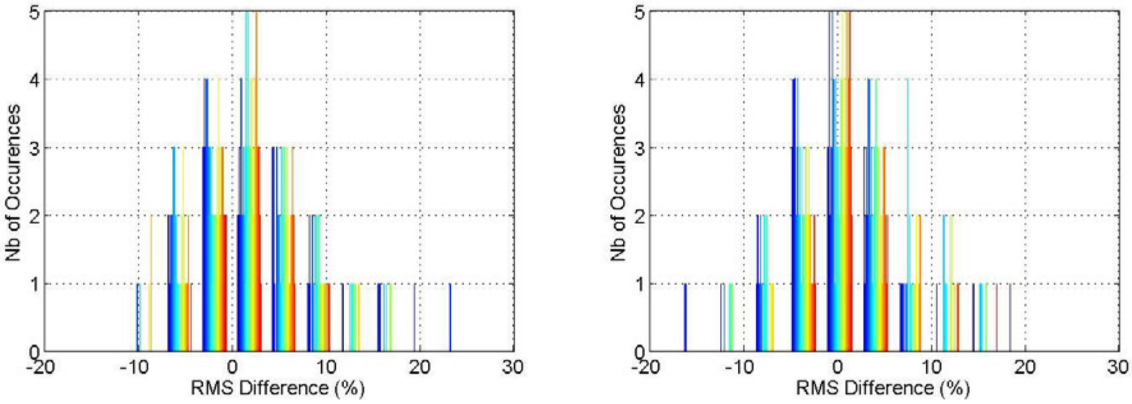

Figure 143 – RMS difference percentage distribution for GPS I-free for Pattonville 50 m (left side) and 100 m (right side), each color represents a satellite

Because the inter-frequencies correlation values, especially in negative values, the RMS of the I-free combination can be bigger than the one computed according the model proposed in literature. This results confirm the need to inflate the I-free model to bind the standard deviation.

C.8 Averaged Noise and Multipath

In this section the results of averaging the CMCs of two antennas are shown for the other days analyzed from Toulouse Blagnac.

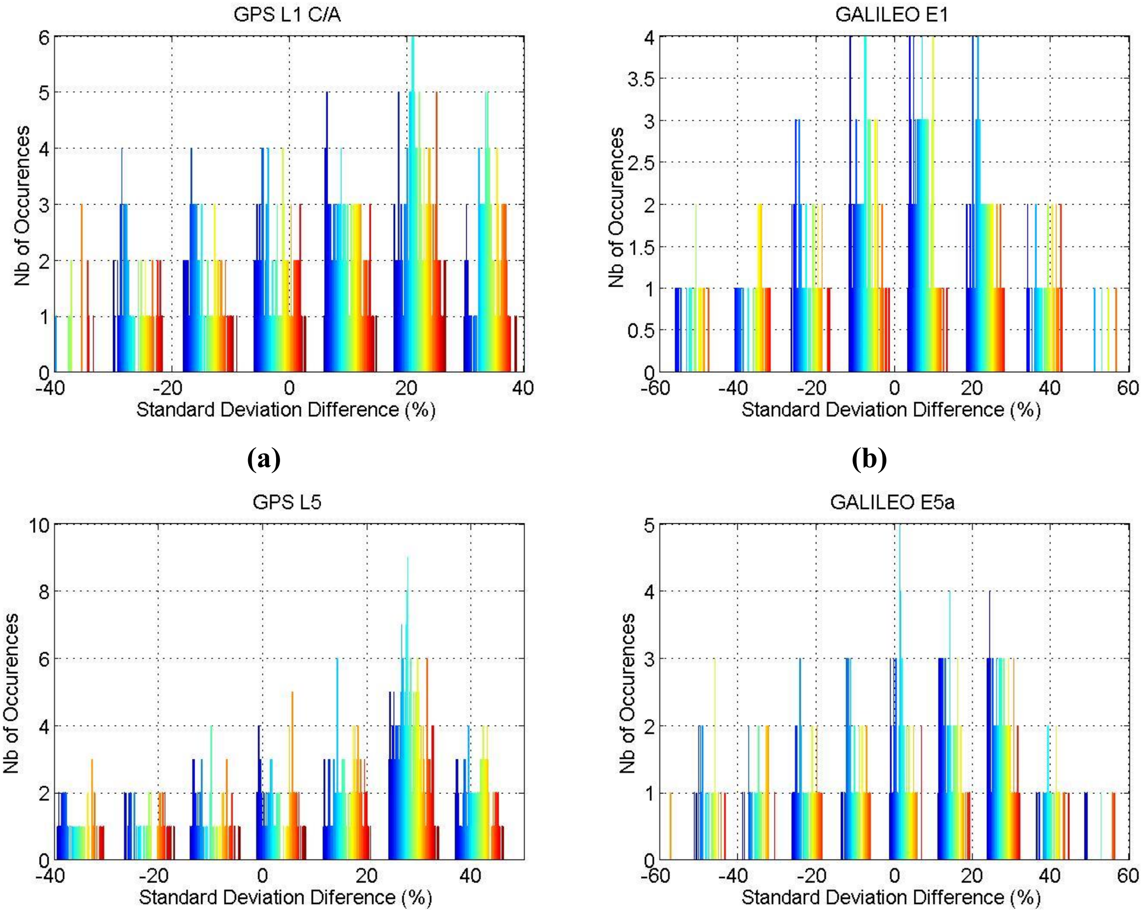

(a) **(b)**

(c) **(d)**

Figure 144 – Standard deviation comparison between empirical and theoretical value for GPS CMCs (a, c) and Galileo CMCs (b, d) 03/04/2016

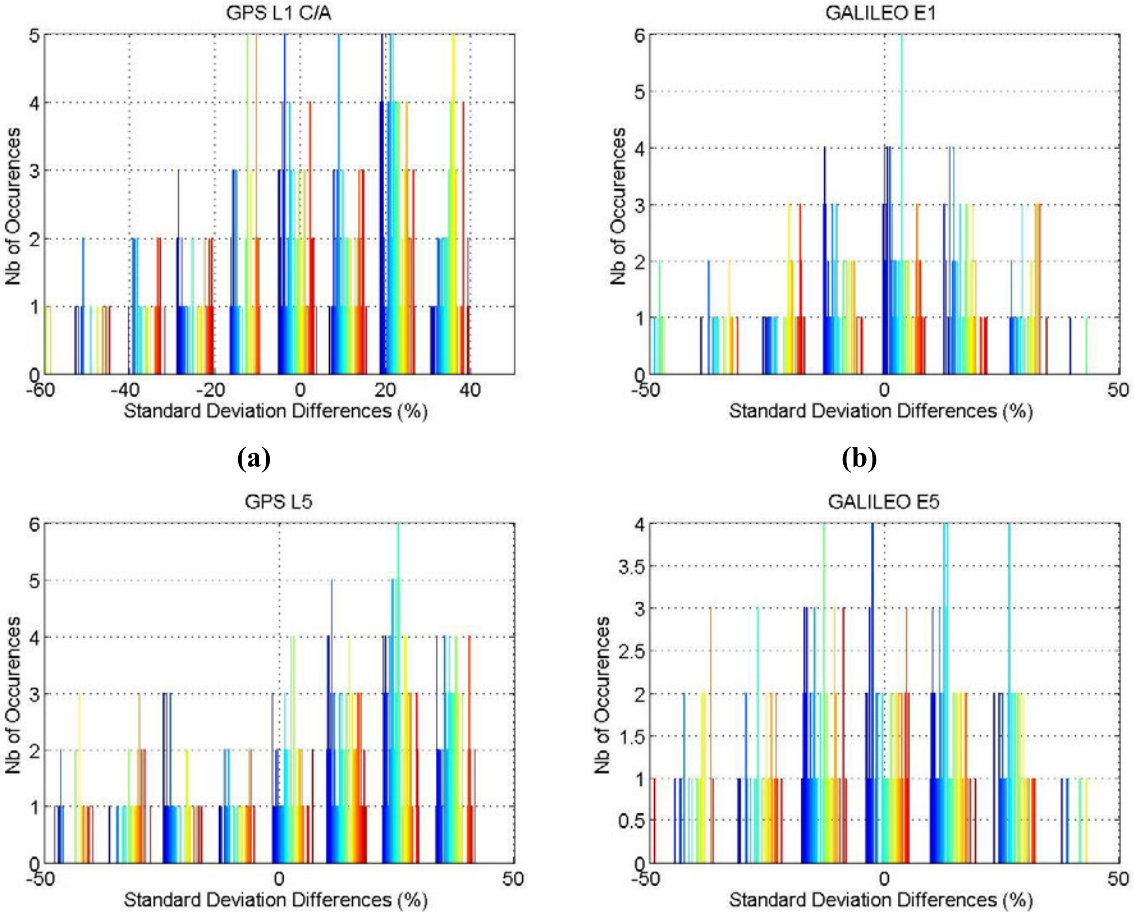

(a) **(b)** **(c)** **(d)**

Figure 145 – Standard deviation comparison between empirical and theoretical value for GPS CMCs (a, c) and Galileo CMCs (b, d) 06/04/2016

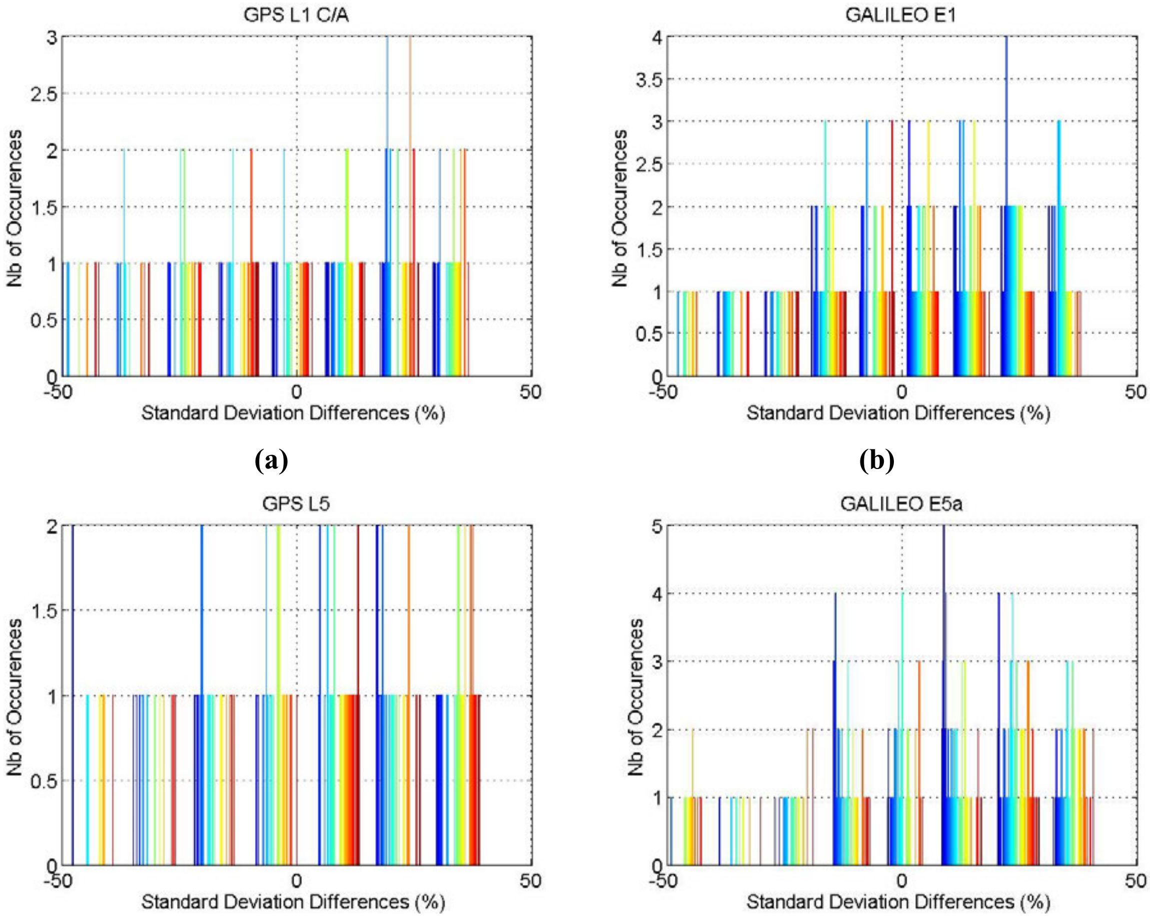

(a) **(b)**

(c) **(d)**

Figure 146 – Standard deviation comparison between empirical and theoretical value for GPS CMCs (a, c) and Galileo CMCs (b, d) 09/04/2016

Resume : Dans le domaine de l'aviation civile les activités de recherche sont guidées par la volonté d’améliorer la capacité de l'espace aérien. En ce que concerne la navigation, les objectifs devraient être atteints par l'amélioration des performances des services existants grâce au développement des nouvelles aides à la navigation. La navigation par satellite, grâce au concept de Global Navigation Satellite System (GNSS), est reconnue comme une technologie clé pour fournir des services de navigation précis avec une couverture mondiale. Le GNSS comprend une fonction de surveillance de l'intégrité fournie par un système d’augmentation en plus de la constellation de base. Un entre eux est le système GBAS qui est actuellement standardisé pour fournir des services de navigation, comme l'approche de précision, jusqu’à la Catégorie I (CAT I) en utilisant les constellations GPS ou Glonass et des signaux dans la bande L1. Ce service est connu sous le nom de GBAS Approach Service Type-C (GAST-C). Afin d'étendre ce concept jusqu'à des approche de précision CAT II/II (GAST-D), les activités de recherche sont en cours. Grâce au développement des nouvelles constellations, Galileo et Beidou, l'avenir du GNSS sera Multi-Constellation (MC) et Multi-Fréquence (MF). En Europe, les activités de recherche se sont concentrées sur un système GNSS Bi-Constellation (Dual-Constellation, DC) basé sur GPS et Galileo. Afin de surmonter les problèmes rencontrés par en fonctionnement Mono-Fréquence (Single-Frequency, SF) en présence d’anomalies ionosphériques, l'utilisation de deux fréquences (Dual-Frequency, DF) a été sélectionnée comme un moyen d'améliorer la détection des anomalies ionosphériques et d'atténuer les erreurs résiduelles ionosphériques. Cependant, l'utilisation de nouveaux signaux et d’une nouvelle constellation, n’apporte pas que des avantages. Elle soulève également une série de défis qui doivent être résolus de profiter pleinement de ce nouveau concept. Dans cette thèse, certains défis, liés à un système DC/DF GBAS ont été étudiés. Un d’entre eux, causé par l'utilisation de nouveaux signaux GNSS, est de déterminer l'impact des sources d'erreur qui sont décorrélées entre la station au sol et l'avion et qui induisent une erreur sur la position estimée. Un autre problème soulevé par l'utilisation de DC/DF GBAS est l'augmentation du nombre de satellites et la présence d'une deuxième fréquence. Cela nécessite un grand nombre de canaux dans les récepteurs pour poursuivre tous les signaux disponibles. Dans cette thèse, l'impact de certains algorithmes proposés dans la littérature a été analysé sur un système GBAS DC simulé. La dernière analyse effectuée dans cette thèse concerne le domaine de la surveillance de l'intégrité. Le travail effectué dans cette thèse a mis l'accent sur le suivi des conditions ionosphériques qui entravent la validation du GAST-D. Une solution combinant un algorithme de type RAIM et les moniteurs prévus en GAST-D est proposée. La prise en compte d’une deuxième constellation avec la même combinaison de fonctions de contrôle d'intégrité a également été étudiée, en tant que mode de repli possible de GAST-F lorsque l'une des deux fréquences est perdue. L'ionosphère n’est pas le seul problème d'intégrité pour GAST-F. D'autres analyses doivent être faites compte tenu de l'impact des nouveaux signaux ou de nouveaux modes de traitement sur les moniteurs existants. Sur ce sujet, l'impact d'un taux de mise à jour plus bas des corrections différentielles sur le moniteur « Excessive Acceleration » a été analysé.

Abstract: In Civil Aviation domain research activities are pointed toward the optimization of the airspace capacity. Focusing on the navigation aspect, the goals are expected to be met by improving performances of the existing services through the developments of new NAVigation AIDS (NAVAIDS). The Global Navigation Satellite System (GNSS) is recognized as a key technology in providing accurate navigation services with a worldwide coverage. GNSS concept includes the provision of an integrity monitoring function by an augmentation system in addition to the core constellations. One of the augmentation systems developed in civil aviation, is the Ground Based Augmentation System (GBAS) that is currently standardized to provide precision approach navigation services down to Category I (CAT I) using GPS or Glonass constellations and L1 band signals denoted as GBAS Approach Service Type-C (GAST-C). In order to extend this concept down to CAT II/III service (GAST-D), research activities is ongoing. Thanks to the deployment of new constellations, Galileo and Beidou, the future of GNSS is envisaged to be Multi-Constellation (MC) and Multi-frequency (MF). In Europe, research activities have been focused on a Dual-Constellation (DC) GBAS services based on GPS and Galileo constellations. Moreover, to overcome the problems experienced by Single-Frequency (SF) GBAS due to ionosphere anomalies, the use of two frequencies (Dual Frequency, DF) has been selected as a mean to improve ionosphere anomalies detection and to mitigate ionosphere residual errors. The use of new signals, however, and a new constellation, does not bring only benefits. It also raises a series of challenges that have to be solved to fully benefit from the new concept. In this thesis, some challenges, related to DC/DF GBAS, have been investigated. Using new GNSS signals is necessary to determine the impact of error sources that are uncorrelated between the ground station and the aircraft and that induce an error on the estimated position. Another issue raised by the use of DC/DF GBAS is the increased number of satellites and the presence of a second frequency. This leads to the constraint of having a big number of channels to track all available signals. The impact of some algorithms proposed in literature has been analyzed on a simulated DC GBAS system. The last analysis performed in this thesis regards some of the challenges in the integrity monitoring domain. The work done has focused on the monitoring of the ionospheric conditions that are impeding GAST-D to be validated. A solution relying on RAIM and foreseen GAST-D monitors is proposed. The consideration of dual constellation in the same mix of integrity monitoring functions has also been studied. The ionosphere is not the only integrity issue for GAST-F. Other analysis have to be done considering the impact of new signals or new processing modes on the existing monitors. Concerning this, the impact of a lower update rate, for the PRC and RRC, on the Excessive Acceleration (EA) monitor has been analyzed.